



HAL
open science

Development and explicit integration of a thermo-mechanical model for saturated clays

Peng-Yun Hong

► **To cite this version:**

Peng-Yun Hong. Development and explicit integration of a thermo-mechanical model for saturated clays. Materials and structures in mechanics [physics.class-ph]. Université Paris-Est, 2013. English. NNT : 2013PEST1028 . pastel-01058617

HAL Id: pastel-01058617

<https://pastel.hal.science/pastel-01058617>

Submitted on 27 Aug 2014

HAL is a multi-disciplinary open access archive for the deposit and dissemination of scientific research documents, whether they are published or not. The documents may come from teaching and research institutions in France or abroad, or from public or private research centers.

L'archive ouverte pluridisciplinaire **HAL**, est destinée au dépôt et à la diffusion de documents scientifiques de niveau recherche, publiés ou non, émanant des établissements d'enseignement et de recherche français ou étrangers, des laboratoires publics ou privés.

THÈSE

Présentée pour obtenir le grade de

**DOCTEUR DE
L'UNIVERSITÉ PARIS-EST**

Discipline : Géotechnique

Présentée par :

Pengyun Hong

Sujet de la thèse :

**Development and explicit integration of a
thermo-mechanical model for saturated clays**

Mémoire provisoire

Jury :

Prof. Henry WONG	Ecole Nationale des Travaux Publics de l'Etat	Rapporteur
Prof. Jean VAUNAT	Technical University of Catalonia	Rapporteur
Prof. Zhen-shun HONG	Southeast University	Examineur
Dr. Xiang-Ling LI	Euridice Group, SCK/CEN	Examineur
Dr. Frédéric COLLIN	Université de Liège	Examineur
Dr. Anh Minh TANG	Ecole des Ponts ParisTech	Examineur
Dr. Jean-Michel PEREIRA	Ecole des Ponts ParisTech	Examineur
Prof. Yu-Jun CUI	Ecole des Ponts ParisTech	Directeur de thèse

Résumé

Cette étude est consacrée à la modélisation du comportement thermo-mécanique des argiles raides saturées et au développement d'un algorithme d'intégration efficace de contrainte correspondant. Le comportement mécanique de l'argile de Boom naturelle dans des conditions isothermes a été caractérisé. Le modèle Cam Clay modifié (MCC) a été ensuite appliquée pour simuler le comportement de l'argile de Boom naturel. Il a été constaté que le MCC donne des prédictions de mauvaise qualité pour le comportement de l'argile de Boom naturel. Ainsi, un modèle Cam Clay (ACC-2) adapté a été développé en introduisant une nouvelle surface de charge et un nouveau potentiel plastique ainsi que d'un mécanisme plastique de Deux-surface. Ce modèle permet la description satisfaisante des caractéristiques principales du comportement mécanique de l'argile de Boom naturelle. De plus, les équations de ce modèle peuvent être formulées mathématiquement comme dans un modèle élasto-plastique classique. L'algorithme d'intégration de contrainte classique peut donc être appliqué.

Les effets thermiques ont été examinés par l'évaluation de la pertinence de trois lois thermomécaniques avancées (Cui et al, 2000; Abuel-Naga et al, 2007; Laloui et François, 2008; 2009). Il apparaît que tous les trois modèles peuvent décrire les caractéristiques principales du comportement thermo-mécanique des argiles saturées. Cependant, chaque modèle a ses limites ou des points peu clairs du point de vue théorique. L'algorithme d'intégration de contrainte du modèle thermo-mécanique de Cui et al. (2000) au point de contrainte a également été développé spécifiquement en utilisant une méthode adaptative du pas de temps. Le temps de calcul nécessaire pour obtenir une précision donnée est ainsi

largement réduit pour des chemins de chargements thermiques et mécaniques.

Un modèle thermo-mécanique à Deux-surface (modèle TEAM) a été développé en se basant sur le mécanisme plastique de Deux-surface. Le modèle proposé a étendu le modèle de Cui et al. (2000) à une formulation de Deux-surface considérant le couplage entre les déformations plastiques des chemins de chargements thermiques et mécaniques. La simulation des essais drainés montre que ce modèle peut décrire les caractéristiques principales thermo-mécaniques de l'argile de Boom naturelle le long de différents chemins de chargements. Le modèle TEAM a finalement été étendu à des conditions non drainées. Après la clarification du concept des contraintes effectives et la définition d'une condition de déformation volumique, le processus d'échauffement non drainé est analysé. La validité des équations thermo-hydro-mécaniques de ce modèle a été examinée en se basant sur des résultats d'essais typiques.

Mots clés : Argile de Boom naturelle; Comportement thermo-mécanique; Elaboration de lois de comportement; Couplage thermo-mécanique; Intégration de contrainte; Intégration temporelle.

Abstract

This study is devoted to the thermo-mechanical constitutive modeling for saturated stiff clays and the development of a corresponding efficient stress integration algorithm. The mechanical behavior of natural Boom Clay in isothermal conditions was first characterized. The Modified Cam Clay model (MCC) was then applied to simulate the natural Boom Clay behavior. It has been found that the MCC gives poor-quality predictions of the natural Boom Clay behavior. Thereby, an adapted Cam Clay model (ACC-2) was developed by introducing a new yield surface and a new plastic potential as well as a Two-surface plastic mechanism. This model allows satisfactory prediction of the main features of the mechanical behavior of natural Boom Clay. Moreover, the constitutive equations of this model can be formulated mathematically as in a classic elasto-plastic model. Thus, the classic stress integration algorithm can be applied.

The thermal effects were considered by assessing the performance of some advanced thermo-mechanical models (Cui et al., 2000; Abuel-Naga et al., 2007; Laloui and François, 2008; 2009). It appears that all the three models can capture the main features of the thermo-mechanical behavior of saturated clays. However, each constitutive model has its own limitations or unclear points from the theoretical point of view. The stress integration algorithm of the thermo-mechanical model proposed by Cui et al. (2000) at the stress point level was also developed using a specifically designed adaptive time-stepping scheme. The computation time required to achieve a given accuracy is largely reduced with the adaptive sub-stepping considered for both mechanical and thermal loadings.

A Two-surface thermo-mechanical model (TEAM model) was developed based on the

Two-surface plastic mechanism. The proposed model extends the model of Cui et al. (2000) to a Two-surface formulation, considering the plastic strain coupling between the thermal and the mechanical loading paths. The simulation of drained tests shows that this model can capture the main thermo-mechanical features of natural Boom Clay along different loading paths. The TEAM model was finally extended to undrained conditions. After setting up an appropriate effective stress principle and defining a volumetric strain condition, the undrained heating process was analyzed. The validity of the thermo-hydro-mechanical constitutive equations was examined based on the data from typical tests.

Keywords: Natural Boom Clay; Thermo-mechanical behavior; Constitutive modeling; Thermo-mechanical coupling; Stress integration; Time integration.

Contents

Résumé	I
Abstract	III
Introduction	1
1 Application of MCC model to natural Boom Clay in isothermal conditions	5
1.1 Introduction	5
1.2 Main characteristics	6
1.3 Elasto-plastic constitutive models	18
1.4 Explicit integration of Modified Cam Clay model	26
1.5 Evaluation of the Modified Cam Clay model	30
1.6 Conclusion	41
2 Development of a Two-surface model for isothermal conditions	43
2.1 Introduction	43
2.2 An adapted Cam Clay model (ACC-1)	45
2.3 A Two-surface model incorporating progressive plastic hardening mechanism	57
2.4 Conclusion	77
3 On some advanced TM models and explicit integration improvements	79
3.1 Introduction	79
3.2 On some advanced thermo-mechanical models for saturated clays	81

3.3	Explicit integration of a thermo-mechanical model for clays	113
4	A Two-surface thermo-mechanical model	157
4.1	Introduction	157
4.2	An isotropic Two-surface thermo-mechanical model	158
4.3	Extension of the model to triaxial stress states	177
4.4	Conclusion	189
5	Extension of TEAM model to undrained conditions	191
5.1	Introduction	191
5.2	Temperature effects under undrained conditions	193
5.3	Undrained heating analyses	194
5.4	Thermo-elasto-plastic constitutive relations	202
5.5	Thermo-mechanical model for undrained heating process	205
5.6	Determination of the additional parameters	207
5.7	Experimental validation	209
5.8	Conclusion	214
	Conclusion	215
	Bibliography	219

List of Figures

1.1	Underground Research Facility HADES at Mol [52].	7
1.2	Isotropic test results.	9
1.3	Oedometer test results.	10
1.4	Loading paths of drained triaxial shear tests	12
1.5	Drained triaxial shear tests under different confining pressures.	12
1.6	Comparison between drained triaxial shear tests CD-4 and CD-7.	13
1.7	Comparison between drained triaxial shear tests CD-3 and CD-6.	14
1.8	Total stress path and effective stress path in test CU-1.	15
1.9	Experimental results from test CU-1.	16
1.10	Pore water pressure versus axial strain in test CU-2 and CU-3.	16
1.11	Critical state line.	17
1.12	Critical state line.	20
1.13	Isotropic compression behavior in the MCC.	21
1.14	MCC yield surface in $p' - q$ plane.	23
1.15	Schematic illustration of the bounding surface.	24
1.16	Influence of parameter λ	33
1.17	Influence of parameter κ	34
1.18	Influence of parameter ν	35
1.19	Influence of parameter p'_{c0}	36
1.20	Influence of parameter M	36
1.21	Comparison between numerical simulations by MCC and experimental results.	38

1.22 Comparison between numerical simulation by MCC and experimental results from oedometer tests.	38
1.23 Numerical simulations of drained triaxial shear tests CD-1 ($p'_0=2.0$ MPa), CD-7 ($p'_0=2.3$ MPa) and CD-4 ($p'_0=2.5$ MPa).	40
1.24 Numerical simulations of drained triaxial shear tests CD-2 ($p'_0=3.0$ MPa), CD-5 ($p'_0=3.5$ MPa) and CD-3 ($p'_0=4.0$ MPa).	40
1.25 Numerical simulations of an undrained triaxial shear test CU-1 ($p'_0=2.3$ MPa).	41
2.1 Classic yield definition from stress–strain response.	47
2.2 Yield stress determination from a drained triaxial shear test CD-1 ($p'_0=2.0$ MPa).	49
2.3 Yield stress determination from a drained triaxial shear test CD-3 ($p'_0=4.0$ MPa).	50
2.4 Yield curve of natural Boom clay.	51
2.5 Evolution of the yield surface in $p' - q$ plane with respect to M_f	53
2.6 Evolution of the yield surface in $p' - q$ plane with respect to k_f	53
2.7 Model prediction for the drained triaxial shear test CD-2 ($p'_0=3.0$ MPa).	56
2.8 Model prediction for the drained triaxial shear test CD-3 ($p'_0=4.0$ MPa).	56
2.9 Schematic representation of the isotropic compression behavior of natural Boom Clay.	58
2.10 Yield surfaces of ACC-2.	60
2.11 Isotropic compression test results in $\varepsilon_v - p'$ plot.	66
2.12 Variations of r with respect to volumetric strain in an isotropic compression test.	67
2.13 Drained triaxial shear test results in $q - \varepsilon_1$ and $\varepsilon_v - \varepsilon_1$ plot.	68
2.14 Variations of r with respect to axial strain in a drained triaxial shear test.	69
2.15 Numerical simulations of isotropic tests.	70
2.16 Numerical simulations of oedometer test.	71

2.17	Numerical simulations of drained triaxial shear test CD-1 ($p'_0=2.0$ MPa). . .	72
2.18	Numerical simulations of drained triaxial shear test CD-4 ($p'_0=2.5$ MPa). . .	73
2.19	Numerical simulations of drained triaxial shear test CD-2 ($p'_0=3.0$ MPa). . .	73
2.20	Numerical simulations of drained triaxial shear test CD-5 ($p'_0=3.5$ MPa). . .	74
2.21	Numerical simulations of drained triaxial shear test CD-3 ($p'_0=4.0$ MPa). . .	75
2.22	Numerical simulations of undrained triaxial shear test CU-1 ($p'_0=2.3$ MPa). .	76
3.1	Isotropic thermo-mechanical loading path followed during TBoom9 test on natural Boom Clay (adapted from Baldi et al. [7]).	85
3.2	Volumetric strain for thermo-mechanical test TBoom9 (from Baldi et al. [7]) obtained from two methods: Method 1 - volumetric strain calculated as three times the axial strain; Method 2 - volumetric strain calculated from the volume of drained out water and the thermal expansion of pore water and solids; (\triangle = path C-D-E; \square = path F-G-H; \circ = path I-J-K).	87
3.3	Thermo-mechanical elastic domain in (p', T) plane.	93
3.4	Evolution of yield surface under thermo-mechanical loading in $p' - T$ plane. .	95
3.5	Thermo-mechanical yield limits (TY and LY).	101
3.6	Comparison between observed and predicted thermally induced volumetric strain in Simulation 1.	102
3.7	Comparison between Simulation 1 and Simulation 2 by the three models: (a) Model C, (b) Model A, (c) Model L.	104
3.8	Isotropic thermo-mechanical loading path of Simulation 3.	105
3.9	Predicted response of the soil in Simulation 3.	106
3.10	Loading path in the effective stress and temperature space.	107
3.11	Evolution of LY curve in a heating-cooling cycle in Model A. (a) Heating process, (b) Cooling process at T_1 and (c) Cooling process at T_0	109
3.12	Evolution of TY curve during heating process in Model A.	110

3.13	Plastic mechanism over a mechanical isotropic loading-unloading-reloading cycle in Model L.	110
3.14	Yield surfaces in the $(p' - q - T)$ space.	118
3.15	Yield locus in (a) $(p' - q)$ plane at two different temperatures (with $T > T_0$) and (b) $(p' - T)$ plane.	120
3.16	Different possibilities of activation of the plastic mechanisms during the elastic trial.	131
3.17	A special situation for TY surface intersection.	133
3.18	TY and LY intersection.	138
3.19	Isotropic thermo-mechanical paths.	150
3.20	Comparison between experimental results ([7]) and numerical predictions for Boom clay.	151
3.21	Thermo-mechanical loading paths in triaxial stress space.	152
3.22	Drained triaxial compression tests on Boom Clay in Path 1 and 2 at 25°C.	152
3.23	Numerical prediction of the volumetric strain induced by temperature changes.	153
3.24	Drained triaxial compression tests on Boom Clay in Path 3 at 60°C.	154
4.1	(a): Determination of the yield temperature for remolded Boom clay under different isotropic stresses according to Sultan et al. [80], (b): Comparison between the experimental yield points and the proposed thermal yield curve (TY).	161
4.2	(a): Shape of LY in (p', T) plane and thermo-mechanical loading path, (b): Volumetric response of the thermo-mechanical loading for a normally consolidated clay in the $(v,')$ space.	162
4.3	Inner yield surfaces and Yield surfaces.	165
4.4	Comparison between predicted and measured results on reconstituted Pontida Clay [6].	174

4.5	Comparison between the experimental results and numerical predictions for natural Boom Clay.	175
4.6	Test program for TBoom10 and TBoom11 tests.	176
4.7	Numerical simulations of isotropic compression tests at different temperatures.	177
4.8	Thermo-mechanical loading paths in triaxial stress space.	178
4.9	Comparison of drained triaxial shear at 25 °C and 76 °C from a same/similar initial mean effective stress.	179
4.10	Critical state line.	180
4.11	Yield stress determination for a drained triaxial shear test TCD-1 ($T=76^{\circ}\text{C}$, $p'_0=2.5$ MPa).	182
4.12	Yield stress determination for a drained triaxial shear test TCD-2 ($T=76^{\circ}\text{C}$, $p'_0=3.8$ MPa).	183
4.13	Yield surface of natural Boom clay at 25°C and 76°C	184
4.14	Yield locus in (a): ($p' - q$) plane at two different temperatures (with $T_1 > T_0$) and (b): ($p' - T$) plane.	185
4.15	Numerical simulations of drained triaxial compression tests CD-4 ($T= 25^{\circ}\text{C}$, $p'_0=2.5$ MPa) and TCD-1 ($T= 76^{\circ}\text{C}$, $p'_0=2.5$ MPa).	188
4.16	Numerical simulations of drained triaxial compression tests CD-3 ($T= 25^{\circ}\text{C}$, $p'_0=4.0$ MPa) and TCD-2 ($T= 76^{\circ}\text{C}$, $p'_0=3.8$ MPa).	188
5.1	Saturated soil: soil skeleton and pore water.	194
5.2	Numerical simulation results with different C_s values.	205
5.3	Different possibilities during undrained heating process.	206
5.4	Variation of properties of free water with temperature and pressure: (a) thermal expansion coefficient; (b) compressibility.	208
5.5	Thermal expansion coefficients of free bulk water and adsorbed pore water (Simulation 1 and 2, respectively).	210
5.6	Undrained heating test on natural Boom clay from 25°C to 65°C.	211

5.7 Thermal expansion coefficients of free bulk water and adsorbed pore water
(Simulation 3 and 4, respectively). 212

5.8 Undrained heating-cooling test on reconstituted Pontida Clay. 213

List of Tables

1.1	Physical properties of Boom Clay.	7
1.2	Summary of the isotropic tests reported in literature.	9
1.3	Summary of the odometer tests reported in literature.	10
1.4	Summary of the drained triaxial tests reported in literature.	11
1.5	Summary of the undrained triaxial tests reported in literature.	15
1.6	MCC parameters for the natural Boom Clay.	32
2.1	Summary of yield points from the drained triaxial shear tests.	48
2.2	ACC-1 parameters for natural Boom Clay.	55
2.3	ACC-2 parameters for natural Boom Clay.	69
3.1	Main thermo-mechanical equations	90
3.2	Volumetric thermal expansion coefficient for natural Boom Clay (TBoom9) obtained from volumetric strains estimated using Method 1 and Method 2	92
3.3	Input parameters for the simulations of natural Boom Clay behaviour	100
3.4	TM model: equations and parameters.	122
3.5	Euler method with a constant loading step scheme for triaxial test.	146
3.6	Modified Euler method with a sub-stepping scheme for triaxial test.	146
3.7	Model parameters for Boom clay.	148
3.8	Euler method with a constant loading step scheme for heating test.	148
3.9	Modified Euler method with a sub-stepping scheme for heating test.	148

4.1	Model parameters for the validation of the proposed model on natural Boom Clay and reconstituted Pontida Clay.	173
4.2	Model parameters for natural Boom Clay.	187
5.1	Numerical simulations of an undrained heating test with different values of C_s .	204

Introduction

Deep geological repository of high-level radioactive waste (HLW) is being investigated by many countries worldwide. This disposal concept is based on the use of geological and engineered barriers to ensure the isolation. For the engineered barriers, compacted bentonite-based materials are in general used, while for the geological barriers, relatively homogeneous clay formations (stiff clays, claystones etc.) or salt formations are preferred.

In the Belgian program on the geological disposal of nuclear waste disposal, natural Boom Clay (160 to 270 m deep) under the Mol-Dessel nuclear site is considered as a possible host formation. Under the storage conditions, the natural Boom Clay will undergo the effects of temperature changes. Moreover, these effects are coupled to the mechanical ones. In this regard, it is important to investigate its thermo-mechanical behavior.

In this context, a number of laboratory studies have been performed on natural Boom Clay under different loading paths (e.g. Horseman et al., 1987; Baldi et al., 1991; Sultan, 1997; Coll, 2005; Le, 2008). Based on the experimental evidence, some advanced thermo-mechanical constitutive models were developed (Cui et al., 2000; Abuel-Naga et al., 2007; Laloui and François, 2008; 2009). It appears that all the three models can capture the main features of the thermo-mechanical behavior of saturated clays. However, each constitutive model has its own limitations or unclear points from the theoretical point of view. In addition, the experimental results used for validating these models are not always clear. In order to model the thermo-mechanical behavior of saturated stiff clays like Boom clay, it is necessary to revisit the available and relevant experimental results as well as the constitutive models including the relatively simple one as the Modified Cam Clay model

(MCC). Especial attention should be paid to the undrained heating conditions since in practice the excess of pore water pressure represents a critical situation.

On the other hand, when considering the constitutive modeling of the thermo-mechanical behavior of clays, efficient stress integration algorithm should be adopted. However, this kind of studies conducted till now mainly concern isothermal constitutive models, and few studies involve numerical implementation of thermo-mechanical models for saturated clays. The introduction of temperature as an extra-variable and the existence of thermo-mechanical couplings require significant changes of the integration algorithm.

The main objectives of this study are:

1. To characterize the behavior of natural Boom Clay under different loading conditions on the basis of the existing experimental data.
2. To develop a constitutive model that accounts for the key features of the behaviour of natural Boom Clay, in terms of both mechanical responses and coupled thermo-mechanical responses.
3. To develop an efficient stress integration algorithm for the thermo-mechanical model within the framework of explicit integration scheme.

Following these objectives, the study is conducted in steps, starting from a constitutive model for isothermal conditions and then extending it to non-isothermal conditions.

The dissertation is composed of 5 chapters.

The first chapter focuses on the assessment of the relevance of Modified Cam Clay model for the natural Boom Clay under isothermal conditions. The main characteristics of the natural Boom Clay are first presented based on the results from the laboratory tests. The performance of MCC in describing the mechanical behavior of natural Boom Clay is then assessed by comparing its predictions with the experimental results.

The second chapter is devoted to the development of a Two-surface model namely ACC-2 for isothermal conditions. Some improvements are introduced in order to better describe the behavior of Boom Clay. These improvements include the adoption of a new yield surface

and a new plastic potential as well as an additional plastic mechanism enabling a flexible description of the variations of the plastic modulus throughout the plastic loading. This model is finally validated by numerical simulations of laboratory tests on natural Boom Clay.

The third chapter corresponds to the work presented in two papers. The first one, published in the *Journal of Computers and Geotechnics*, assesses the performance of the recent advanced thermo-mechanical models proposed by Cui et al., (2000), Abuel-Naga et al., (2007) and Laloui and François (2008, 2009) in terms of elasto-plasticity and thermodynamic requirements as well as their capabilities to capture the main experimental evidence. The second, published in the *International Journal for Numerical and Analytical Methods in Geomechanics*, develops a numerical integration algorithm for the thermo-mechanical model proposed by Cui et al., (2000) using an explicit scheme. Note that the conclusions drawn can be generalized to other thermo-mechanical models.

The fourth chapter develops a Two-surface thermo-mechanical model. For this purpose, the thermo-mechanical model proposed by Cui et al., (2000) is improved by linking the thermal plastic strain and the mechanical one and defining a unique plastic strain along different loading paths. The model is then extended to a Two-surface thermo-mechanical model by applying the Two-surface model developed in Chapter 2 for isothermal conditions. The proposed model termed as TEAM model is validated based on the available experimental data.

The fifth chapter extends the TEAM model developed in Chapter 4 to undrained conditions. The main features of temperature effects on the undrained behavior of saturated clays are briefly analyzed. After setting up an appropriate effective stress principle and defining a volumetric strain condition, the undrained heating process is analyzed using the TEAM model. The performance of TEAM model for undrained heating condition is finally examined based on the data from typical tests.

Nota Bene

Throughout this dissertation, the sign convention of soil mechanics is used, where con-

tractive strain and compressive (effective and total) stress are taken as positive and expansive strain and tensile (effective and total) stress are negative. The bulk moduli and the thermal expansion coefficients are always taken as positive.

Chapter 1

Application of Modified Cam Clay model to natural Boom Clay in isothermal conditions

1.1 Introduction

In the Belgian program on geological disposal for nuclear waste disposal, Boom Clay (160 to 270 m deep) under the Mol-Dessel nuclear site is considered as a possible host formation and has been investigated widely over the last decades. For the purpose of design and safety assessment, it is important to characterize the mechanical behavior of natural Boom Clay and establish an appropriate mechanical constitutive model to describe the clay behavior.

Prior to theoretical analysis, relevant results from laboratory test on natural Boom Clay are required to be collected. Examination of the existing experimental data about natural Boom clay shows that the saturation process under a low stress gives rise to soil swelling, thereby modifying the soil microstructure, and in turn the soil hydro-mechanical behavior [28]. Thus, the representative data are those from the tests with a specific procedure allowing the initial state to be preserved.

6 Application of MCC model to natural Boom Clay in isothermal conditions

The concept of Critical State [69] is one of the most important developments in soil mechanics. Within this framework, number of models has been developed for describing soil behavior, among them the Modified Cam Clay model (MCC). The MCC is now widely used for its good description of the main features of soft clay behavior [67]. To evaluate the performance of MCC on natural Boom Clay, in this study, numerical simulation tests are performed. Emphasis is put on the investigation of the effective stress integration procedure.

In this chapter, the main characteristics of the nature Boom Clay are presented, including the initial state, the physical properties and the isothermal mechanical behavior. For the constitutive modeling, the commonly used models within the framework of critical state theory are firstly reviewed. Then, the numerical integration of MCC at the stress point level is implemented using an explicit scheme with an adaptive time stepping as proposed by Sloan et al. [75]. The performance of MCC in describing the mechanical behaviour of natural Boom Clay is finally assessed by comparing its predictions to the experimental results.

1.2 Main characteristics

1.2.1 Geological origins and physical properties

The samples used in the experimental tests considered are taken from the underground research facility (URF), namely HADES, in Mol-Dessel (Belgium) at a depth of 223 m (see Figure 1.1).

The Boom Clay at Mol is a thick deposit of overconsolidated marine clay and belongs to the Oligocene series (around 30 million years ago) [38]. The Boom Clay is chosen as a candidate host formation for the nuclear waste disposal due to its favorable properties: (1) it has been steady for a long geological age; (2) it has a very low permeability and thus a good retention capacity of radionuclide; (3) it is a plastic clay and has a swelling potential high enough to ensure its function of self-sealing [12, 18].

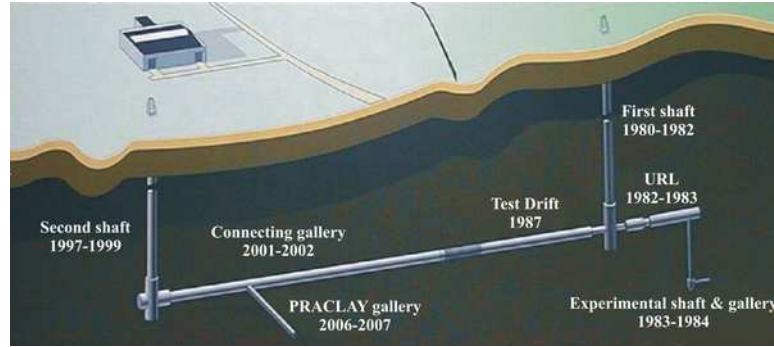


Figure 1.1: Underground Research Facility HADES at Mol [52].

Table 1.1: Physical properties of Boom Clay.

Density ρ (Mg/m ³)	2.026
Water content w (%)	22-27
Plastic limit w_P (%)	23-29
Liquid limit w_L (%)	55-80
Plasticity index I_P (%)	32-51

Boom Clay samples from HADES present heterogeneity and have a relatively large variation in terms of mineralogy and water content, as reported by several researchers [7, 10, 60]. It is mainly constituted of clay minerals (30% to 70%) dominated by illite (20%-30%), kaolinite (20%-30%) and smectite (10%-20%). The non-clay part mainly consists of quartz (25%) and feldspar. A small part of pyrite and calcite is also found in it [18, 66]. Some basic physical properties of Boom Clay are summarized in Table 1.1.

Baldi et al. [7] pointed out that the variability in physical properties (such as the liquid limit, plasticity index) are due to the variability in mineral compositions and water content of soil samples. Romero [66] indicated that this variability may be related to the lithological and stratigraphic difference in the Boom Clay formation.

1.2.2 Mechanical behavior from the laboratory tests

As mentioned above, Boom clay samples are taken at a depth of 223 m in the URL of Mol. At this depth, the total vertical stress is around 4.5 MPa and the pore pressure is equal to 2.2 MPa, defining an effective stress of 2.3 MPa [11]. The value of K_0 is about 0.8,

8 Application of MCC model to natural Boom Clay in isothermal conditions

that is determined based on the in-situ stresses estimation [39]. The initial effective stress state can then be approximated by an isotropic one in the laboratory tests.

A number of experimental results show that the saturation process in the sample preparation plays an important role in the mechanical response of Boom Clay. Significant swelling occurs while saturating sample under low effective stress states (referred to as Process I) [7, 18, 51, 80]. A volumetric swell of around 6 to 11% was measured by Coll [18] during the sample saturation process in the triaxial apparatus under a mean effective stress of 0.4 MPa. Similarly, a swell of around 18% was found by Le [51] under zero stress during the saturation process in oedometer. Realizing that swelling may alter the mechanical behaviour of natural Boom Clay, Balid et al. [7] improved the saturation process to minimize this relatively high swelling by loading the sample at its natural water content to the in-situ effective stress state (around 2.3 MPa) under drained conditions prior adding water for saturation (referred to as Process II). A reduced swelling was identified by Process II. Indeed, a volumetric swell of around 1.5% was measured by Le [51] by this process, much smaller than that by Process I. It is observed that the samples with different saturation processes present different mechanical behavior since they show significantly different values of yield stress. A preconsolidation pressure of 0.37 MPa, even lower than the in-situ effective stress, was measured by Sultan [80] using Process I, whereas a value of around 6 MPa was obtained using Process II by other researchers [7, 18, 51]. In the former case, the peculiar behaviour is due to the changes in microstructure induced by this swelling process. Therefore, only the data obtained from the experiments with Process II are representative of the natural Boom Clay, and these data are considered in this study. The results that are taken into account include those from isotropic compression tests, oedometer compression tests and triaxial shear tests, carried out in different laboratories.

1.2.2.1 Isotropic tests

Various isotropic compression tests on natural Boom Clay samples have been performed, some of which are summarized in Table 1.2.

Table 1.2: Summary of the isotropic tests reported in literature.

Test	Reference	Sample depth (m)	Initial void ratio	Void ratio after saturation
Iso-1	Baldi et al. (1991)	223	0.677	-
Iso-2	Le (2008)	223	0.620	0.590
Iso-3	Deng et al. (2010)	223	-	0.610

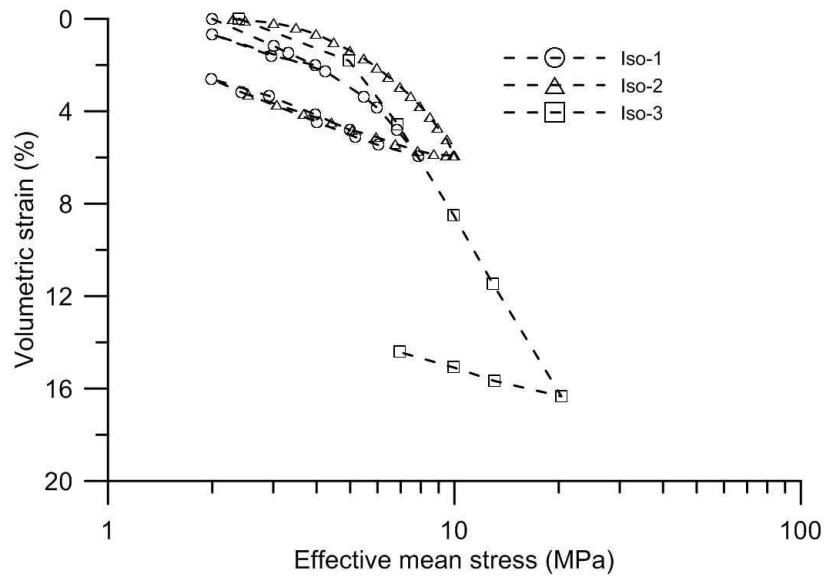


Figure 1.2: Isotropic test results.

All the samples were saturated under a pressure close to the in-situ mean effective stress (2 MPa in Iso-1, 2.3 MPa in Iso-2 and Iso-3), the back pressure being 2 MPa in Iso-1, 1 MPa in Iso-2 and Iso-3. After completion of the saturation process, isotropic compression was applied under drained conditions: in Iso-1, loading isotropically up to a mean effective stress of 4 MPa and then unloading to 2 MPa, reloading to 8 MPa, unloading again to 2 MPa, and reloading again to 5 MPa; in test Iso-2, loading isotropically up to a mean effective stress of 10 MPa and then unloading to 2 MPa; in test Iso-3, loading isotropically up to 20 MPa and then unloading to 7 MPa. The volumetric strains were obtained from the volume of drained-out water in all the three tests. The results are shown in Figure 1.2 in terms of volumetric strain versus mean effective stress.

10 Application of MCC model to natural Boom Clay in isothermal conditions

Table 1.3: Summary of the odometer tests reported in literature.

Test	Reference	Sample depth (m)	Initial void ratio	Void ratio after saturation
Oed-1	Horseman et al. (1987)	247	-	0.608
Oed-2				0.615
Oed-3	Baldi et al. (1991)	223	0.696-0.717	-

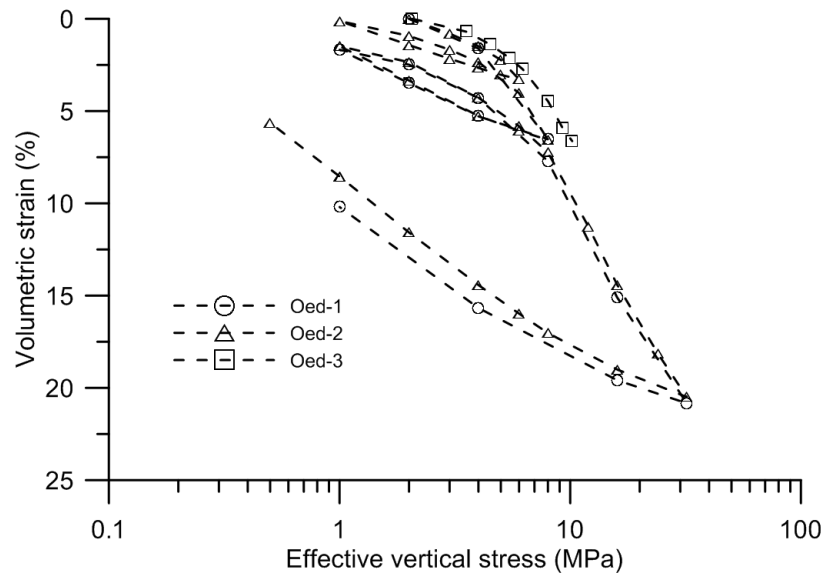


Figure 1.3: Oedometer test results.

1.2.2.2 Oedometer tests

The oedometer tests conditions reported are summarized in Table 1.3.

In Oed-1, the sample was saturated under a vertical effective stress of 1 MPa and no obvious swelling was found in the saturation process. Compression cycles were applied under drained conditions: 2; 8; 1; 32; 1 MPa of vertical effective stress in Oed-1 test and 2; 6; 1; 8; 1; 32; 0.5 MPa of effective vertical stress in Oed-2 test. In Oed-3, the sample was saturated under a vertical effective stress of 2.3 MPa. The subsequent loading stages are as follows: 2; 10 MPa of effective vertical stress.

The oedometer test results are shown in Figure 1.3 in terms of volumetric strain versus mean vertical stress.

Table 1.4: Summary of the drained triaxial tests reported in literature.

Test	Reference	Sample depth (m)	Water content (%)	Mean effective stress before shearing	Initial void ratio	Shear rate ($\mu\text{m}/\text{min}$)
CD-1	Baldi et al. (1991)	223	24.8-26.5	2	-	
CD-2				3		
CD-3				4		
CD-4	Le (2008)	223	19.6	2.5	0.59	1.00
CD-5			20.0	3.5	0.56	0.90
CD-6			20.3	4.0	0.51	0.50
CD-7	Coll (2005)	223	23.8	2.3	0.61	0.25

1.2.2.3 Drained triaxial shear tests

The drained triaxial tests reported are summarized in Table 1.4.

The effective stress paths are shown in Figure 1.4, with a saturation process following Process II, an isotropic loading path and a triaxial shear path. In CD-1, the triaxial shearing started from an isotropic effective stress of 2 MPa. Two unloading-reloading cycles were applied at 0.6% and 2.8% axial strain, respectively. In CD-2, an isotropic loading was performed by applying an isotropic effective stress from 2 MPa to 3 MPa. At 3 MPa, the shear phase was started and two unloading-reloading cycles were applied at 0.56% and 2.13% axial strain, respectively. In CD-3, an isotropic loading was performed by applying an isotropic effective stress from 2 MPa to 4 MPa under drained conditions. At 4 MPa, the shear phase was started and two unloading-reloading cycles were applied at 0.6% and 3.8% axial strain, respectively. In CD-4, CD-5, CD-6 and CD-7, the samples were loaded from an isotropic mean effective stress of 2.5, 3.5, 4 and 2.3 MPa, respectively, and then sheared under constant confining pressures.

The results from drained shear tests are shown in Figure 1.5 in terms of deviator stress and volumetric strain versus axial strain.

Figures 1.6 and 1.7 compare the results from CD-4 ($p'_0 = 2.5$ MPa) by Le [51] and CD-7 ($p'_0 = 2.3$ MPa) by Coll [18], test CD-3 ($p'_0 = 4$ MPa) by Baldi et al. [7] and test CD-6 ($p'_0 = 4$ MPa) by Le [51]. Note that these tests were carried out under the same/similar

12 Application of MCC model to natural Boom Clay in isothermal conditions

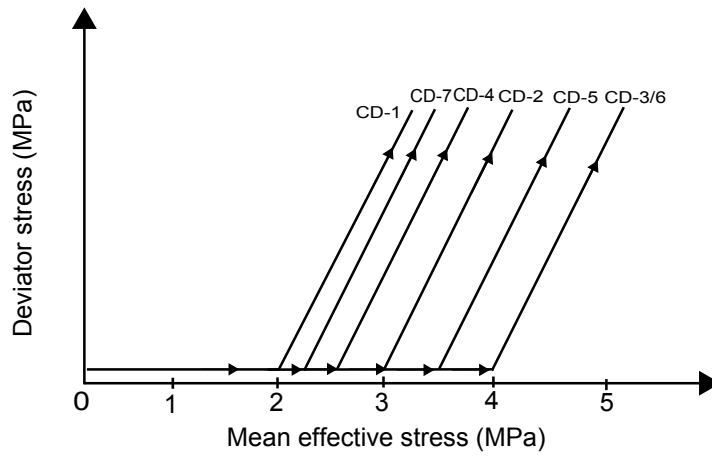


Figure 1.4: Loading paths of drained triaxial shear tests .

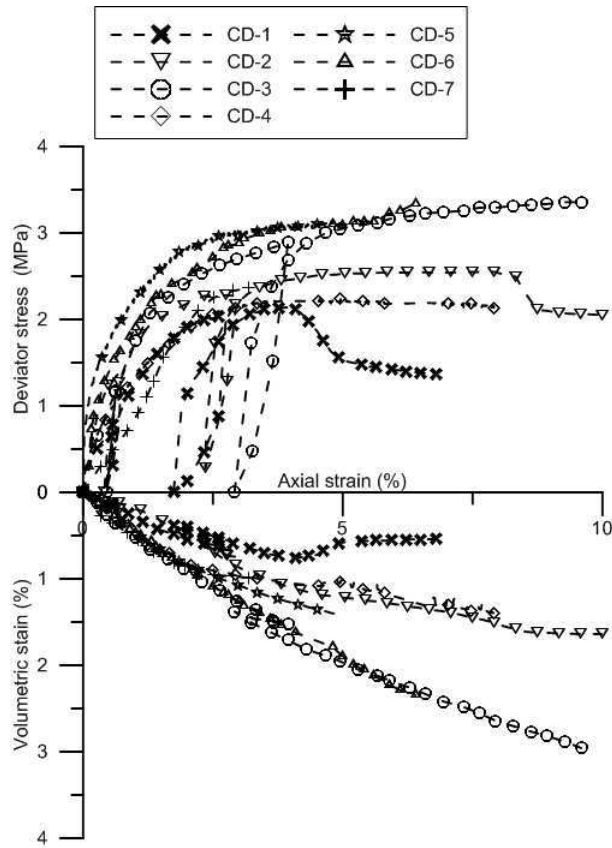


Figure 1.5: Drained triaxial shear tests under different confining pressures.

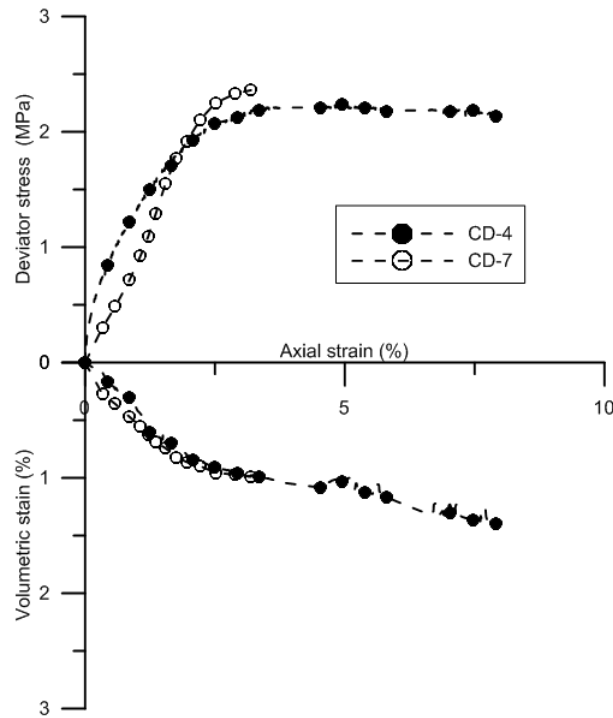


Figure 1.6: Comparison between drained triaxial shear tests CD-4 and CD-7.

initial mean effective stress in different laboratories. Between CD-4 and CD-7 (See Figure 1.6), the experimental results of the two tests agree well in the volumetric strain-axial strain plane but relatively large difference appears in the stress-axial strain plane. The experimental results of CD-7 shows relatively lower deviator stress at small axial strains (around 0-2%) but higher deviator stress at larger axial strains (around 2-5%) in comparison with those of CD-4. This difference may be related to the different physical properties or experimental operations (e.g. shear rate), etc. for different samples. As presented in Figure 1.7, the experimental results from CD-3 agree well with the experimental results from test CD-6 in both volumetric strain-axial strain plane and stress-axial strain plane. On the whole, similar stress-strain behaviors were identified in different laboratories along a same or similar loading path.

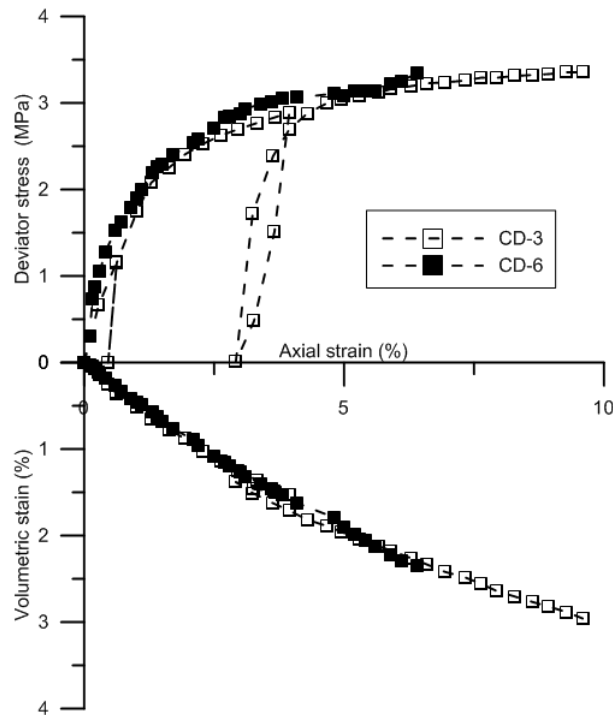


Figure 1.7: Comparison between drained triaxial shear tests CD-3 and CD-6.

1.2.2.4 Undrained triaxial shear tests

As pointed out in the final report of Timodaz project [52], a number of undrained shear tests were realized on natural Boom Clay but without pore pressure measurement. Recently, several conventional undrained triaxial tests on natural Boom Clay have been performed in the 3S-R laboratory of Grenoble University and the laboratory of University of Liege [17]. These tests are summarized in Table 1.5. In CU-1, the sample was saturated in the in-situ state defined by a mean effective stress of 2.3 MPa with a back pressure of 2.2 MPa. In CU-2 and CU-3, the samples were isotropically loaded up to a mean effective stress of 2.5 MPa and then saturated. After completion of the saturation process, the sample was isotropically loaded in undrained condition until a total confining pressure of 4.5 MPa and a pore water pressure of 1 MPa were reached. This defined a mean effective stress of 3.5 MPa. The sample was then sheared under constant confining pressure.

Figures 1.8 and 1.9 present the experimental results from test CU-1. As shown in Figure 1.8, the effective stress path seems parallel to the total stress path with small variations

Table 1.5: Summary of the undrained triaxial tests reported in literature.

Test	Reference	Sample depth (m)	Water content (%)	Mean effective stress before shearing	Initial void ratio	Shear rate (MPa/s)
CU-1	TIMODAZ report (2007)	223	-	2.3	-	-
CU-2			26.8	3.5	0.54	5×10^{-5}
CU-3						5×10^{-6}

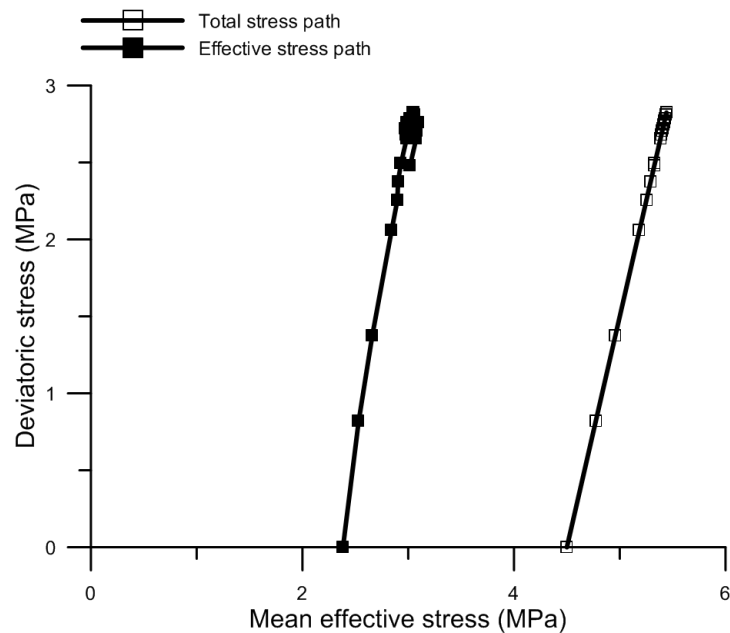


Figure 1.8: Total stress path and effective stress path in test CU-1.

of the total pore water pressure. This can be clearly seen from Figure 1.9. Low values of excess pore water pressure are measured with a maximum value of 0.2 MPa at the initial stage followed by stabilization. It is questionable that the sample is under a fully undrained condition.

Figure 1.10 presents the experimental results from CU-2 and CU-3 in terms of pore water pressure versus axial strain. The measured pore water pressures are unstable and erratic. In CU-2, the initial pore water pressure should be 1 MPa as described in the experimental program but the measured value is around 1.5 MPa. This shows that the actual situation of the samples is undefined.

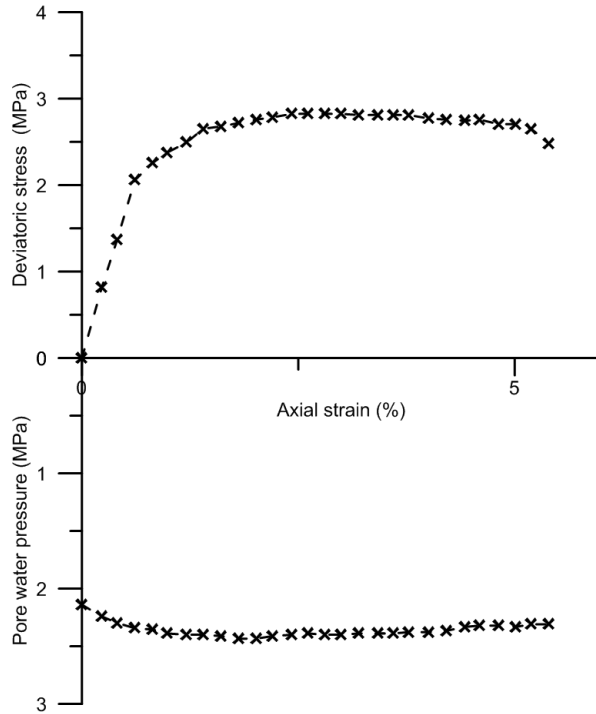


Figure 1.9: Experimental results from test CU-1.

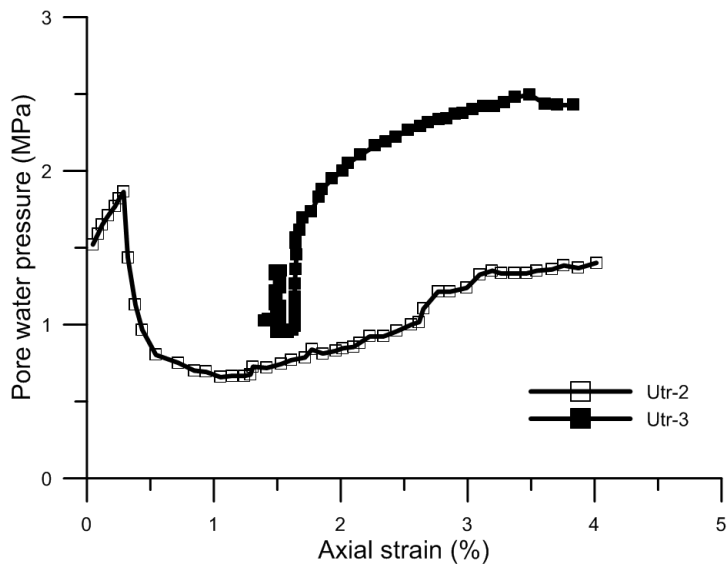


Figure 1.10: Pore water pressure versus axial strain in test CU-2 and CU-3.

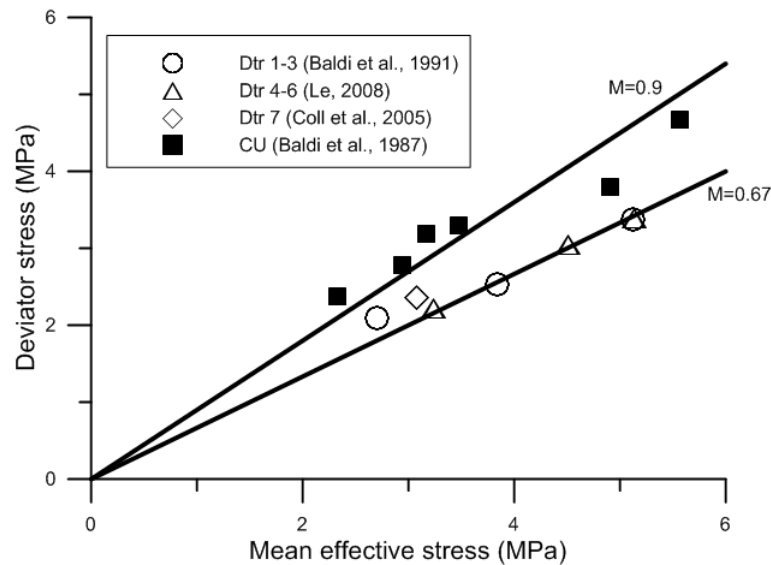


Figure 1.11: Critical state line.

A typical series of undrained triaxial tests with pore water pressure measurement were reported by Baldi et al. [5]. The results obtained are commonly used to describe the undrained shear behaviour of Boom Clay. Note however that in these tests the soil samples were saturated at low effective stress state. The values of parameter M (slope of critical state line in $p' - q$ plane) range from 0.87 to 1, with an average value of 0.9, significantly higher than that determined from the drained triaxial tests, as shown in Figure 1.11.

The difference of the critical shear strength between drained and undrained triaxial tests may be due to:

1. The samples for the undrained triaxial tests were not saturated under the in-situ effective stress and significant swelling was observed. As mentioned previously, this influences the mechanical behavior of natural Boom Clay;
2. The hydraulic conditions are different;
3. The pore water pressure measured from the bottom of the sample may be smaller than the actual one within the sample. The measured values may be influenced by several factors such as shear rate.

Obviously, the existing results are not concluding for the undrained condition and fur-

18 Application of MCC model to natural Boom Clay in isothermal conditions

ther experimental investigation is required to well characterize the undrained shear behaviour of natural Boom Clay. In this study, only purely numerical simulation is performed to verify the relevance of some models in describing the undrained behavior.

1.2.2.5 Remarks on the mechanical behavior of natural Boom Clay

The laboratory test results (isotropic, odometer, drained and undrained triaxial shear tests) obtained with an appropriate saturation process as mentioned above are gathered. Comparison between the results along a same or similar loading path shows that the results obtained in different laboratories are quite consistent except that from the undrained triaxial tests. Thus, a global description of these results is possible. It is important to note that there is a highly non-linear stress-strain response after brief linear stress-strain behaviour. Further, significant irreversible strain is observed in the unloading-reloading cycle at a small strain (0.6%), showing that the purely elastic zone is quite limited. Moreover, smooth compression behaviour without sharp change is observed, indicating a smooth transition from elastic to plastic response.

1.3 Elasto-plastic constitutive models

1.3.1 The critical state concept

The critical state concept is initially introduced and formulated in the triaxial stress space ($p' - q$) [69]. The mean effective stress $p' = p - u$ and deviator stress q are defined using the effective stress tensor $\sigma'_{ij} = \sigma_{ij} - u \delta_{ij}$, $i, j = \{1, 2, 3\}$ as follows (using the Einstein's notation repeated indices mean summation):

$$p' = \frac{1}{3} \sigma'_{ij} \delta_{ij} \quad ; \quad q = \sqrt{\frac{3}{2}} \sqrt{s_{ij} s_{ij}} \quad (1.1)$$

with u , the pore water pressure; δ_{ij} , Kronecker's symbol, and $s_{ij} = \sigma'_{ij} - \frac{1}{3} p' \delta_{ij}$, the deviator stress tensor.

Most critical state models are elaborated and verified in the conventional triaxial test conditions. In the conventional triaxial stress space, the mean effective stress p' and deviator stress q are simplified as follows:

$$p' = \frac{1}{3}(\sigma'_1 + 2\sigma'_3) \quad ; \quad q = \sigma'_1 - \sigma'_3 \quad (1.2)$$

Correspondingly, the strain components, volumetric strain ε_v and the shear strain ε_s , in the conventional triaxial stress space are defined as:

$$\varepsilon_v = \varepsilon_1 + 2\varepsilon_3 \quad ; \quad \varepsilon_s = \frac{2}{3}(\varepsilon_1 - \varepsilon_3) \quad (1.3)$$

where ε_1 and ε_3 are the axial strain and lateral strain, respectively.

According to Schofield and Wroth [69], the kernel of the critical state concept is that granular materials like soils, if continuously distorted until they flow as a frictional fluid, will reach a well-defined critical state. For a given soil, the critical state points form a unique line in the (p', q, v) space, namely the critical state line (Figure 1.12) and can be expressed by the following two equations:

$$q = Mp' \quad (1.4)$$

$$v = \Gamma - \lambda \ln p' \quad (1.5)$$

where M , Γ , and λ are soil constants, v is the specific volume.

According to the critical state, a soil will flow as a frictional fluid at a constant specific volume v when, and only when, the mean effective stress p' and the deviator stress q satisfy Equations 1.4 and 1.5. Thus, a soil sample presents volume changes (dilate or contract) in a shear test eventually tends to a critical state in which the plastic shearing could continue indefinitely. Especially, if the volume and effective stress is assumed constant in the critical

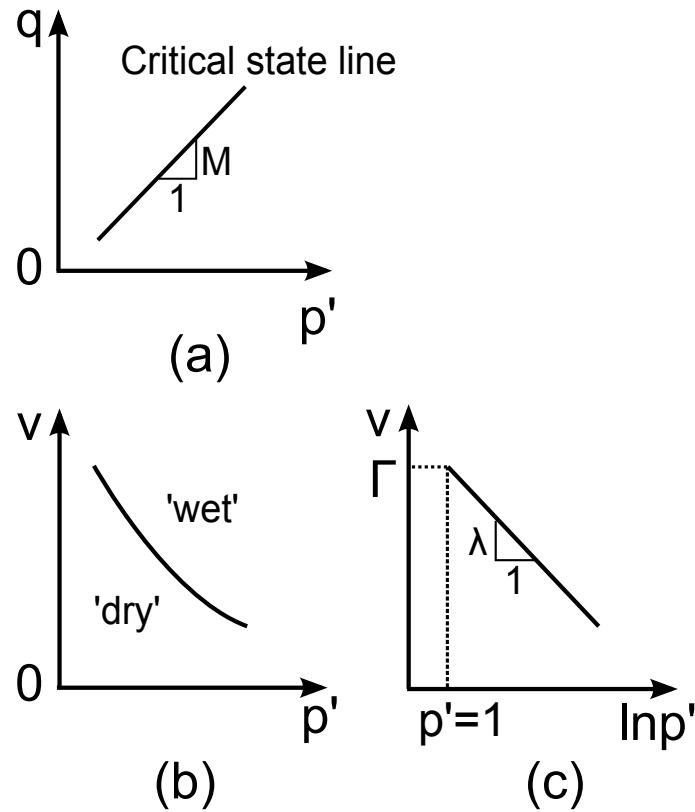


Figure 1.12: Critical state line.

state, this condition can be expressed by:

$$\frac{\partial p'}{\partial \varepsilon_v} = \frac{\partial q}{\partial \varepsilon_s} = \frac{\partial \varepsilon_v}{\partial \varepsilon_s} = 0 \quad (1.6)$$

Combing the effective stress (p' and q) and specific volume (v), the state of a soil sample under any stress state can be determined in the $p' - q - v$ space (Figure 1.12). With the critical state as reference, the soil state with a specific volume lower than the critical state one is called 'dry' since the soil tends to increase its volume by sucking up water and would dry our hands when we remold it, whereas the soil state with a specific volume higher than the critical state one is called 'wet' since the soil tends to decrease its volume by bleeding out water.

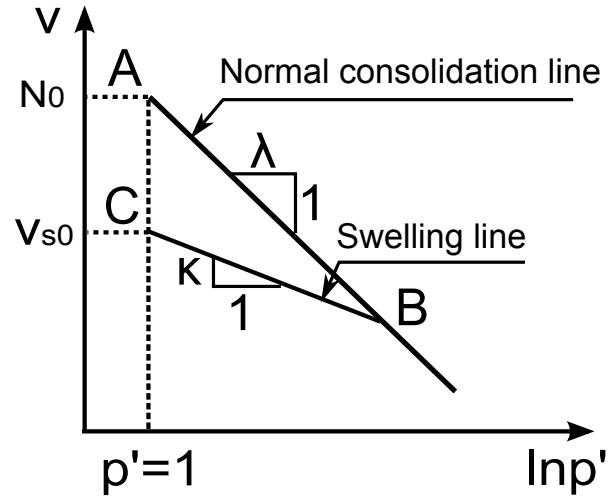


Figure 1.13: Isotropic compression behavior in the MCC.

1.3.2 Modified Cam-clay model

Roscoe and Burland [67] developed the MCC by changing the shape of the yield curve of original Camclay model, overcoming the discontinuous derivative of the yield surface at $q = 0$ in the original Cam-clay model. The MCC describes the isotropic compression behaviour in $v-p'$ plane using a virgin consolidation line and a set of swelling lines, as seen in Figure 1.13.

When loading from point A to B, the soil moves down along the normal consolidation line (NCL) and the sample behaves elastoplastically. If the soil is subsequently unloaded from point B to C and reloaded before reaching point C, the soil behavior is purely elastic and the path moves up and back along the swelling line BC. After reaching point B again, further loading leads to a moving down along the virgin consolidation line again. The normal consolidation line and the swelling lines are assumed to be straight in $v-p'$ plane and the relations can be expressed as follows:

$$\begin{aligned} v &= N_0 - \lambda \ln p' \quad (\text{normal consolidation line}) \\ v &= v_{s0} - \kappa \ln p' \quad (\text{swelling line}) \end{aligned} \tag{1.7}$$

where λ and κ are the slopes of normal consolidation line and swelling line, respectively;

22 Application of MCC model to natural Boom Clay in isothermal conditions

N_0 and v_{s0} are the specific volumes at $p'=1$ kPa of normal consolidation line and swelling line, respectively; λ , κ and N_0 are soil constants, depending on the soil type, whereas v_{s0} depends on the stress history.

As mentioned above, elastic behavior occurs along the swelling line and the elastic volumetric strain increment $d\varepsilon_v^e$ can be determined from Equation 1.7:

$$d\varepsilon_v^e = \frac{dp'}{K} \quad (1.8)$$

with the elastic bulk modulus K expressed as:

$$K = \frac{v_0 p'}{\kappa} \quad (1.9)$$

Note that in the original Camclay model, no elastic shear strain is assumed. To avoid numerical problems and to achieve a better modeling of elastic behavior, elastic shear strains are usually computed from an elastic shear modulus G [62]. The elastic shear strain increment $d\varepsilon_s^e$ is given by:

$$d\varepsilon_s^e = \frac{dq}{3G} \quad (1.10)$$

The shear modulus G can be obtained from K and a constant Poisson's ratio ν :

$$G = \frac{3(1-2\nu)}{2(1+\nu)}K \quad (1.11)$$

It is worth noting that such a choice is not thermodynamically consistent since the Maxwell symmetry relations are not satisfied in this case [40, 93].

The MCC adopts an elliptical-shaped yield surface in $p' - q$ plane as shown in Figure 1.14, the expression of which takes the form:

$$f \equiv q^2 + M^2 p' (p' - p'_c) = 0 \quad (1.12)$$

where p'_c is the preconsolidation pressure that controls the size of the yield surface.

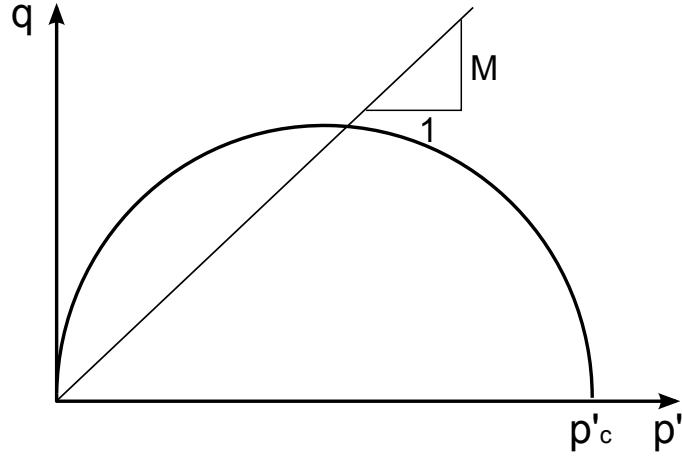


Figure 1.14: MCC yield surface in $p' - q$ plane.

The hardening law is isotropic and controlled by parameter p'_c which is assumed to be related to the plastic volumetric strain ε_v^p by,

$$dp'_c = \frac{v_0 p'_c}{\lambda - \kappa} d\varepsilon_v^p \quad (1.13)$$

An associated flow rule is adopted and the plastic potential (g) is the same as the yield surface (f):

$$g(p', q, p'_c) = q^2 + M^2 p' (p' - p'_c) \quad (1.14)$$

The flow rule can be expressed as:

$$\frac{d\varepsilon_v^p}{d\varepsilon_s^p} = \frac{\partial g / \partial p'}{\partial g / \partial q} = \frac{M^2 - \eta^2}{2\eta} \quad (1.15)$$

where η is the stress ratio of q/p' .

1.3.3 Bounding surface model

A major step in the development of the constitutive modeling within the framework of the critical state theory was the introduction of bounding surface concept first by Krieg [48] and Dafalias and Popov [26]. This theory makes use of two surfaces, a loading surface and

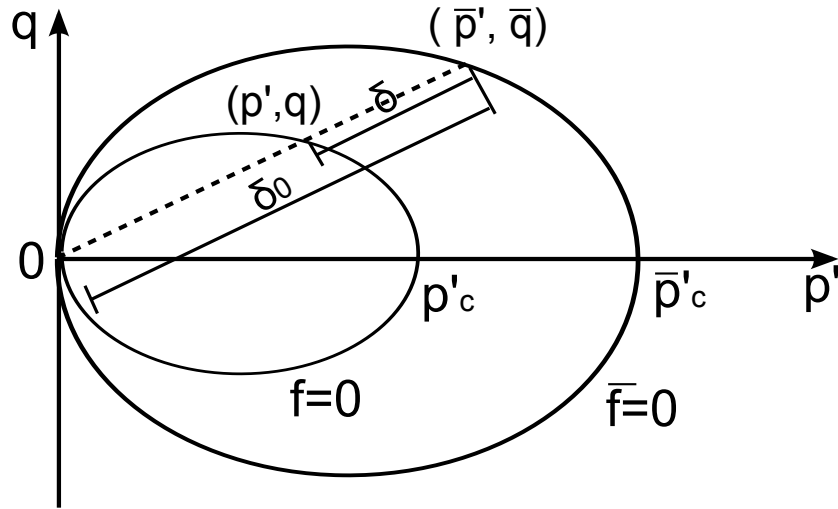


Figure 1.15: Schematic illustration of the bounding surface.

an outer bounding surface and the plastic deformation may occur when the stress state lies on or within the bounding surface. The salient feature of this concept is that the plastic modulus is defined as a decreasing function of the distance between the current stress state and the corresponding point on the bounding surface, through a so-called mapping rule. This allows smooth transition prediction from elastic to fully plastic state as often observed experimentally on soils. Following this concept, many constitutive models have been developed (e.g. [8, 24, 25, 92]).

A well-known bounding surface formulation was due to Dafalias et al. [24, 25] with a radial mapping rule. To describe this formulation, the bounding surface ($\bar{f}=0$) takes a form as the yield surface of MCC, and the loading surface ($f=0$) exists that enclose all the stress state σ' inside the bounding surface. The plastic strain on the loading surface can be calculated by the corresponding image point $\bar{\sigma}'$ on the bounding surface by a radial mapping rule. The radial mapping rule can be expressed by:

$$\bar{\sigma}' = b\sigma', \quad b = \frac{\delta_0}{\delta_0 - \delta} \quad (1.16)$$

where δ and δ_0 denote the distance and the maximum distance between the current effective stress point and the image effective stress point, respectively, as seen in Figure 1.15.

With the mapping rule and the bounding surface, the loading surface ($f = 0$) is defined, which is homologous to the bounding surface. Assuming that the effective stress increment $d\boldsymbol{\sigma}'$ on the loading surface and the corresponding image effective stress increment $d\bar{\boldsymbol{\sigma}}'$ on the bounding surface can produce the same plastic strain increment, we have:

$$\begin{aligned} d\varepsilon^p &= \langle dL \rangle \mathbf{n}_f \\ dL &= \frac{\mathbf{n}_f : d\boldsymbol{\sigma}'}{K_p} = \frac{\mathbf{n}_f : d\bar{\boldsymbol{\sigma}}'}{\bar{K}_p} \end{aligned} \quad (1.17)$$

with

$$\mathbf{n}_f = \left(\frac{\partial f}{\partial \boldsymbol{\sigma}'} \right)^t / \left| \frac{\partial f}{\partial \boldsymbol{\sigma}'} \right| \quad (1.18)$$

where dL is the loading index; the Macauley brackets $\langle dL \rangle$ define the operation $\langle dL \rangle = h(dL) dL$, where $h(dL)$ is the Heavyside step function defined as zero when $dL \leq 0$; K_p and \bar{K}_p are plastic modules associated with $d\boldsymbol{\sigma}'$ and $d\bar{\boldsymbol{\sigma}}'$, respectively; $\left(\frac{\partial f}{\partial \boldsymbol{\sigma}'} \right)^t$ and $\left| \frac{\partial f}{\partial \boldsymbol{\sigma}'} \right|$ denote the transpose and the norm of the vector $\frac{\partial f}{\partial \boldsymbol{\sigma}'}$, respectively.

From Equation 1.17 and the consistency condition $d\bar{f} = 0$, the plastic modulus at image point \bar{K}_p can be obtained:

$$\bar{K}_p = \frac{-1}{\left| \frac{\partial \bar{f}}{\partial \boldsymbol{\sigma}'} \right|^2} \frac{\partial \bar{f}}{\partial \varepsilon_v^p} \frac{\partial \bar{f}}{\partial \bar{p}'} \quad (1.19)$$

K_p and \bar{K}_p are related by:

$$K_p = \bar{K}_p + S(\boldsymbol{\sigma}', \varepsilon^p) \frac{\delta}{\delta_0 - \delta} \quad (1.20)$$

where S is the hardening function. The plastic strain increment at the current stress state can be thus calculated with K_p .

1.3.4 Kinematic hardening model

Mroz et al. [58] introduced a kinematic hardening yield surface below a critical state bounding surface following the bounding surface concept. The bounding surface takes

26 Application of MCC model to natural Boom Clay in isothermal conditions

the same elliptical shape as the MCC yield surface, and a small kinematic surface having the same shape as the bounding surface represents a small truly elastic region. As the effective stress path engages the kinematic surface, this surface will move on to the bounding surface during the plastic loading process. The kinematic surface is allowed to translate and expand or contract during plastic loading and both isotropic and kinematic hardening plastic mechanisms are involved. Certain rules to control the movement and interaction of these two surfaces and also a mapping rule to describe the variation of the plastic modulus are proposed. With this concept, some of the most important features of soil behaviour especially the cyclic behavior can be well described. Many such model formulations were developed in the past 20 years for predicting the nonlinear small-strain behavior as well as the cyclic behavior, such as the so-called bubble model proposed by Al-Tabbaa and Wood [4] and the 3SKH model proposed by Stallebrass and Taylor [79].

1.3.5 Other critical state models

Some important aspects such as anisotropy, destructuration and time-dependency/creep have been considered in a number of constitutive models within the critical state framework. Advanced models were developed by incorporating new plastic mechanisms to incorporate these aspects into the MCC (or on bounding surface model). For example, Wheeler et al. [88, 89] extended MCC to an anisotropic elasto-plastic model (called S-CLAY1) with the anisotropy of plastic behavior considered through an inclined yield surface and a rotational component of hardening law to model the development or erasure of fabric anisotropy during plastic straining.

1.4 Explicit integration of Modified Cam Clay model

1.4.1 Constitutive equations

The constitutive equations of MCC are described briefly in this section.

The total strain increment can be split into an elastic part ($d\boldsymbol{\varepsilon}^e$) and a plastic part ($d\boldsymbol{\varepsilon}^p$), respectively:

$$d\boldsymbol{\varepsilon} = d\boldsymbol{\varepsilon}^e + d\boldsymbol{\varepsilon}^p \quad (1.21)$$

The effective stress and elastic strain can be expressed in the following incremental relationship:

$$d\boldsymbol{\sigma}' = \mathbf{D}_e d\boldsymbol{\varepsilon}^e \quad (1.22)$$

where \mathbf{D}_e is the elastic stiffness matrix.

The effective stress increment can be calculated in turn according to Equations 1.21 and 1.22 :

$$d\boldsymbol{\sigma}' = \mathbf{D}_e (d\boldsymbol{\varepsilon} - d\boldsymbol{\varepsilon}^p) \quad (1.23)$$

The consistency condition for the yield surface of MCC can be expressed as:

$$df = \frac{\partial f}{\partial \boldsymbol{\sigma}'} d\boldsymbol{\sigma}' + \frac{\partial f}{\partial p'_c} dp'_c = 0 \quad (1.24)$$

where f is the yield function.

The plastic strain increment is computed from the plastic potential:

$$d\boldsymbol{\varepsilon}^p = d\lambda \frac{\partial g}{\partial \boldsymbol{\sigma}'} \quad (1.25)$$

where $d\lambda$ is the positive scalar, called plastic multiplier, and g is the plastic potential. Since $g = f$, an associated flow rule is adopted.

The hardening law controlling the evolution of the yield surface is expressed as:

$$dp'_c = \frac{\partial p'_c}{\partial \varepsilon_v^p} d\varepsilon_v^p = \frac{\partial p'_c}{\partial \varepsilon_v^p} d\lambda \frac{\partial g}{\partial p'} \quad (1.26)$$

Substituting Equations 1.23, 1.25 and 1.26 into Equation 1.24, the differential form of

28 Application of MCC model to natural Boom Clay in isothermal conditions

the consistency condition can be rewritten as:

$$\left(\frac{\partial f}{\partial \boldsymbol{\sigma}'}\right)^t : d\boldsymbol{\sigma}' - h d\lambda = 0 \quad (1.27)$$

where $h = -\frac{\partial f}{\partial p'_c} \frac{\partial p'_c}{\partial \varepsilon_v^p} \frac{\partial g}{\partial p'}$ is the hardening modulus.

The expression of the plastic multiplier is then obtained from Equations 1.23 and 1.27:

$$d\lambda = \frac{(\mathbf{a})^t \mathbf{D}_e d\boldsymbol{\varepsilon}}{(\mathbf{a})^t \mathbf{D}_e \mathbf{b} + h} \quad (1.28)$$

where: $\mathbf{a} = \frac{\partial f}{\partial \boldsymbol{\sigma}'}$, $\mathbf{b} = \frac{\partial g}{\partial \boldsymbol{\sigma}'}$.

The differential stress–strain equation can finally be given:

$$\begin{aligned} d\boldsymbol{\sigma}' &= \mathbf{D}_{ep} d\boldsymbol{\varepsilon} \\ dp'_{c0} &= \mathbf{R}_{ep} d\boldsymbol{\varepsilon} \end{aligned} \quad (1.29)$$

where:

$$\mathbf{D}_{ep} = \mathbf{D}_e - \frac{\mathbf{D}_e \mathbf{b} (\mathbf{a})^t \mathbf{D}_e}{(\mathbf{a})^t \mathbf{D}_e \mathbf{b} + h} \quad (1.30)$$

and

$$\mathbf{R}_{ep} = \frac{B (\mathbf{a})^t \mathbf{D}_e}{(\mathbf{a})^t \mathbf{D}_e \mathbf{b} + h} \quad (1.31)$$

with $B = \frac{\partial p'_{c0}}{\partial \varepsilon_v^p} \frac{\partial g}{\partial p'}$.

For the undrained condition, Terzaghi's effective stress principle is applied, assuming that the total stress consists of the effective stress sustained by the soil skeleton and pore water pressure. It can be expressed as:

$$d\boldsymbol{\sigma} = \mathbf{D}_{ep} d\boldsymbol{\varepsilon} + \mathbf{m}^t du \quad (1.32)$$

where $\mathbf{m}^t = (1, 1, 1)$ is a unit vector.

According to the poro-mechanics [21], the excess of pore-water pressure can be defined

by (assuming the incompressibility of solid grains):

$$du = \frac{K_w}{n} d\varepsilon_v \quad (1.33)$$

where K_w is the bulk modulus of water, n is the porosity of soil.

Substituting Equation 1.33 into Equation 1.32, the constitutive equation in terms of total stress is obtained:

$$d\boldsymbol{\sigma} = \mathbf{D}_{ep} d\varepsilon + \mathbf{m}^t \frac{K_w}{n} d\varepsilon_v \quad (1.34)$$

The undrained behavior can then be described using Equation 1.34.

1.4.2 Adaptive sub-stepping integration algorithm

For the numerical resolution of the constitutive equations, an explicit stress integration scheme with an adaptive time-stepping process is adopted in this study because of its straightforward implementation and high accuracy control as mentioned in Sloan et al. [75]. This is particularly important when considering numerical integration of advanced elasto-plastic constitutive models, e.g., thermo-mechanical models (c.f. Chapter 3). Details of the stress integration algorithm for the MCC can be referred to the work of Sloan et al. [75] or Hong et al. [36]. Some key points of this algorithm applied to the MCC are summarized below:

1. At the beginning of the n th step, different situations (purely elastic state, change from elastic to elasto-plastic state, plastic state), can be determined by the values obtained from the yield criteria before and after the application of the elastic trial stress.
2. In the elastic loading process, the secant elastic stiffness matrix is employed to address the elastic non-linearity.
3. In the change from elastic to elasto-plastic loading process, the Pegasus method is used to search for the transition point.

30 Application of MCC model to natural Boom Clay in isothermal conditions

4. In the plastic loading process, a pseudo-time t is introduced. For each time step, the size of the sub-increment can be found automatically by maintaining the local integration error below a specified tolerance. The error is calculated by taking the difference between an Euler solution and a modified Euler solution.
5. At the end of each sub-step during the plastic loading process, a drift correction algorithm is applied to ensure the effective stress state to lie on the yield surface if the effective stress state deviates from the yield surface.

1.5 Evaluation of the Modified Cam Clay model

1.5.1 Selection of parameters

In this section, the parameters of MCC for natural Boom Clay are determined based on the synthesis of the experimental results. The mechanical meaning of each parameter is noted and the corresponding determination methods are described.

The complete description of the MCC requires 5 parameters, each of which has a clear physical meaning:

1. λ , slope of the consolidation line in $v-v'$ plane.
2. κ , slope of the swelling line in $v-v'$ plane.
3. ν , Poisson's ratio.
4. p'_{c0} , preconsolidation pressure which defines the initial size of yield surface.
5. M , the critical state stress ratio.

The value of λ can be obtained from the slope of normal consolidation compression line in $v-v'$ plane. For λ determination, the oedometer tests can be also used in addition to the isotropic tests since the slope of the normal consolidation line in $v - \ln \sigma'_v$ plane for an oedometer test is also λ . This is because the value of coefficient K_0 (the ratio of horizontal to vertical effective stresses) is constant in the normally consolidated state ($K_0 = K_{0nc}$),

leading to the following relation [90]:

$$\begin{aligned}\lambda &= \frac{v_2 - v_1}{\ln p'_1 - \ln p'_2} = \frac{v_2 - v_1}{\ln \left(\frac{1}{3} (\sigma'_{v1} + 2K_{0nc}\sigma'_{v1}) \right) - \ln \left(\frac{1}{3} (\sigma'_{v2} + 2K_{0nc}\sigma'_{v2}) \right)} \\ &= \frac{v_2 - v_1}{\ln \sigma'_{v1} - \ln \sigma'_{v2}}\end{aligned}\quad (1.35)$$

where indices 1, 2 refer to two different states on normally consolidated line, σ'_v is the vertical effective stress.

κ can be determined by the slope of swelling line in the isotropic compression test. The oedometer test is not a good choice according to Wood [90] since κ does not hold for the slope of the swelling line in $v - \ln \sigma'_v$ plane. The coefficient K_0 is assumed to be applicable for the overconsolidated state, where it is not constant and can be calculated as (by Wood [90]):

$$K_0 = \frac{\sigma'_{v \max}}{\sigma'_v} K_{0nc} - \left(\frac{\sigma'_{v \max}}{\sigma'_v} - 1 \right) \frac{\nu}{1 - \nu} \quad (1.36)$$

where σ'_v denotes the vertical effective stress in the overconsolidated state and $\sigma'_{v \max}$ is the maximum value of σ'_v reached in the normally consolidated state.

Then, it gives,

$$\begin{aligned}\kappa &= \frac{v_2 - v_1}{\ln p'_1 - \ln p'_2} = \frac{v_2 - v_1}{\ln \left(\frac{1}{3} (\sigma'_{v1} + 2K_{01}\sigma'_{v1}) \right) - \ln \left(\frac{1}{3} (\sigma'_{v2} + 2K_{02}\sigma'_{v2}) \right)} \\ &= \frac{v_2 - v_1}{\ln \left(\frac{(1 + 2K_{01}) \sigma'_{v1}}{(1 + 2K_{02}) \sigma'_{v2}} \right)}\end{aligned}\quad (1.37)$$

where indices 1, 2 refer to two different states in the overconsolidated state, K_{01} and K_{02} are coefficients associated with the effective stress states σ'_{v1} and σ'_{v2} , respectively. It can be clearly seen that κ cannot be determined in the swelling state in $v - \ln \sigma'_v$ plane from Equation 1.37 since $K_{01} \neq K_{02}$.

The isotropic test is the best choice for the preconsolidation pressure determination. For the natural Boom Clay, with the isotropic test results plotted together in the $v - \ln \sigma'_v$ plane, $\lambda=0.17$, $\kappa=0.02$ and $p'_{c0}=6$ MPa are finally chosen.

32 Application of MCC model to natural Boom Clay in isothermal conditions

Table 1.6: MCC parameters for the natural Boom Clay.

Parameters	SCK-CEN (1997)	Delahaye and Alonso (2002)	TIMODAZ (2007)	This study
λ	0.130	0.260	0.130-0.178	0.170
κ	0.020	0.026	0.013-0.046	0.020
ν	0.125	0.33	-	0.3
p'_{e0} (MPa)	6	6	5-6	6
M	0.81	1	0.67-1	0.67

The Poisson's ratio ν is the ratio of the lateral strain increment to the axial elastic strain increment if the soil is subjected to a vertical stress increment. According to this definition, ν can be determined in the elastic part (at a low strain level around 0.5%) in the $\varepsilon_v - \varepsilon_1$ plane: $\nu = (1 - \varepsilon_v/\varepsilon_1)/2$. For the natural Boom Clay, $\nu=0.3$ is determined.

M can be determined by the effective stress ratio of the critical state along different loading paths. $M = 0.67$ is determined for the natural Boom Clay from the drained triaxial tests as shown in Figure 1.11.

The MCC parameters for the natural Boom Clay are gathered in Table 1.6. The parameters compiled from the literature are also included [11, 29, 52, 85].

1.5.2 Parameters sensitivity analyses

As described above, a set of the input parameters has been determined from available test data. When simulating standard triaxial tests, the parameters considered can influence the simulation results in different levels. To help better understand the model behavior, it appears important to investigate the effect of each parameter. Thereby, a parametric sensitive study is conducted, in which only one parameter varies (around $\pm 30\%$) each time while others are kept constant as in Table 1.6. The example taken involves a conventional drained triaxial test on natural Boom Clay. The sample was saturated under an initial mean effective stress of 2.0 MPa with $e_0=0.61$, and then isotropically loaded up to $p'=3$ MPa. Drained triaxial compression was then conducted.

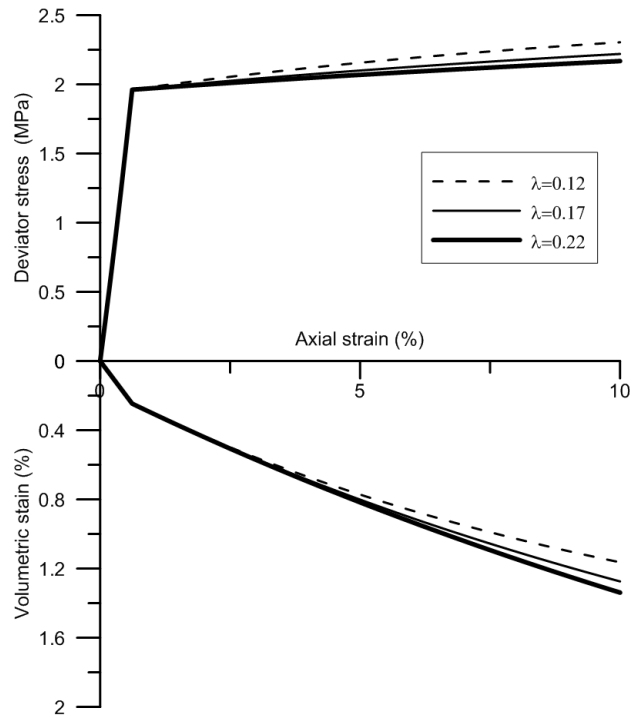


Figure 1.16: Influence of parameter λ .

1.5.2.1 Influence of parameter λ

The values of parameter λ are chosen as 0.12, 0.17 and 0.22, respectively. The influence of parameter λ on the shear behavior is assessed in Figure 1.16.

From the simulation results, it can be observed that λ doesn't influence the elastic behavior but the elasto-plastic behaviour after the yield surface is activated. For the elasto-plastic behavior, a larger value of λ gives a smaller deviator stress but a larger volumetric strain at a given axial strain.

1.5.2.2 Influence of parameter κ

The values of parameter κ are chosen as 0.014, 0.020 and 0.026, respectively. Figure 1.17 shows the influence of parameter κ on the shear behavior. It is observed that the elastic slope in $q - \varepsilon_1$ plane is dependent on the κ value (a higher slope with a smaller κ value) whereas the elasto-plastic part is independent on κ value. In $\varepsilon_v - \varepsilon_1$ plane, κ does not influence the curve slope, neither in elastic part nor in elasto-plastic part, but it

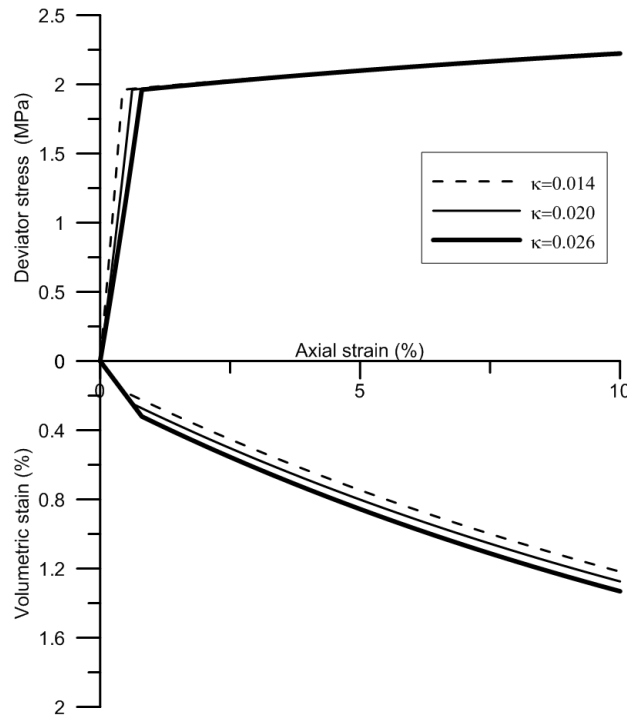


Figure 1.17: Influence of parameter κ .

influence the volumetric strain obtained: a higher value of κ gives a larger volumetric strain increment in the elastic part and thus a larger total volumetric increment.

1.5.2.3 Influence of parameter ν

The values of parameter ν are chosen as 0.21, 0.30 and 0.39, respectively. From the simulation results in Figure 18, it appears that the elastic slope in $\varepsilon_v - \varepsilon_1$ plane is dependent on the value of ν due to $\nu = (1 - \varepsilon_v^e / \varepsilon_1^e) / 2$, and therefore the elastic slope in $q - \varepsilon_1$ plane is influenced. A small influence of ν on the elasto-plastic part is identified since the ratio between $\varepsilon_v - \varepsilon_1$ is dominated by the plastic strain ratio or the plastic flow rule.

1.5.2.4 Influence of parameter p'_{c0}

The values of parameter p'_{c0} are chosen as 4.2, 6.0 and 7.8, respectively. As shown in Figure 1.19, p'_{c0} influences the magnitude of elastic zone in both $q - \varepsilon_1$ and $\varepsilon_v - \varepsilon_1$ planes but without influencing the behavior within the elastic zone. For the elasto-plastic behavior, a

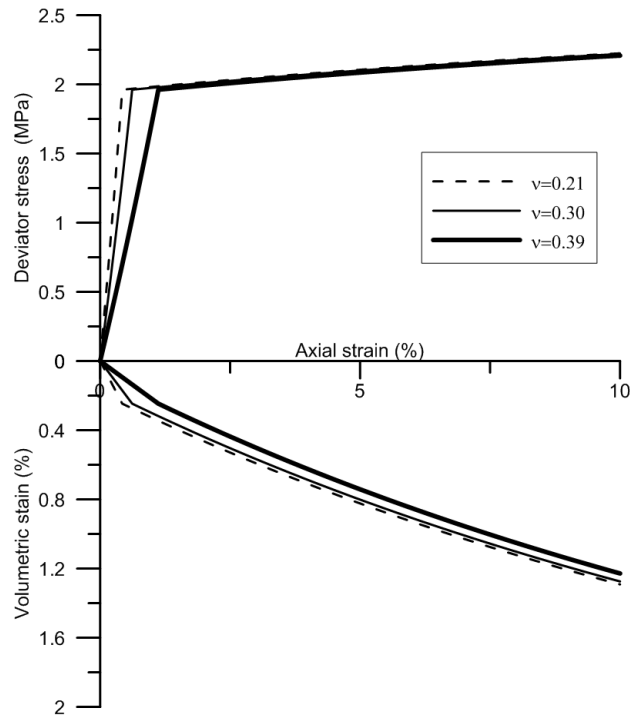


Figure 1.18: Influence of parameter ν .

smaller deviator stress but a larger volumetric strain with a smaller p'_{c0} are obtained at a given axial strain.

1.5.2.5 Influence of parameter M

The values of parameter M are chosen as 0.47, 0.67 and 0.87, respectively. The results obtained are shown in Figure 1.20. M determines the critical state. In addition, it also affects the yield surface shape and also the flow rule since associated flow rule is adopted. Thus in the following, the influence of M on the elasto-plastic phase is considered. In the $q - \varepsilon_1$ plane, at a given strain level, a larger value of M results in a higher deviator stress. In the $\varepsilon_v - \varepsilon_1$ plane, a larger slope of the stress strain curve in the elasto-plastic part is found with a larger value of M through the flow rule changes. Moreover, a larger value of M gives rise to a larger final volumetric strain since the loading zone becomes larger.

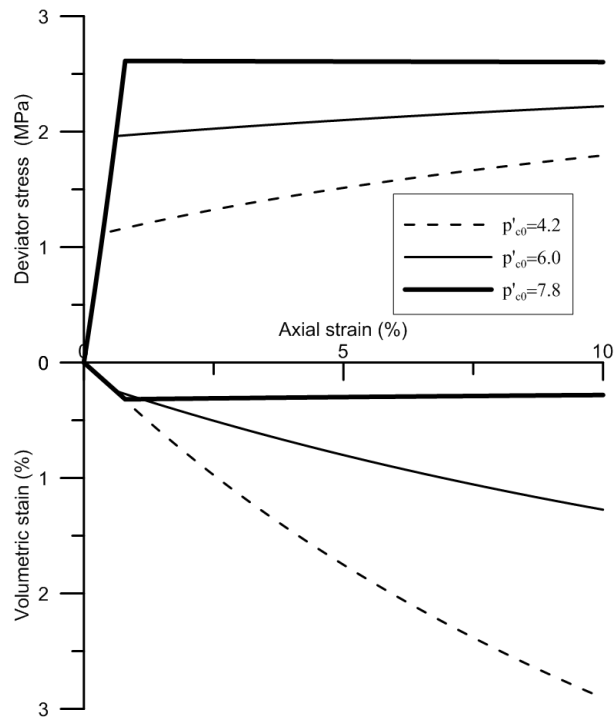


Figure 1.19: Influence of parameter p'_{c0} .

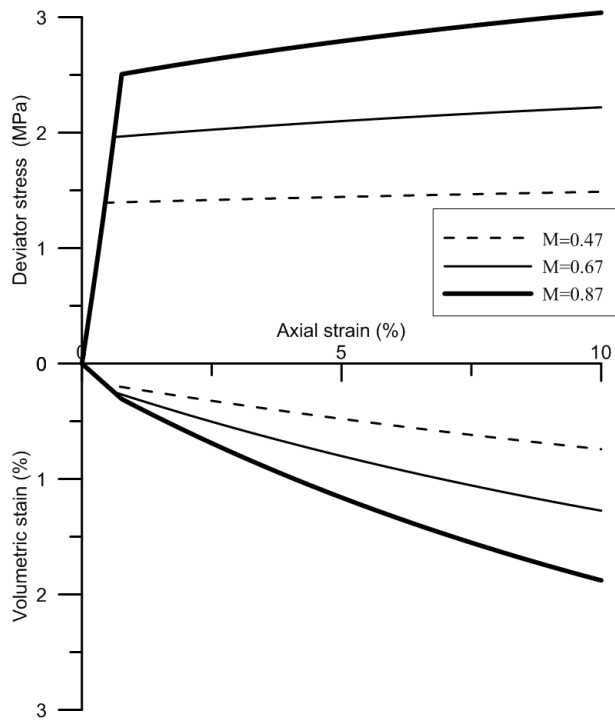


Figure 1.20: Influence of parameter M .

1.5.3 Analysis of laboratory tests using MCC

In this section, the performance of MCC is assessed by analyzing the behavior of natural Boom Clay evidenced by the experimental tests described above. As mentioned previously, purely numerical simulation is performed for the undrained behavior. Test CU-1 corresponds to a conventional undrained shear test under $p'=2.3$ MPa. All the simulations are performed from a common point ($p'_0=2$ MPa, $e_0=0.61$). The MCC parameters used have been chosen in Section 1.5.1 as shown in Table 1.6.

1.5.3.1 Isotropic tests

Figure 1.21 compares the simulations by MCC and the experimental results from isotropic compression tests. Though the experimental data with the same loading path from different samples are little scattered, it can be observed that the MCC can roughly capture the main features of the compression behavior during the loading and unloading processes (neglecting the hysteretic behavior). However, it should be noted that the MCC cannot capture the smooth behavior at low stress level ($p' < 10$ MPa) as observed from the experimental curve. Furthermore, the MCC cannot predict the irrecoverable strain during the unloading process from $p'=4$ MPa (Iso-1) since purely elastic strain is assumed.

1.5.3.2 Oedometer tests

Figure 1.22 compares the numerical predictions by MCC and the experimental results from oedometer compression tests. It shows that the simulation can roughly capture the main trend of the experimental curve of Oed-3, but cannot capture the smooth stress-strain behavior as observed from experimental results. Obvious difference appears between the predicted curve and the observed curves of Oed-1 and Oed-2.

1.5.3.3 Drained triaxial tests

Figures 1.23-1.24 show the comparison between the results of MCC and the experimental data from drained triaxial tests. The results are presented in terms of variations of deviator

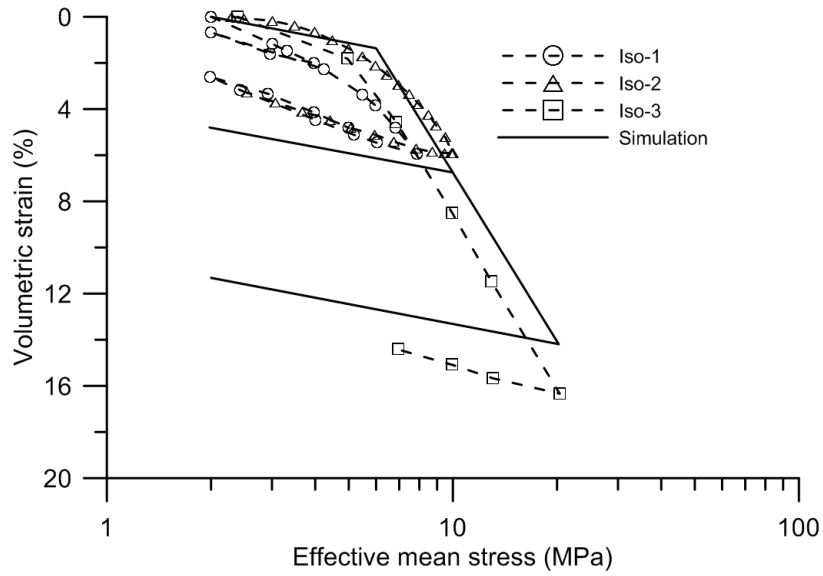


Figure 1.21: Comparison between numerical simulations by MCC and experimental results.

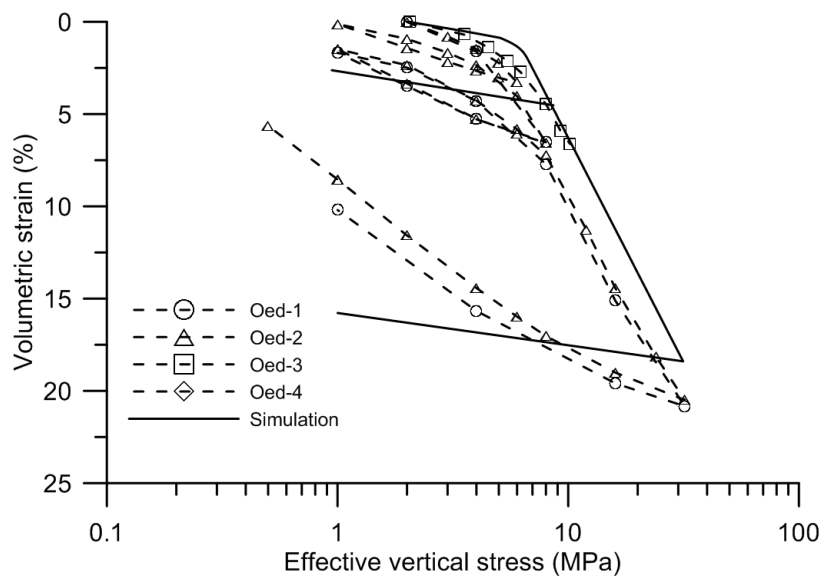


Figure 1.22: Comparison between numerical simulation by MCC and experimental results from oedometer tests.

stress and volumetric strain against axial strain. In general, the MCC provides predictions of poor quality. Hence, MCC is restricted in its ability to well predict the natural Boom Clay behaviour and more advanced mechanical models are required. Several conclusions can be drawn from this comparison:

1. In all the tests, the predicted effective stress is much lower than the experimental one at large strains ($\varepsilon_1 > 1\%$) as shown in the figures. This is mainly because that the yield surface defined in the MCC cannot well capture the yield behavior of natural Boom Clay along the shear loading path.
2. The predicted volumetric strains are much smaller than the experimental values especially for the tests starting from the initial mean effective stress close to the in-situ effective stress as shown in Figure 1.23. This is because that these loading paths are almost in the elastic zone and the elastic volumetric strains are dominant.
3. The MCC cannot simulate the highly nonlinear behavior at small strains and cannot describe the smooth elasto-plastic transition behavior. This can mainly be attributed to the fact that the MCC is based on the classic plasticity with a sharp elastic-plastic transition.
4. For the unloading process, MCC can just predict the irrecoverable strain during the unloading process from the high strain level but cannot predict such a behavior during unloading from the small strain level. This is because the MCC defines a relatively large elastic zone.

1.5.3.4 Undrained triaxial tests

Figure 1.25(a) shows the simulation results in $q - \varepsilon_1$ plot for an undrained triaxial test. The deviator stress varies linearly with the axial strain in the initial stage since just elastic behavior occurs, and then the deviator stress decreases gradually with larger axial strain changes. Figure 1.25 (b) shows the undrained effective stress paths predicted by the MCC. The mean effective stress remains constant at the initial stage until the yield surface

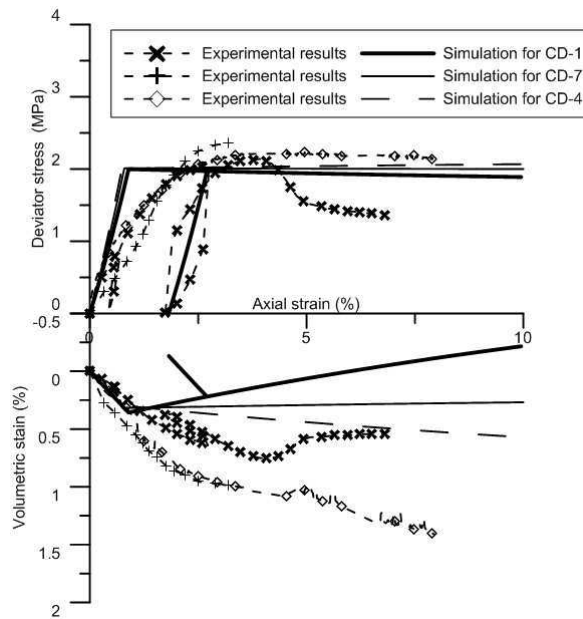


Figure 1.23: Numerical simulations of drained triaxial shear tests CD-1 ($p'_0=2.0$ MPa), CD-7 ($p'_0=2.3$ MPa) and CD-4 ($p'_0=2.5$ MPa).

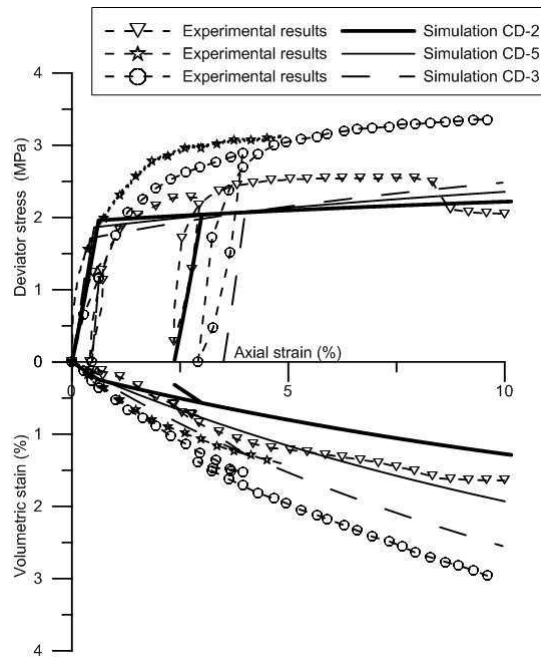


Figure 1.24: Numerical simulations of drained triaxial shear tests CD-2 ($p'_0=3.0$ MPa), CD-5 ($p'_0=3.5$ MPa) and CD-3 ($p'_0=4.0$ MPa).

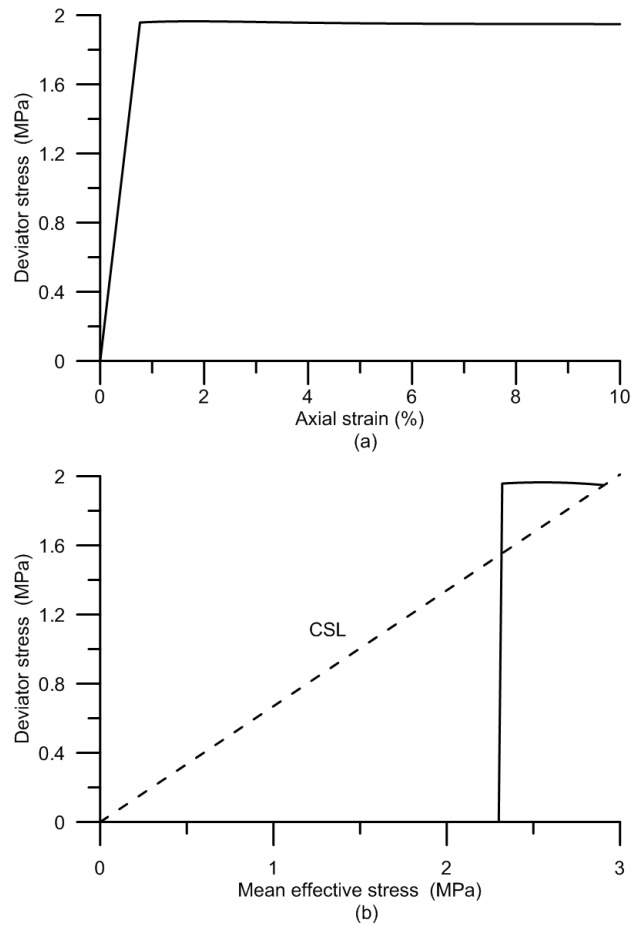


Figure 1.25: Numerical simulations of an undrained triaxial shear test CU-1 ($p'_0=2.3$ MPa).

is reached without any plastic volumetric changes. After reaching the yield surface, the undrained effective stress path curves to the right (dilatant behaviour type with generation of negative pore water pressure) until reaching the CSL.

1.6 Conclusion

The representative experimental data reported in the literature on the natural Boom Clay samples saturated under in-situ effective stress state are gathered. On the whole, the natural Boom Clay behavior is characterized by a limited elastic zone, a highly nonlinear stress-strain response after a brief linear stress-strain behavior and a smooth transition from elastic to plastic response.

42 Application of MCC model to natural Boom Clay in isothermal conditions

The MCC is applied to simulate the natural Boom Clay behavior. The parameters are carefully examined according to their mechanical meaning. A sensitivity study of the parameters has been carried out to verify the influence of each on the model performance. It has been found that the MCC provides poor-quality predictions for the natural Boom Clay. This may be because the yield surface defined in the MCC cannot well capture the yield behavior of this stiff soil along different loading paths. In addition, the MCC is based on the classic plasticity with a sharp elastic–plastic transition and thus cannot describe the smooth elasto-plastic transition behavior.

Chapter 2

Development of a Two-surface model for isothermal conditions

2.1 Introduction

As shown in Chapter 1, the Modified Cam Clay model (MCC) is not capable of well describing the observed behavior of natural Boom Clay. When trying to render the model prediction to the experimental results, it appears that some important modifications are required for the model. These modifications can be classified into two levels, a low one and a high one. The former refers to the modifications that are brought in a traditional fashion to the yield surface, plastic potential and elastic law inside the yield surface, while the latter refers to the consideration of the plastic behavior inside the conventional yield surface.

In the low level, an adapted Cam Clay model (ACC-1) is developed. The main feature of ACC-1 is that a new yield surface and a new plastic potential are used. To adequately describe the elastic behavior of Boom Clay, non-linear elastic rules are considered. This is motivated by the observation of Potts et al. [61]: a better prediction of elastic behavior of soil may be made by adopting appropriate expressions for the shear modulus in the family of traditional critical state models.

However, it appears that, as for MCC, ACC-1 cannot satisfactorily model the behavior of natural Boom Clay. Indeed, the important behavior of natural Boom Clay, i.e. the smooth transition from elastic to plastic state, cannot be well described by this model. Further, compared to the experimental data, smaller volumetric strain is predicted. This may be attributed to the sharp elastic–plastic transition and purely elastic behavior within the yield surface, on which the classic plasticity and thus ACC-1 are based.

On the other hand, the well-known bounding surface model introduced by Dafalias et al. [24, 25] is widely used for describing the smooth transition from elastic to plastic regimes. The plastic strains may appear inside the conventional yield surface and the plastic modulus varies flexibly along the loading path. It should be noted that in such models the loading surface systematically follows the stress point so that $f = 0$ is always true. This is not the case for a conventional yield surface that could be either activated or not, in the sense of the classic elasto-plasticity ($f < 0$ is possible).

Furthermore, the plastic modulus of the current stress state is not rationally formulated by considering the consistency condition of the associated surface, but is merely given by an interpolation function of the distance from the current stress point to the bounding surface. In this study, from ACC-1 and based on the experimental observations, a simple Two-surface model (ACC-2) is developed. An extra yield surface (termed as Inner yield surface) associated with the plastic strain at small strain level is introduced to well describe soil behavior inside the existing ACC-1 surface (termed as Yield surface). Indeed, ACC-2 has a structure similar to that of bounding surface models. However, ACC-2 considers the Inner yield surface as a true yield surface in the sense of conventional elasto-plasticity. Instead of defining an interpolation function for the plastic hardening modulus, a specific hardening law associated with the Inner yield surface is defined, enabling the Inner surface to approach without touching the Yield surface and also the plastic modulus to vary smoothly along a plastic loading process.

Thereby, an important feature of ACC-2 is that the constitutive equation can be simply formulated using the consistency condition of the Inner yield surface which is equivalent

to the classic yield surface. Hence, all the features of the stress integration schemes for the classic elasto-plastic model can be applied to ACC-2 with a few modifications in the numerical implementation.

In a first part of this chapter, a simple elasto-plastic model (ACC-1) is developed including adoption of a new yield surface and a new plastic potential as well as a new non-linear elasticity law in the framework of classic critical state. The proposed model is then checked using available experimental data. In a second part, ACC-1 is extended to a Two-surface model ACC-2 incorporating a new plastic mechanism to describe the plastic strain inside the ACC-1 surface. An additional hardening law enabling flexible description of the plastic modulus throughout the plastic loading process is introduced. Finally, the constitutive equations are given. Numerical simulations are performed to validate ACC-2.

2.2 An adapted Cam Clay model (ACC-1)

2.2.1 Elastic part of the model

As in the MCC, the elastic volumetric strain increment is given by Equation 2.1:

$$d\varepsilon_v^e = \frac{\kappa dp'}{v_0 p'} \quad (2.1)$$

giving the elastic bulk modulus:

$$K = \frac{v_0 p'}{\kappa} \quad (2.2)$$

The shear strain increment can be calculated by:

$$d\varepsilon_s^e = \frac{dq}{3G} \quad (2.3)$$

As pointed out by Potts et al. [61], Equation 2.1 is one of the basic assumptions in a critical state model and the unique relationship between the critical state stresses and the specific volume would not hold if the elastic volumetric strain does not follow Equation 2.1. As a

consequence, attention should be paid to the shear stiffness G and to improve the nonlinear behavior inside the yield surface.

With a constant Poisson's ratio ν , G can be calculated by:

$$G = \frac{3(1 - 2\nu)K}{2(1 + \nu)} \quad (2.4)$$

Alternative expressions of G were proposed on the basis of the experimental observations and interpretations by a number of researchers (e.g. [35, 41, 63]). Housbly et al. [42] concluded that G depends on the following variables: the current void ratio e , the mean effective stress p' and the overconsolidation ratio OCR. Since the soil does not experience a significant variation of void ratio, the expression for shear modulus varying with OCR proposed by Housbly et al. [41] is adopted:

$$G = G_{nc}OCR^{-m} \quad (2.5)$$

where G_{nc} is the shear modulus in the normally consolidated state, m is a dimensionless material constant used to describe the OCR effect and its m is proposed to be between 0 and 1 by Housbly et al. [41].

Even though these choices for shear modulus (Equations 2.4 and 2.5) help in simulating experimental observations, it is worth noting that they are not thermodynamically consistent since the Maxwell symmetry relations are not satisfied in this case [40, 93].

2.2.2 Yield surface

The results from drained triaxial tests, isotropic and oedometer compression tests can be used to investigate the yield surface of natural Boom Clay. The approach of defining the yield surface should be within the framework of elasto-plasticity. In the classic plasticity theory, the yield surface divides the stress space to a relatively high stiffness elastic region where strains remains mainly reversible and an elasto-plastic region which can be further

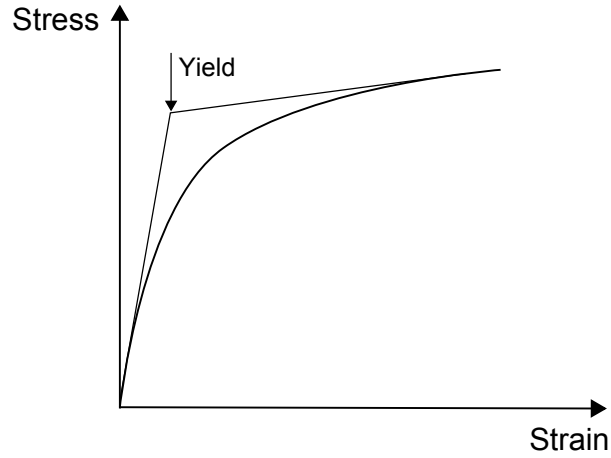


Figure 2.1: Classic yield definition from stress–strain response.

changed with plastic strain generation. As the initial yield surface is reached, pronounced changes in strain and significant reduction in stiffness can occur. Within this framework, a number of approaches have been proposed to determine the stress state at yield. The yield points can be classically determined by the sharp slope change in stress–strain plots (Figure 2.1), such as mean effective stress (p') versus volumetric strain (ε_v), deviator stress (q) versus shear strain (ε_s), etc. [23, 56, 82]. However, the yield points determined in the various plots of stress–strain components (e.g. $p' - \varepsilon_v$ curve and $q - \varepsilon_s$ curve) do not agree always. To avoid this problem, Tavenas et al. [83] proposed an energy-based approach arguing that the yield surface corresponds to a given level of total energy. In this approach, the yield point is defined by the discontinuity in the energy–stress plot, with the energy described by:

$$w = w_v + w_s = \int p d\varepsilon_v + \int q d\varepsilon_s \quad (2.6)$$

where w_v and w_s are volumetric and shear strain energy, respectively.

For the yield point determination by undrained tests, the component of excess pore water pressure (Δu) is used instead of ε_v along the stress path which corresponds to an approximately constant volumetric strain ($\varepsilon_v \approx 0$).

As pointed out by Wood [91], yield stress can be commonly defined as the intersection point of two linear extrapolations representing the pre–yield and post–yield portions of the

Table 2.1: Summary of yield points from the drained triaxial shear tests.

Test	p'_0 (MPa)	Yield stress	
		p' (MPa)	q (MPa)
CD-1	2	2.69	2.05
CD-2	3	3.80	2.37
CD-3/6	4	4.9	2.70
CD-4	2.5	3.23	2.20
CD-5	3.5	4.45	2.84
CD-7	2.3	3.10	2.30

stress-strain curve, as shown in Figure 2.1. In this work, the yield stresses are identified from both $p' - \varepsilon_v$ and $q - \varepsilon_s$ curves along each stress path. The experimental tests described in Chapter 1 are used. Taking CD-1 and CD-3 tests for example, Figures 2.2 and 2.3 present the yield points determination for the drained triaxial experiments on natural Boom Clay. In CD-1, the determined yield points correspond to $p' = 2.70$ MPa, $q = 2.10$ MPa in $p' - \varepsilon_v$ plot and $p' = 2.67$ MPa, $q = 2.00$ MPa in $q - \varepsilon_s$ plot. In CD-4, identical yield stresses with $p' = 4.9$ MPa, $q = 2.70$ MPa are determined from both $p' - \varepsilon_v$ plot and $q - \varepsilon_s$ plot. Similarly, it is found that both curves in $p' - \varepsilon_v$ plot and $q - \varepsilon_s$ plot provide close values for the yield point for tests CD-2, CD-3, CD-5, CD-6 and CD-7. In the following, the average of the two values obtained is taken as the yield stress. The yield points obtained from all the triaxial tests considered are summarized in Table 2.1.

Figure 2.4 shows the yield points obtained in a $p' - q$ plot for all the drained tests described in Chapter 1. The yield curve predicted by the MCC and the corresponding critical state line are also drawn with the parameters determined in Chapter 1. Inspection of Figure 2.4 shows that significant difference exists between the MCC surface and the experimental data, showing that the MCC surface is not appropriate for describing the yield behavior of natural Boom Clay. This point is supported by the numerical simulation using MCC in Chapter 1. It needs therefore to find a new yield surface that allows satisfactory description of the yield behavior observed experimentally.

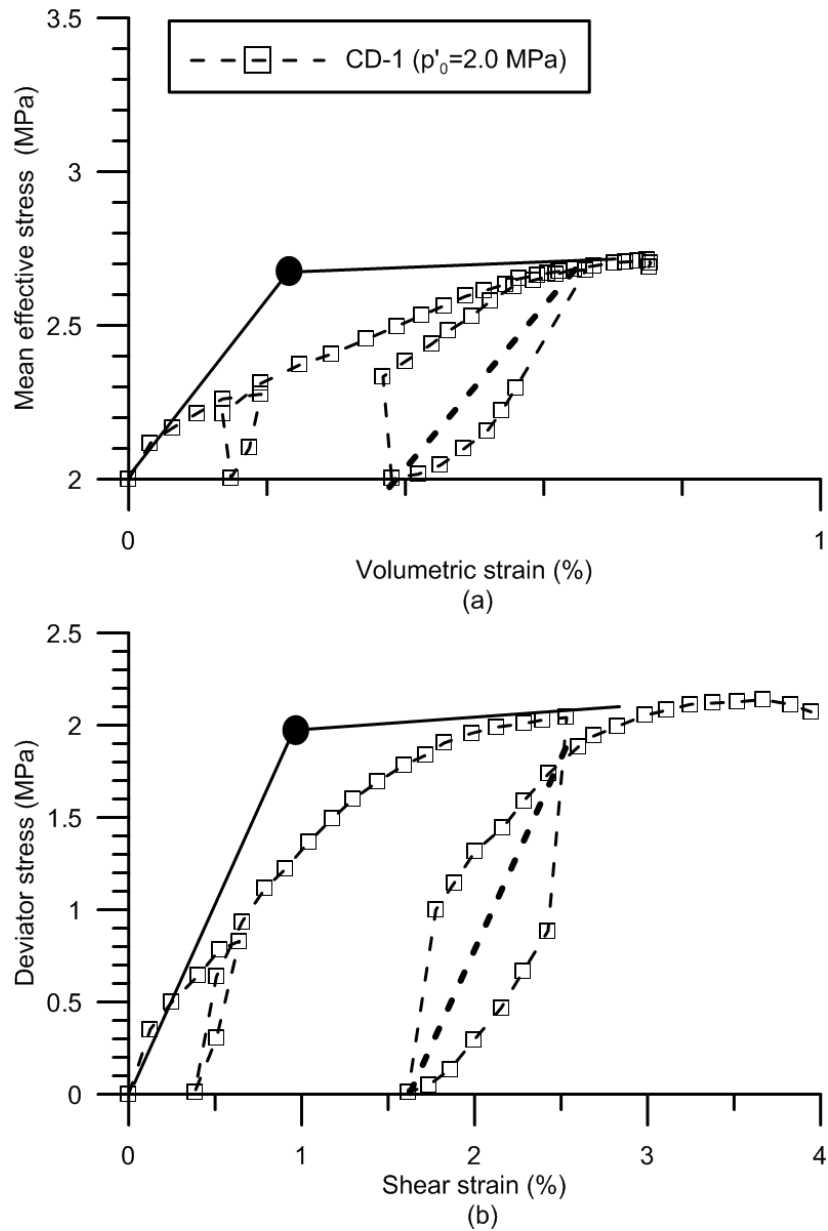


Figure 2.2: Yield stress determination from a drained triaxial shear test CD-1 ($p'_0=2.0$ MPa).

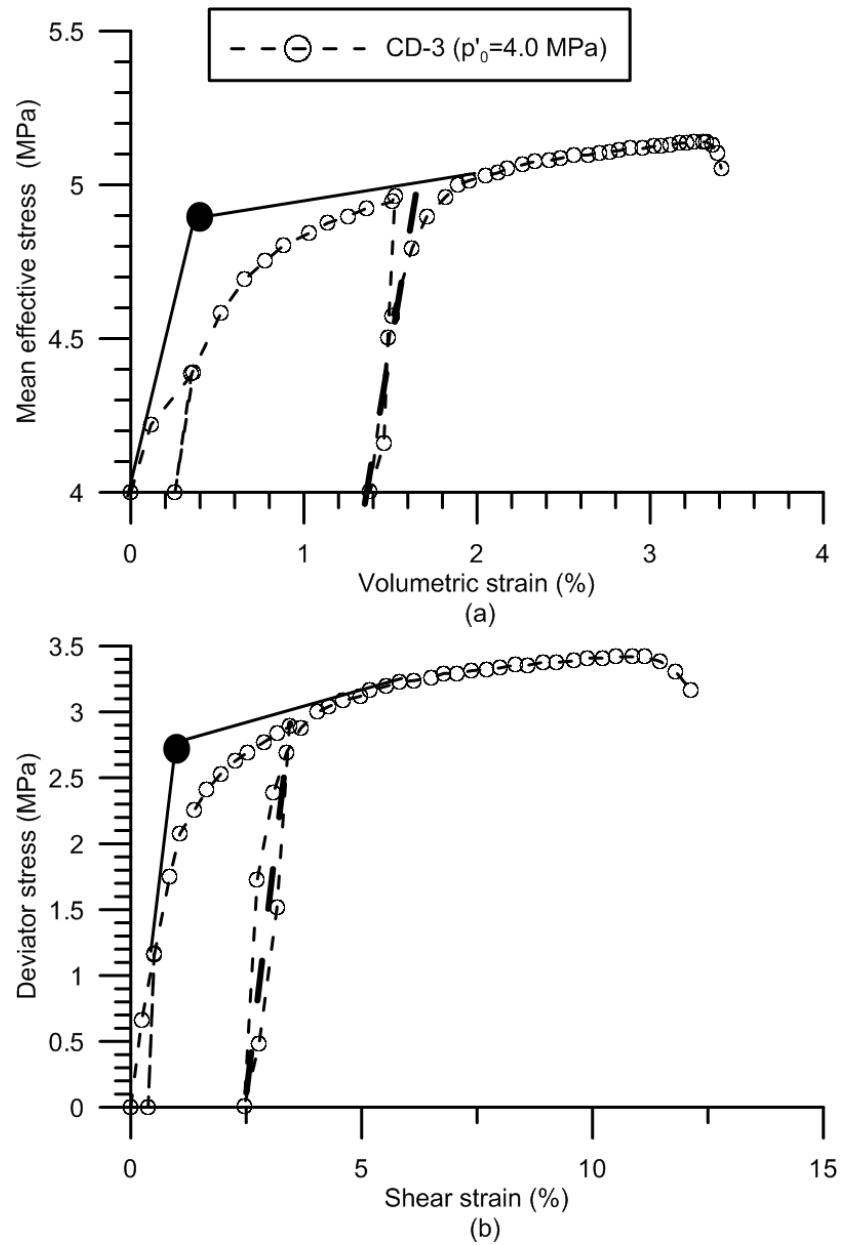


Figure 2.3: Yield stress determination from a drained triaxial shear test CD-3 ($p'_0=4.0$ MPa).

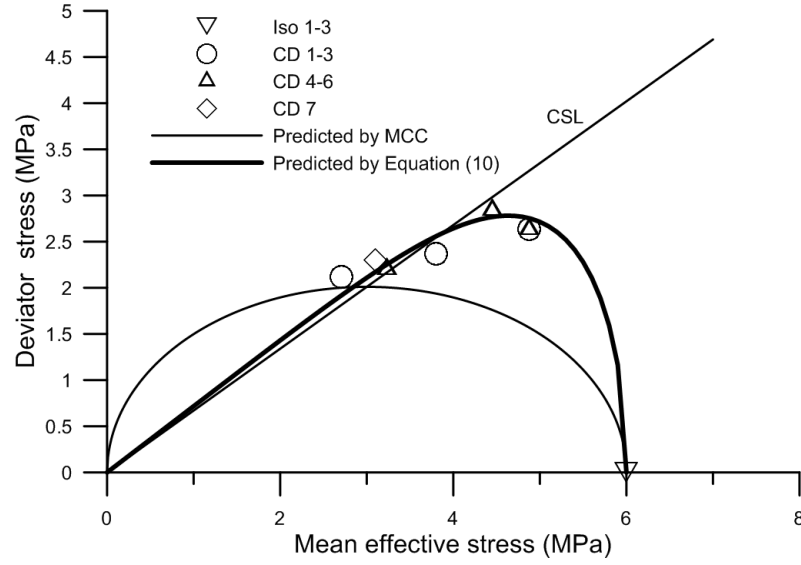


Figure 2.4: Yield curve of natural Boom clay.

2.2.3 Yield surface and plastic potential

Based on the experimental observations (see Figure 2.4), a generalized yield surface proposed by McDowell [54] is used to model the yielding behavior of natural Boom Clay. From the flow rule for triaxial compression,

$$\frac{d\varepsilon_v^p}{d\varepsilon_s^p} = \frac{M_g^2 - \eta^2}{k_g \eta} \quad (2.7)$$

a generalized plastic potential can be determined by integration of Equation 2.7:

$$g(p', q, p'_c) = q^2 + \frac{M_g^2}{1 - k_g} \left(\frac{p'}{p'_c} \right)^{2/k_g} p'_c{}^2 - \frac{M_g^2 p'^2}{1 - k_g} \quad (\text{if } k_g \neq 1) \quad (2.8)$$

and

$$g(p', q, p'_c) = q - M_g p' \sqrt{2 \ln(p'_c/p')} \quad (\text{if } k_g = 1) \quad (2.9)$$

where η is the stress ratio q/p' , M_g is the critical state slope defining the stress ratio at failure when there is no further volumetric strain increment, k_g is a parameter used to specify the shape of the surface, p'_c is the isotropic preconsolidation pressure. As in the

MCC, the generalized plastic potential is continuously differentiable for $\eta = 0$. In Equation 2.7, $k_g = 2$ is the case of MCC and the plastic potential of MCC (with an associated flow rule) is recovered.

To achieve a wide variety of yield surface shapes, the expression of the plastic potential (Equation 2.8) can be used as yield surface. The equation of the yield surface has the form:

$$f \equiv q^2 + \frac{M_f^2}{1 - k_f} \left(\frac{p'}{p'_c} \right)^{2/k_f} p'^2 - \frac{M_f^2 p'^2}{1 - k_f} = 0 \quad (\text{if } k_f \neq 1) \quad (2.10)$$

and

$$f \equiv q - M_f p' \sqrt{2 \ln(p'_c/p')} = 0 \quad (\text{if } k_f = 1) \quad (2.11)$$

where M_f defines the stress ratio at the apex of the yield surface, k_f is a parameter used to specify the shape of the yield surface. If $k_f = k_g$ and $M_f = M_g$, an associated flow rule is recovered. Otherwise, a non-associated flow rule is applied. The intersection point between the critical state line and the yield surface would not occur at the apex of the yield surface (contrary to MCC) if $M_f \neq M_g$.

Figures 2.5-2.6 show the shapes of the yield surface with different variables of M_f and k_f . In Figure 2.5, the shapes of the yield surface are shown for different values of M_f (0.5, 1, and 1.5), at constant values of $p'_c = 6$ MPa and $k_f=0.6$. It shows that the yield surface grows only in the direction of shear stress with an increase of M_f , keeping the mean effective stress at the peak point constant. In Figure 2.6, the shapes of the yield surfaces are shown for different values of k_f (0.6, 1.2, and 2), at constant values of $p'_c = 6$ MPa and $M_f=1$. It shows that the yield surface develops with the apex stress state moves down along the M_f line (line with a slope of M_f) with an increase of k_f .

2.2.4 Hardening law

The isotropic hardening law of MCC is adopted. The yield behaviour is controlled by the preconsolidation pressure (p'_c) and it evolves with volumetric plastic strain according

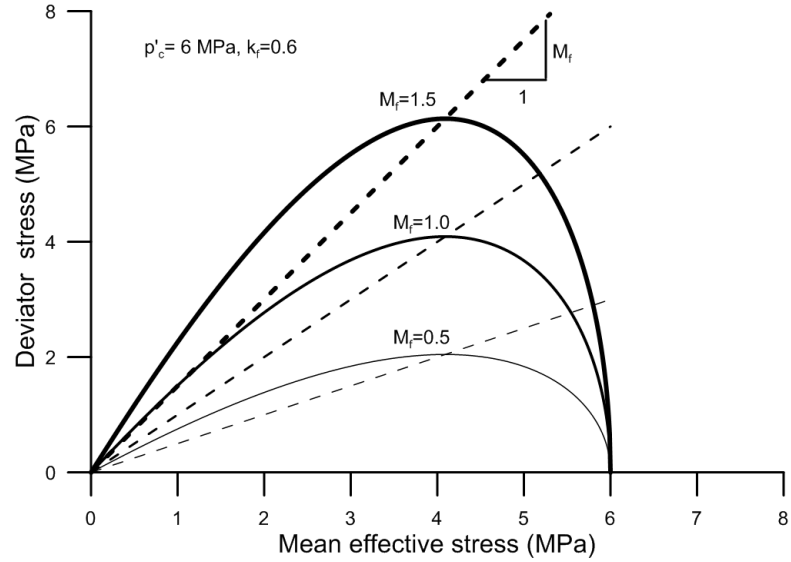


Figure 2.5: Evolution of the yield surface in $p' - q$ plane with respect to M_f .

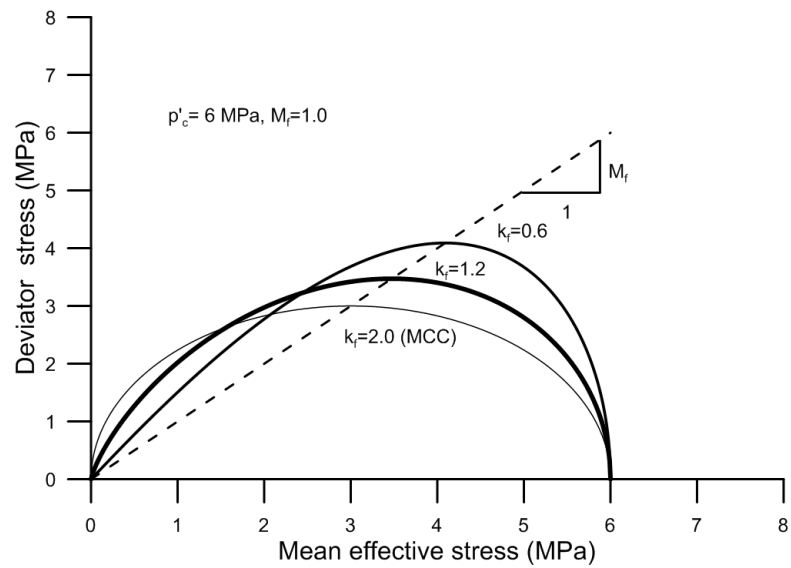


Figure 2.6: Evolution of the yield surface in $p' - q$ plane with respect to k_f .

to the following expression:

$$dp'_c = \frac{v_0 p'_c}{\lambda - \kappa} d\varepsilon_v^p \quad (2.12)$$

2.2.5 Determination of parameters

In total, ACC-1 requires calibration of 7 or 8 parameters (depending on the choice of the expression for the shear modulus): λ , κ , ν (or G_{nc} , m), p'_{c0} , k_f , M_f , k_g , M_g . The procedure for determining these parameters is described below.

1. λ , κ , p'_{c0} , M_g (same as M in MCC) are common parameters of MCC and can be determined in a common fashion as described in Chapter 1. The elastic shear modulus G can be calculated according to Equation 2.4 or 2.5. In the former case, ν is required and its determination has been also described in Chapter 1. In the latter case, two material constants (G_{nc} and m) are needed. With the classic definition of elasticity (reversible behavior), G at a given mean effective pressure can be obtained from the slope of $q - \varepsilon_s$ curve at small strains in monotonic loading or the slope of an unloading-reloading loop. G_{nc} and m can be calibrated by fitting the experimental data of (p', G) .
2. M_f and k_f are calibrated by fitting the yield surface shape to the yield points determined from experimental tests performed at various stress ratios (see Figure 2.4).
3. k_g is used to describe the plastic flow rule and can be determined by the values of $d\varepsilon_v^p/d\varepsilon_s^p$ obtained from drained triaxial shear tests for instance.

2.2.6 Evaluation of the model

In this section, numerical validation of the proposed model (ACC-1) is performed using the experimental results on natural Boom Clay presented in Chapter 1. The numerical implementation of the model is a simple extension of MCC's one, considering the changes in yield surface and plastic potential definitions and the shear modulus expression. As done in Chapter 1, all the simulations are performed from the initial state for Boom Clay

Table 2.2: ACC-1 parameters for natural Boom Clay.

λ	κ	ν	G_{nc} (MPa)	m
0.170	0.02	0.3	75	0.5
p'_{c0} (MPa)	M_f	k_f	M_g	k_g
6	0.60	0.30	0.67	0.7

defined by $p'=2$ MPa, $e_0=0.61$. The ACC-1 parameters (considering different choices of the expression for the shear modulus) for natural Boom Clay are given in Table 2.2.

The simulations of drained triaxial shear tests under different mean effective stresses are performed and discussed. Both non-linear shear modulus G calculated using Equation 2.4 and Equation 2.5 respectively, are used in the simulations by ACC-1 along different loading paths. These two cases are referred to as ACC-1 (1) and ACC-1 (2), respectively. The comparisons between the experimental observations and the ACC-1 predictions are shown in Figures 2.7-2.8. The predictions of MCC are also presented in these figures.

It is found that ACC-1 is better than MCC for modeling stress-strain behavior in $q - \varepsilon_1$ plane. The results show that the yield point in terms of deviator stress is well captured by ACC-1, indicating the performance of the new yield surface. However, it is shown that the predictions by ACC-1 are not better than those by MCC in $\varepsilon_v - \varepsilon_1$ plane. This is because a larger elastic zone is adopted in ACC-1 (see Figure 2.4) and thereby the effective stress path undergoes larger elastic loading part and smaller plastic loading part before reaching the critical state, resulting in smaller volumetric strain. This limitation is associated with the conventional plastic mechanism that no plastic volumetric strain is allowed inside the conventional yield surface. From the simulation results of ACC-1 (1) and ACC-1 (2), it appears that the adopted non-linear elastic rules are too simple to adequately model the smooth behavior of natural Boom Clay inside the conventional yield surface. Thereby, a new plastic mechanism inside the conventional yield surface should be considered to obtain better simulations.

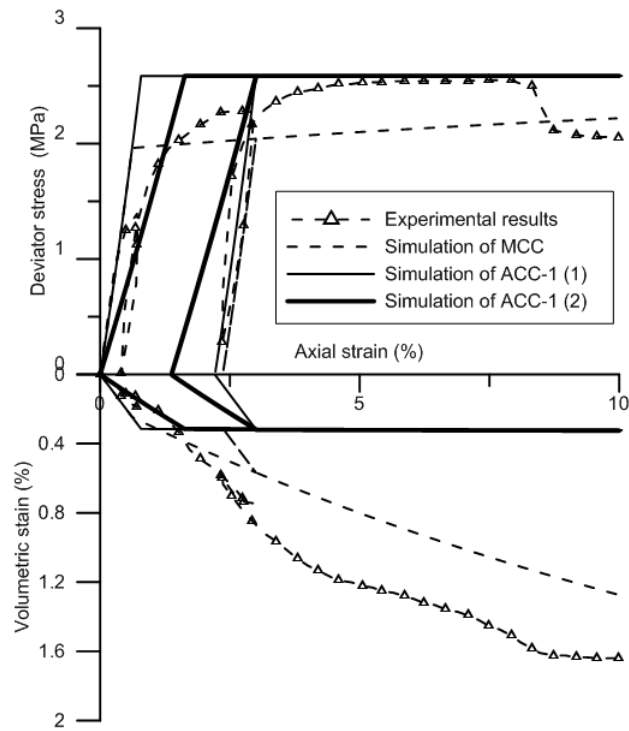


Figure 2.7: Model prediction for the drained triaxial shear test CD-2 ($p'_0=3.0$ MPa).

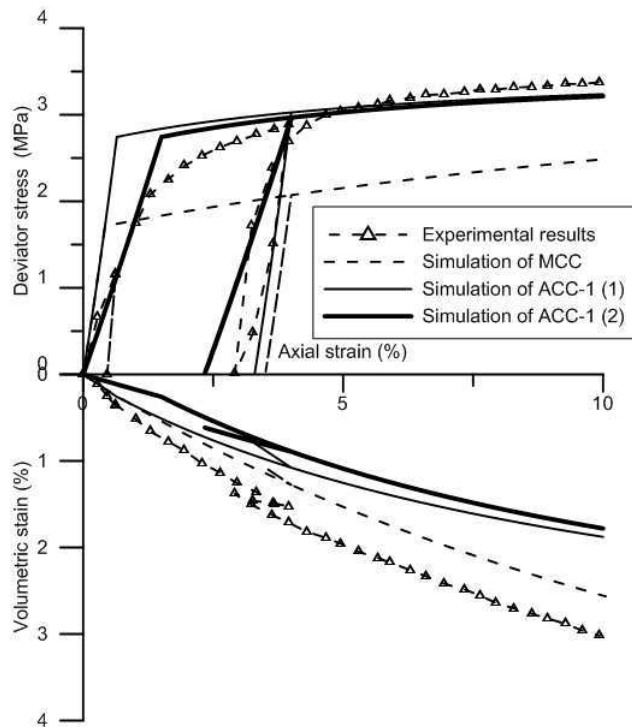


Figure 2.8: Model prediction for the drained triaxial shear test CD-3 ($p'_0=4.0$ MPa).

2.3 A Two-surface model incorporating progressive plastic hardening mechanism (ACC-2)

2.3.1 Elastic behavior

The elastic part of this model is expressed in terms of the bulk and shear modulus, K and G . The bulk modulus K is the same as for the MCC model whereas the shear modulus G is obtained by assuming a constant Poisson's ratio, as shown in Equation 2.2 and 2.4, respectively.

2.3.2 Progressive plastic hardening mechanism

As mentioned in Chapter 1, the isotropic hardening law of MCC is based on the assumption of bilinear compression curve in the $v-v'$ plane. Experimental observations (see Figure 2.9) have shown that such bilinear relationship is not suitable for describing the smooth transition from the elastic regime to the plastic one as in the case of natural Boom Clay. In this section, an isotropic hardening law that incorporates the plastic mechanism for progressive stiffness degradation is introduced on the basis of the experimental compression behavior in $v-v'$ plane.

The isotropic compression curve of natural Boom Clay can be divided into three phases according to Smith et al. [76]. The first stage is represented by the 'true' elastic region where the strains are fully recoverable. In general, the size of this region is very small. In the second phase (O-B), 'true' yield begins to occur since plastic strain is produced. The tangent stiffness is reduced gradually with increasing strain, leading to a smooth compression curve, i.e. the plastic strain increases progressively. The behavior of this phase is usually described by the term 'smooth elasto-plastic transition behavior' (e.g. [24]). In the third phase, large-scale changes in soil particle occur. The compression behavior in this stage is commonly represented by a normal consolidation line (NCL) with a slope λ as in the MCC.

A soil at a given yield state (point A in Figure 2.9) on the compression curve can be

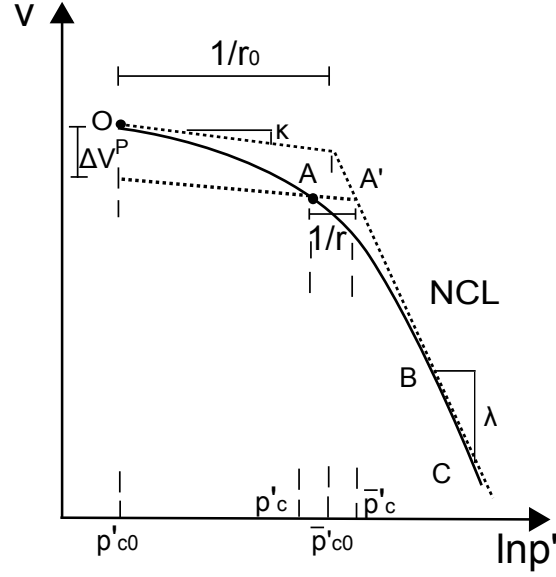


Figure 2.9: Schematic representation of the isotropic compression behavior of natural Boom Clay.

linked to a reference yield state on NCL (point A' in Figure 2.9) by a scalar r measuring the distance of the current yield state to the reference yield state along an elastic line with slope κ :

$$r = \frac{p'_c}{\bar{p}'_c} \quad (2.13)$$

where p'_c is the actual loading yield stress, \bar{p}'_c is the reference yield stress on the normal consolidation line.

The evolution of \bar{p}'_c depends on the plastic volumetric strain, as in the MCC, and is described by:

$$d\bar{p}'_c = \frac{v_0}{\lambda - \kappa} \bar{p}'_c d\varepsilon_v^p \quad (2.14)$$

To account for the progressive increment of plastic strain, a simple exponential law is used to describe the evolution of r :

$$r = 1 + (r_0 - 1) \exp\left(\frac{-v_0 s \varepsilon_v^p}{\lambda - \kappa}\right) \quad (2.15)$$

where r_0 is the initial value of r and the value of r_0 is always smaller than or equal to 1 ($r_0 \leq$

1), s is a material constant controlling the rate of stiffness degradation with strain. Equation 2.15 shows that r increases monotonically with the plastic strain increased (hardening process) for $r_0 < 1$. r is always lower than 1 to which it tends asymptotically, unless the initial condition is such that $r = r_0 = 1$ at all times.

The incremental form of the hardening law for r can be defined as:

$$dr = \frac{v_0}{\lambda - \kappa} s(1 - r) d\varepsilon_v^p \quad (2.16)$$

The evolution law of p'_c can thus be described as:

$$\begin{aligned} dp'_c &= d(r\bar{p}'_c) = \bar{p}'_c dr + r d\bar{p}'_c \\ &= \frac{v_0}{\lambda - \kappa} [1 + s(1/r - 1)] p'_c d\varepsilon_v^p \end{aligned} \quad (2.17)$$

Accounting for the contribution of r , the overall hardening modulus decreases as r increases from r_0 to 1. This hardening law enables a smooth elastic–plastic transition.

2.3.3 Yield surfaces

In view of the yielding concept defined in Section 2.3.1, two yield surfaces are introduced: an Inner yield surface describing the yielding behavior with plastic strain inside the existing conventional yield surface called Yield surface representing the normal consolidation behavior, as indicated in Figure 2.10. It should be pointed out that the Inner yield surface is defined as a yield limit as used in the conventional elasto-plasticity. It has a clear physical meaning since the plastic deformation begins when the stress state reaches it and its evolution verifies the standard Kuhn-Tucker condition. In this sense, the present model deviates from the well known bounding surface model developed by Dafalias and his co-workers [24, 25] where the inner surface (termed 'loading surface') located inside the conventional yield surface is not a yield surface but a quasi-elastic surface that does not follow the conventional yield limit concept. In fact, the proposed model is closer to the advanced elasto-plastic models called bubble models like the one developed by Rouainia

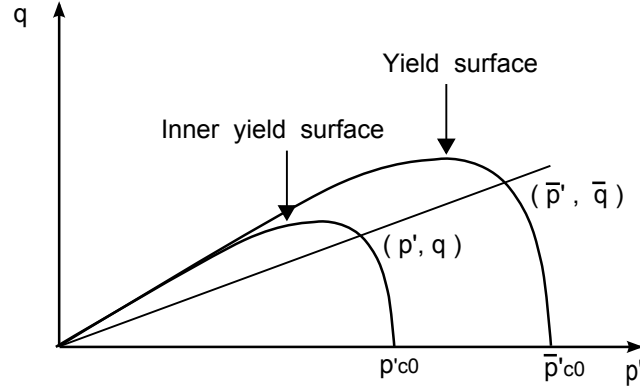


Figure 2.10: Yield surfaces of ACC-2.

and Wood [68].

The yield stress on the Inner yield surface in triaxial stress state is denoted by (p', q) while (\bar{p}', \bar{q}) is the corresponding reference yield stress on the Yield surface. Since the Inner yield surface is homologous to the Yield surface with respect to the origin in $p' - q$ space, therefore:

$$\frac{p'}{\bar{p}'} = \frac{q}{\bar{q}} = \frac{p'_c}{\bar{p}'_c} = r \quad (2.18)$$

The Yield surface (f_Y) uses the same surface as ACC-1 and can be expressed as:

$$f_Y \equiv q^2 + \frac{M_f^2}{1 - k_f} \left(\frac{p'}{\bar{p}'_c} \right)^{2/k_f} \bar{p}'_c^2 - \frac{M_f^2 p'^2}{1 - k_f} = 0 \quad (2.19)$$

For the sake of brevity but without losing generality, it is assumed that k_f does not equal 1. Substituting Equation 2.18 into Equation 2.19 gives the mathematical equation of the Inner yield surface (f_I):

$$f_I \equiv r^2 f_Y \quad (2.20)$$

and therefore:

$$f_I \equiv q^2 + \frac{M_f^2}{1 - k_f} \left(\frac{p'}{r \bar{p}'_c} \right)^{2/k_f} (r \bar{p}'_c)^2 - \frac{M_f^2 p'^2}{1 - k_f} = 0 \quad (2.21)$$

The Inner yield surface has a similar shape and a size r ($0 \leq r \leq 1$) times the size of the Yield surface.

2.3.4 Plastic potentials

The plastic potentials associated with the Inner yield surface and the Yield surface read, respectively:

$$g_I(p', q, \bar{p}'_c) = q^2 + \frac{M_g^2}{1 - k_g} \left(\frac{p'}{r\bar{p}'_c} \right)^{2/k_g} (r\bar{p}'_c)^2 - \frac{M_g^2 p'^2}{1 - k_g} \quad (2.22)$$

$$g_Y(p', q, \bar{p}'_c) = q^2 + \frac{M_g^2}{1 - k_g} \left(\frac{p'}{\bar{p}'_c} \right)^{2/k_g} \bar{p}'_c^2 - \frac{M_g^2 p'^2}{1 - k_g} \quad (2.23)$$

For the sake of brevity but without losing generality, it is also assumed that k_g does not equal 1.

2.3.5 Hardening law

Two hardening parameters \bar{p}'_c and r are introduced to control the size of the Yield surface and the Inner yield surface, respectively. The internal variables \bar{p}'_c and r are dependent on the volumetric plastic strain as shown in Equation 2.14 and Equation 2.16, respectively. The evolution of the yield surfaces is discussed in the following and two distinct situations are encountered depending on the value of r_0 .

1. $0 \leq r_0 < 1$

The Inner yield surface is completely inside the Yield surface. When the stress state reaches the Inner yield surface, plastic strain begins and the Inner yield surface and the Yield surface evolve simultaneously according to Equation 2.14 and Equation 2.16, respectively. The Inner yield surface moves faster than the outer yield surface but without touching it thanks to the chosen hardening law. The approaching rate depends on the parameter s .

2. $r_0 = 1$

The Inner yield surface and the Yield surface coincide. Both the surfaces evolve at the same rate since Equations 2.14 and 2.17 are equivalent if $r = r_0 = 1$. It is as if the Inner surface is cancelled and ACC-2 thus reduces to ACC-1.

For unloading from the Inner yield surface, purely elastic behavior is assumed as in the conventional elasto-plasticity theory and the stress state moves back inside the Inner yield surface verifying the standard Kuhn-Tucker condition. In the reloading process, still purely elastic behavior occurs before reaching the Inner yield surface again. Obviously, such mechanism following the conventional elasto-plasticity theory can not describe the closed hysteresis loop behavior of soils along an unloading-reloading process; however, this is out of the scope of this study.

2.3.6 Constitutive relations

Plastic strain is generated if the Inner yield surface is activated. In what follows, the equations for plastic strain rate are formulated by considering the consistency condition for the Inner yield surface.

The plastic strain increment is computed from the plastic potential:

$$d\boldsymbol{\varepsilon}^p = d\lambda \frac{\partial g_I}{\partial \boldsymbol{\sigma}'} \quad (2.24)$$

where $d\lambda$ is the plastic multiplier, and g_I is the plastic potential corresponding to the activation of the Inner yield surface.

\bar{p}'_c and r act as constitutive hardening variables in the model and \mathbf{X} denotes a vector of hardening variables:

$$\mathbf{X} = \{X_1, X_2\}^t = \{\bar{p}'_c, r\}^t \quad (2.25)$$

The hardening law can thus be written in a general form:

$$d\mathbf{X} = d\lambda \mathbf{B} \quad (2.26)$$

where:

$$\mathbf{B} = \{B_1, B_2\}^t \quad (2.27)$$

$$B_1 = \frac{\partial \bar{p}'_c}{\partial \varepsilon_v^p} \frac{\partial g_I}{\partial p'} \quad (2.28)$$

$$B_2 = \frac{\partial r}{\partial \varepsilon_v^p} \frac{\partial g_I}{\partial p'} \quad (2.29)$$

The consistency condition on the Inner surface is given by:

$$\left(\frac{\partial f_I}{\partial \boldsymbol{\sigma}'} \right)^t : d\boldsymbol{\sigma}' - h d\lambda = 0 \quad (2.30)$$

with h being the hardening modulus:

$$h = - \left(\frac{\partial f_I}{\partial \bar{p}'_c} B_1 + \frac{\partial f_I}{\partial r} B_2 \right) \quad (2.31)$$

The differential stress–strain equations can finally be given:

$$\begin{aligned} d\boldsymbol{\sigma}' &= \mathbf{D}_{ep} d\boldsymbol{\varepsilon} \\ d\mathbf{X} &= \mathbf{R}_{ep} d\boldsymbol{\varepsilon} \end{aligned} \quad (2.32)$$

where:

$$\mathbf{D}_{ep} = \mathbf{D}_e - \frac{\mathbf{D}_e \mathbf{b}(\mathbf{a})^t \mathbf{D}_e}{(\mathbf{a})^t \mathbf{D}_e \mathbf{b} + h} \quad (2.33)$$

$$\mathbf{R}_{ep} = (\mathbf{R}_{ep1}, \mathbf{R}_{ep2})^t \quad (2.34)$$

$$\mathbf{R}_{ep1} = \frac{B_1(\mathbf{a})^t \mathbf{D}_e}{(\mathbf{a})^t \mathbf{D}_e \mathbf{b} + h} \quad (2.35)$$

$$\mathbf{R}_{ep2} = \frac{B_2(\mathbf{a})^t \mathbf{D}_e}{(\mathbf{a})^t \mathbf{D}_e \mathbf{b} + h} \quad (2.36)$$

with \mathbf{D}_e being the elastic stiffness matrix, $\mathbf{a} = \frac{\partial f_I}{\partial \boldsymbol{\sigma}'}$, $\mathbf{b} = \frac{\partial g_I}{\partial \boldsymbol{\sigma}'}$.

2.3.7 Stress integration algorithm

The explicit stress integration scheme with an adaptive time-stepping scheme is used here to solve the above stress-strain relations. It must be emphasized that consideration of

the Inner yield surface (f_I) is sufficient even though two yield surfaces co-exist. Thus, the implementation of ACC-2 is similar to that of ACC-1. This is because:

1. The Inner yield surface is treated as a 'true' yield surface following the conventional plasticity. All the features of the stress integration schemes (e.g. loading criterion) for the classic elasto-plastic models can be applied to the Inner yield surface.
2. In the general case $0 \leq r_0 < 1$, it is guaranteed that the effective stress would reach the Inner surface but never reach the Yield surface by the chosen hardening law.
3. If $r_0 = 1$, the Inner yield surface and the Yield surface coincide at any stress state and the same constitutive relations are provided from the consistency condition for any of the two yield surfaces. And so the algorithm can solve only one yield surface (f_I is chosen).

However, a small modification is necessary and is described below. For the plastic loading process, the increments of stress and hardening parameters can be calculated by an Euler solution and a modified Euler solution. The error is calculated by taking the difference between the Euler solution and the modified Euler solution. The size of the increment can be adapted automatically by maintained the local integration error below a specified tolerance. Since here two hardening parameters are associated with the Inner yield surface, the error measure R with respect to the hardening parameters is evaluated as:

$$R = \sqrt{\frac{(\bar{p}'_{c1} - \bar{p}'_{c2})^2}{(\bar{p}'_{c2})^2} + \frac{(r_1 - r_2)^2}{(r_2)^2}} \quad (2.37)$$

where subscripts 1 and 2 denotes values obtained by Euler solution and modified Euler solution, respectively.

2.3.8 Parametric study

2.3.8.1 Selection of parameters

The proposed model ACC-2 requires 10 parameters ($\lambda, \kappa, \nu, \bar{p}'_{c0}, k_f, M_f, k_g, M_g, s, r_0$). The first eight parameters are common to ACC-1. Note that the notation of p'_{c0} in ACC-1 is replaced by \bar{p}'_{c0} in ACC-2 denoting conventional isotropic preconsolidation pressure. r_0 specifies the size of Inner yield surface associated with the first occurrence of plastic strains. For the natural Boom clay, the initial size of the Inner yield surface is defined by the initial in-situ effective stress (around 2 MPa) assuming that plastic strain is generated after loading from the the in-situ effective stress state. It is worth noting that r is the inverse of the OCR, as classically defined. Thus, $r_0=0.33$ is adopted for natural Boom Clay.

Parameter s determines the hardening rate of Inner yield surface approaching the Yield surface. It influences the variation rate of the plastic modulus. This parameter can be calibrated by an isotropic loading compression test.

2.3.8.2 Sensitivity study on parameter s

A sensitivity study on parameter s is carried out to check its influence in the simulations. The study involves an isotropic loading compression test and a conventional triaxial compression test on natural Boom Clay sample from the initial in-situ state ($p'_0=2$ MPa, $e_0=0.61$). An axial strain of 10% is imposed. s varies between 1 and 100 and the other model parameters used in the sensitivity study are kept unchanged. Their values are summarized in Table 2.3.

As expected, ACC-2 predicts a smooth response in the isotropic compression test, i.e. a smooth relation of volumetric strain and logarithmic effective mean stress, as shown in Figure 2.11. It clearly shows that the curvature of stress-strain curve depends on the material constant s . A smaller value of s gives a more gentle transition from elastic to plastic state. With a larger value of s , the model present a stiffness closer to the elastic

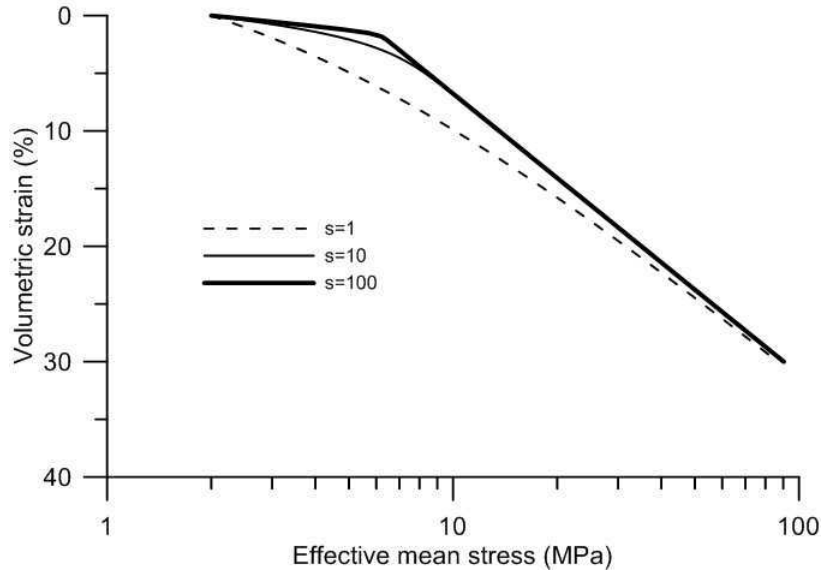


Figure 2.11: Isotropic compression test results in $\varepsilon_v - p'$ plot.

one before approaching the Yield surface. Thus, if large values are used for s , ACC-2 gives results similar to ACC-1.

From Figure 2.12, we can see that r evolves with strain and approaches 1 asymptotically. This means that the Inner yield surface would not go across the Yield surface. This feature leads to a simple stress implementation algorithm, as mentioned previously.

Figure 2.13 shows the drained triaxial shear test results in $q - \varepsilon_1$ and $\varepsilon_v - \varepsilon_1$ plots. From the curve of $q - \varepsilon_1$, it appears again that the curvature of the stress-strain curve is influenced by the material constant s . Larger volumetric strain is predicted with a smaller value of s as it can be seen in the $\varepsilon_v - \varepsilon_1$ plot. Also, r does not reach 1 as shown in Figure 2.14. This is because a volumetric hardening rule is adopted and therefore hardening stops when the effective stress reaches the critical state line ($\frac{\partial g}{\partial p'} = 0$). The effective stress can not go over the critical state line and the evolution of r is stopped. Determining plastic modulus, $h = 0$ is obtained at this state as it be clearly seen from the detailed expression

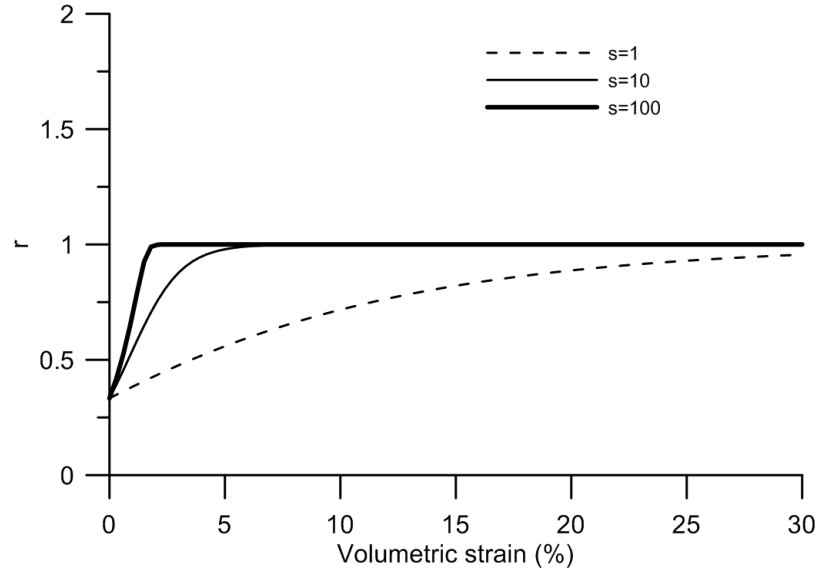


Figure 2.12: Variations of r with respect to volumetric strain in an isotropic compression test.

of plastic modulus in the following form:

$$h = \frac{2M_f^2}{k_f} p'^{(2/k_f)} (r \bar{p}'_c)^{(2-2/k_f)} \frac{v_0}{\lambda - \kappa} [1 + s(1/r - 1)] \frac{\partial g}{\partial p'} \quad (2.38)$$

Considering the contribution of shear plastic strain to the hardening variable r , the stress can increase over the critical state line. A generalized plastic strain is proposed by Wood [59]:

$$d\varepsilon_d = \sqrt{A_d (d\varepsilon_v^p)^2 + (1 - A_d) (d\varepsilon_s^p)^2} \quad (2.39)$$

and a new evolution law of r can be given:

$$dr = \frac{v_0}{\lambda - \kappa} s(1 - r) d\varepsilon_d^p \quad (2.40)$$

where A_d is a parameter controls the relative influence of shear plastic strain and volumetric plastic strain effect in hardening. The detailed expression of plastic modulus now can be

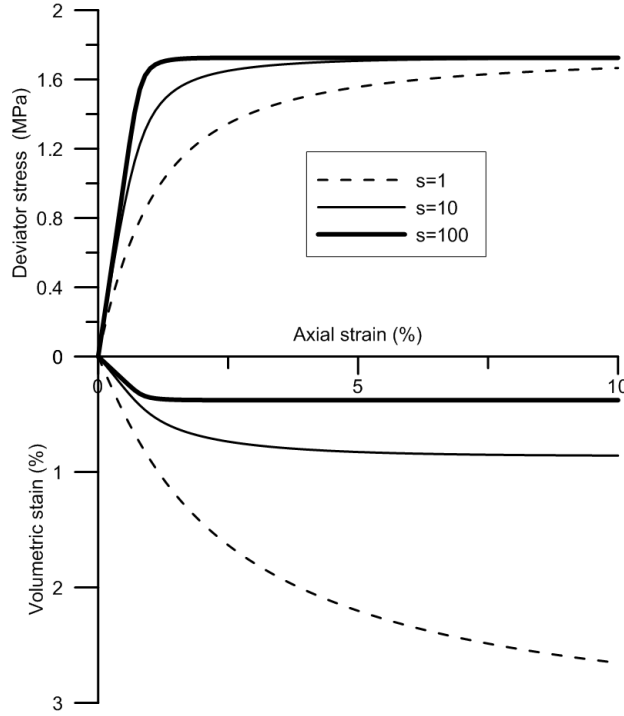


Figure 2.13: Drained triaxial shear test results in $q - \varepsilon_1$ and $\varepsilon_v - \varepsilon_1$ plot.

expressed in a new form:

$$h = \frac{2M_f^2}{k_f} p^{(2/k_f)} (r\bar{p}'_c)^{(2-2/k_f)} \frac{v_0}{\lambda - \kappa} \left(\frac{\partial g}{\partial p'} + s(1/r - 1) \sqrt{A_d \left(\frac{\partial g}{\partial p'} \right)^2 + (1 - A_d) \left(\frac{\partial g}{\partial q} \right)^2} \right) \quad (2.41)$$

As seen from the above equation, $h > 0$ holds even when the effective stress reach the critical state line with $\frac{\partial g}{\partial p'} = 0$ but $\frac{\partial g}{\partial q} > 0$ and then hardening continues with the effective stress increase over the critical state line. The adoption of shear plastic strain hardening could indeed make the model more flexible, however, the magnitude of its contribution can not be clearly validated.

2.3.9 Evaluation of the model

In this section, the performance of ACC-2 is assessed by predicting the behavior of natural Boom Clay based on the experimental tests described in Chapter 1. With respect to the undrained behavior, purely numerical simulation is performed as mentioned in Chapter

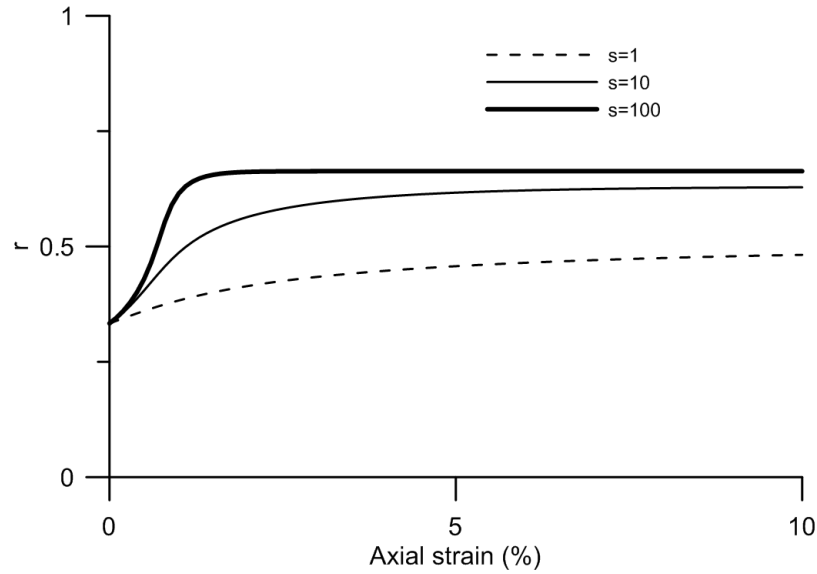


Figure 2.14: Variations of r with respect to axial strain in a drained triaxial shear test.

Table 2.3: ACC-2 parameters for natural Boom Clay.

λ	κ	ν	\bar{p}'_{c0} (MPa)	M_f
0.17	0.02	0.3	6	0.60
k_f	M_g	k_g	r_0	s
0.30	0.67	0.70	0.33	10

1. The test (CU-1) involves a conventional undrained shear path from $p'=2.3$ MPa. All the simulations are performed from the common point ($p'_0=2$ MPa, $e_0=0.61$). For the comparison purposes, the predictions by ACC-1 (G is calculated by a constant Poisson's ratio) are also presented. The model parameters for natural Boom Clay are presented in Table 2.3.

2.3.9.1 Isotropic test

Figure 2.15 compares the simulations of isotropic tests by both ACC-1 and ACC-2. It is worth noting that the experimental data with the same loading path from different samples presents a little scatter and the simulations can not satisfies all the experimental data in either loading or unloading process. Keeping this in mind, it can be noticed that ACC-

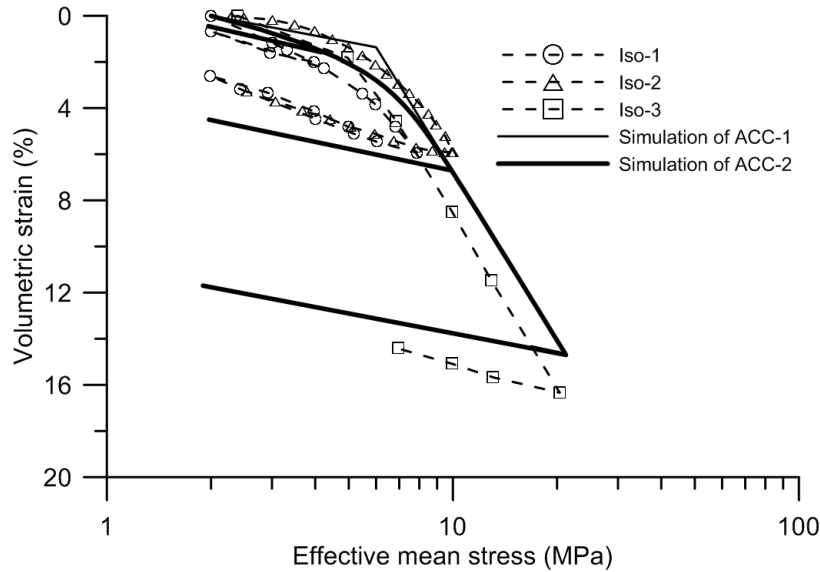


Figure 2.15: Numerical simulations of isotropic tests.

2 can capture the general trend of the experimental data in both loading and unloading processes (neglecting the hysteretic behavior) even though the difference between them is small. At low stress level ($p' < 10$ MPa), the simulation curve of ACC-2 is as smooth as the experimental curve and the parameter s can be determined by fitting the simulation curve to the experimental data. However, the prediction curve of ACC-1 does not capture such smooth behavior. At high stress levels ($p' > 10$ MPa), both ACC-2 and ACC-1 give the same simulation results. For the unloading process from $p' = 4$ MPa, it appears that ACC-1 cannot predict the irrecoverable strain as observed from the experimental results, since purely elastic strain is assumed in this regime. On the contrary, ACC-2 can predict such irrecoverable strain.

2.3.9.2 Oedometer test

Figure 2.16 shows the numerical predictions of oedometer compression test by ACC-2 and ACC-1. It can be observed clearly that the simulation curve of ACC-2 agrees quite well with the smooth experimental curve of Oed-3, underlining again the capability of ACC-2 in simulating smooth stress-strain behavior as observed from experimental results. The

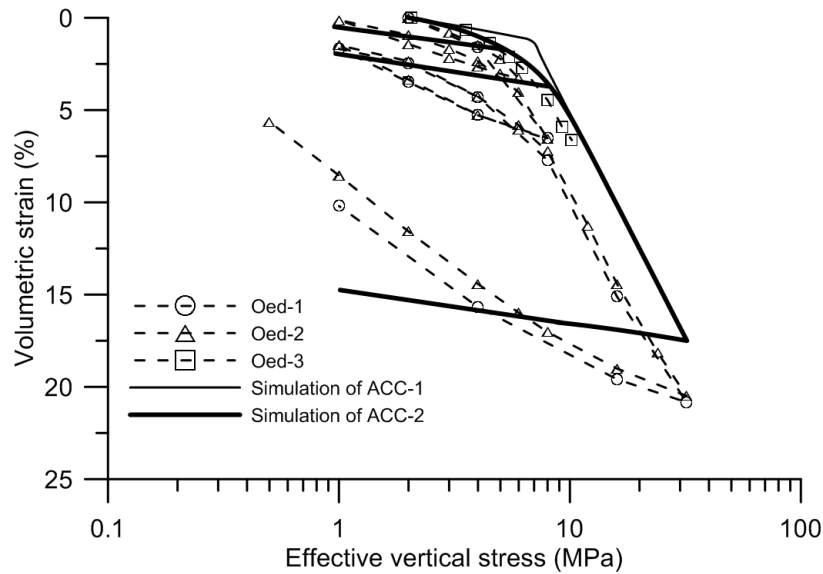


Figure 2.16: Numerical simulations of oedometer test.

difference appears between the predicted curve of ACC-2 with the observed curves of Oed-1 and Oed-2. This is mainly due to the scatter existing in the experimental data. Still, ACC-2 cannot capture the unconventional unloading behavior of oedometer test - the swelling slope of the stress-strain curve appears to increase greatly with compression.

2.3.9.3 Drained triaxial test

Figures 2.17-2.21 present the comparisons of ACC-1 and ACC-2 in simulating the drained triaxial tests. The results are presented in terms of variations of deviator stress and volumetric strain against axial strain.

For test CD-1, though underpredicting the yield stress as ACC-1, ACC-2 gives smoother simulation results and agrees better with the experimental results at small strain levels (around 0-1%) as shown in Figure 2.17. Further, ACC-2 gives better volumetric strain predictions. By contrast, ACC-1 gives predictions of poor-quality for the volume change. For the unloading process, ACC-2 can predict both the irrecoverable strain during the unloading process from a small strain level ($\epsilon_1=0.6\%$) and a large strain level ($\epsilon_1=2.8\%$); however, ACC-1 can only predict such behavior just for unloading from a high strain level.

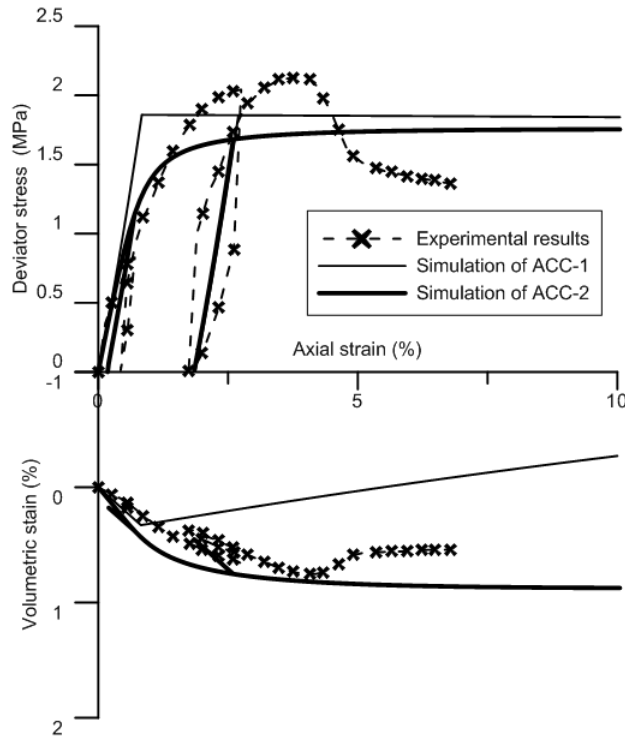


Figure 2.17: Numerical simulations of drained triaxial shear test CD-1 ($p'_0=2.0$ MPa).

When ignoring the hysteretic behavior, the unloading slope of the stress-strain curve can be relatively well captured by both models.

Figure 2.18 indicates that the predictions of test CD-4 test by ACC-2 are consistently better than those by ACC-1 for both the deviator stress-axial strain and volumetric strain-axial strain relationships. It shows clearly that ACC-2 can well capture the smooth elasto-plastic transition behavior on the deviator stress-axial strain curve. Again, the predictions of volume change are greatly improved by ACC-2 compared to ACC-1.

For test CD-2, the predictions by ACC-2 agree well with the experimental results with a smooth elasto-plastic transition behavior on the deviator stress-axial strain curve as shown in Figure 2.19. Though not fully agreeing with experimental results, the volumetric strain predictions by ACC-2 follow the trend of the experimental results much better than those by ACC-1. A final volumetric strain of 1.45% is obtained by ACC-2, which is quite close to the experimental one: $\varepsilon_v=1.63\%$.

As shown in Figure 2.20, a small difference appears between the predicted results of

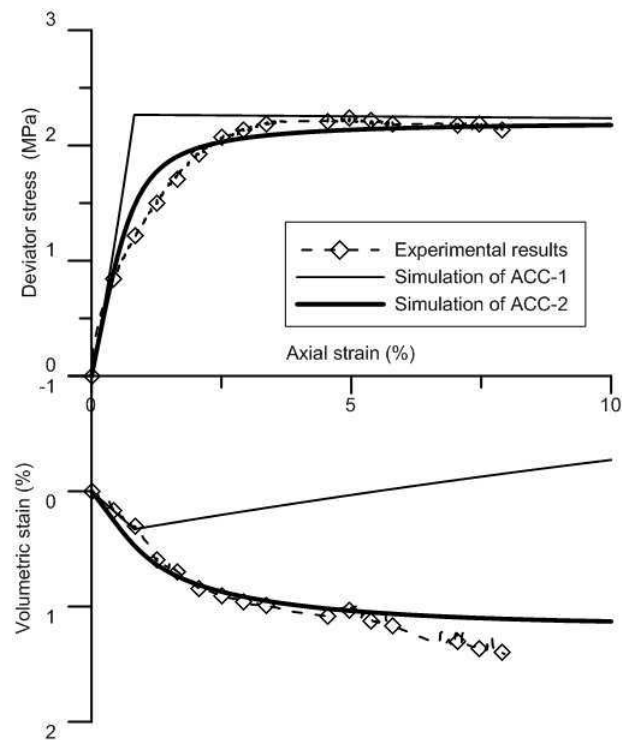


Figure 2.18: Numerical simulations of drained triaxial shear test CD-4 ($p'_0=2.5$ MPa).

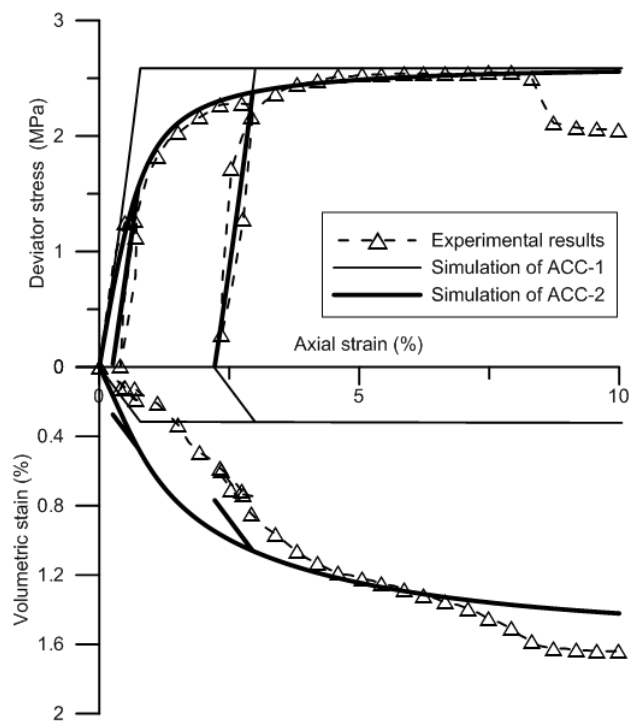


Figure 2.19: Numerical simulations of drained triaxial shear test CD-2 ($p'_0=3.0$ MPa).

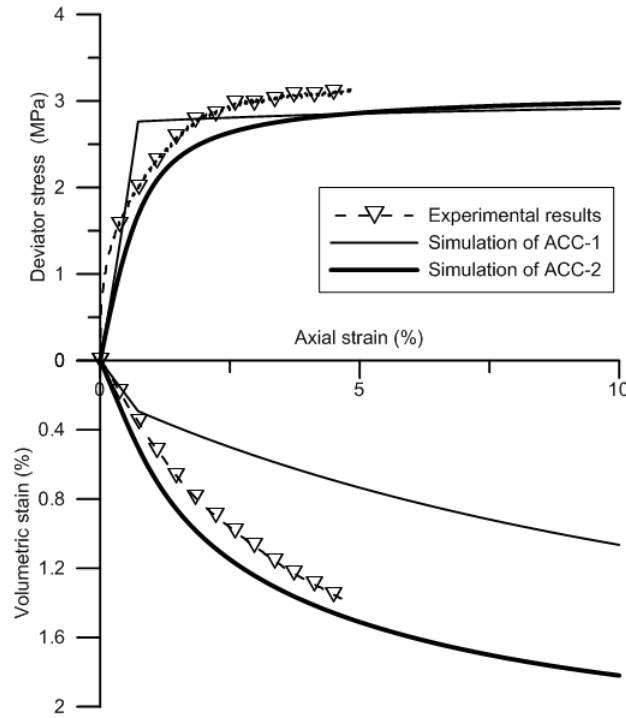


Figure 2.20: Numerical simulations of drained triaxial shear test CD-5 ($p'_0=3.5$ MPa).

ACC-2 and the experimental observations from test CD-5. However, the general trend of the smooth stress strain curve can be captured by ACC-2. Moreover, the volumetric strain prediction is greatly improved by ACC-2 in comparison with ACC-1.

For test CD-3, it appears that the predictions by ACC-2 agree quite well with the experimental results for the deviator stress-axial strain relationship as shown in Figure 2.21. For the volumetric strain, ACC-2 predicts relatively larger values at small axial strain levels around 0-3% but relatively smaller values at larger axial strain levels around 3-10%.

In summary, compared to ACC-1, ACC-2 provides better predictions for natural Boom Clay under drained triaxial loading conditions. The smooth elasto-plastic behavior can be well predicted by ACC-2. This shows that the plastic mechanism that allows flexible plastic modulus variation with the stress state inside the conventional yield surface is suitable for describing the natural Boom Clay behavior. In addition, the volumetric strain is better described by ACC-2.

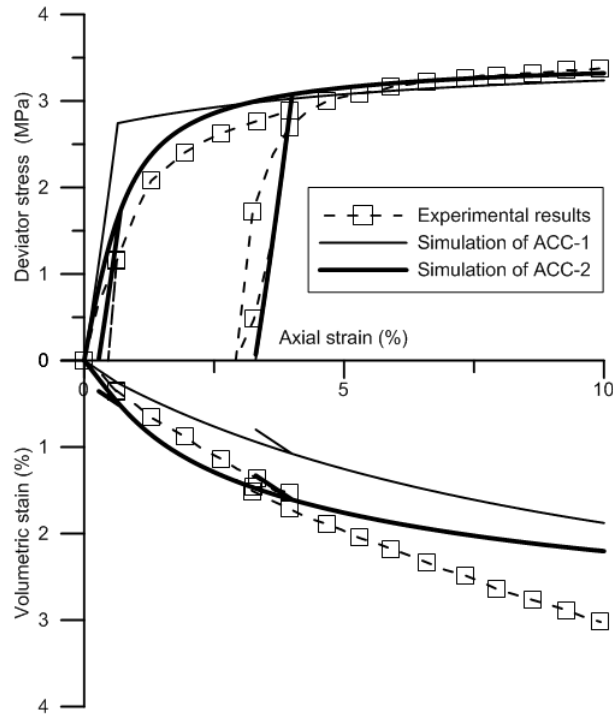


Figure 2.21: Numerical simulations of drained triaxial shear test CD-3 ($p'_0=4.0$ MPa).

2.3.9.4 Undrained triaxial test

Figure 2.22(a) compares the undrained triaxial test result predicted by ACC-1 and ACC-2 in $q - \varepsilon_1$ plot. For ACC-1, the deviator stress varies linearly with the axial strain in the initial stage since just elastic behavior occurs. Then, the deviator stress goes up gradually with larger axial strain change since softening behavior begins, which can be clearly seen in Figure 2.22(b). For ACC-2, the curve predicted is smoother before reaching the critical deviator stress after a reduced hardening part. Indeed, the smooth effect is not obvious in this simulation depending on the value adopted for s .

Figure 2.22(b) compares the undrained effective stress paths predicted by ACC-1 and ACC-2. Both the undrained effective stress paths approach the critical state line (CSL). For ACC-1, the undrained effective stress path is vertical before it reaches the yield surface without plastic volumetric change. After reaching the yield surface, the undrained effective stress path curves to the right (dilatant type behaviour with generation of negative pore water pressure) until it reaches the CSL. For ACC-2, due to the Inner yield surface inside

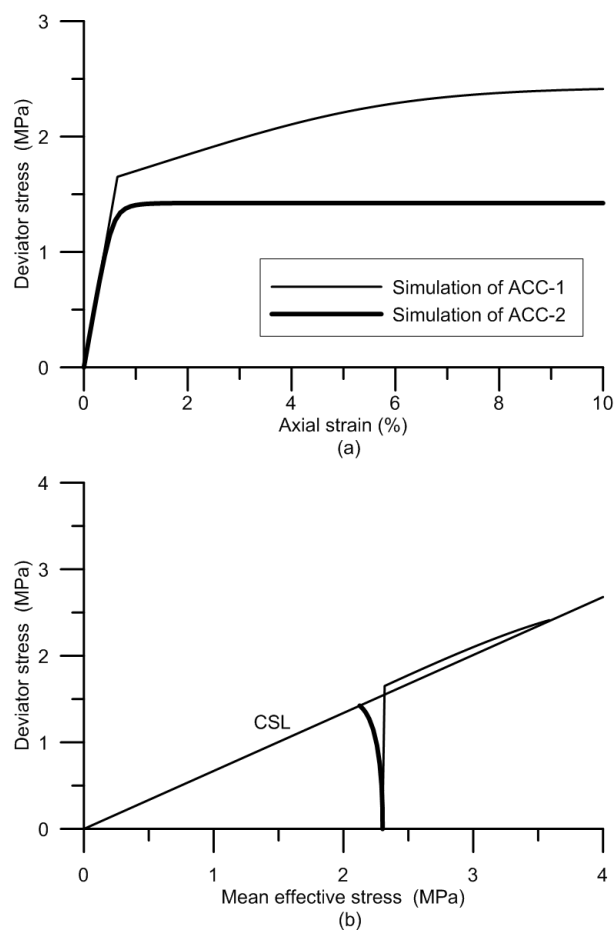


Figure 2.22: Numerical simulations of undrained triaxial shear test CU-1 ($p'_0 = 2.3$ MPa).

the Yield surface the effective stress path goes near the Inner yield surface with plastic volumetric strain change and curves to the left until it reaches the CSL (contractant behaviour type with generation of positive pore water pressure).

2.3.10 Discussion

It is certain that feasible classes of constitutive models should be used to describe the smooth elasto-plastic transition behavior. The study carried out here aims at developing a suitable model within a simple framework with clear physical meaning for parameters. Further, this model can be easily formulated and implemented in a numerical code.

The ACC-2 model developed can significantly improve the prediction of tests with monotonic loading, but still cannot predict the hysteresis loop behavior of unloading/reloading. This is because it predicts only an elastic strain rate in the unloading process. A better prediction for unloading/reloading behavior could be obtained by assuming an elasto-plastic behavior in the unloading process, i.e. plastic strains are not maintained constant during this process. This assumption is consistent with the recent work of Collins [19], which accounts for the recovery of plastic strain during unloading processes, in a thermodynamically consistent manner.

2.4 Conclusion

In this chapter, an adapted Cam Clay model is developed in two stages. In the first-level model (ACC-1), new expressions of the yield and plastic potential have been proposed. The new yield surface allows satisfactory description of the yield behavior as experimentally observed on natural Boom Clay. A non-associated flow rule is then adopted. Further, classic non-linear elastic rules in the critical state model are adopted with the elastic shear modulus G calculated in two fashions : (1) assuming that the Poisson's ratio ν is constant (2) G varying with OCR as proposed by Housbly et al. [41]. ACC-1 has been evaluated by simulating experimental tests on natural Boom Clay under drained triaxial conditions.

The simulation results of ACC-1 have been compared to those of MCC. It has been found that ACC-1 is better in yield shear stresses prediction than MCC. However, the volumetric predictions of ACC-1 are not consistently better than those of MCC. It is also found that both the adopted non-linear elastic rules are too simple to adequately model the smooth behavior of natural Boom Clay inside the ACC-1 surface.

To overcome the deficiency of ACC-1 in natural Boom Clay prediction, a simple Two-surface model (ACC-2) is developed. To account for the plastic behavior inside the ACC-1 yield surface (called Yield surface), a new plastic mechanism is proposed based on an additional yield surface called the Inner yield surface. A respective hardening law associated with the Inner yield surface is introduced, enabling the plastic modulus to vary flexibly when the stress approaches the Yield surface and the Inner surface approaches but not goes across the Yield surface. The constitutive equation can be simply formulated based on the consistency condition for the Inner yield surface. Since only the Inner yield surface has to be treated, ACC-2 can be efficiently implemented using an explicit stress integration scheme with automatic substepping and error control as for ACC-1.

Two new parameters (s and r) are introduced in ACC-2 to describe a smooth elasto-plastic transition. A sensitivity study of the new parameter (s) shows that the curvature of the stress-strain curve is dependent on parameter s . ACC-2 comes back to ACC-1 if $r=1$.

Simulations of the experimental tests on natural Boom Clay have been performed to assess the performance of ACC-2. It has been observed that ACC-2 gives better predictions than ACC-1. In particular, the smooth stress-strain behavior can be captured, and in addition, the volumetric strain is well predicted by ACC-2.

Chapter 3

On some advanced thermo-mechanical models and explicit integration improvements

3.1 Introduction

In the context of geological disposal for nuclear waste disposal, the host clay formation may undergo the effects of temperature changes. In addition, these effects are coupled to the mechanical ones. In this regard, it is important to investigate the thermo-mechanical behavior of the host formation.

The thermo-mechanical behavior of clays has been investigated by several researchers (e.g. [3, 7, 27, 31, 81]) on the basis of the available experimental results. The main features of this behaviour have been summarized by Cui et al. [22]. Various thermo-mechanical models have been developed to describe such behavior with different theoretical approaches; some for soft clays and some for stiff clays. In the present study, to develop an appropriate thermo-mechanical model for the natural Boom Clay, an assessment of the existing advanced models is carried out. Prior to any theoretical analysis, the test results on natural Boom Clay commonly used in constitutive models validation are clarified.

On the other hand, when considering the constitutive modeling of the thermo-mechanical behavior of clays, efficient stress integration algorithm should be investigated. This is crucial because the performance of the stress integration algorithm directly influences the overall performance of a Finite Element code in which the constitutive model is implemented. In the present study, an explicit stress integration algorithm is developed for the thermo-mechanical model proposed by Cui et al. [22] with a specifically designed adaptive time-stepping scheme. Although the developed algorithm refers to a specific model, the conclusions can be generalised to other thermo-mechanical models.

This chapter consists of two parts. In the first part, a classic isotropic thermo-mechanical experiment conducted on natural Boom Clay by Baldi et al. [7] is firstly clarified. Then the performance of the recent advanced thermo-mechanical models proposed by Cui et al. [22], Abuel-Naga et al. [1] and Laloui and François [31, 50] is assessed in terms of elasto-plasticity and thermodynamic requirements as well as their capabilities to capture the main features of experimental evidence. In the second part, the numerical integration algorithm of the thermo-mechanical model proposed by Cui et al. [22] at the stress point level using an explicit scheme is developed and analyzed.

The first part was published in « Computers and Geotechnics » [36] and the second part has been published in « International Journal for Numerical and Analytical Methods in Geomechanics » [37]. The articles are presented here in their original version.

3.2 On some advanced thermo-mechanical models for saturated clays

INTERNATIONAL JOURNAL FOR NUMERICAL AND ANALYTICAL METHODS IN GEOMECHANICS
Int. J. Numer. Anal. Meth. Geomech. (2013)
Published online in Wiley Online Library (wileyonlinelibrary.com). DOI: 10.1002/nag.2170

On some advanced thermo-mechanical models for saturated clays

P. Y. Hong, J. M. Pereira^{*,†}, A. M. Tang and Y. J. Cui

Université Paris-Est, Laboratoire Navier (UMR 8205), CNRS, ENPC, IFSTTAR, F-77455 Marne-la-Vallée, France

SUMMARY

This paper aims to evaluate the performance of several recent constitutive models in simulating the thermo-mechanical behaviour of saturated clays. A classic thermo-mechanical test on natural Boom Clay, commonly used in constitutive modelling, was first clarified. Different methods commonly used to measure volumetric strain in drained heating tests were then discussed. Model evaluation was performed in terms of thermodynamic and elasto-plastic requirements. The capability of the models to capture the observed behaviour was assessed on the basis of the experimental evidence. It was shown that all the models provide reasonable predictions of the thermo-mechanical behaviour of saturated clays. However, each constitutive model has its own limitations or unclear points from the theoretical point of view. Copyright © 2013 John Wiley & Sons, Ltd.

Received 25 July 2012; Revised 6 December 2012; Accepted 14 December 2012

KEY WORDS: thermo-mechanical behaviour; saturated clay; constitutive model; theoretical analysis

3.2.1 Introduction

Relevant thermo-mechanical constitutive models for clays are important in analysing geomechanical problems such as nuclear waste geological disposals, reservoir engineering, etc.

Various thermo-mechanical models have been developed allowing the description of the thermo-mechanical behaviour of saturated clays, though with different theoretical approaches. The thermo-mechanical behaviour of clays has been discussed in detail by several

researchers (e.g. [7, 22, 31, 70]) on the basis of the available experimental results. The main features of the thermo-mechanical behaviour of saturated clays are summarized below:

1. the volume change upon heating depends on the overconsolidation ratio (OCR): at low OCR values (close to 1), only thermal contraction occurs, but at high OCR values there is first thermal expansion followed by thermal contraction;
2. the soil compressibility is independent of temperature;
3. the preconsolidation pressure decreases with increasing temperature;
4. the preconsolidation pressure at a given temperature increases after a heating–cooling cycle due to the thermal hardening effect.

Several constitutive models for describing the thermo-mechanical behaviour of soils were proposed in the last two decades. Hueckel et al. [43, 44] developed the first thermo-mechanical models (TM) by extending the well-known Modified Cam Clay model (MCC). A yield surface accounting for temperature effects on the preconsolidation pressure was introduced to reproduce the plastic strains due to temperature changes. It was shown however that this model is not capable to predict the behaviour of soils in overconsolidated state. Robinet et al. [65] established a thermo-elasto-plastic model to govern the macroscopic behaviour using a microscopic mechanism, in which irreversible thermal strains were originally introduced to control thermal softening. Graham et al. [34] proposed a non-isothermal modified Cam Clay model in an accessible semi-graphical framework rather than the mathematical framework used by Hueckel and co-workers but still without considering thermoplastic behaviour in overconsolidated state. Cui et al. [22] introduced an extra yield surface in the plane of mean effective stress p' –temperature T , namely thermal yield surface (TY), to better describe the thermal plastic strains especially in the overconsolidated state. In their models, the conventional yield limit which characterises the isotropic plastic mechanism and which gives the preconsolidation pressure as a function of temperature is referred to as the loading yield surface (LY). Consequently, a double yield surface with TY and LY delimits the reversible elastic domain in the (p', T) plane. Fol-

lowing this development, multi-yield surfaces have been adopted in the recent constitutive models. Abuel-Naga et al. [1] developed a thermo-mechanical model using an approach similar to Cui et al.'s one [22]. Laloui and François [31, 50] developed a thermoplastic model by extending the work of Hujieux [47] based on the multi-surface plasticity theory. Furthermore, to improve the thermo-mechanical behaviour observed at high and intermediate overconsolidation ratios, Laloui and François [31, 50] applied the bounding surface theory to the isotropic plastic mechanism. This permits to describe the occurrence of plastic strains inside the conventional yield domain in the sense of classic plasticity theory. These different thermo-mechanical models for saturated clays present certain advantages and limitations that will be discussed later.

To investigate the thermally induced volume changes, extensive experimental work has been done by applying heating-cooling cycles on soils with different OCRs [3, 7, 16, 27, 81]. The thermo-mechanical test (TBoom9) carried out by Baldi et al. [7] on natural Boom Clay is often used to validate the performance of thermo-mechanical models in predicting thermally-induced plastic volumetric strains. However, it has been observed that the precise loading path and the experimental results obtained during this test have not been accurately considered. This could lead to misinterpretations of the experimental results, and thus make the validation of constitutive models questionable.

The present paper aims at clarifying the results from the thermo-mechanical experiments conducted on natural Boom Clay by Baldi et al. [7] and assessing the performance of the recent thermo-mechanical models proposed by Cui et al. [22], Abuel-Naga et al. [1], and Laloui and François [31, 50]. For the clarification of the experimental data, the experimental procedure was presented and a discussion on the methods of calculating the drained thermal volumetric strain was made. For the models' performance assessment, the constitutive modelling approaches were briefly reviewed and compared; the capabilities of the three models to describe the observed experimental behaviour were analysed by simulating two sets of tests with combined thermo-mechanical loadings on natural Boom Clay; these models were analysed from a fundamental point of view, in terms of elasto-plasticity

and thermodynamic consistency.

3.2.2 Thermo-mechanical test on natural Boom Clay

Baldi et al. [7] reported a thermo-mechanical test on natural Boom Clay (TBoom9) sampled at 240 m depth in the underground research laboratory of Mol, Belgium. The preconsolidation pressure was evaluated at 6 MPa from isotropic compression tests. The thermo-mechanical loading path followed in the test is shown in Figure 3.1, and can be summarised as follows:

1. The specimen was first saturated under a constant mean effective stress of 2 MPa (point A) which was close to the in situ effective stress of 2.3 MPa. It was then loaded up to a mean effective stress of 4 MPa (path A-B) and unloaded to 1 MPa at a constant temperature of 21.5°C (path B-C).
2. A heating-cooling cycle of 21.5°C–95°C–21.5°C (path C-D-E) was applied under a constant mean effective stress of 1 MPa.
3. Mechanical isotropic re-loading up to 3 MPa was applied (path E-F) and followed by the same heating-cooling cycle as in step 2 (path F-G-H) under a constant mean effective stress of 3 MPa.
4. Mechanical isotropic re-loading up to 6 MPa (path H-I) was applied and followed by the same heating-cooling cycle as in step 2 or 3 (path I-J-K) under a constant mean effective stress of 6 MPa.

In the data reported by Baldi et al. [7], the drained thermal volumetric strain was calculated following two different methods. Thus, two different series of experimental results for the same test were presented by the authors. It is recalled that the sign convention of soil mechanics is used, where contractive strain and compressive (effective and total) stress are taken as positive and expansive strain and tensile (effective and total) stress are negative. The bulk moduli and the thermal expansion coefficients are always taken as positive. In addition, volume expansion means volume change $\Delta V > 0$.

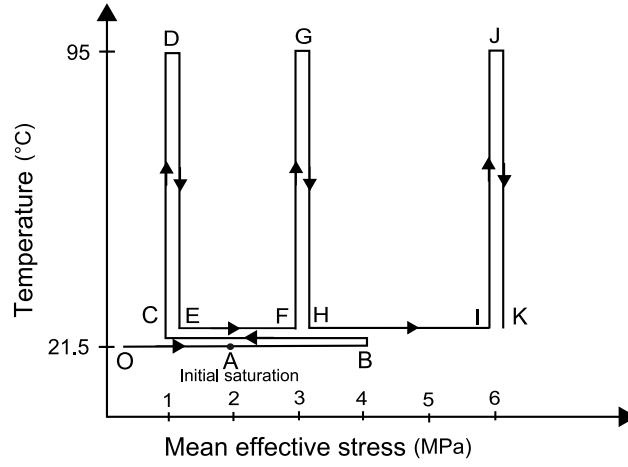


Figure 3.1: Isotropic thermo-mechanical loading path followed during TBoom9 test on natural Boom Clay (adapted from Baldi et al. [7]).

In Method 1, the soil was assumed to be thermo-mechanically isotropic. Drained thermal volumetric strain was calculated as three times the axial strain measured by an external displacement transducer: $\varepsilon_v = 3\varepsilon_a$.

In Method 2, the drained thermal volumetric strain was computed by subtracting the calculated thermal expansion attributed to both the pore water and the solid phase from the measured volume of water expelled from the soil sample. This method was firstly suggested by Campanella and Mitchell [15] and then improved by Baldi et al. [7]. Campanella and Mitchell [15] gave the following expression for the drained thermal volumetric strain:

$$\varepsilon_v = -\frac{(\Delta V_m)_{\Delta T}}{V_0} \quad (3.1)$$

$$= -\frac{(\Delta V_{DR})_{\Delta T} + (\Delta V_s)_{\Delta T} + (\Delta V_w)_{\Delta T}}{V_0} \quad (3.2)$$

where $(\Delta V_m)_{\Delta T}$ is the volume change of the whole specimen, V_0 is the initial volume of the specimen, $(\Delta V_{DR})_{\Delta T}$ is the volume of the water drained out, $(\Delta V_s)_{\Delta T}$ and $(\Delta V_w)_{\Delta T}$ are the volume changes due to a temperature increment ΔT of the solid phase and the pore water respectively. The negative sign in the right side of Equation 3.1 is necessary since expansive volumetric strain (negative) is produced with volume expansion (positive) during

temperature increase. The last two terms are calculated according to:

$$(\Delta V_s)_{\Delta T} = \alpha_s V_s \Delta T \quad (3.3)$$

and considering the thermal properties of free water:

$$(\Delta V_w)_{\Delta T} = \alpha_w V_w \Delta T \quad (3.4)$$

where α_s and α_w are the thermal expansion coefficients of the solid phase and free water respectively. v_s and v_w stand for the volumes of solids and pore water respectively.

Considering adsorbed water only in dense plastic clays and using the double-layer theory instead of Equation 3.4, Baldi et al. [6] proposed the following expression for the volume change due to the thermal expansion of pore water:

$$(\Delta V_w)_{\Delta T} = V_0 \Delta V_a S_s \rho_d \Delta T \quad (3.5)$$

where ΔV_a is the volume of expanded adsorbed water per unit surface area of mineral solid and per Kelvin. S_s is the specific surface of the soil, and ρ_d is the dry unit mass of the soil.

Since in reality the pore water is in the form of both free water and adsorbed water, a special procedure was defined to evaluate the actual thermal expanded volume of the pore water $(\Delta V_w)_{\Delta T}$ in Equation 3.1 without applying Equation (3.3) for free water only or Equation (3.4) for adsorbed water only. Two specimens of similar physical properties were prepared, one of which (TBoom9) was trimmed vertically to the bedding plane and the additional one (TBoom13) was trimmed horizontally to the bedding plane. In TBoom13, a heating and cooling cycle was applied under a constant mean effective stress of $p' = 3$ MPa. During the corresponding heating-cooling cycle under the mean effective stress of 3 MPa (Figure 3.1, path F-G-H), the lateral strain ε_l of TBoom9 was assumed to be identical to the axial strain measured in test TBoom13. Thus, the thermal volumetric strain ε_v in path F-G-H of TBoom9 could be calculated using $\varepsilon_v = \varepsilon_a + 2\varepsilon_l$, where the axial strain ε_a and

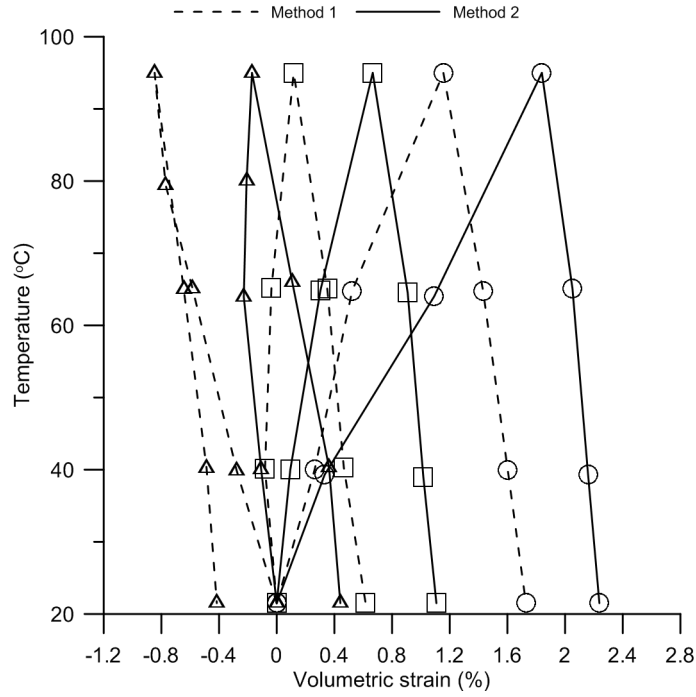


Figure 3.2: Volumetric strain for thermo-mechanical test TBoom9 (from Baldi et al. [7]) obtained from two methods: Method 1 - volumetric strain calculated as three times the axial strain; Method 2 - volumetric strain calculated from the volume of drained out water and the thermal expansion of pore water and solids; (Δ = path C-D-E; \square = path F-G-H; \circ = path I-J-K).

lateral strain ε_l were deduced from the measures of the axial displacement during the two tests TBoom9 and Tboom13, respectively. Considering the calculated thermal volumetric strain ε_v along path F-G-H of test TBoom9 and the thermal expansion parameter of the solid phase of natural Boom Clay (α_s), the actual thermal expanded volume of the pore water $(\Delta V_w)_{\Delta T}$ was obtained according to Equations 3.1 and 3.3.

Assuming that the actual thermal expanded volume of the pore water $(\Delta V_w)_{\Delta T}$ was the same for all the three heating-cooling cycles (i.e, paths C-D-E, F-G-H, I-J-K), the volumetric strain was calculated from the drained pore water volume according to Equation 3.1. The volumetric strain thus obtained is plotted in Figure 3.2 (solid line).

The volumetric strain calculated by Method 1 and Method 2 are compared in Figure 3.2. The difference was attributed to the thermo-mechanical anisotropy of natural Boom Clay. The former volumetric strain was referred to as isotropic volumetric strain and the

latter as anisotropic volumetric strain.

Comparing these two methods for estimating the volumetric strain, it appears clearly that Method 1 constitutes a much simpler solution which assumes the thermo-mechanical isotropy of natural Boom Clay. However, this assumption does not hold true since available experimental data (including TBoom9 test) showed significant thermo-mechanical anisotropy for this material. Thus, the results obtained from Method 1 are not accurate and do not reflect the actual volumetric thermo-mechanical behaviour of natural Boom Clay. As opposed to Method 1, Method 2 is more sophisticated and should provide more accurate results. It should however be noted that applying the volumetric change of pore water from a single heating-cooling cycle (F-G-H) to the three heating-cooling cycles would also induce some errors.

Volume changes during heating-cooling cycles is an important feature in the thermo-mechanical behaviour of soils. The existence of various interpretations of TBoom9 test as reported here (in terms of loading path and volumetric strain estimation) may lead to different choices when developing or calibrating constitutive models.

3.2.3 Thermo-mechanical models

In this section, the thermo-mechanical models proposed by Cui et al. [22], Abuel-Naga et al. [1], Laloui and François [31, 50] are reviewed. In the following, these models are referred to as Model C, Model A and Model L respectively. The main equations governing the thermo-mechanical behaviour are briefly summarized in Table 3.1. Only isotropic stress states are considered. Some of the original notations are changed to avoid confusion between the three models.

3.2.3.1 Thermo-mechanical elastic behaviour

In all the three models, the total elastic volumetric strain increment ($d\varepsilon_v^e$) consists of two parts, due to either thermal or mechanical loadings, respectively. This increment reads

as follows for Models C and Model L:

$$d\varepsilon_v^e = -\alpha_d dT + \frac{dp'}{K} \quad (3.6)$$

and for Model A:

$$d\varepsilon_v^e = -\frac{\alpha_A}{T} dT + \frac{dp'}{K} \quad (3.7)$$

where α_d and α_A are drained volumetric thermal expansion coefficients in Models C or L and Model A respectively, K is the bulk modulus which is temperature independent.

Table 3.1: Main thermo-mechanical equations

	Model C	Model A	Model L
Elastic part	$d\varepsilon_v^e = -\alpha_d dT + \frac{dp'}{K}$ with $\alpha_d = \text{material constant}$ $K = \frac{v_0 p'}{\kappa}$	$d\varepsilon_v^e = -\frac{\alpha_A}{T} dT + \frac{dp'}{K}$ with $\frac{d\alpha_A}{\alpha_A} = b \frac{dp'}{p'}$ $K = \frac{v_0 p'}{\kappa}$	$d\varepsilon_v^e = -\alpha_d dT + \frac{dp'}{K}$ with $\alpha_d = [\alpha_{d0} + \zeta (T - T_0)] \frac{1}{d} \frac{p'_{c0}}{p'}$ $K = K_{ref} \left(\frac{p'}{p'_{ref}} \right)^{n^e}$
Yield limits	TY: $T = T_0 + (T_c - T_0) \exp(-\beta p')$ LY: $\frac{p'_{cT}}{p'_{c0}} = \exp(-r_0(T - T_0))$	TY: $\frac{p'_{c0}}{p'} = r^{TY} \sqrt{\ln \left(\frac{T}{T_0} \right) + 1}$ LY: $\frac{p'_{cT}}{p'_{c0}} = 1 - r^{LY} \log_{10} \left(\frac{T}{T_0} \right)$	Loading surface: $\frac{p'}{r_{iso} p'_{c0}} = 1 - r_T \log_{10} \left(\frac{T}{T_0} \right)$ Bounding surface: $\frac{p'_{cT}}{p'_{c0}} = 1 - r_T \log_{10} \left(\frac{T}{T_0} \right)$
Plastic strain	TY: $d\varepsilon_{v1}^{T,p} = \alpha_p [\exp(\alpha_p(T - T_0)) - a] dT, d\varepsilon_{v1}^{\sigma,p} = \frac{\alpha_1}{v_0} \frac{dp'}{p'}$ LY: $d\varepsilon_{v2}^{T,p} = \alpha_p [\exp(\alpha_p(T - T_0)) - a] dT, d\varepsilon_{v2}^{\sigma,p} = \frac{\lambda - \kappa}{v_0} \frac{dp'}{p'}$ with $\alpha_p = \frac{\alpha_d}{1 - a} \quad \text{if } OCR \leq 1/c_1$ $\alpha_p = \frac{\alpha_d}{\exp \left(\frac{\alpha_p}{c_2} \ln \left(\frac{1}{c_1} \frac{p'}{p'_{c0}} \right) \right) - a} \quad \text{if } OCR > 1/c_1$	TY: $d\varepsilon_{v1}^p = \frac{\omega_T}{v_0} \frac{dp'}{p'}$ with $\omega_T = (\lambda - \kappa) \frac{-\ln(1 - r^{LY} \log_{10}(T/T_0))}{\ln(r^{TY} \ln(T/T_0) + 1)}$ LY: $d\varepsilon_{v2}^p = \frac{\lambda - \kappa - \omega_T}{v_0} \frac{dp'}{p'}$	--- ---
Hardening laws	TY: $d\beta = \frac{-\exp(\beta p')}{p'(T_c - T_0) \alpha_p [\exp(\alpha_p(T - T_0)) - a]} d\varepsilon_{v1}^{T,p} - \frac{\beta}{\alpha_1} d\varepsilon_{v1}^{\sigma,p}$ LY: $dp'_{c0} = \left\{ \frac{r_0}{\alpha_p [\exp(\alpha_p(T - T_0)) - a]} d\varepsilon_{v2}^{T,p} + \left(\frac{v_0}{\lambda - \kappa} \right) (d\varepsilon_{v2}^{\sigma,p} + d\varepsilon_{v1}^{\sigma,p}) + \left(\frac{r_0}{\alpha_p [\exp(\alpha_p(T - T_0)) - a]} + \frac{kv_0}{\lambda - \kappa} \right) d\varepsilon_{v1}^{T,p} \right\} p'_{c0}$	TY: --- LY: $dp'_{c0} = \frac{v_0}{\lambda - \kappa - \omega_T} p'_{c0} d\varepsilon_{v2}^p$	$dr_{iso} = \frac{(1 - r_{iso})^2}{c} d\varepsilon_v^p$ $dp'_{c0} = hp'_{c0} d\varepsilon_v^p$

It is worth noting that in Model A, the thermal elastic volumetric strain increment varies logarithmically with temperature (see equation (3.7)). As a consequence, coefficient α_A is necessarily dimensionless, contrary to α_d which has the dimension of the inverse of a temperature, as classically (see equation (3.6)). In this context, calling α_A a volumetric thermal expansion coefficient is misleading, but this was the choice originally made by the authors of [1].

In Model C, α_d is a material constant independent of effective stress (p') and temperature (T). The elastic volumetric strains are thus assumed to vary linearly with temperature. In Model A, however, α_A varies with the mean effective stress level as follows:

$$\frac{d\alpha_A}{\alpha_A} = b \frac{dp'}{p'} \quad (3.8)$$

where b is a soil parameter describing the effect of mechanical stress.

In Model L, α_d increases with temperature and OCR values:

$$\alpha_d = [\alpha_{d0} + \zeta (T - T_0)] \frac{1}{d} \frac{p'_{c0}}{p'} \quad (3.9)$$

where α_{d0} is the thermal expansion coefficient at a reference temperature T_0 and ζ is the slope of the variation of α_d with respect to temperature T , p'_{c0} is the preconsolidation pressure at temperature T_0 and d is a model parameter related to the shape of the yield surface in (p', q) plane.

The volumetric thermal expansion coefficient α_d for natural Boom Clay was determined from TBoom9 test during the three cooling stages at different mean effective stresses using the volumetric strains estimated by the two methods previously introduced. The values obtained are given in Table 3.2. For this test and in this particular range of temperature and OCR values, the changes of α_d with respect to temperature or stress are of the same order of magnitude. As a consequence, the general trends for the evolution of α_d with temperature and stress state (or OCR) are not completely clear. For instance, depending on

Table 3.2: Volumetric thermal expansion coefficient for natural Boom Clay (TBoom9) obtained from volumetric strains estimated using Method 1 and Method 2

Temperature range	α_d at $p'=1$ MPa ($\times 10^{-5}/^\circ\text{C}$)		α_d at $p'=3$ MPa ($\times 10^{-5}/^\circ\text{C}$)		α_d at $p'=6$ MPa ($\times 10^{-5}/^\circ\text{C}$)	
	Method 1	Method 2	Method 1	Method 2	Method 1	Method 2
21.5°C – 40°C	3.85	4.23	8.15	4.90	6.83	4.23
40°C – 65°C	6.32	9.94	4.61	4.34	6.82	4.34
65°C – 95°C	6.73	9.31	7.76	8.09	9.20	7.07

the OCR value, α_d sometimes increases monotonically with temperature and sometimes not. Furthermore, depending on the method used to obtain the volumetric strains, the variations of α_d with temperature and stress can be different. It is thus difficult to corroborate the evolution predicted by Models A and L. It is thus recommended to adopt a constant thermal expansion coefficient as in Model C. Such a choice gives simple predictions without losing accuracy. This suggestion will be further supported when dealing with numerical simulations and elasto-plastic theory.

The bulk modulus K is the same as for the common Cam-Clay model in both Model C and Model A:

$$K = \frac{v_0 p'}{\kappa} \quad (3.10)$$

where κ is the elastic slope in $(\ln p', v)$ space and v_0 is the initial specific volume. In Model L, a hypoelastic modulus is adopted:

$$K = K_{ref} \left(\frac{p'}{p'_{ref}} \right)^{n^e} \quad (3.11)$$

where K_{ref} is the bulk modulus at a reference effective mean pressure p'_{ref} , and n^e is a soil parameter.

3.2.3.2 Plastic behaviour

3.2.3.2.1 Thermo-mechanical yield limit Figure 3.3 presents a schematic view of the thermo-mechanical elastic domain in (p', T) plane for the three models. In both Models C and A, the elastic zone is delimited by two yield curves: the conventional thermo-

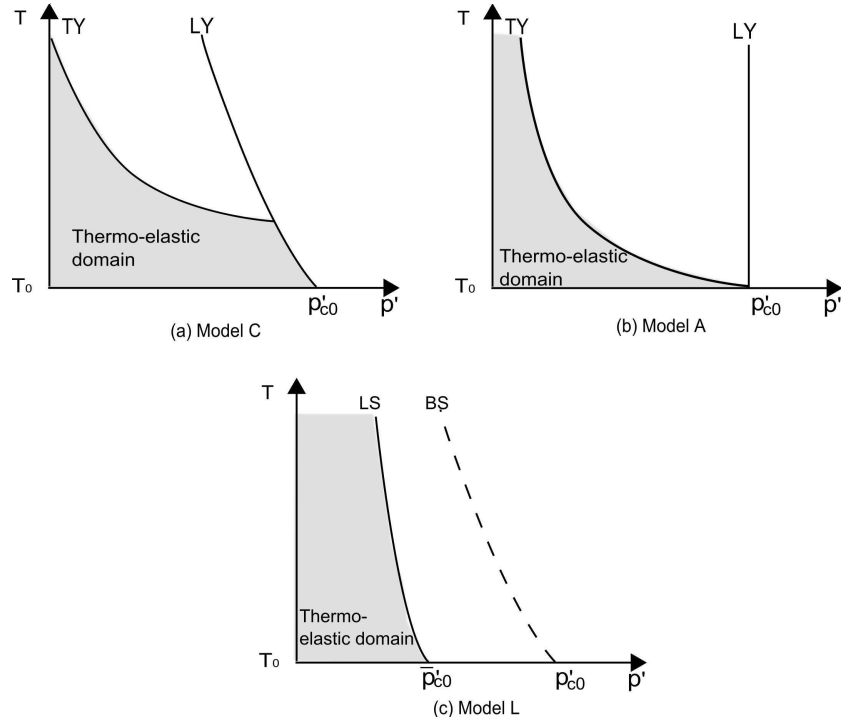


Figure 3.3: Thermo-mechanical elastic domain in (p', T) plane.

mechanical yield curve controlling the evolution of the preconsolidation pressure with temperature is denoted LY (loading yield limit), and the yield curve governing the thermal plastic behaviour is denoted TY (thermal yield limit).

The expressions of TY curves for Model C and Model A are given in Equation (3.12) and Equation (3.13), respectively:

$$T = T_0 + (T_c - T_0) \exp(-\beta p') \quad (3.12)$$

$$\frac{p'_{c0}}{p'} = 1 + r^{TY} \sqrt{\ln \left(\frac{T}{T_0} \right)} \quad (3.13)$$

where p'_{c0} is the preconsolidation pressure at the reference temperature T_0 , T_c is the temperature at which TY intersects the temperature axis in Model C, and β , r^{TY} are shape parameters in Model C and Model A, respectively.

In Model C, the preconsolidation pressure decreases with increasing temperature and

the expression of LY reads:

$$\frac{p'_{cT}}{p'_{c0}} = \exp(-r_0(T - T_0)) \quad (3.14)$$

where p'_{cT} is the preconsolidation pressure at a certain temperature T , r_0 governs the curvature of LY. A cooling phase is associated with an elastic unloading and the point representing the material's state in (p', T) plane will not reach LY, which therefore will not be affected by any hardening process. In Model A, LY is defined with a different concept: the preconsolidation pressure will not be affected during a heating stage but will increase during a cooling stage according to an equation similar to that used in Model L:

$$\frac{p'_{cT}}{p'_{c0}} = 1 - r^{LY} \log_{10} \left(\frac{T}{T_0} \right) \quad (3.15)$$

where r^{LY} is the model parameter that depends on the soil nature, r^{LY} is zero in the heating process and non-zero for the cooling process.

In Model L, the bounding surface concept is introduced. It can be seen from Figure 3.3 that a loading surface (denoted by LS) is defined so that it can deal with both normally consolidated and overconsolidated states. The conventional thermo-mechanical loading surface is taken as the bounding surface (denoted by BS). The bounding surface is defined in a similar approach as the LY of Model C without changes in the cooling phase:

$$\frac{p'_{cT}}{p'_{c0}} = 1 - r_T \log_{10} \left(\frac{T}{T_0} \right) \quad (3.16)$$

where p'_{c0} and p'_{cT} are the mean effective stresses on the bounding surface corresponding to T_0 and T respectively, r_T governs the curvature of the yield surface. The expression of the loading surface is the same as the bounding surface:

$$\frac{p'}{r_{iso} p'_{c0}} = 1 - r_T \log_{10} \left(\frac{T}{T_0} \right) \quad (3.17)$$

with a scalar hardening parameter r_{iso} being defined as the ratio of the mean effective stress

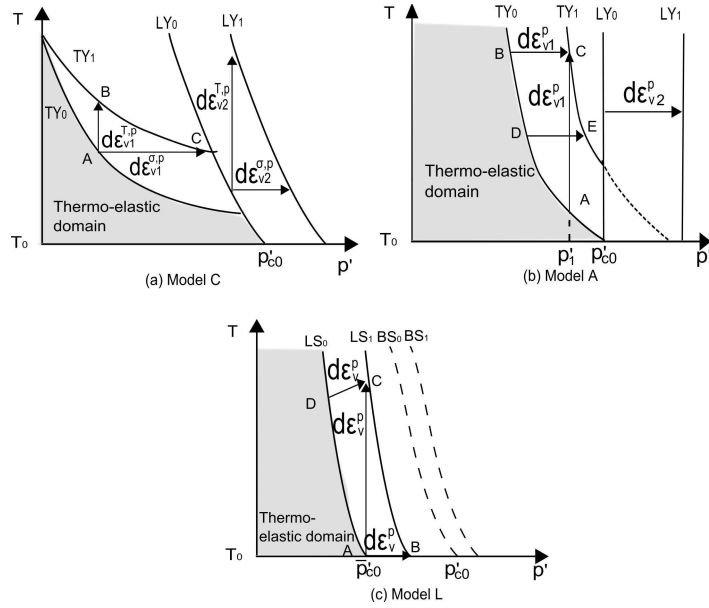


Figure 3.4: Evolution of yield surface under thermo-mechanical loading in $p' - T$ plane.

\bar{p}'_{c0} on the loading surface at T_0 to p'_{c0} on the bounding surface at T_0 :

$$\frac{\bar{p}'_{c0}}{p'_{c0}} = r_{iso} \quad (3.18)$$

The value of r_{iso} is always smaller than or equal to 1. For $r_{iso} = 1$, the loading and bounding surfaces coincide, and for $0 \leq r_{iso} < 1$, the loading surface is completely inscribed in the bounding surface.

3.2.3.2.2 Plastic mechanism Model C and Model A used two separate yield surfaces to describe the yielding behaviour in $p' - T$ plane and correspondingly two plastic mechanisms are proposed. The plastic strains produced when increasing either the mean effective stress or the temperature and associated with the yielding of TY or LY curves are represented in Figure 3.4 (a)&(b).

In Model C, the volumetric plastic strain $d\varepsilon_v^{T,p}$ induced along thermal loading paths is different from that induced along mechanical loading paths, $d\varepsilon_v^{\sigma,p}$. The thermally induced plastic volumetric strain $d\varepsilon_{v1}^{T,p}$ on TY or $d\varepsilon_{v2}^{T,p}$ on LY associated with changes in temperature

at constant effective stress can be determined according to the following equation:

$$d\varepsilon_{vi}^{T,p} = \alpha_p [\exp(\alpha_p(T - T_0)) - a] dT \quad \text{with } i \in \{1, 2\} \quad (3.19)$$

where α_p and a are parameters describing the variation of $d\varepsilon_v^{T,p}$ with respect to a temperature increment dT . To describe OCR effects on $d\varepsilon_v^{T,p}$, α_p is taken as dependent on the value of OCR. For lightly overconsolidated and normally consolidated states ($OCR \leq 1/c_1$), α_p is constant and given by:

$$\alpha_p = \frac{\alpha_d}{1 - a} \quad (3.20)$$

and for highly overconsolidated states ($OCR > 1/c_1$), α_p decreases with OCR increases, as follows:

$$\alpha_p = \frac{\alpha_d}{\exp\left(\frac{\alpha_p}{c_2} \ln\left(\frac{1}{c_1} \frac{p'}{p'_{c0}}\right)\right) - a} \quad (3.21)$$

where c_1 and c_2 are parameters that can be determined from the transition point between expansion and contraction of the total volume change associated with temperature changes. $d\varepsilon_{v1}^{\sigma,p}$, induced along mechanical loading paths on TY, is expressed as follows:

$$d\varepsilon_{v1}^{\sigma,p} = \frac{\alpha_1}{v_0} \frac{dp'}{p'} \quad (3.22)$$

where α_1 is the slope of the inelastic part in $(\ln p', v)$ space in the overconsolidated state. $d\varepsilon_{v2}^{\sigma,p}$, obtained along mechanical loading paths on LY, has the following expression as in the common Cam Clay Model:

$$d\varepsilon_{v2}^{\sigma,p} = \frac{\lambda - \kappa}{v_0} \frac{dp'}{p'} \quad (3.23)$$

where λ is the normal-consolidation slope in $(\ln p', v)$ space.

p'_{c0} and β appearing in the definition of TY and LY in Model C are hardening variables that control the evolution of TY and LY respectively. The hardening laws read:

$$d\beta = \frac{-\exp(\beta p')}{p'(T_c - T_0) \alpha_p [\exp(\alpha_p(T - T_0)) - a]} d\varepsilon_{v1}^{T,p} - \frac{\beta}{\alpha_1} d\varepsilon_{v1}^{\sigma,p} \quad (3.24)$$

and

$$\begin{aligned}
 dp'_{c0} = & \left\{ \frac{r_0}{\alpha_p[\exp(\alpha_p(T - T_0)) - a]} d\varepsilon_{v2}^{T,p} + \left(\frac{v_0}{\lambda - \kappa} \right) (d\varepsilon_{v2}^{\sigma,p} + d\varepsilon_{v1}^{\sigma,p}) \right. \\
 & \left. + \left(\frac{r_0}{\alpha_p[\exp(\alpha_p(T - T_0)) - a]} + \frac{kv_0}{\lambda - \kappa} \right) d\varepsilon_{v1}^{T,p} \right\} p'_{c0}
 \end{aligned} \tag{3.25}$$

where k is a positive parameter that describes the coupling effects between TY and LY. These hardening laws provide a one-way coupling between TY and LY plastic mechanisms in the sense that LY moves when TY is activated, but not reciprocally. This behaviour is observed experimentally [80].

Model A defines a theoretical mechanism to interpret the plastic strain induced along a thermal loading path. As shown in Figure 3.4(b), during heating at p'_1 (path A-C), the hardening effective stress p' on TY decreases with temperature increase according to Equation 3.13 and the plastic strain is generated once the hardening effective stress p' reaches p'_1 . The volumetric plastic strain increment $d\varepsilon_v^p$, along the thermal loading path at a constant mean effective stress (path A-C) is assumed to be identical to that generated along the mechanical loading path (path B-C). When TY is reached, the volumetric plastic strain $d\varepsilon_{v1}^p$, along mechanical and (or) thermal load paths can be determined:

$$d\varepsilon_{v1}^p = \frac{\omega_T}{v_0} \frac{dp'}{p'} \tag{3.26}$$

where ω_T is the plastic modulus at temperature T , a function of r^{TY} , r^{LY} and temperature T ,

$$\omega_T = (\lambda - \kappa) \frac{-\ln\left(1 - r^{LY} \log_{10}(T/T_0)\right)}{\ln(r^{TY} \ln(T/T_0) + 1)} \tag{3.27}$$

The plastic volumetric strain $d\varepsilon_{v2}^p$, associated to LY, can be generated only along mechanical loading paths when the applied stress exceeds LY and can be determined by:

$$d\varepsilon_{v2}^p = \frac{\lambda - \kappa - \omega_T}{v_0} \frac{dp'}{p'} \tag{3.28}$$

For TY, no explicit hardening law is given. The evolution of LY is controlled by the

hardening parameters p'_{c0} . It depends on the plastic volumetric strain increment $d\varepsilon_{v2}^p$:

$$dp'_{c0} = \frac{v_0}{\lambda - \kappa - \omega_T} p'_{c0} d\varepsilon_{v2}^p \quad (3.29)$$

In Model L, the volumetric plastic strains $d\varepsilon_v^p$ along thermal loading paths and mechanical loading paths are produced by the same mechanism of plastic hardening of \bar{p}'_{c0} as shown in Figure 3.4(c). These two loading paths are coupled and a common hardening law is provided for effective stress and temperature increases. The volumetric plastic strain between LY_0 and LY_1 is independent of the loading path.

During loading, the scalar variable r_{iso} represents the progressive plastification in relation to the plastic volumetric strain and controls the ratio between the sizes of loading surface and bounding surface. The following law is adopted:

$$dr_{iso} = \frac{(1 - r_{iso})^2}{c} d\varepsilon_v^p \quad (3.30)$$

where c is a soil parameter.

During an unloading-reloading cycle, r_{iso} decreases to follow the decrease of the effective mean pressure p' in the unloading process and will be adjusted in a sudden fashion with a new value of r_{iso} at the moment of change in loading direction (unloading-reloading):

$$r_{iso} = r_{iso}^e + \frac{p'_{cyc}}{p'_{c0}} \quad (3.31)$$

where r_{iso}^e represents the size of the purely elastic nuclei, p'_{cyc} is the mean effective stress at the last change in loading direction (unloading-reloading). The widely used hardening law based on the relationship between the preconsolidation pressure, p'_{c0} , and the volumetric plastic strain, ε_v^p , in $(\ln p', v)$ plane is given by:

$$dp'_{c0} = h p'_{c0} d\varepsilon_v^p \quad (3.32)$$

where $h p'_{c0}$ is the plastic modulus.

3.2.4 Numerical simulations

The performance of the thermo-mechanical models presented above is investigated. Natural Boom Clay is considered and the predicted results are compared to the experimental results. To evaluate the capability of models in predicting the thermally induced volume change following different loading paths and the thermally induced hardening effect (two key features of the thermo-mechanical behaviour of saturated clays), two sets of tests with combined thermo-mechanical loadings are simulated. Note that because of the lack of relevant data about natural Boom Clay (data obtained from experiments on samples saturated under the in-situ stress are exclusively considered in this work), set 2 is purely numerical.

In set 1, two cases are simulated. The first case (Simulation 1) corresponds to TBoom9 test on a single soil specimen with the loading path shown in Figure 3.1. The second case (Simulation 2) corresponds to the same experimental path but with three different natural specimens (one per thermal cycle). The three specimens are first saturated at $p' = 2$ MPa and loaded up to $p' = 6$ MPa. After that, two samples are unloaded to 3 MPa and 1 MPa, respectively. Doing so, three specimens with three distinct overconsolidation ratios are obtained. From these consolidation pressures, a particular heating-cooling cycle (21.5°C-95°C-21.5°C) is applied on each specimen.

Table 3.3 shows the input parameters of the three models. Note that all the parameters can be calibrated from the experimental results and the values are proposed by the authors in their respective original papers [1, 22, 31]. It can be observed that Model A and Model L require less parameters for the plastic strains prediction since the plastic strains induced along the mechanical loading path and the thermal loading path are coupled. It should be mentioned that although Model L considers the effect of temperature and effective stress on the thermal expansion coefficient (see Equation 3.9), a constant thermal expansion coefficient (see Table 3.3) was adopted in their simulation. Moreover, in the original work of parameters calibration, the experimental results determined using Method

Table 3.3: Input parameters for the simulations of natural Boom Clay behaviour

	Model C	Model A	Model L
Elastic part	$\alpha_d = 5.1 \times 10^{-5} \text{C}^{-1}$ -- $\kappa = 0.046$ --	$\alpha_{ref}^* = 1.11 \times 10^{-2}$ $b = 0.31$ $\kappa = 0.046$ --	$\alpha_d = 1.3 \times 10^{-5} \text{C}^{-1}$ -- $K_{ref} = 130 \text{ MPa}$ $n^e = 0.4$
Yield limits	TY: $\beta = 100 \text{ MPa}^{-1}$ $T_c = 2000 \text{ }^\circ\text{C}$ -- LY: $r_0 = 3.93 \times 10^{-3} \text{C}^{-1}$ $p'_{c0} = 6 \text{ MPa}$	TY: $r_{TY} = 1.56$ $p'_{c0} = 6 \text{ MPa}$ -- LY: $r_{LY} = 0.31$ --	Loading surface: $r_T = 0.55$ $p'_{c0} = 6 \text{ MPa}$ $r_{iso}^e = 0.001$ Bounding surface: -- --
Plastic strain	TY: $a = 0.982$ $\alpha_1 = 2.51 \times 10^{-4}$ $c_1 = 0.5833$ $c_2 = -0.019 \text{C}^{-1}$ LY: $\lambda = 0.178$	TY: $\lambda = 0.178$ -- -- -- LY: --	-- -- -- -- --
Hardening laws	TY: -- LY: $k = 0.012$	TY: -- LY: --	$c = 0.012$ $h = 18$

* Thermal expansion coefficient at 0.1 MPa.

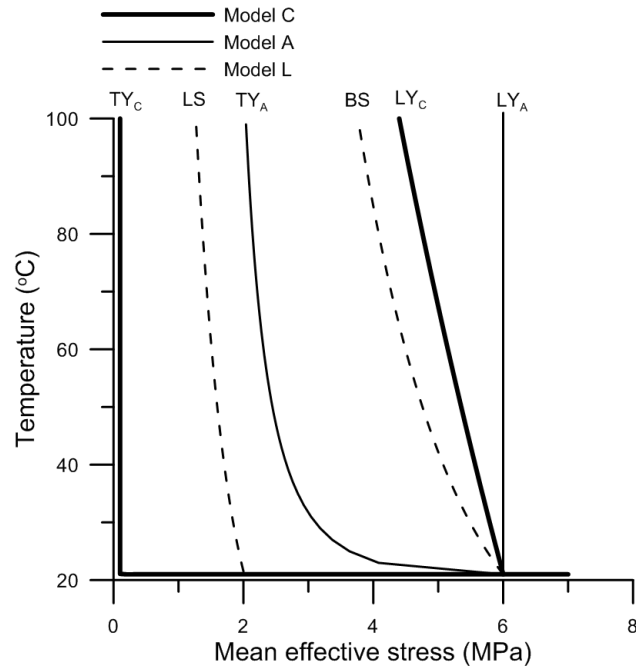


Figure 3.5: Thermo-mechanical yield limits (TY and LY).

1 (thermal isotropic strains) were used for Model A and Model L, whereas experimental results determined using Method 2 (thermal anisotropic strains) were used for Model C.

As seen in Section 3.2.3, depending on the model, a logarithmic or a power function is chosen for the thermo-mechanical yield limit for $T = T_0$. Figure 3.5 compares the size of the thermo-mechanical elastic zone predicted by the three models at $p' = 2$ MPa and $T = 21.5^\circ\text{C}$ (point A in Figure 3.1). It can be observed that the thermo-mechanical elastic zone (being delimited by TY_C and LY_C) adopted in Model C is the smallest and the one in Model A (being delimited by TY_A and LY_A) is the largest.

Figure 3.6 compares the volumetric strain predictions in case of Simulation 1 with the experimental results. It shows that all the three proposed models give similar results and can capture the essential features of the thermo-mechanical behaviour. However, none of them can describe the expansive irreversible isotropic volumetric strain (calculated using Method 1) at $p' = 1$ MPa, generated after a heating-cooling cycle. Note that this behaviour was also observed on other soils such as the Bangkok soft clay as reported by Abuel-Naga et al. [1].

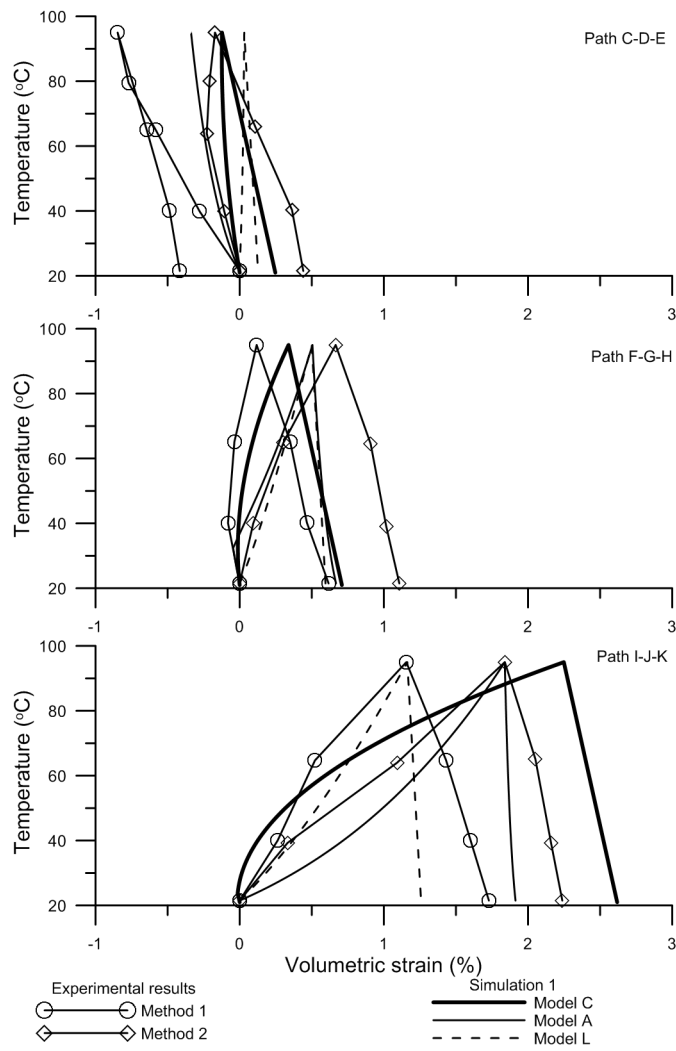


Figure 3.6: Comparison between observed and predicted thermally induced volumetric strain in Simulation 1.

Figure 3.7 compares the volumetric strain predictions in case of Simulation 1 and Simulation 2. It can be observed that Simulation 1 and Simulation 2 give different predictions for all the three models, and Model L give the largest difference because of its high sensitivity to the loading history. Taking $p' = 6$ MPa at $T = 21.5^\circ\text{C}$ (point I in Figure 3.1) for Model L for instance, the yield limits can be determined by considering their evolution according to the loading history. Even though the previously applied loading path is located inside the Bounding surface, plastic strains are generated due to the activation of the Loading surface. The preconsolidation pressure thus increases. Because of the different loading histories in Simulation 1 and in Simulation 2, different preconsolidation pressures (being 10.5 MPa and 8.7 MPa, respectively) are obtained at point I, resulting in different predictions for the subsequent heating-cooling path (path I-J-K in Figure 3.1).

In set 2 (Simulation 3), the soil specimen is first saturated at $p' = 2$ MPa and loaded up to 8 MPa (point B in Figure 3.8), giving a normal consolidated state. Afterwards, a heating-cooling cycle of 21.5°C – 95°C – 21.5°C (path B-C-D) is applied under this consolidation pressure followed by a mechanical re-loading up to 20 MPa (path D-E).

Figure 3.9 compares the results for Simulation 3 as predicted by the three models which provide similar results. During the isotropic loading up to 8 MPa at 21.5°C , the sample behaves elastically and then elasto-plastically. The classic bilinear compression behaviour is predicted by Model C and Model A in $\varepsilon_v - \log p'$ space since MCC is adopted in the isothermal condition, but the soil behaviour by Model L is smoother due to the contribution of the bounding surface plasticity concept, as shown in Figure 3.9 (A-B).

During the heating process (B-C), in Model C, TY curve is activated, and the TY-LY coupling also moves LY forward. At the end of the heating stage (point C), a value of 11.1 MPa for p'_{c0} can be obtained using Equations 3.24 and 3.25. The cooling stage (C-D) does not produce any plastic strain, thus keeping p'_{c0} constant. In Model A, the preconsolidation pressure is kept constant (8 MPa) in the heating phase and increases during the cooling phase. A final value of 10.0 MPa at point D is predicted for p'_{c0} using Equation 3.15. In Model L, LS mechanism is activated and moves forward together with

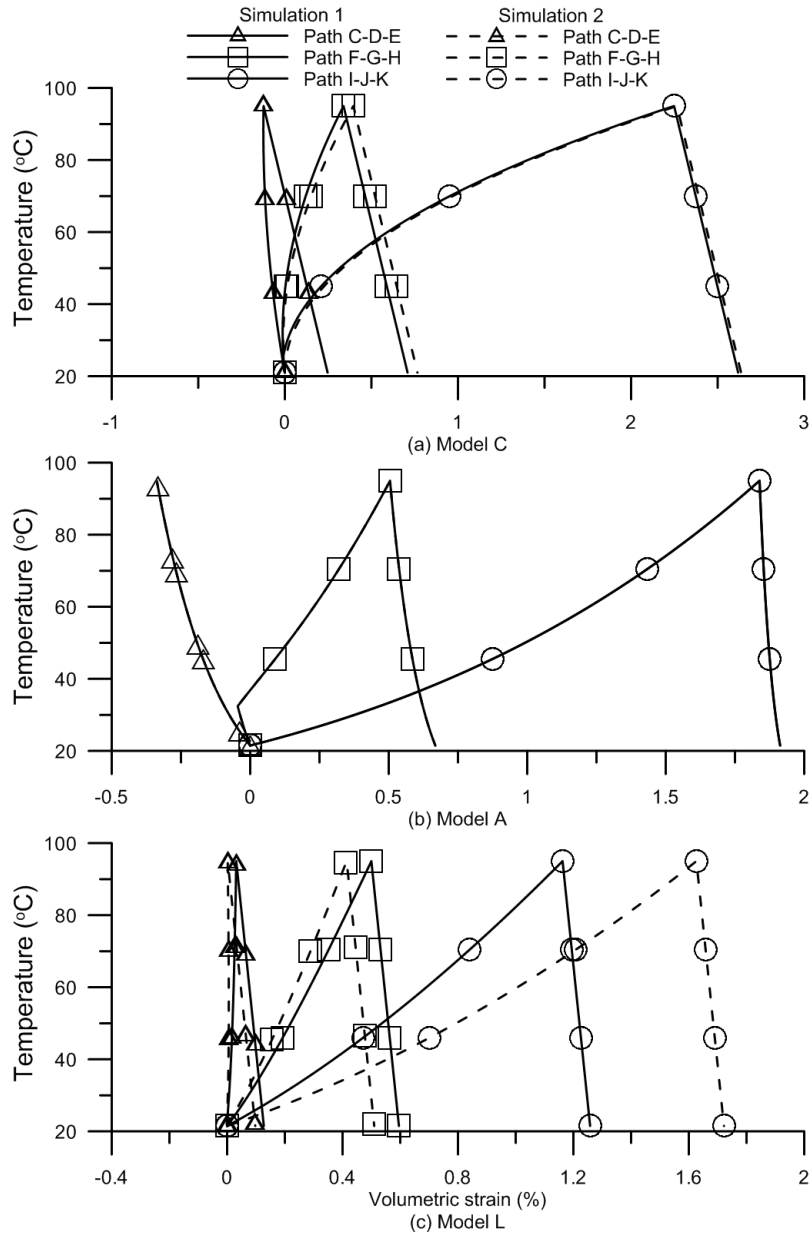


Figure 3.7: Comparison between Simulation 1 and Simulation 2 by the three models: (a) Model C, (b) Model A, (c) Model L.

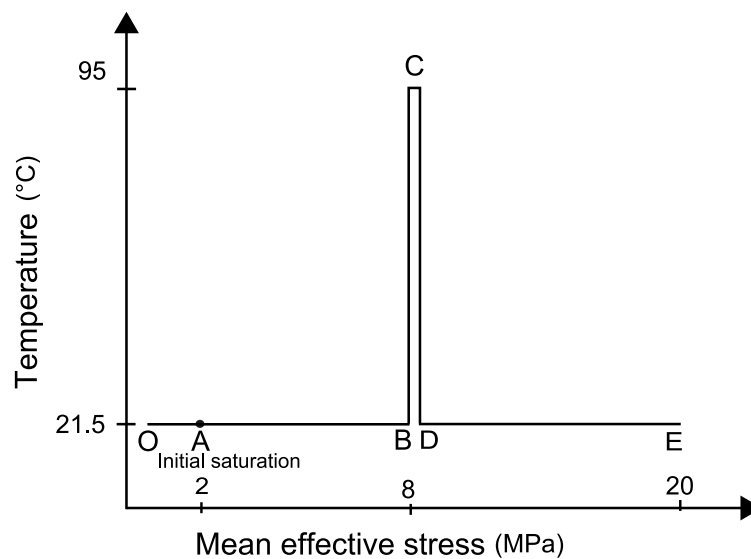


Figure 3.8: Isotropic thermo-mechanical loading path of Simulation 3.

BS surface during the heating phase. During the cooling-reloading process, the size of LS defined by r_{iso} is reinitialised according to Equation 3.31 and a small elastic nucleus is assumed at the beginning of the reloading process. For the three models, the soil response is first elastic and then elastoplastic during the reloading process, predicting the slightly overconsolidated behaviour when a mechanical loading is performed after a thermal cycle in normally consolidated state. Even though no direct comparison with experimental results is made here for the reasons mentioned above, it can be seen that the three models can satisfactorily capture the thermal hardening phenomenon as observed in [81] for instance.

3.2.5 Discussion

The numerical simulations in the previous section have shown the capability of the constitutive models to catch the main experimental evidences. The constitutive models are now discussed in terms of elasto-plastic theory and thermodynamic theory.

The thermo-elastic behaviour is one of the most fundamental issues in the thermo-mechanical constitutive model. Examination of the three models investigated shows that the elastic strain in Model A and Model L is loading-path dependent whereas the elastic

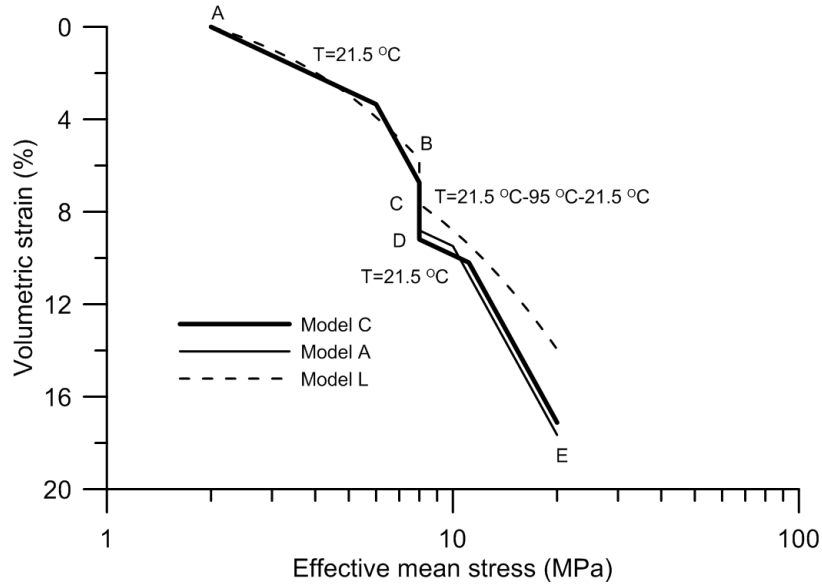


Figure 3.9: Predicted response of the soil in Simulation 3.

strain in Model C is loading-path independent. To illustrate this point, the volumetric strain along path A-B-D and path A-C-D in Figure 3.10 is analysed. For Model L, the volumetric strain along path B-D is equal to that along path A-C since the elastic modulus K is independent of temperature. However, according to Equation 3.9, the volumetric strain along path A-B is different from that along path C-D since the thermal expansion coefficient changes between these two paths characterised by two distinct mean effective stresses. Thus, the total volumetric strains along path A-B-D and A-C-D are not identical even if the loading path is inside the thermo-elastic zone. In other words, the elastic strain increment depends on the order of application of temperature and effective stress changes:

$$\frac{\partial^2 \varepsilon_v^e}{\partial p' \partial T} \neq \frac{\partial^2 \varepsilon_v^e}{\partial T \partial p'} \quad (3.33)$$

Such an un-closed loop traduces the loading-path dependency of the elastic behaviour which poses some problems when developing a constitutive model in the framework of the elasto-plasticity theory. Model A defines a similar loading-path dependent elastic behaviour as Model L, whereas Model C defines an identical volumetric strain along path A-B-D and A-C-D, with no loading-path dependency of the elastic behaviour.

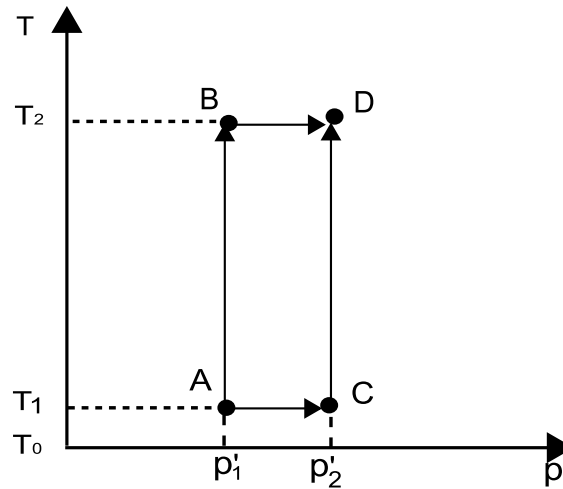


Figure 3.10: Loading path in the effective stress and temperature space.

The thermo-mechanical elastic zones defined by all the three models have a common and salient change in comparison with the early models. In the early models (e.g. [43, 44]), the thermo-mechanical elastic zone is defined by a conventional yield surface accounting for thermal evolution of the preconsolidation pressure. Inside this zone, purely elastic strain is generated. The parameter governing the thermo-elastic behavior (that is the thermal expansion coefficient) is thereby always determined along heating tests lying inside the conventional yield surface. However, the three models studied in this paper assume that thermally induced plastic strain would occur during such heating stages even when the stress state of soil is inside the conventional yield surface. To be consistent with this new thermo-elasto-plastic framework, specimens with different OCR values should be subjected to heating-cooling cycles and the thermal-elastic behavior should be characterised from the cooling stages instead of the heating stages.

As seen in Section 3.2.3, different plastic strain variables are chosen by the three models. In Model C, the volumetric plastic strain generated during thermo-mechanical hardening is split into two parts: $d\varepsilon_v^{\sigma,p}$ along a mechanical loading path at an given temperature and $d\varepsilon_v^{T,p}$ along a thermal loading path at a constant effective stress. This conveniently describes the thermo-mechanical behaviour and thus gives a hardening law depending on the loading path. As seen in Figure 3.4(a), the loading paths AB and AC result in the same change of the

yield surface from TY_0 to TY_1 . However, these two paths give rise to different volumetric plastic strains. Furthermore, as seen in Table 3.3, distinct parameters are required to predict the plastic strain generated along thermal loading paths and mechanical loading paths. This induces a higher number of parameters to be identified and thus increases the complexity of the model. Also, it should be noted that although the volumetric plastic strain $\varepsilon_v^{T;p}$ is induced by temperature changes, this variable is not thermodynamically conjugated to temperature.

In the concept of Model A, there is no distinction between thermo-mechanical plastic strains induced by either thermal or mechanical loadings. However, distinct flow rules are adopted for each yield surface (TY or LY). And the plastic strain increment when TY is activated $d\varepsilon_{v1}^p$ is loading path dependent since the plastic modulus ω_T depends on temperature. For instance, mechanical loading paths BC and DE (see Figure 3.4(b)) will produce different plastic volumetric strains.

In Model L, the plastic volumetric deformation induced by the different loading paths (Figure 3.4(c)) is calculated according to a single flow rule. It can be determined by the change in size of the yield surface from LS_0 to LS_1 , irrespective of loading paths.

From the simulation results presented in Section 3.2.4, Model A is able to predict the plastic strain induced along a thermal loading path in both normally consolidated and overconsolidated conditions thanks to the introduction of an additional plastic mechanism in the effective stress–temperature space, namely TY. However, the two plastic mechanisms associated with yield surfaces TY and LY are not discussed in the light of the classic elasto-plastic theory. The evolution of LY during a heating-cooling cycle is firstly studied. As presented earlier, in Model A, the thermal evolution of the preconsolidation pressure follows a concept different from the other two models. Figure 3.11 shows the evolution of LY during a heating-cooling cycle. During heating from T_0 to T_2 (C to D in Figure 3.11(a)) of a normally consolidated specimen, the preconsolidation pressure is temperature independent, and LY_1 during this process thus keeps constant, as illustrated in Figure 3.11(a). Under the subsequent cooling process from T_2 back to T_1 and then to T_0 (D-E-F), as seen in

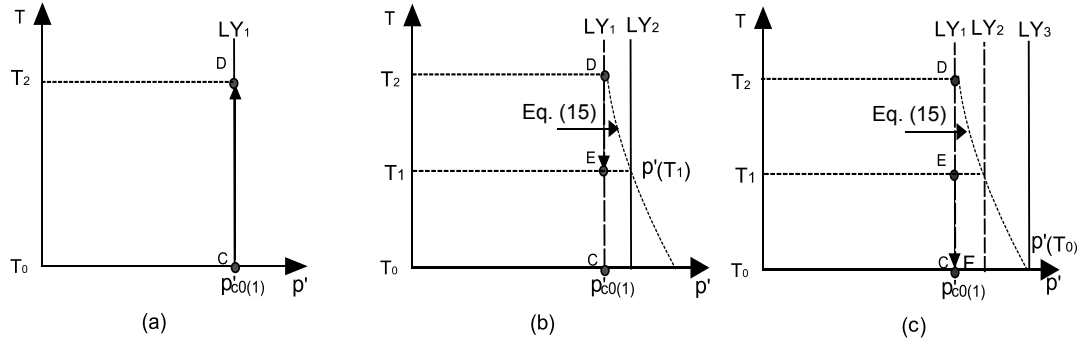


Figure 3.11: Evolution of LY curve in a heating-cooling cycle in Model A. (a) Heating process, (b) Cooling process at T_1 and (c) Cooling process at T_0

Figure 3.11(b)&(c), the preconsolidation pressure increases. Its value at temperatures T_1 and T_2 can be determined using Equation 3.15. LY thus evolves from LY_1 to LY_2 and then LY_3 during the cooling process. It should be noted that according to Model A the preconsolidation pressure increase and the corresponding evolution of the yield surface are even adopted during a purely elastic process. This is not consistent with the conventional elasto-plastic theory stating that the preconsolidation pressure is increased and the yield surface evolves with the plastic strain increment, and that they keep unchanged in a purely elastic process [90]. As for TY, Figure 3.12 shows its evolution in a heating process from T_0 to T_2 at effective stress point p'_1 , which corresponds to a lightly overconsolidated state at room temperature. During a heating phase A-C, TY evolves from TY_1 to TY_2 according to Equation 3.13. To maintain TY at stress point p'_1 , the value of p'_{c0} would change from $p'_{c0(1)}$ to $p'_{c0(2)}$. However, LY will keep unchanged and p'_{c0} will remain constant (still equal to $p'_{c0(1)}$) in a heating process as described above. This point shows the inconsistency between TY and LY plastic mechanisms.

In Model L, the bounding surface theory is introduced and a single plastic mechanism is adopted to simulate the thermo-plastic behavior in both overconsolidated and normally consolidated states. To this aim, the loading surface expands and shrinks according to the evolution of r_{iso} during a loading-unloading-reloading cycle. Model L appears as more simple than the two others, with a single plastic mechanism in (p', T) space. This constitu-

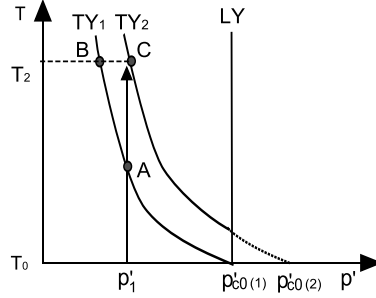


Figure 3.12: Evolution of TY curve during heating process in Model A.

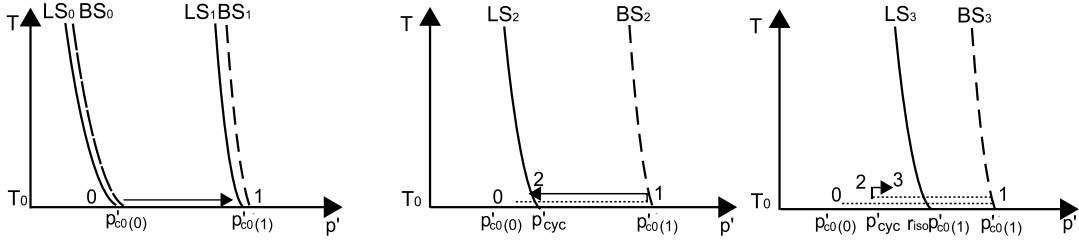


Figure 3.13: Plastic mechanism over a mechanical isotropic loading-unloading-reloading cycle in Model L.

tive model can thus be implemented into a numerical code more easily than Model C and Model A which both include two plastic mechanisms. In the following part, the evolution mechanism of the loading surface is discussed.

As an illustration, Figure 3.13 schematically presents the evolution of the yield limit in a loading-unloading-reloading process. During the first loading (path 0-1), loading surface (LS) and bounding surface (BS) coincide when $r_{iso} = 1$. The preconsolidation pressure at T_0 evolves from $p'_{c0(0)}$ to $p'_{c0(1)}$ with the plastic strain evolving from ε_{v0}^p to ε_{v1}^p . During the subsequent unloading process (path 1-2), no plastic strain is generated and thus BS keeps constant. However, the model assumes that LS will move back to follow the decrease of the mean effective pressure p' . At the start of the reloading process (path 2-3), the size of LS will be adjusted suddenly from LS_2 to LS_3 with a new r_{iso} according to Equation 3.31 ($r_{iso} = r_{iso}^e + \frac{p'_{cyc}}{p'_{c0(1)}}$; $\varepsilon_v^p = \varepsilon_{v1}^p$ remains constant). This peculiar behaviour is possible because LS is treated as a “loading surface” in the sense of the bounding surface plasticity concept introduced by Dafalias et al. [24, 25] (where the loading function f is always null) and not

as a yield surface that could be either activated or not, in the sense of classic elastoplasticity (where the yield criterion f may be negative). However, a difference appears between the treatment of the LS locus and the original concept from Dafalias. It concerns the fact that the stress point does not pertain to the LS surface at any time. This is the case when the loading direction is changed within the elastic nucleus (from unloading to loading, see for instance Figure 3.13). At this point, the size of the LS locus is “adjusted” to coincide with the elastic nucleus (and thus f_{LS} becomes negative) whereas according to Dafalias et al., this locus should remain attached to the stress point (and thus $f_{LS} = 0$ at any time). In this latter case, plastic strains are cancelled within the elastic nucleus by imposing an infinite plastic modulus. Apart from this different treatment of stress paths within the elastic nucleus, Model L provides simulations that would be similar to those obtained using strictly Dafalias et al. concept.

3.2.6 Conclusion

Several advanced thermo-mechanical models as Cui et al. [22], Abuel-Naga et al. [1] and Laloui and François [31, 50] have been proposed recently and most of them are based on the experimental test carried out by Baldi et al.[7] on natural Boom Clay. It is however observed that the experimental results obtained by Baldi et al. were not correctly accounted for in these models. Moreover, these models present some similarities and also some differences in different aspects. It appears then necessary to clarify the test by Baldi et al. and to make a comparison of the models.

For this purpose, the experimental test (TBoom9) conducted on natural Boom Clay by Baldi et al. was presented with special attention on the successive thermal mechanical loading path and the drained thermal volumetric strain results. A discussion on the methods to obtain volumetric strain was made. It has been shown that there are two distinct series of experimental data depending on the method adopted, the difference between them being significant. Obviously, this difference can have significant impact on the development of constitutive models which are based on one or another data series.

The assessment of the isotropic part of the models of Cui et al. [22] – Model C, Abuel-Naga et al. [1] – Model A, Laloui and François [31, 50] – Model L showed that each model has its advantages and drawbacks. The main conclusions are as follows:

- Although the three models are elaborated with different concepts with respect to elastic behaviour and plastic mechanism(s), all of them can capture the main features of the thermo-mechanical isotropic behaviour of saturated clays.
- One of the main differences on thermo-elastic equations amongst the three models is the choice made for the evolution of the thermal expansion coefficient with temperature and stress: only Model C considers a constant value. The assessment performed showed that taking a constant value permits to remain simple and relatively accurate in describing the thermo-elastic behaviour as well as to ensure that the elastic behavior is loading-path independent.
- In both Model C and Model A, two yield surfaces are introduced to describe the thermo-mechanical plastic behavior. Correspondingly, two plastic mechanisms were proposed. Model L uses the bounding surface theory and a single plastic mechanism is used. Thus, Model L can be implemented more easily into a numerical code.
- The plastic strain variables along a mechanical loading path and a thermal loading path are distinct and defined for each plastic mechanism in Model C. In Model A, the thermal plastic strain is not differentiated from the mechanical one and a single plastic strain variable is used for each plastic mechanism. Model L links stress and temperature-induced hardening process and a unique plastic strain along different loading paths is defined.

3.3 Explicit integration of a thermo-mechanical model for clays

Computers and Geotechnics 46 (2012) 13–25

Contents lists available at [SciVerse ScienceDirect](#)

Computers and Geotechnics

journal homepage: www.elsevier.com/locate/compgeo

Explicit integration of a thermo-mechanical model for clays

P.Y. Hong^a, J.M. Pereira^{a,*}, Y.J. Cui^{a,b}, A.M. Tang^a^aUniversité Paris-Est, Laboratoire Navier, École des Ponts ParisTech, France^bTongji University, Department of Geotechnical Engineering, China

ARTICLE INFO

Article history:

Received 30 August 2011

Received in revised form 18 May 2012

Accepted 28 May 2012

Available online 28 June 2012

Keywords:

Thermo-mechanical behavior

Constitutive model

Stress integration

Time integration

Numerical algorithm

ABSTRACT

This paper considers the numerical implementation of an existing constitutive model that was developed to simulate the thermo-mechanical behavior of clays. The model, which combines two plastic mechanisms, has been reformulated using generalized stress and strain variables accounting for the presence of temperature as an additional variable.

Mixed control conditions are introduced to simulate standard thermo-mechanical laboratory tests. An explicit integration scheme is used with an adaptive time-stepping scheme specifically designed for the considered thermo-mechanical model. This sub-stepping procedure enables the constitutive model to be integrated accurately and efficiently by automatically adjusting the size of sub-steps to maintain the local integration error below a specified tolerance. Special attention is paid to the cases where the two yield surfaces are activated simultaneously. The correction of the drift of the stress point from the yield surface is also accounted for.

This thermo-elastoplastic model has been implemented in a constitutive driver aiming at simulating thermo-mechanical tests in the triaxial stress space. The efficiency of this integration algorithm is discussed and the clear advantage of using the adaptive sub-stepping procedure is shown. The constitutive model is finally used to simulate thermo-mechanical tests. The results are compared to available experimental data and show the good capabilities of the constitutive model.

© 2012 Elsevier Ltd. All rights reserved.

3.3.1 Introduction

The thermo-mechanical behavior of clays has been widely investigated over the past decades due to the increasing interest in geomechanical problems involving thermal effects such as nuclear waste disposals and oil production activities (see, among others, [2, 16, 22, 34, 44]). When considering constitutive modelling of the thermo-mechanical behavior of geomaterials, efficient integration strategies of the stress-temperature-strain relationship should be investigated at the stress point level. This is indeed a starting point before

considering numerical analyses on the scale of boundary value problems using finite element codes.

Several constitutive models accounting for temperature effects in soils have been proposed in the last two decades. Hueckel and his co-workers [43, 44] developed one of the first thermo-mechanical constitutive models. This model is an extension of the well-known Modified Cam Clay model (MCC) and aims at describing the thermo-elasto-plastic behavior of clays. Following these developments, several new advanced thermo-mechanical constitutive models have been proposed within the framework proposed by Hueckel & Borsetto [1, 22, 34, 49, 65]. Most of these models are extensions of relatively simple elasto-plastic constitutive models (such as MCC model) to account for temperature effects. This is particularly the case for the thermo-mechanical model (TM) of Cui *et al.* [22], who introduced a volumetric thermal plastic mechanism to predict thermal plastic strains which are known to largely depend on the consolidation state of the soil. This plastic mechanism accounts for the influence of the overconsolidation ratio (OCR) on the mechanical behavior of soils subjected to thermal loadings. It also catches the apparent overconsolidation effect due to heating as observed experimentally on normally consolidated soils. A double yield surface, comprising a thermal yield surface (TY) and a loading surface (LY), delimits the reversible domain in the mean effective stress-temperature space.

The numerical resolution of the constitutive equations can be performed using either implicit or explicit schemes. These two kinds of schemes distinguish from each other by a very basic assumption about the plastic strains calculation over an increment. Implicit schemes assume that the plastic strain increment is calculated at the final stress state of the current increment, whereas explicit schemes calculate the plastic strain increment at the initial stress state. In an implicit method, the resulting stresses achieved by iteration are generally accurate and automatically satisfy the yield criterion (up to a yield tolerance). Furthermore, it is not required to localize the intersection of the stress path with the yield surface when the stress point goes from an elastic state to a plastic state [75]. Although attractive because of the advantages mentioned above, implicit schemes are not straightfor-

ward to implement especially for advanced and complicated soil models. On the contrary, for explicit schemes, a drift of the stress point from the yield surface may be observed. A drift correction is then needed to bring the stress point back to the yield surface. In addition, the intersection point between the yield surface and the stress path has to be identified if the stress path goes from an elastic state to a plastic state. The accuracy and efficiency is largely dependent on the implementation method and a special attention has to be paid to the increments length. Despite these drawbacks, explicit schemes have the prominent advantage of being implemented more straightforwardly than implicit schemes. Some methods have been proposed to overcome some of the drawbacks of explicit schemes. In particular, a significant enhancement of their accuracy and efficiency can be achieved by using an adaptive sub-stepping method as initially proposed by Sloan and his co-workers [74, 75].

For geomaterials, the two types of stress integration schemes mentioned above have been largely studied for the integration of saturated and unsaturated constitutive models. Implicit algorithms for the saturated MCC are presented in [13, 14] and for the unsaturated Barcelona Basic model (BBM) in [86]. The explicit integration techniques of Sloan [74] that include adaptive sub-stepping procedures have been extended to MCC. These procedures consist in subdividing the imposed strain increments into a numbers of sub-steps. The number of sub-steps is automatically adapted to ensure that an error measure remains within a given tolerance at each sub-step. This algorithm has significant advantage in terms of efficiency and accuracy. More recently, this advanced explicit integration algorithm has been successfully applied to solve constitutive equations for unsaturated soils (see [71, 72]).

The aforementioned studies concern isothermal constitutive models, and few studies involve numerical implementation of thermo-mechanical models for saturated or unsaturated soils. The introduction of temperature as an extra-variable and the existence of thermo-mechanical couplings require significant changes of the integration algorithm. Actually, the same difficulty was met when extending computational methods used for saturated soils to the case of unsaturated soils. In this latter case, it is suction that has to be introduced

as an additional variable. Several algorithms tackling this problem have been proposed [71, 77, 86]. In Vaunat *et al.* [86], an implicit stress integration scheme was presented. Generalized stress and strain variables, although not thermodynamically conjugated, are introduced for convenience. Suction is associated with the mechanical stress to define a new stress variable and an extra suction-related strain component is used to build a new strain variable. The resolution algorithm works with mixed control conditions. The increment of total strain from the new strain vector and the increment of suction from the new stress vector are considered as input variables. In the explicit algorithms presented by [71, 77], changes in suction are directly treated as a strain variable, the obtained generalized strain being used as the input variable. The way suction is numerically handled in the previous algorithms, either implicit or explicit, is thus similar.

In this study, the thermo-elasto-plastic model for clays proposed by Cui *et al.* [22] is used as it can well predict the main features of the thermo-mechanical behavior of saturated clays. Some difficulties in the implementation of the adopted elastoplastic law arise from the main features provided by the model:

1. strains are induced by both stress and temperature changes, which makes total strain-driven algorithms more difficult to implement;
2. two yield surfaces that can be activated simultaneously delimit the elastic domain in the stress-temperature space and couplings between these surfaces are introduced.

This paper presents the numerical integration of the TM model at the stress point level using an explicit scheme. This scheme accounts for non-isothermal conditions and is improved by adding an adaptive time stepping procedure inspired from the work of Sloan *et al.* [75]. Furthermore, the performance of the developed algorithm is analyzed and the capabilities of this model to describe the thermo-mechanical behavior of clays in the triaxial stress space are investigated. Firstly, the elasto-plastic constitutive equations of the considered thermo-mechanical model are briefly recalled. The constitutive relations are presented using generalized stress-strain variables, considering the temperature as a stress variable and an additional temperature-related strain component. Secondly, a mixed control

procedure is considered and an explicit integration with adaptive sub-stepping accounting for non-isothermal loadings is proposed. Finally, the TM model has been implemented in a constitutive driver and used to simulate various thermo-mechanical solicitation paths in order to check the efficiency of the developed algorithm. The constitutive model itself is also evaluated by predicting some thermo-mechanical loading tests.

3.3.2 Constitutive modeling of the thermo-mechanical behavior of clays

3.3.2.1 Thermo-mechanical model (TM)

The thermo-mechanical model (TM) developed by Cui and his co-workers [22] is an extension of the MCC model to account for temperature effects on the behavior of saturated clays. For saturated soils under isothermal conditions, the TM model simplifies into MCC model. The original model is formulated in the triaxial stress space ($p' - q$) extended to temperature T .

The mean effective stress $p' = p - u$ and deviator stress q are defined from the effective stress tensor $\sigma'_{ij} = \sigma_{ij} - u \delta_{ij}$, $i, j = \{1, 2, 3\}$ as (following Einstein's notation repeated indices mean summation):

$$p' = \frac{1}{3} \sigma'_{ij} \delta_{ij} \quad ; \quad q = \sqrt{\frac{3}{2}} \sqrt{s_{ij} s_{ij}} \quad (3.34)$$

with u , the pore water pressure δ_{ij} , Kronecker's symbol and $s_{ij} = \sigma'_{ij} - \frac{1}{3} p' \delta_{ij}$, the deviatoric stress tensor. In the triaxial stress space, the mean effective stress p' and deviator stress q simplify as follows:

$$p' = \frac{1}{3} (\sigma'_1 + 2\sigma'_3) \quad ; \quad q = \sigma_1 - \sigma_3 \quad (3.35)$$

3.3.2.1.1 Elastic behavior The incremental volumetric elastic strain is defined as:

$$d\varepsilon_v^e = d\varepsilon_v^{T,e} + d\varepsilon_v^{\sigma,e} = -\alpha_d dT + \frac{dp'}{K} \quad (3.36)$$

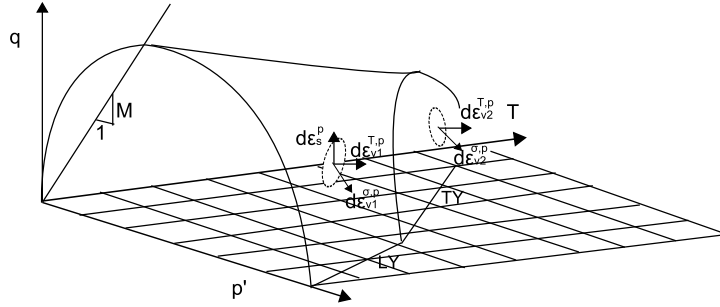


Figure 3.14: Yield surfaces in the $(p' - q - T)$ space.

where $d\varepsilon_v^{T,e}$ and $d\varepsilon_v^{\sigma,e}$ are the incremental elastic volumetric strains due to temperature and stress changes respectively, α_d is the drained volumetric thermal coefficient of expansion and K is the elastic bulk modulus. The elastic shear strain is assumed to be purely mechanical (that is not influenced by temperature changes), thus:

$$d\varepsilon_s^e = \frac{dq}{3G} \quad (3.37)$$

The bulk modulus K is the same as for the MCC model whereas the shear modulus G is obtained by assuming a constant Poisson's ratio ν :

$$K = \frac{vp'}{\kappa} \quad ; \quad G = \frac{3(1-2\nu)}{2(1+\nu)}K \quad (3.38)$$

where κ is the elastic slope in $(\ln p', v)$ space and v is the specific volume.

3.3.2.1.2 Plastic behavior The elastic domain in the triaxial stress space (p', q) is assumed to be temperature dependent. According to experimental observations, the size of this reversible domain decreases with increasing temperatures. Figure 3.14 presents a schematic view of the elastic domain in the $(p' - q - T)$ three-dimensional space.

The elastic domain is bounded by two yield surfaces called loading yield surface (LY) and thermal yield surface (TY), which can be seen in Figure 3.15. The expression for the

thermal yield surface (TY) reads as follows:

$$F^{TY} \equiv (T - T_0) - (T_c - T_0) \exp(-\beta p') = 0 \quad (3.39)$$

where T_c is a reference temperature corresponding to the point at which the yield curve crosses the temperature axis, T_0 is the initial temperature and β is a hardening variable affecting the shape of TY and controlling its evolution. The expression for the loading yield surface (LY) reads as follows:

$$F^{LY} \equiv q^2 - M^2 p'(p'_{cT} - p') = 0 \quad (3.40)$$

with

$$p'_{cT} = p'_{c0} \exp\left(-\alpha_0(T - T_0)\right) \quad (3.41)$$

where p'_{c0} and p'_{cT} are defined as the apparent preconsolidation pressures at an initial temperature T_0 and the actual temperature T respectively, α_0 governs the curvature of LY and M is the slope of the critical state line in $(p' - q)$ plane. p'_{c0} is a hardening variable that controls the evolution of the loading yield surface (LY).

The thermal plastic volumetric strain $d\varepsilon_v^{T,p}$ associated with changes of temperature at constant effective stress can be observed by heating a soil at a constant applied stress. The following equations in the $(\varepsilon_v^p - T)$ plane is proposed to catch experimental observations:

$$d\varepsilon_v^{T,p} = \alpha_p \left[\exp\left(\alpha_p(T - T_0)\right) - a \right] dT \quad (3.42)$$

where α_p is related to the slope of the curve and a is a shape parameter. For lightly overconsolidated and normally consolidated states ($OCR \leq c_1$, α_p) is constant and given by:

$$\alpha_p = \frac{\alpha_d}{1 - a} \quad (3.43)$$

For highly overconsolidated ($OCR > c_1$), α_p varies with the overconsolidation ratio (OCR)

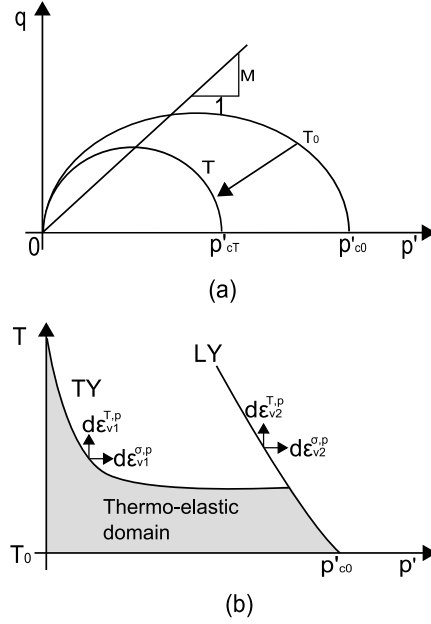


Figure 3.15: Yield locus in (a) $(p' - q)$ plane at two different temperatures (with $T > T_0$) and (b) $(p' - T)$ plane.

as follows:

$$\alpha_p = \frac{\alpha_d}{\exp\left(\frac{\alpha_p}{c_2} \ln\left(\frac{1}{c_1} \frac{p'}{p'_{c0}}\right)\right) - a} \quad (3.44)$$

where c_1 and c_2 are parameters that can be determined from the transition point between expansion and contraction of the total volume change associated with temperature changes.

Assuming that hardening due to LY activation has no effect on the plastic mechanism involving TY, the hardening law related to TY is given by the following relation:

$$\begin{aligned} d\beta &= - \left(\frac{\partial F^{TY}}{\partial T} \frac{\partial T}{\partial \varepsilon_{vTY}^{T,p}} d\varepsilon_{vTY}^{T,p} + \frac{\partial F^{TY}}{\partial p'} \frac{\partial p'}{\partial \varepsilon_{vTY}^{\sigma,p}} d\varepsilon_{vTY}^{\sigma,p} \right) / \frac{\partial F^{TY}}{\partial \beta} \\ &= \frac{- \exp(\beta p')}{p'(T_c - T_{c0}) \alpha_p \left[\exp\left(\alpha_p(T - T_0)\right) - a \right]} d\varepsilon_{vTY}^{T,p} - \frac{\beta}{\alpha_1} d\varepsilon_{vTY}^{\sigma,p} \end{aligned} \quad (3.45)$$

where $d\varepsilon_{vTY}^{T,p}$ and $d\varepsilon_{vTY}^{\sigma,p}$ correspond to plastic strain increments associated with, respectively, thermal and mechanical loadings activating the TY surface and α_1 is the mechanical plastic modulus of TY mechanism.

In order to account for the thermal overconsolidation effect, it is assumed that the

movement of TY surface has an influence on the position of LY. Therefore, a partial coupling phenomena between these two plastic mechanisms is introduced so that the increment of the hardening variable dp'_{c0} of the LY surface reads as:

$$\begin{aligned}
 dp'_{c0} &= - \left[\frac{\partial F^{LY}}{\partial T} \frac{\partial T}{\partial \varepsilon_{vTY}^{T,p}} (d\varepsilon_{vTY}^{T,p} + \frac{kv_0}{\lambda - \kappa} d\varepsilon_{vLY}^{T,p}) + \frac{\partial F^{LY}}{\partial p'} \frac{\partial p'}{\partial \varepsilon_{vLY}^{\sigma,p}} (d\varepsilon_{vLY}^{\sigma,p} + d\varepsilon_{vTY}^{\sigma,p}) \right] / \frac{\partial f}{\partial p'_{c0}} \\
 &= \left\{ \frac{\alpha_0}{\alpha_p \left[\exp \left(\alpha_p (T - T_0) \right) - a \right]} d\varepsilon_{vLY}^{T,p} + \left(\frac{v_0}{\lambda - \kappa} \right) (d\varepsilon_{vLY}^{\sigma,p} + d\varepsilon_{vTY}^{\sigma,p}) \right. \\
 &\quad \left. + \left(\frac{\alpha_0}{\alpha_p \left[\exp \left(\alpha_p (T - T_0) \right) - a \right]} + \frac{kv_0}{\lambda - \kappa} \right) d\varepsilon_{vTY}^{T,p} \right\} p'_{c0}
 \end{aligned} \tag{3.46}$$

where the mechanical plastic volumetric strain $d\varepsilon_{vLY}^{\sigma,p}$ and the thermal plastic volumetric strain $d\varepsilon_{vLY}^{T,p}$ are associated with plastic loadings on the LY yield surface and k is a positive parameter that describes the coupling effects between TY and LY.

The complete definition of TM model requires the calibration of 13 parameters. Five of them (M , λ , κ , p'_{c0} , G) have the same physical meaning as for the MCC model. Equations and parameters of the TM model are summarized in Table (3.4). Interested readers can refer to the original paper [22] for more details.

3.3.2.2 Variables for TM

In view of the following section devoted to the implementation of the TM model, the stress and strain tensors are generalized to account for the temperature T and the temperature-driven strains ε_v^T , this latter being totally isotropic. The generalized stress, $\bar{\sigma}$, is built from the effective stress and the temperature. The generalized strain $\bar{\varepsilon}$ is built from the total strain ε and the temperature-induced volumetric strain ε_v^T . These generalized variables write as follows:

$$\bar{\sigma} = \begin{Bmatrix} \sigma' \\ T \end{Bmatrix} ; \quad \bar{\varepsilon} = \begin{Bmatrix} \varepsilon \\ \varepsilon_v^T \end{Bmatrix} \tag{3.47}$$

Table 3.4: TM model: equations and parameters.

Equation	Parameter
<p><i>Elastic part</i></p> $d\varepsilon_v^e = -\alpha_d dT + \frac{dp'}{K}$ $d\varepsilon_s^e = \frac{dq}{3G}$	α_d, K G
<p><i>Yield functions</i></p> $F^{TY} = T - (T_c - T_0) \exp(-\beta p') - T_0$ $F^{LY} = q^2 - M^2 p' (p'_{cT} - p') = 0$ <p>with $p'_{cT} = p'_{c0} \exp[-\alpha_0(T - T_0)]$</p>	T_c, β M p_{c0}, α_0
<p><i>Hardening laws</i></p> $d\varepsilon_v^{T,p} = \alpha_p [\exp(\alpha_p(T - T_0)) - a] dT$ <p>where:</p> $\alpha_p = \frac{\alpha_d}{1 - a} \quad \text{if } OCR \leq 1/c_1 ;$ $\alpha_p = \frac{\alpha_d}{\exp\left(\frac{\alpha_p}{c_2} \ln\left(\frac{1}{c_1} \frac{p'}{p'_{c0}}\right)\right) - a - \exp(\beta p')} \quad \text{if } OCR > 1/c_1.$ $d\beta = \frac{\alpha_0}{p'(T_c - T_0) \alpha_p [\exp(\alpha_p(T - T_0)) - a]} d\varepsilon_{vTY}^{T,p} - \frac{\beta}{\alpha_1} d\varepsilon_{vTY}^{\sigma,p}$ $\frac{dp'_{c0}}{p'_{c0}} = \frac{\alpha_0}{\alpha_p [\exp(\alpha_p(T - T_0)) - a]} d\varepsilon_{vLY}^{T,p}$ $+ \left(\frac{v_0}{\lambda - \kappa}\right) (d\varepsilon_{vLY}^{\sigma,p} + d\varepsilon_{vTY}^{\sigma,p})$ $+ \left(\frac{\alpha_0}{\alpha_p [\exp(\alpha_p(T - T_0)) - a]} + \frac{kv_0}{\lambda - \kappa}\right) d\varepsilon_{vTY}^{T,p}$	a c_1, c_2 α_1 k

It is worth noting that these two variables are not thermodynamically associated. For convenience but without losing generality, in the following the equations are formulated in the principal stress and strain directions, so that:

$$\bar{\boldsymbol{\sigma}} = (\sigma'_1, \sigma'_2, \sigma'_3, T)^t \quad ; \quad \bar{\boldsymbol{\varepsilon}} = (\varepsilon_1, \varepsilon_2, \varepsilon_3, \varepsilon_v^T)^t \quad (3.48)$$

An extension of the proposed formulation to general stress and strain spaces could be derived straightforwardly.

Considering these generalized variables, a new explicit stress-strain incremental formulation ($d\bar{\boldsymbol{\sigma}} - d\bar{\boldsymbol{\varepsilon}}$) can be proposed. Note that $d\boldsymbol{\varepsilon}$ is the total strain increment which can be split into two parts: a stress-driven strain increment $d\boldsymbol{\varepsilon}^\sigma$ and an temperature-driven isotropic strain increment $d\varepsilon_v^T$:

$$d\boldsymbol{\varepsilon} = d\boldsymbol{\varepsilon}^\sigma + \frac{1}{3}\mathbf{m}d\varepsilon_v^T \quad (3.49)$$

where $\mathbf{m} = (1, 1, 1)^t$.

We assume that $d\boldsymbol{\varepsilon}^\sigma$ and $d\varepsilon_v^T$ can be split into an elastic part ($d\boldsymbol{\varepsilon}^{\sigma,e}$ and $d\varepsilon_v^{T,e}$) and a plastic part ($d\boldsymbol{\varepsilon}^{\sigma,p}$ and $d\varepsilon_v^{T,p}$), respectively:

$$\begin{aligned} d\boldsymbol{\varepsilon}^\sigma &= d\boldsymbol{\varepsilon}^{\sigma,e} + d\boldsymbol{\varepsilon}^{\sigma,p} \\ d\varepsilon_v^T &= d\varepsilon_v^{T,e} + d\varepsilon_v^{T,p} \end{aligned} \quad (3.50)$$

The generalized stress and elastic strain variables are linked through the following incremental relation:

$$d\bar{\boldsymbol{\sigma}} = \bar{\mathbf{D}}^e d\bar{\boldsymbol{\varepsilon}}^{\sigma,e} \quad (3.51)$$

where $d\bar{\boldsymbol{\varepsilon}}^{\sigma,e} = (d\boldsymbol{\varepsilon}^{\sigma,e}, d\varepsilon_v^{T,e})^t$ and $\bar{\mathbf{D}}^e$ is the generalized elastic stiffness matrix.

Assuming geometrical and material symmetries, the generalized stress-strain constitutive relation given by Eq. (3.51) writes in the principal stress and strain directions (referred

to by indices $\{1, 2, 3\}$) as follows:

$$\begin{pmatrix} d\sigma'_1 \\ d\sigma'_2 \\ d\sigma'_3 \\ dT \end{pmatrix} = \begin{bmatrix} K + \frac{4}{3}G & K - \frac{2}{3}G & K - \frac{2}{3}G & 0 \\ K - \frac{2}{3}G & K + \frac{4}{3}G & K - \frac{2}{3}G & 0 \\ K - \frac{2}{3}G & K - \frac{2}{3}G & K + \frac{4}{3}G & 0 \\ 0 & 0 & 0 & -\frac{1}{\alpha_d} \end{bmatrix} \begin{pmatrix} d\varepsilon_1^{\sigma,e} \\ d\varepsilon_2^{\sigma,e} \\ d\varepsilon_3^{\sigma,e} \\ d\varepsilon_v^{T,e} \end{pmatrix} \quad (3.52)$$

The elastic matrix $\overline{\mathbf{D}}^e$ can be split into two parts: one is the usual solely mechanical elastic stiffness matrix involving the bulk and shear elastic moduli K and G respectively and the other corresponds to the temperature–strain relationship which writes as follows:

$$d\varepsilon_v^{T,e} = -\alpha_d dT \quad (3.53)$$

where the thermal coefficient α_d is assumed constant in the present model.

In this study, ΔT and $\Delta \boldsymbol{\varepsilon}$ are considered as prescribed inputs and $\Delta \boldsymbol{\sigma}$ as an output that has to be obtained from the integration algorithm. Therefore, a mixed calculation procedure is required to solve Eq. (3.52) at the stress point level. From Eq. (3.49), the stress-driven strain increment ($d\boldsymbol{\varepsilon}^\sigma$) can be expressed in the following form:

$$d\boldsymbol{\varepsilon}^\sigma = d\boldsymbol{\varepsilon} - \frac{1}{3} \mathbf{m} d\varepsilon_v^T \quad (3.54)$$

The strain component $d\varepsilon_v^T$ is temperature-driven, in the sense that this thermal volumetric strain increment can be determined from the knowledge of the temperature increment dT , as it will be seen later. Hence the stress-driven strain increment $d\boldsymbol{\varepsilon}^\sigma$ can be determined from the input of the temperature increment dT and the total strain increment $d\boldsymbol{\varepsilon}$.

From Eq. (3.49), the total elastic strain $d\overline{\boldsymbol{\varepsilon}}^e$ can be calculated according to the following equation:

$$d\overline{\boldsymbol{\varepsilon}}^e = d\overline{\boldsymbol{\varepsilon}}^{\sigma,e} + \frac{1}{3} \overline{\mathbf{m}} d\varepsilon_v^{T,e} \quad (3.55)$$

where $\bar{\mathbf{m}} = (1, 1, 1, 0)^t$. Substituting Eq. (3.55) into Eq. (3.51), the generalized stress-strain relation can be rewritten as:

$$d\bar{\boldsymbol{\sigma}} = \bar{\mathbf{D}}^{e*} d\bar{\boldsymbol{\varepsilon}}^e \quad (3.56)$$

where the elastic stiffness tensor $\bar{\mathbf{D}}^{e*}$ is defined by:

$$\bar{\mathbf{D}}^{e*} = \bar{\mathbf{D}}^e \left(\boldsymbol{\delta} - \frac{1}{3} \bar{\mathbf{m}} \bar{\mathbf{n}} \right) \quad (3.57)$$

with $\boldsymbol{\delta}$ is the second order identity tensor and $\bar{\mathbf{n}} = (0, 0, 0, 1)$.

In the space of the principal stresses directions, Eq. (3.52) rewrites as follows:

$$\begin{pmatrix} d\sigma'_1 \\ d\sigma'_2 \\ d\sigma'_3 \\ dT \end{pmatrix} = \begin{bmatrix} K + \frac{4}{3}G & K - \frac{2}{3}G & K - \frac{2}{3}G & -K \\ K - \frac{2}{3}G & K + \frac{4}{3}G & K - \frac{2}{3}G & -K \\ K - \frac{2}{3}G & K - \frac{2}{3}G & K + \frac{4}{3}G & -K \\ 0 & 0 & 0 & -\frac{1}{\alpha_d} \end{bmatrix} \begin{pmatrix} d\varepsilon_1^e \\ d\varepsilon_2^e \\ d\varepsilon_3^e \\ d\varepsilon_v^{T,e} \end{pmatrix} \quad (3.58)$$

3.3.2.3 Constitutive equation

Using the newly defined generalized variables, the consistency conditions for the two yield surfaces of the TM model writes in the following synthetic form:

$$dF^Y = \left(\frac{\partial F^Y}{\partial \bar{\boldsymbol{\sigma}}} \right)^t : d\bar{\boldsymbol{\sigma}} + \left(\frac{\partial F^Y}{\partial X^Y} \right)^t dX^Y = 0 \quad (3.59)$$

where the superscript $Y = \{LY, TY\}$ stands for the considered yield surface and $X^Y = \{p'_{c0}, \beta\}$ is the hardening variable associated with that yield surface. The derivation of a yield function with respect to the generalized stress is defined as $\frac{\partial F^Y}{\partial \bar{\boldsymbol{\sigma}}} = \left(\frac{\partial F^Y}{\partial \boldsymbol{\sigma}'}, \frac{\partial F^Y}{\partial T} \right)^t$.

The stress increment $d\bar{\boldsymbol{\sigma}}$ is calculated according to Eq. (3.56) from the total elastic strain $d\bar{\boldsymbol{\varepsilon}}^e$, which in turn can be given by the difference between the total strain $d\bar{\boldsymbol{\varepsilon}}$ and

the total plastic strain $d\bar{\boldsymbol{\varepsilon}}^p$:

$$d\bar{\boldsymbol{\sigma}} = \bar{\mathbf{D}}^{e*} d\bar{\boldsymbol{\varepsilon}}^e = \bar{\mathbf{D}}^{e*} (d\bar{\boldsymbol{\varepsilon}} - d\bar{\boldsymbol{\varepsilon}}^p) \quad (3.60)$$

where $d\bar{\boldsymbol{\varepsilon}}^p = d\bar{\boldsymbol{\varepsilon}}^{\sigma,p} + \frac{1}{3}\bar{\mathbf{m}}d\varepsilon_v^{T,p}$.

As commonly done, the plastic strain increment induced by the mechanical effective stress is calculated from the plastic potential:

$$d\bar{\boldsymbol{\varepsilon}}^{\sigma,p} = d\lambda_Y^{\sigma} \frac{\partial G^Y}{\partial \bar{\boldsymbol{\sigma}}} \quad (3.61)$$

where $d\lambda_Y^{\sigma}$ is the plastic multiplier, $G^Y = F^Y(\bar{\boldsymbol{\sigma}}, X^Y)$ is the plastic potential (equal to the yield function for standard materials), $\frac{\partial G^Y}{\partial \bar{\boldsymbol{\sigma}}} = \left(\frac{\partial G^Y}{\partial \boldsymbol{\sigma}'}, 0 \right)^t$.

The volumetric plastic strain induced by temperature at a fixed effective stress is defined as:

$$d\varepsilon_v^{T,p} = Q dT \quad (3.62)$$

where $Q = Q(\bar{\boldsymbol{\sigma}}) = \alpha_p \left[\exp \left(\alpha_p (T - T_0) \right) - a \right]$ is the plastic coefficient for changes in temperature, as defined in Eqs. (3.42)–(3.44). It corresponds to the slope of the experimental curve in $(\varepsilon_{vT}^p - T)$ plane.

From Eqs. (3.61) and (3.62), the total thermoplastic strain can therefore be written as:

$$d\bar{\boldsymbol{\varepsilon}}^p = d\lambda_Y^{\sigma} \frac{\partial G^Y}{\partial \bar{\boldsymbol{\sigma}}} + \frac{1}{3}\bar{\boldsymbol{\zeta}}QdT \quad (3.63)$$

where $\bar{\boldsymbol{\zeta}} = (1, 1, 1, 3)^t$.

The hardening laws controlling the evolution of the yield surfaces can be expressed as:

$$\begin{aligned} dX^Y &= \left(\frac{\partial X^Y}{\partial \bar{\boldsymbol{\varepsilon}}^p} \right)^t d\bar{\boldsymbol{\varepsilon}}^p \\ &= \frac{\partial X^Y}{\partial \varepsilon_v^{\sigma,p}} \bar{\boldsymbol{\zeta}}^t d\bar{\boldsymbol{\varepsilon}}^{\sigma,p} + \frac{\partial X^Y}{\partial \varepsilon_v^{T,p}} Q dT \end{aligned} \quad (3.64)$$

and their detailed formulations are given in Eqs. (3.45) and (3.46).

Introducing Eqs. (3.60)–(3.64) into Eq. (3.59), the differential form of the consistency condition can be rewritten as:

$$\left(\frac{\partial F^Y}{\partial \bar{\sigma}}\right)^t : d\bar{\sigma} - hd\lambda_Y^\sigma - bdT = 0 \quad (3.65)$$

$$\text{where } h = -\frac{\partial F^Y}{\partial X^Y} \frac{\partial X^Y}{\partial \varepsilon_v^{\sigma,p}} \bar{\zeta}^t \frac{\partial G^Y}{\partial \bar{\sigma}}, \quad b = -\frac{\partial F^Y}{\partial X^Y} \frac{\partial X^Y}{\partial \varepsilon_v^{T,p}} Q.$$

The expression of the plastic multiplier can be obtained from Eqs. (3.60) and (3.65):

$$d\lambda_Y^\sigma = \frac{\mathbf{a}^t \bar{\mathbf{D}}^{e*} - \left[\frac{1}{3} \mathbf{a}^t \bar{\mathbf{D}}^{e*} \bar{\zeta} Q + b\right] \mathbf{d}}{\mathbf{a}^t \bar{\mathbf{D}}^{e*} \mathbf{g} + h} d\bar{\varepsilon} \quad (3.66)$$

$$\text{where } \mathbf{a} = \frac{\partial F^Y}{\partial \bar{\sigma}}, \quad \mathbf{d} = \frac{\bar{\mathbf{n}}}{Q - \alpha_d} \text{ and } \mathbf{g} = \frac{\partial G^Y}{\partial \bar{\sigma}}.$$

The differential stress-strain equation can finally be written in the following form:

$$d\bar{\sigma} = \mathbf{D}_{ep}^\varepsilon d\bar{\varepsilon} + \mathbf{D}_{ep}^T dT = \left(\mathbf{D}_{ep}^\varepsilon + \mathbf{D}_{ep}^T \mathbf{d}\right) d\bar{\varepsilon} = \bar{\mathbf{D}}^{ep} d\bar{\varepsilon} \quad (3.67)$$

where

$$\mathbf{D}_{ep}^\varepsilon = \bar{\mathbf{D}}^{e*} - \frac{\bar{\mathbf{D}}^{e*} \mathbf{g} \mathbf{a}^t \bar{\mathbf{D}}^{e*}}{\mathbf{a}^t \bar{\mathbf{D}}^{e*} \mathbf{g} + h} \quad (3.68)$$

and

$$\mathbf{D}_{ep}^T = \frac{\bar{\mathbf{D}}^{e*} \left(\frac{1}{3} \mathbf{a}^t \bar{\mathbf{D}}^{e*} \bar{\zeta} Q + b\right)}{\mathbf{a}^t \bar{\mathbf{D}}^{e*} \mathbf{g} + h} \mathbf{g} - \frac{1}{3} \bar{\mathbf{D}}^{e*} \bar{\zeta} Q \quad (3.69)$$

Similarly, the hardening law can be expressed as follows:

$$dX^Y = \mathbf{R}_{ep}^\varepsilon d\bar{\varepsilon} + \mathbf{R}_{ep}^T dT = \left(\mathbf{R}_{ep}^\varepsilon + \mathbf{R}_{ep}^T \mathbf{d}\right) d\bar{\varepsilon} = \bar{\mathbf{R}}^{ep} d\bar{\varepsilon} \quad (3.70)$$

where

$$\mathbf{R}_{ep}^\varepsilon = \frac{\partial X^Y}{\partial \varepsilon_v^{\sigma,p}} \bar{\zeta}^t \mathbf{g} \frac{\mathbf{a}^t \bar{\mathbf{D}}^{e*}}{\mathbf{a}^t \bar{\mathbf{D}}^{e*} \mathbf{g} + h} \quad (3.71)$$

and

$$\mathbf{R}_{ep}^T = \frac{\partial X^Y}{\partial \varepsilon_v^{T,p}} Q - \frac{\partial X^Y}{\partial \varepsilon_v^{\sigma,p}} \bar{\zeta}^t \mathbf{g} \frac{\left(\frac{1}{3} \mathbf{a}^t \bar{\mathbf{D}}^{e*} \bar{\zeta} Q + b\right)}{\mathbf{a}^t \bar{\mathbf{D}}^{e*} \mathbf{g} + h} \quad (3.72)$$

The total plastic strain increment is the sum of the plastic strains due to each mechanism (TY and LY):

$$d\bar{\boldsymbol{\varepsilon}}^p = d\lambda_{TY}^\sigma \frac{\partial G^{TY}}{\partial \bar{\boldsymbol{\sigma}}} + d\lambda_{LY}^\sigma \frac{\partial G^{LY}}{\partial \bar{\boldsymbol{\sigma}}} + \frac{2}{3} \bar{\zeta} Q dT \quad (3.73)$$

where G^{TY} and G^{LY} are the plastic potentials.

Thus, the dual consistency condition can be re-written as follows:

$$\left\{ \begin{array}{l} \frac{\partial F^{TY}}{\partial \bar{\boldsymbol{\sigma}}} \bar{\mathbf{D}}^{e*} \left(d\boldsymbol{\varepsilon} - d\lambda_{TY}^\sigma \mathbf{g}^{TY} - d\lambda_{LY}^\sigma \mathbf{g}^{LY} - \frac{2}{3} \bar{\zeta} Q dT \right) \\ + \frac{\partial F^{TY}}{\partial X^{TY}} \left(\frac{\partial X^{TY}}{\partial \varepsilon_v^{\sigma,p}} \bar{\zeta}^t d\lambda_{TY}^\sigma \mathbf{g}^{TY} + \frac{\partial X^{TY}}{\partial \varepsilon_v^{T,p}} Q dT \right) = 0 \\ \\ \frac{\partial F^{LY}}{\partial \bar{\boldsymbol{\sigma}}} \bar{\mathbf{D}}^{e*} \left(d\boldsymbol{\varepsilon} - d\lambda_{TY}^\sigma \mathbf{g}^{TY} - d\lambda_{LY}^\sigma \mathbf{g}^{LY} - \frac{2}{3} \bar{\zeta} Q dT \right) \\ + \frac{\partial F^{LY}}{\partial X^{LY}} \left(\frac{\partial X^{LY}}{\partial \varepsilon_v^{\sigma,p}} \bar{\zeta}^t d\lambda_{TY}^\sigma \mathbf{g}^{TY} + \frac{\partial X^{LY}}{\partial \varepsilon_v^{T,p}} Q dT + \frac{\partial X^{LY}}{\partial \varepsilon_v^{\sigma,p}} \bar{\zeta}^t d\lambda_{LY}^\sigma \mathbf{g}^{LY} \right. \\ \left. + \frac{\partial X^{LY}}{\partial \varepsilon_v^{T,p}} Q dT \right) = 0 \end{array} \right. \quad (3.74)$$

If the two plastic mechanisms are activated simultaneously, the two consistency conditions must be jointly satisfied so that the consistency condition given by Eq. (3.65) has to be rewritten into a more general form:

$$d\mathbf{F} = \left(\frac{\partial \mathbf{F}}{\partial \bar{\boldsymbol{\sigma}}} \right)^t : d\bar{\boldsymbol{\sigma}} - \mathbf{H} d\boldsymbol{\lambda}^\sigma - \mathbf{B} dT = 0 \quad (3.75)$$

$$d\mathbf{F} = \begin{pmatrix} dF^{TY} \\ dF^{LY} \end{pmatrix} \quad (3.76)$$

where $d\boldsymbol{\lambda}^\sigma = \begin{pmatrix} d\lambda_{TY}^\sigma \\ d\lambda_{LY}^\sigma \end{pmatrix}$,

$$\frac{\partial \mathbf{F}}{\partial \bar{\boldsymbol{\sigma}}} = \begin{pmatrix} \frac{\partial F^{TY}}{\partial \sigma_1} & \frac{\partial F^{TY}}{\partial \sigma_2} & \frac{\partial F^{TY}}{\partial \sigma_3} & \frac{\partial F^{TY}}{\partial T} \\ \frac{\partial F^{LY}}{\partial \sigma_1} & \frac{\partial F^{LY}}{\partial \sigma_2} & \frac{\partial F^{LY}}{\partial \sigma_3} & \frac{\partial F^{LY}}{\partial T} \end{pmatrix}^t$$

$$\mathbf{H} = \begin{bmatrix} -\frac{\partial F^{TY}}{\partial X^{TY}} \frac{\partial X^{TY}}{\partial \varepsilon_v^{\sigma,p}} \bar{\boldsymbol{\zeta}}^t g^{TY} & 0 \\ -\frac{\partial F^{LY}}{\partial X^{LY}} \frac{\partial X^{LY}}{\partial \varepsilon_v^{\sigma,p}} \bar{\boldsymbol{\zeta}}^t g^{TY} & -\frac{\partial F^{LY}}{\partial X^{LY}} \frac{\partial X^{LY}}{\partial \varepsilon_v^{\sigma,p}} \bar{\boldsymbol{\zeta}}^t g^{LY} \end{bmatrix},$$

and $\mathbf{B} = \begin{bmatrix} -\frac{\partial F^{TY}}{\partial X^{TY}} \frac{\partial X^{TY}}{\partial \varepsilon_v^{T,p}} Q \\ -\frac{\partial F^{LY}}{\partial X^{LY}} \frac{\partial X^{LY}}{\partial \varepsilon_v^{T,p}} Q - \frac{\partial F^{LY}}{\partial X^{LY}} \frac{\partial X^{LY}}{\partial \varepsilon_v^{TY}} Q \end{bmatrix}.$

The stress increment can be expressed as:

$$d\bar{\boldsymbol{\sigma}} = \bar{\mathbf{D}}^{e*} (d\boldsymbol{\varepsilon} - \bar{\mathbf{g}} d\boldsymbol{\lambda}^\sigma - \frac{2}{3} \bar{\boldsymbol{\zeta}} Q dT) \quad (3.77)$$

where $\bar{\mathbf{g}} = (\mathbf{g}^{TY}, \mathbf{g}^{LY})$.

This system of equations provides the value of the two plastic multipliers, $d\lambda_{TY}^\sigma$ and $d\lambda_{LY}^\sigma$. When both values are positive, the two mechanisms are activated simultaneously. However, one of them may appear to be negative. This means that the corresponding mechanism is finally not activated and the plastic multiplier has to be set to zero. In such a case, the other plastic mechanism is the only active mechanism.

3.3.3 Explicit stress integration of the TM model

3.3.3.1 Mixed control

The integration at the Gauss point level of the stress-strains equations of the constitutive model presented above is now described. The mechanical stress variation $\Delta\boldsymbol{\sigma}$ due to the prescribed values of total strain $\Delta\boldsymbol{\varepsilon}$ and temperature ΔT variations has to be computed. This is performed in this study by using an explicit scheme that includes an adaptive sub-stepping procedure in order to maintain numerical errors within a given tolerance.

When considering the newly defined strain increment $\Delta\bar{\boldsymbol{\varepsilon}} = (\Delta\boldsymbol{\varepsilon}, \Delta\varepsilon_v^T)^t$, component $\Delta\varepsilon_v^T$ appears as an unknown since it is the temperature induced increment. A mixed

stress-strain (in the generalized sense) controlled procedure is thus required in the stress integration algorithm.

The elastic part $\Delta\varepsilon_v^{T,e}$ can be calculated from Eq. (3.53) and the plastic part $\Delta\varepsilon_v^{T,p}$ generated during a thermal plastic loading can be obtained from Eq. (3.62). For any mechanism, it comes:

$$\begin{aligned}\Delta\varepsilon_v^T &= \Delta\varepsilon_v^{T,e} + \Delta\varepsilon_v^{T,p} \\ &= (Q - \alpha_d)\Delta T\end{aligned}\tag{3.78}$$

If the two plastic mechanisms are activated simultaneously, the total thermal volumetric strain $\Delta\varepsilon_v^T$ is computed from:

$$\Delta\varepsilon_v^T = (2Q - \alpha_d)\Delta T\tag{3.79}$$

3.3.3.2 Elastic trial and yield surface intersection

In a first stage, the total generalized strain increment is assumed to be purely elastic. Under this assumption, the temperature induced strain component $\Delta\varepsilon_v^T$ can be simply determined from the imposed temperature increment ΔT and writes $\Delta\varepsilon_v^T = -\alpha_d\Delta T$.

Given a strain increment $\Delta\bar{\varepsilon}_n$ imposed at the beginning of step n , an elastic trial stress increment can be calculated from:

$$\Delta\bar{\sigma}_n^{tr} = \bar{D}^{e*}\Delta\bar{\varepsilon}_n\tag{3.80}$$

The elastic law adopted here is derived from the MCC model and the tangent elastic moduli are those given in Eq. (3.38). Many techniques have been proposed to properly address such elastic non-linearity. Following [13, 75], the secant elastic stiffness matrix is employed. The elastic stiffness matrix can be obtained once the secant elastic moduli \bar{K} and \bar{G} are calculated using the following equations:

$$\begin{aligned}\bar{K} &= \frac{\Delta p'}{\Delta\varepsilon_v^{p,e}} = \frac{p'_0 \exp(v_0 \Delta\varepsilon_v^{p,e} / \kappa)}{\Delta\varepsilon_v^{p,e}} \\ \bar{G} &= \frac{3(1 - 2\nu)\bar{K}}{2(1 + \nu)}\end{aligned}\tag{3.81}$$

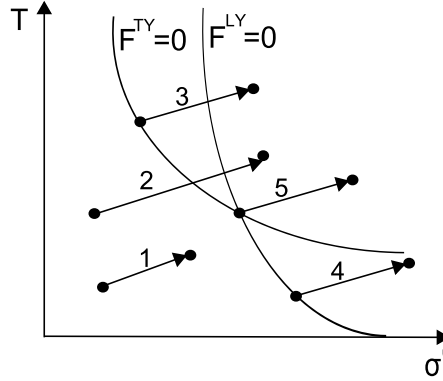


Figure 3.16: Different possibilities of activation of the plastic mechanisms during the elastic trial.

where $\Delta\varepsilon_v^{p,e}$ is the mechanical elastic volumetric strain, p'_0 is the mean effective stress corresponding to the start of $\Delta\varepsilon_v^{p,e}$, v_0 is the initial specific volume, κ is the slope of the unload-reload line in the $v - \ln p'$ plane and ν is Poisson's ratio. The elastic trial stress at step n then reads:

$$\bar{\sigma}_{n+1}^{tr} = \bar{\sigma}_n + \bar{D}^{e*}(\bar{K}, \bar{G}, \alpha_d) \Delta \bar{\varepsilon}_n \quad (3.82)$$

where $\bar{\sigma}_n$ is the stress state at the beginning of the n^{th} step.

Plastically active yield surfaces will be searched for within the set of admissible yield surfaces by checking the following condition:

$$F^Y(\bar{\sigma}_{n+1}^{tr}, X_n^Y) \geq 0 \quad (3.83)$$

where X_n^Y is the hardening variable obtained at the end of the previous step.

The stress state obtained through the elastic trial will be located on the yield surface if the following condition is met (FTOL being a fixed tolerance):

$$\left| F^Y(\bar{\sigma}_{n+1}^{tr}, X_n^Y) \right| \leq FTOL \quad (3.84)$$

In the present model, because of the co-existence of two yield surfaces, the following situations may be encountered depending on the values of $F_0^Y = F^Y(\bar{\sigma}_n, X_n^Y)$ and $F_1^Y =$

$F^Y(\bar{\sigma}_{n+1}^{tr}, X_n^Y)$ respectively obtained from the yield criteria before and after the application of the elastic trial (see Figure 3.16):

1. If $F_1^Y \leq FTOL$, the current loading increment is purely elastic and the final stress can be set to the elastic trial stress.
2. If $F_0^{TY} < -FTOL$, $F_1^{TY} > FTOL$ and $F_1^{LY} \leq FTOL$, the stress path starts from the elastic region and reaches TY;
If $F_0^{LY} < -FTOL$, $F_1^{LY} > FTOL$ and $F_1^{TY} \leq FTOL$, the stress path starts from the elastic region and reaches LY;
If $F_0^{TY} < -FTOL$, $F_1^{TY} > FTOL$ and $F_0^{LY} < -FTOL$, $F_1^{LY} > FTOL$, the stress path starts from the elastic region and reaches both TY and LY;
3. If $|F_0^{TY}| \leq FTOL$, $F_1^{TY} > FTOL$ and $F_0^{LY} < -FTOL$, TY is active from the end of the previous increment.
4. If $|F_0^{LY}| \leq FTOL$, $F_1^{LY} > FTOL$ and $F_0^{TY} < -FTOL$, LY is active from the end of the previous increment.
5. If $|F_0^Y| \leq FTOL$, $F_1^Y > FTOL$, both TY and LY yield surfaces are activated from the end of the previous increment.

When the current loading increment leads to a plastic state starting from a purely elastic state ($F_0^Y < -FTOL$ and $F_1^Y > FTOL$), the intersection of the stress path and the yield surface(s) should be determined. Assuming that the elastic fraction of the total strain increment is $x\Delta\bar{\epsilon}$ (with $0 < x < 1$), the transition point lying on the yield surface satisfies the following equation:

$$F_x^Y = F^Y(\bar{\sigma}_n + x\bar{D}^{e*} \Delta\bar{\epsilon}, X_n^Y) = 0 \quad (3.85)$$

Eq. (3.85) defines a non-linear equation in x that can be solved using several mathematical algorithms such as the basic dichotomy algorithm or the more advanced Newton-Raphson method. Here, following Sloan *et al.* [75], the Pegasus method is used for its good convergence properties and its efficiency.

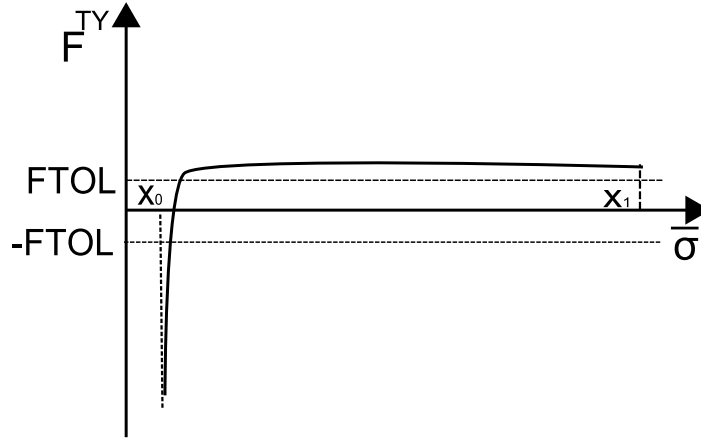


Figure 3.17: A special situation for TY surface intersection.

The resolution is initiated by giving an initial range x_0 and x_1 bracketing the target value of x . The convergence rate is to a certain extent depending on the starting points x_0 and x_1 . A faster convergence rate can be achieved if the starting range is close to the desired root of Eq. (3.85) [9]. Sometimes the convergence rate of Pegasus method may be very slow. This is the case for the TY function in this study since a non-strategic choice of the initial search range $[x_0, x_1]$ can lead to $F_{x=1}^{TY} \gg F_{x=0}^{TY}$. This situation, illustrated in Figure 3.17, requires a particular treatment to achieve reasonable convergence properties of the resolution algorithm.

Better initial values of x_0 and x_1 have to be found to reduce the initial length of the search interval, thereby reducing the number of steps required for the convergence of the Pegasus method. Here a simple method to obtain good initial values of x_0 and x_1 that will finally be used in the Pegasus method is proposed:

1. Enter with initial values $x_0 = 0$, $x_1 = 1$, initial stress $\bar{\sigma}_n$, initial hardening variables X_n^Y , total strain increment $\Delta\bar{\epsilon}$ and temperature increment ΔT .
2. Set the strain component $\Delta\varepsilon_v^T = -\alpha_d\Delta T$ (the strain increment $\Delta\bar{\epsilon}$ is then fully determined).
3. Repeat steps 4-5:
4. Calculate: $F_1^Y = F^Y(\bar{\sigma}_n + x_1\bar{D}^{e*}\Delta\bar{\epsilon}, X_n^Y)$.

5. IF $F_1^Y > FTOL$, set $x_{save} = x_1$, $x_1 = 0.9x_1$ and go to step (4).

ELSEIF $F_1^Y < -FTOL$, exit with $x_0 = x_1$, $x_1 = x_{save}$.

ELSE, exit with $x_0 = x_1$, $x_1 = x_1$.

Several iterations are needed for this algorithm to achieve a satisfactory estimate of the input range for the Pegasus method. This improvement makes the overall calculation more efficient and robust if difficulties are encountered with the Pegasus algorithm when initialised classically (that is with $x_0 = 0$, $x_1 = 1$).

When the convergence of Pegasus algorithm is achieved, the strain increment of length $x\Delta\bar{\epsilon}$ is purely elastic and the stress $\bar{\sigma}_n + x\bar{D}^{e*}\Delta\bar{\epsilon}$ corresponds to the intersection of the stress path with the yield stress. Since it corresponds to the end of a purely elastic part, this point is fully determined and can be saved with no further calculations. This last point can now be considered as the starting point of a purely plastic loading.

If the trial stress path switches from an elastic state to a plastic state intersecting either TY or LY, the fraction x of the loading increment (denoted either x^{TY} or x^{LY}) moving the stress state $\bar{\sigma}_n$ to $\bar{\sigma}_{n+1}$ onto TY or LY respectively will be computed according to Eq. (3.85) with the corresponding yield surface. But if the trial stress path intersects both TY and LY, both x^{TY} and x^{LY} will be computed. Depending on the previous position of both yield surfaces and on the followed stress path, x^{TY} and x^{LY} values could be different. In such a case, the smaller value will be adopted and the corresponding fraction of the loading increment will move the stress point onto a single surface. Otherwise, if both x^{TY} and x^{LY} are equal, the stress point will finally be located at the intersection of both surfaces.

3.3.3.3 Plastic loading

If $|F_0^Y| \leq FTOL$ and $F_1^Y > FTOL$, a plastic loading is applied and the consistency condition is used to ensure that the stress point remains on the surface and moves with it. Following [75], a modified Euler scheme with an adaptive sub-stepping procedure is used to control that the error made on the stresses and hardening variables fall within a given tolerance. If the stress state at the end of the increment lies outside the updated yield

surface, a correction of this apparent drift is also required to bring the stress point back to the yield surface.

The following algorithm, although presented when a unique yield surface is active, is also valid in the case of simultaneous activations of TY and LY. Some technical adaptations of this algorithm are however required to face the different situations presented in Figure 3.16 and are presented hereafter.

3.3.3.3.1 Modified Euler scheme For conventional mechanical constitutive models, explicit stress integration with sub-stepping are generally calculated through the use of a modified Euler scheme or more general Runge-Kutta developments. Here, a modified Euler scheme is used.

Following the adaptive time stepping scheme proposed by Sloan and his co-workers [75], a pseudo-time t is introduced. Actually, only increments of this pseudo-time are sufficient: $0 \leq \Delta t \leq 1$ correspond to a given loading increment (from step n to step $n + 1$). $\Delta t = 0$ corresponds to the start of the loading increment where the initial conditions are known (step n). $\Delta t = 1$ corresponds to the end of the current loading increment (step $n + 1$). As it will be seen later, this overall time increment will then be divided into smaller sub-increments in order to maintain the numerical error on stress and hardening variables within a given tolerance.

In the following, the increments of total strain and temperature are sub-divided. In the $(k)^{th}$ sub-step, Δt_k is the pseudo-time sub-increment and the generalized strains $\Delta \bar{\epsilon}_k = (\Delta \epsilon_k, \Delta \epsilon_{vk}^T)^t$ is given by:

$$\begin{aligned} \Delta T_k &= \Delta t_k \Delta T \\ \Delta \epsilon_k &= \Delta t_k \Delta \epsilon \end{aligned} \tag{3.86}$$

and from Eq. (3.78):

$$\Delta \epsilon_{vk}^T = (Q - \alpha_d) \Delta t_k \Delta T \tag{3.87}$$

where ΔT and $\Delta \epsilon$ are the prescribed increments.

The Euler method is applied and the stress as well as the hardening variables at the

end of the $(k)^{th}$ sub-step read as:

$$\begin{aligned}\bar{\sigma}_{(k+1)1} &= \bar{\sigma}_k + \bar{\mathbf{D}}_{ep}(\bar{\sigma}_k, X_k^Y) \Delta \bar{\epsilon}_k \\ X_{(k+1)1}^Y &= X_k^Y + \bar{\mathbf{R}}_{ep}(\bar{\sigma}_k, X_k^Y) \Delta \bar{\epsilon}_k\end{aligned}\tag{3.88}$$

A modified Euler method which is more accurate is used and the stress increment as well as the hardening variable at the end of the $(k)^{th}$ sub-step read as:

$$\begin{aligned}\bar{\sigma}_{k+1} &= \bar{\sigma}_k + \frac{1}{2} \left[\bar{\mathbf{D}}_{ep}(\bar{\sigma}_k, X_k^Y) + \bar{\mathbf{D}}_{ep}(\bar{\sigma}_{(k+1)1}, X_{(k+1)1}^Y) \right] \Delta \bar{\epsilon}_k \\ X_{k+1}^Y &= X_k^Y + \frac{1}{2} \left[\bar{\mathbf{R}}_{ep}(\bar{\sigma}_k, X_k^Y) + \bar{\mathbf{R}}_{ep}(\bar{\sigma}_{(k+1)1}, X_{(k+1)1}^Y) \right] \Delta \bar{\epsilon}_k\end{aligned}\tag{3.89}$$

An appropriate size for each sub-step is found by comparing the first and second order Runge-Kutta developments as described earlier (see Eqs. (3.88) and (3.89)). This comparison leads to the definition of a numerical error measure R evaluated as:

$$R = \max \left\{ \frac{X_{k+1}^Y - X_{(k+1)1}^Y}{X_{k+1}^Y}, \frac{|\bar{\sigma}_{k+1} - \bar{\sigma}_{(k+1)1}|}{|\bar{\sigma}_{k+1}|} \right\}\tag{3.90}$$

This error measure R is compared to a given tolerance $STOL$ and the current step is accepted if $R \leq STOL$, and rejected otherwise. In this latter case, a smaller sub-step size is computed and the procedure is repeated until a successful sub-increment size is obtained. The size of the sub-increment following an accepted sub-increment can be estimated from the value of R :

$$r = 0.9 \sqrt{STOL/R}\tag{3.91}$$

$$\Delta t_{k+1} = r \Delta t_k\tag{3.92}$$

where r is a factor used to adapt the size of the following sub-increment to the actual error measure R . The safety factor of 0.9 is introduced in order to increase the probability of accepting the next sub-step.

In order to prevent an abrupt change in the sub-step size, r is constrained as follows:

$$0.1 \leq r \leq 1.1 \quad (3.93)$$

Finally, a minimum sub-step size Δt_{\min} is introduced and imposes a maximum number of sub-steps permitted during a given loading increment. A maximum sub-step size is also imposed to prevent the step size from growing immediately after a failed sub-increment. It is worth noting that a maximum number of rejected sub-steps is introduced in order to avoid infinite loops. In such a case, the overall calculation is stopped.

In case 5 (see Fig. 3.16), the corner is reached and the actual number of active plastic mechanisms must be determined from the values of $d\lambda_1^\sigma$ and $d\lambda_2^\sigma$ obtained from Eq. (3.74). If both values are positive, the two plastic mechanisms are indeed activated. Alternatively, if one of them is negative, the corresponding yield surface is not active. In this latter case, a single plastic mechanism (TY or LY) is active and either case 3 or 4 is recovered.

In case 3, TY is active and the incremental unknowns are calculated using the algorithm described above and considering TY plastic mechanism only. Therefore, the stress point at the end of each sub-increment should be checked to ensure its position lies on or inside LY.

Because of the coupling between TY and LY mechanisms presented previously, the activation of TY produces a shift of LY. At sub-step (k), the hardening of LY can be obtained from:

$$X_{k+1}^{LY} = X_k^{LY} + \frac{1}{2}(\Delta X_{k1}^{LY} + \Delta X_{k2}^{LY}) \quad (3.94)$$

where

$$\begin{aligned} \Delta X_{k1}^{LY} &= \overline{\mathbf{R}}_{LY}^{ep}(\overline{\boldsymbol{\sigma}}_k, X_k^{LY})\Delta\overline{\boldsymbol{\varepsilon}}_k \\ \Delta X_{k2}^{LY} &= \overline{\mathbf{R}}_{LY}^{ep}(\overline{\boldsymbol{\sigma}}_k + \Delta\overline{\boldsymbol{\sigma}}_{k1}, X_k^{LY} + \Delta X_{k1}^{LY})\Delta\overline{\boldsymbol{\varepsilon}}_k \end{aligned} \quad (3.95)$$

The stress state can be determined from the value of $F^{LY} = F^{LY}(\overline{\boldsymbol{\sigma}}_{k+1}, X_{k+1}^{LY})$. If $F^{LY} \leq FTOL$, the current loading increment is always on TY and its plastic mechanism is applied, otherwise if $F^{LY} > FTOL$, the stress point B lies outside of LY (see Fig. 3.18)

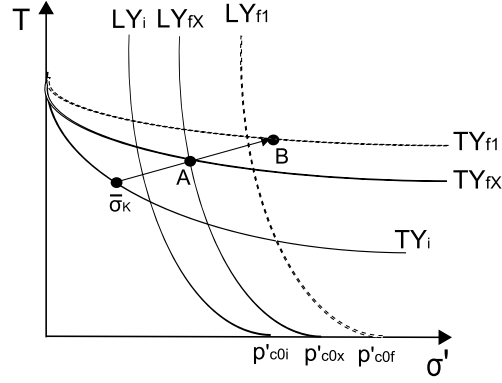


Figure 3.18: TY and LY intersection.

and then the previous sub-increment will be abandoned. The strain increment needs to be reduced to $x\Delta\bar{\epsilon}_k$ ($0 < x < 1$) corresponding to the intersection of TY and LY (point A).

The stress point located at the intersection of TY and LY satisfies the following equation:

$$F^{LY}(\bar{\sigma}_k + \frac{1}{2}(\Delta\bar{\sigma}_{kx1} + \Delta\bar{\sigma}_{kx2}), X_k^{LY} + \frac{1}{2}(\Delta X_{kx1}^{LY} + \Delta X_{kx2}^{LY})) = 0 \quad (3.96)$$

where

$$\begin{aligned} \Delta\bar{\sigma}_{kx1} &= x\Delta\bar{\sigma}_{k1} \\ \Delta X_{kx1}^{TY} &= x\Delta X_{k1}^{TY} \\ \Delta X_{kx1}^{LY} &= x\Delta X_{k1}^{LY} \end{aligned} \quad (3.97)$$

and

$$\begin{aligned} \Delta\bar{\sigma}_{kx2} &= xD_{TY}^{ep}(\bar{\sigma}_k + \Delta\bar{\sigma}_{kx1}, X_k^{TY} + \Delta X_{kx1}^{TY})\Delta\bar{\epsilon}_k \\ \Delta X_{kx2}^{LY} &= xR_{LY}^{ep}(\bar{\sigma}_k + \Delta\bar{\sigma}_{kx1}, X_k^{LY} + \Delta X_{kx1}^{LY})\Delta\bar{\epsilon}_k \end{aligned} \quad (3.98)$$

As described earlier, Eq. (3.96) defines a non-linear equation in x that can be solved by the Pegasus method. The stress point corresponding to the intersection of TY and LY can thus be fully determined.

For case 4, a similar algorithm can be applied but this time no coupling between the plastic mechanisms has to be considered since hardening of TY surface is independent of hardening of LY surface.

3.3.3.4 Drift correction scheme

During plastic loadings, the stress state should satisfy the yield criterion within a fixed tolerance at the end of each sub-increment. However, when using explicit integration schemes, the stress state at the end of any sub-step $(\bar{\sigma}_*, X_*^Y)$ may not strictly fulfil the yield criterion and a drift of the converged stress point from the yield surface may be observed. In this case, a drift correction procedure is required.

Ignoring the second order (and above) terms, a Taylor series expansion of F^Y around the final stress point $(\bar{\sigma}_*, X_*^Y)$ reads:

$$F_*^Y + \left(\frac{\partial F^Y}{\partial \bar{\sigma}} \right)^t : \delta \bar{\sigma} + \left\{ \frac{\partial F^Y}{\partial X^Y} \right\} \delta X^Y = 0 \quad (3.99)$$

where F_*^Y , $\left(\frac{\partial F^Y}{\partial \bar{\sigma}} \right)^t$ and $\left\{ \frac{\partial F^Y}{\partial X^Y} \right\}$ are determined at the final stress point $(\bar{\sigma}_*, X_*^Y)$, $\delta \bar{\sigma}$ is the stress correction, δX is the hardening variable correction.

Since the increment of total strain and temperature are the control variables in the present resolution algorithm, their increments cannot be corrected and must remain unchanged while correcting the stress and the hardening variables. The following conditions can be given:

$$\begin{cases} \delta T = 0 \\ \delta \boldsymbol{\varepsilon} = \delta \boldsymbol{\varepsilon}^{\sigma,e} + \delta \boldsymbol{\varepsilon}^{\sigma,p} + \delta \boldsymbol{\varepsilon}^{T,e} + \delta \boldsymbol{\varepsilon}^{T,p} = \mathbf{0} \end{cases} \quad (3.100)$$

which can be simplified to:

$$\delta \boldsymbol{\varepsilon}^{\sigma,e} + \delta \boldsymbol{\varepsilon}^{\sigma,p} = \mathbf{0} \quad (3.101)$$

This implies that the elastic strain correction due to the mechanical stress is balanced by an equal but opposite plastic strain. Combining Eqs. (3.51) and (3.101) gives the correction of the stress state:

$$\delta \bar{\sigma} = \bar{\mathbf{D}} \delta \bar{\boldsymbol{\varepsilon}}^{\sigma,e} = -\delta \lambda_Y^\sigma \bar{\mathbf{D}} \frac{\partial G^Y}{\partial \bar{\sigma}} \quad (3.102)$$

where $\delta\lambda^\sigma$ is the plastic multiplier. Using the definition of h given previously (see Eq. (3.65)):

$$\frac{\partial F^Y}{\partial X^Y} \delta X^Y = -\delta\lambda_Y^\sigma h \quad (3.103)$$

as well as the stress correction given by Eq. (3.102), Eq. (3.99) allows the plastic multiplier to be determined:

$$\delta\lambda_Y^\sigma = \frac{F_*^Y}{\left(\frac{\partial F^Y}{\partial \bar{\sigma}}\right)^t \bar{D} \frac{\partial G^Y}{\partial \bar{\sigma}} + h} \quad (3.104)$$

When two plastic mechanisms are activated simultaneously, the stress correction is given by:

$$\delta \bar{\sigma} = -\bar{D} \left(\delta\lambda_{TY}^\sigma \frac{\partial G^{TY}}{\partial \bar{\sigma}} + \delta\lambda_{LY}^\sigma \frac{\partial G^{LY}}{\partial \bar{\sigma}} \right) \quad (3.105)$$

The two plastic multipliers $\delta\lambda_{TY}^\sigma$ and $\delta\lambda_{LY}^\sigma$ can be obtained by the resolution of the following equations:

$$\left\{ \begin{array}{l} F_*^{TY} - \left(\frac{\partial F^{TY}}{\partial \bar{\sigma}}\right)^t \bar{D} \left(\delta\lambda_{TY}^\sigma \frac{\partial G^{TY}}{\partial \bar{\sigma}} + \delta\lambda_{LY}^\sigma \frac{\partial G^{LY}}{\partial \bar{\sigma}} \right) \\ + \frac{\partial F^{TY}}{\partial X^{TY}} \frac{\partial X^{TY}}{\partial \varepsilon_{vTY}^{\sigma,p}} \bar{\zeta}^t \delta\lambda_{TY}^\sigma \frac{\partial G^{TY}}{\partial \bar{\sigma}} = 0 \\ \\ F_*^{LY} - \left(\frac{\partial F^{LY}}{\partial \bar{\sigma}}\right)^t \bar{D} \left(\delta\lambda_{TY}^\sigma \frac{\partial G^{TY}}{\partial \bar{\sigma}} + \delta\lambda_{LY}^\sigma \frac{\partial G^{LY}}{\partial \bar{\sigma}} \right) \\ + \frac{\partial F^{LY}}{\partial X^{LY}} \left(\frac{\partial X^{TY}}{\partial \varepsilon_{vTY}^{\sigma,p}} \bar{\zeta}^t \delta\lambda_{TY}^\sigma \frac{\partial G^{TY}}{\partial \bar{\sigma}} + \frac{\partial X^{LY}}{\partial \varepsilon_{vLY}^{\sigma,p}} \bar{\zeta}^t \delta\lambda_{LY}^\sigma \frac{\partial G^{LY}}{\partial \bar{\sigma}} \right) = 0 \end{array} \right. \quad (3.106)$$

The corrections of the elastic and plastic strain, stress and hardening variable δX^Y (standing for either $\delta\beta$ or $\delta p'_{c0}$) are thus computed from either Eq. (3.99) or Eq. (3.106). After this correction, the stress and hardening variable will be updated as follows:

$$\begin{aligned} \bar{\sigma} &= \bar{\sigma}_* + \delta \bar{\sigma} \\ X_*^Y &= X_*^Y + \delta X^Y \end{aligned} \quad (3.107)$$

The above algorithm will be repeatedly used until the new stress state is brought back to

the yield surface within a fixed tolerance.

The following algorithm summarises the explicit integration of the TM model using a modified Euler scheme:

1. At step n , from initial stress $\bar{\sigma}_n$, enter with initial hardening variables X_n (both β_n and $p'_{c0(n)}$), the total strain increment $\Delta\epsilon$, the temperature increment ΔT , the yield surface tolerance FTOL, and the stress integration tolerance STOL.
2. Compute the strain component $\Delta\epsilon_v^T = -\alpha_d\Delta T$; the strain increment $\Delta\bar{\epsilon}$ is deducted.
3. Compute the trial elastic stress increment $\Delta\bar{\sigma}_e^{tr}$ and the trial elastic stress state $\bar{\sigma}_{n+1}^{tr}$ according to:

$$\begin{aligned}\Delta\bar{\sigma}_e^{tr} &= \bar{D}^{e*}(\bar{K}, \bar{G}, \alpha_d)\Delta\bar{\epsilon} \\ \bar{\sigma}_{n+1}^{tr} &= \bar{\sigma}_n + \bar{D}^{e*}(\bar{K}, \bar{G}, \alpha_d)\Delta\bar{\epsilon}\end{aligned}$$

4. Calculate $F_0^{TY} = F^{TY}(\bar{\sigma}_n, \beta_n)$ and $F_1^{TY} = F^{TY}(\bar{\sigma}_{n+1}^{tr}, \beta_n)$;
 $F_0^{LY} = F^{LY}(\bar{\sigma}_n, p'_{c0(n)})$ and $F_1^{LY} = F^{LY}(\bar{\sigma}_{n+1}^{tr}, p'_{c0(n)})$.

5. *Purely elastic case*

IF $F_1^{TY} \leq FTOL$ AND $F_1^{LY} \leq FTOL$, then the stress increment is purely elastic:
 set $\bar{\sigma}_{n+1} = \bar{\sigma}_{n+1}^{tr}$, $\beta_n = \beta_{n+1}$, $p'_{c0(n)} = p'_{c0(n+1)}$ and go to step 19.

6. *Determine yield surface(s) intersection(s)*

IF $F_0^{TY} < -FTOL$, $F_1^{TY} > FTOL$ AND $F_1^{LY} \leq FTOL$;

OR $F_0^{LY} < -FTOL$, $F_1^{LY} > FTOL$ AND $F_1^{TY} \leq FTOL$;

OR $F_0^{TY} < -FTOL$, $F_1^{TY} > FTOL$ AND $F_0^{LY} < -FTOL$, $F_1^{LY} > FTOL$;

then the stress path undergoes a transition from elastic to plastic behavior. Compute the portion x of $\Delta\bar{\epsilon}$ that corresponds to purely elastic deformation using the intersection scheme presented earlier.

7. Update the stress at the onset of plastic yielding as $\bar{\sigma}_{n+1} = \bar{\sigma}_n + x\bar{D}^{e*}\Delta\bar{\epsilon}$. Update the input strain increment to the remaining portion (purely plastic) of the strain increment $\Delta\bar{\epsilon}_{n+1} = (1-x)\Delta\bar{\epsilon}$. Go to step 19.

8. *Plastic cases*

IF $|F_0^{TY}| \leq FTOL$, $F_1^{TY} > FTOL$ AND $F_0^{LY} < -FTOL$, TY is active;

IF $|F_0^{LY}| \leq FTOL$, $F_1^{LY} > FTOL$ AND $F_0^{TY} < -FTOL$, LY is active;

IF $|F_0^{TY}| \leq FTOL$, $F_1^{TY} > FTOL$ AND $|F_0^{LY}| \leq FTOL$, $F_1^{LY} > FTOL$, the intersection point of TY and LY is reached and the actual number of active plastic mechanisms should be determined by Eq. (3.75).

In this case, the increment is entirely plastic and three different possible plastic regimes are involved: TY mechanism is active (IYIELD=1); LY mechanism is active (IYIELD=2); both TY and LY mechanisms are active (IYIELD=3).

9. Modified Euler scheme with sub-stepping

The active plastic mechanism(s) is(are) applied. Set an initial pseudo-time $t = 0$ and pseudo-time increment $\Delta t = 1$.

10. WHILE $t < 1$, repeat steps 10–18.

At the k^{th} sub-step, set the strain component $\Delta \bar{\boldsymbol{\varepsilon}}_k = (\Delta t_k \Delta \boldsymbol{\varepsilon}, -\alpha_d \Delta t_k \Delta T + \Delta t_k \bar{Q} \Delta T)^t$.

Compute $\Delta \bar{\boldsymbol{\sigma}}_{k1}$, X_{k1}^Y using:

$$\begin{aligned}\Delta \bar{\boldsymbol{\sigma}}_{k1} &= \bar{\mathbf{D}}^{ep}(\bar{\boldsymbol{\sigma}}_k, X_k^Y) \Delta \bar{\boldsymbol{\varepsilon}}_k \\ \Delta X_{k1}^Y &= \bar{\mathbf{R}}^{ep}(\bar{\boldsymbol{\sigma}}_k, X_k^Y) \Delta \bar{\boldsymbol{\varepsilon}}_k\end{aligned}$$

Compute $\Delta \bar{\boldsymbol{\sigma}}_{k2}$, X_{k2}^Y using:

$$\begin{aligned}\Delta \bar{\boldsymbol{\sigma}}_{k2} &= \bar{\mathbf{D}}^{ep}(\bar{\boldsymbol{\sigma}}_{(k+1)1}, X_{(k+1)1}^Y) \Delta \bar{\boldsymbol{\varepsilon}}_k \\ \Delta X_{k2}^Y &= \bar{\mathbf{R}}^{ep}(\bar{\boldsymbol{\sigma}}_{(k+1)1}, X_{(k+1)1}^Y) \Delta \bar{\boldsymbol{\varepsilon}}_k\end{aligned}$$

where $\bar{\boldsymbol{\sigma}}_{(k+1)1} = \bar{\boldsymbol{\sigma}}_k + \Delta \bar{\boldsymbol{\sigma}}_{k1}$, $X_{(k+1)1}^Y = X_k^Y + \Delta X_{k1}^Y$.

11. Compute the new stress and hardening variable:

$$\begin{aligned}\bar{\boldsymbol{\sigma}}_{k+1} &= \bar{\boldsymbol{\sigma}}_k + \frac{1}{2}(\Delta \bar{\boldsymbol{\sigma}}_{k1} + \Delta \bar{\boldsymbol{\sigma}}_{k2}) \\ X_{k+1} &= X_k + \frac{1}{2}(\Delta X_{k1} + \Delta X_{k2})\end{aligned}$$

12. Determine the relative error for the current sub-step:

$$R = \frac{1}{2} \max \left\{ \frac{\Delta X_{k2}^Y - \Delta X_{k1}^Y}{X_{k+1}^Y}, \frac{|\Delta \bar{\sigma}_{k2} - \Delta \bar{\sigma}_{k1}|}{|\bar{\sigma}_{k+1}|} \right\}$$

13. Check if the current sub-step is accepted or rejected:

IF $R \leq STOL$, update the stress, hardening variables and the integration time:

$$\bar{\sigma}_{k+1} = \bar{\sigma}_{k+1}, X_{k+1}^Y = X_{k+1}^Y, t_{k+1} = t_k + \Delta t_k.$$

ELSE the sub-step is rejected and the size of this sub-step is reduced according to:

$$\Delta t_k = \max \{q\Delta t, \Delta t_{\min}\}.$$

where

$$r = \max \left\{ 0.9\sqrt{STOL/R}, 0.1 \right\}$$

Go to step 10.

14. Check whether the stress state lies outside the other yield surface

- IF IYIELD=1, then:

IF $F^{LY}(\bar{\sigma}_{k+1}, p'_{c0(k+1)}) \leq FTOL$, the sub-step is accepted;

ELSE the sub-step is rejected as it lies outside LY. Then compute the correct time step (Δt_k) that corresponds to the intersection point of TY and LY according to Eq. (3.96).

- IF IYIELD=2, then:

IF $F^{TY}(\bar{\sigma}_{k+1}, \beta_{(k+1)}) \leq FTOL$, the sub-step is accepted;

ELSE the sub-step is rejected as it lies outside TY. Then compute the correct time step (Δt_k) that corresponds to the intersection point of TY and LY according to Eq. (3.96).

15. Correct the stress state back to the yield surface

IF IYIELD=1 AND $|F^{TY}(\bar{\sigma}_{k+1}, \beta_{k+1})| > FTOL$, then correct $\bar{\sigma}_{k+1}$ and β_{k+1} to back

to TY according to Eqs. (3.99)–(3.107);

IF IYIELD=2 AND $\left|F^{LY}(\bar{\sigma}_{k+1}, p'_{c0(k+1)})\right| > FTOL$, then correct $\bar{\sigma}_{k+1}$ and $p'_{c0(k+1)}$ back to LY according to Eqs. (3.99)–(3.107);

IF IYIELD=3 AND $\left|F^{TY}(\bar{\sigma}_{k+1}, \beta_{k+1})\right| > FTOL$, $\left|F^{LY}(\bar{\sigma}_{k+1}, p'_{c0(k+1)})\right| > FTOL$, then correct $\bar{\sigma}_{k+1}$, β_{k+1} , $p'_{c0(k+1)}$ back to TY and LY according to Eqs. (3.99)–(3.107);

16. Extrapolate to obtain the size of the $(k+1)^{th}$ sub-step by computing

$$r = \min \left\{ 0.9\sqrt{STOL/R}, 1.1 \right\}$$

If the previous step failed, limit further the step size growth by enforcing

$$r = \min \{r, 1\}$$

The initial size for $(k+1)^{th}$ sub-step can be obtained from

$$\Delta t_{k+1} = r \Delta t_k$$

17. Ensure that the step size is not smaller than the minimum step size and that the integration pseudo-time will not be higher than one at the end of the next sub-step:

$$\Delta t_{k+1} = \max \{ \Delta t_{k+1}, \Delta t_{\min} \}$$

and then

$$\Delta t_{k+1} = \min \{ \Delta t_{k+1}, 1 - t_k \}$$

18. If a unique plastic mechanism is active (IYIELD=1 OR IYIELD=2) and the intersection point of TY and LY has been found ($\left|F^{TY}(\bar{\sigma}_{k+1}, \beta_{k+1})\right| \leq FTOL$ AND $\left|F^{LY}(\bar{\sigma}_{k+1}, p'_{c0(k+1)})\right| \leq FTOL$), or $t_{k+1} = 1$, exit with the final stress and hardening states $\bar{\sigma}_{n+1} = \bar{\sigma}_{k+1}$, $\beta_{n+1} = \beta_{k+1}$, $p'_{c0(n+1)} = p'_{c0(k+1)}$ at the end of the $(n)^{th}$ step.

19. Go to the $(n + 1)^{th}$ step.

3.3.4 Performance of the algorithm and TM model

The efficiency of the explicit stress integration scheme presented in the previous section and the performance of the implemented thermo-mechanical model are analysed in this section.

The results shown hereafter use the following numerical values: $FTOL = 10^{-7}$; $STOL = 10^{-4}$; $\Delta t_{\min} = 10^{-5}$.

3.3.4.1 Efficiency study of the proposed stress integration scheme

In this section, the efficiency of the stress integration scheme is studied in terms of computational time required to calculate with different errors the response of the soil during common experiments. All the results presented in this section are obtained with an Intel Pentium[®] 1400 MHz processor.

3.3.4.1.1 Mechanical loading path The first example deals with the numerical simulation of a drained triaxial compression performed at a constant temperature (higher than room temperature). For this purpose, the shear test of Path 3 (FF' in Fig. 3.21) is simulated with a target axial strain of 10%. All the calculations presented hereafter are obtained with the parameters given in Table (3.7).

A global quantifiable error function F_{error} is introduced in order to measure the overall difference between a given numerically predicted response and a reference data set. The error function used in this test is defined as follows:

$$F_{error} = \frac{\sum_{i=1}^n |\bar{\sigma}_{ref,i} - \bar{\sigma}_{c,i}|}{\sum_{i=1}^n |\bar{\sigma}_{ref,i}|} \quad (3.108)$$

where n is the number of data points, subscripts 'ref' and 'c' stand for reference result and a given computation result respectively. The reference loading path with n_f increments

Table 3.5: Euler method with a constant loading step scheme for triaxial test.

No. load increments	CPU time (s)	Total steps	Global error F_{error}
10	1.58	10	$6.70 \cdot 10^{-3}$
100	4.35	100	$5.80 \cdot 10^{-4}$
1000	27.40	1000	$5.30 \cdot 10^{-5}$
10 000	180.50	10 000	–

Table 3.6: Modified Euler method with a sub-stepping scheme for triaxial test.

No. load increments	STOL	CPU time (s)	Total steps	Global error F_{error}
10	10^{-1}	1.37	11	$1.20 \cdot 10^{-3}$
10	10^{-2}	1.59	25	$6.08 \cdot 10^{-4}$
10	10^{-3}	2.55	36	$9.02 \cdot 10^{-5}$
10	10^{-4}	3.15	106	$1.10 \cdot 10^{-5}$

will pass through all the strain points ($\bar{\epsilon}_{1(c,i)} = i\Delta\bar{\epsilon}_1/n_c, i = 1, 2 \dots n_c$) of the computation loading path with n_c increments. $\bar{\sigma}_{ref,i}$ and $\bar{\sigma}_{c,i}$ thus correspond to the same strain value $\bar{\epsilon}_{1(c,i)}$.

The reference data set are obtained using the modified Euler algorithm as presented before, using a very large number of loading increments of constant size (that is with no adaptive sub-stepping) and the drift correction. In this work, 10,000 equally-sized loading increments have been used for the reference calculation $\bar{\sigma}_{ref}$.

For the Euler method with a constant loading step, various numbers of equally sized load increments (10, 100, 1000 and 10,000) are used. The CPU time, total steps and F_{error} values obtained for these simulations are given in Table (3.5). It is observed as expected that the global stress error decreases as the number of load increments increases. The global stress error of this scheme is approximately a linear function of the step size.

To assess the performance of the Modified Euler scheme with an adaptive sub-stepping procedure, different local stress integration error tolerances (STOL) are adopted. It is recalled that this tolerance is used to adjust the size of sub-steps used for a given loading increment. The results are summarized in Table (3.6).

Decreasing STOL by three orders of magnitude, from 10^{-1} to 10^{-4} with a constant number of coarse loading increments (fixed to 10), reduces the global error (F_{error}) by two orders of magnitude from $1.20 \cdot 10^{-3}$ to $1.10 \cdot 10^{-5}$, showing the effects of STOL on the global error control. In all of the four runs, the number of total sub-steps is larger than the number of coarse loading increment, since sub-stepping is activated. Due to the generation of smaller sub-steps to satisfy a smaller STOL, the total number of sub-steps increases with decreasing STOL. In consequence, the global error decreases and the computation time increases. In other words, the accuracy is increased at the cost of computation time.

Efficiency evaluation of the algorithm is carried out by considering computation time and global error together. From the data presented in Tables (3.5) and (3.6), it appears clearly that the computation time increases significantly when the global error decreases for the constant load step scheme. The results obtained using the sub-stepping scheme also show an increase of the computation time but this increase is much lower even if the error is decreased by several orders of magnitude. The modified Euler method with a sub-stepping scheme thus shows a great advantage in the efficiency since it takes a much shorter computation time to achieve a similar accuracy in comparison with the constant load step scheme. This advantage is highlighted when a higher accuracy is required.

3.3.4.1.2 Thermal loading path The second example deals with a thermal loading performed at constant total stress. The simulated test corresponds to an experimental study on the thermo-mechanical behavior of Boom clay reported by Baldi *et al.* [7]. The efficiency of the algorithm is studied along one of the heating paths presented in Fig. 3.19: path C-C'. In the computation, the thermal loading path is simulated by imposing a total temperature increase of 73.5°C .

The error function used to evaluate the algorithm used along the heating process at constant total stress considered here has to be changed and is defined as follows:

$$F_{error} = \frac{\sum_{i=1}^n \left| \boldsymbol{\varepsilon}_{v(c,i)}^T - \boldsymbol{\varepsilon}_{v(ref,i)}^T \right|}{\sum_{i=1}^n \left| \boldsymbol{\varepsilon}_{v(ref,i)}^T \right|} \quad (3.109)$$

Table 3.7: Model parameters for Boom clay.

λ	κ	ν	p'_{c0} (MPa)	M	T_c (°C)	α_0 (1/°C)
0.052	0.017	0.4	7	0.7	2000	0.0039
α_1 (1/°C)	α_d (1/°C)	a (-)	k (-)	c_1 (-)	c_2 (1/°C)	
2.51×10^{-5}	5.1×10^{-5}	0.979	0.012	0.583	-0.019	

Table 3.8: Euler method with a constant loading step scheme for heating test.

No. load increments	CPU time (s)	Total steps	Global error F_{error}
10	0.44	10	$9.00 \cdot 10^{-2}$
100	1.84	100	$8.91 \cdot 10^{-3}$
1000	16.30	1000	$8.06 \cdot 10^{-4}$
10 000	174.07	10 000	–

where $\boldsymbol{\varepsilon}_{v(c,i)}^T$ and $\boldsymbol{\varepsilon}_{v(ref,i)}^T$ are the computed volumetric strain and the reference volumetric strain, respectively.

The performance of the Euler method with different numbers of equally sized load increments (10, 100, 1000 and 10 000) are summarized in Table (3.8) for the heating test case. As in the first treated example, 10 000 equally-sized loading increments have been used for the reference calculation. The trends in terms of calculation time and global error are similar to the ones observed previously.

The performance of the Modified Euler scheme with an adaptive sub-stepping procedure is summarized in Table (3.9). As in the previous example, varying STOL from 10^{-1} to 10^{-4} , while keeping coarse loading increments (10 increments where used), has a significant effect

Table 3.9: Modified Euler method with a sub-stepping scheme for heating test.

No. load increments	STOL	CPU time (s)	Total steps	Global error F_{error}
10	10^{-1}	0.45	14	$2.10 \cdot 10^{-3}$
10	10^{-2}	0.86	32	$4.91 \cdot 10^{-4}$
10	10^{-3}	1.69	87	$1.29 \cdot 10^{-4}$
10	10^{-4}	3.92	243	$2.82 \cdot 10^{-5}$

on the global error, which is reduced by two orders of magnitude. The CPU time is also increased significantly due to the increasing number of sub-steps required to achieve the imposed tolerance.

From data summarised in Tables (3.8) and (3.9), it appears that the modified Euler method with a sub-stepping scheme shows great advantages in terms of efficiency along heating paths. These advantages become prominent when a higher accuracy is required.

3.3.4.2 Evaluation of the constitutive model

The performance of TM model itself is now investigated. This is done by simulating several thermo-mechanical tests performed on Boom clay. In all the following simulations, a single set of parameters is used. Their values are reported in Table (3.7). The parameters coming directly from MCC model were calibrated using 2 triaxial shear tests at room temperature (see section 3.3.4.2.2) and the remaining parameters are given by Cui *et al.* [22] and have been calibrated along the isotropic thermo-mechanical loading path on Boom clay reported by Baldi *et al.* [7] (see section 3.3.4.2.1).

3.3.4.2.1 Isotropic thermo-mechanical loading The tests on Boom clay reported by Baldi *et al.* are now simulated using the TM model. The thermo-mechanical loading stages carried out in the experimental program are shown in Figure 3.19 and can be summarized as follows:

- The specimen was loaded and saturated at a mean effective stress of 2 MPa (point A), loaded up to an effective stress of 4 MPa (path A-B) and unloaded to 1 MPa at 21.5°C (path B-C).
- A heating-cooling cycle 21.5°C-95°C-21.5°C (path C-C'-C'') was applied with a constant mean effective stress of 1 MPa, which corresponds to an overconsolidation ratio of 6.
- Mechanical isotropic re-loading up to 3 MPa (path C-D) was applied and followed by the same heating-cooling cycle (path D-D'-D'') at a constant overconsolidation ratio

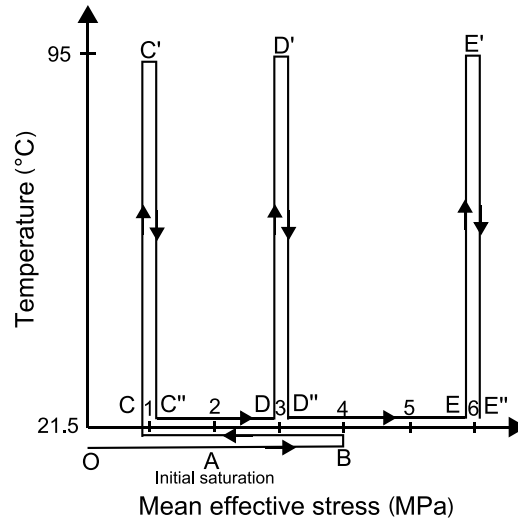


Figure 3.19: Isotropic thermo-mechanical paths.

of 2.

- Mechanical isotropic re-loading up to 6 MPa (path D-E) was applied and followed by the same heating-cooling cycle (path E-E'-E'') at a constant overconsolidation ratio of 1.

The volume change behavior of Boom clay in response to this loading path is simulated using the TM model. Figure 3.20 shows the experimental results and the numerical prediction. During the heating process (path C-C'), TY is activated and thermal elastoplastic volumetric strain is generated. During the subsequent cooling path (path C'-C''), thermal volumetric strain is then elastic back to point C. During the subsequent heating process (path D-D'), thermal elastic volumetric strain is elastic up to 22.1°C, and elastoplastic from 22.1°C to 95°C. During the third heating process (path E-E'), hardening takes place for both TY and LY at $T = 23.7^\circ\text{C}$. At this point, the loading path remains on TY according to Eq. (3.106), since hardening of TY is slower than hardening of LY. A good prediction of the soil behavior can be observed along this loading path involving both heating and cooling cycles at various overconsolidation ratios.

3.3.4.2.2 Triaxial shear tests after a thermal loading A qualitative validation of the proposed model was performed by Cui *et al.* [22] along the isotropic thermo-mechanical

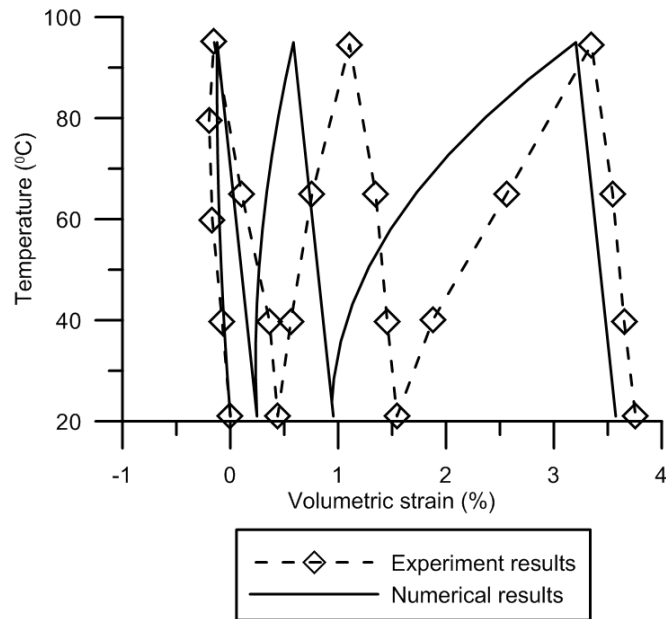


Figure 3.20: Comparison between experimental results ([7]) and numerical predictions for Boom clay.

loading paths on natural Boom Clay. Here, more quantitative validations are looked for and triaxial loading paths are considered. To this end, the calibrated model is used to predict the response of Boom clay along various triaxial loading paths at different temperatures.

A series of experiments on Boom clay has been carried out by Sultan [80] and the considered thermo-mechanical paths are presented in Figure 3.21. These paths may be summarized as follows:

- Path 1 (A-B-D-D'): Specimen 1 was isotropically loaded up to a mean effective stress of 9 MPa (A-B) and then unloaded to 5 MPa (OCR=1.8) (B-D) at room temperature (25°C). A standard drained triaxial compression test at 25°C was finally applied (D-D').
- Path 2 (A-B-C-C'): Specimen 2 was isotropically loaded up to a mean effective stress of 9 MPa (path A-B) and then unloaded to 7.1 MPa (OCR=1.25) (B-C) at room temperature (25°C). As for path 1, the sample was then sheared at room temperature (C-C').
- Path 3 (A-E-G-F-F'): Specimen 3 was subjected to an isotropic mechanical con-

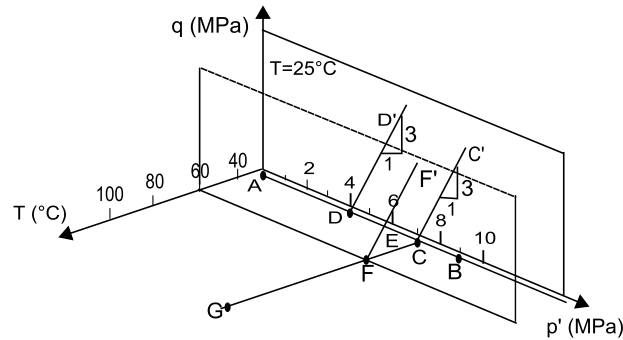


Figure 3.21: Thermo-mechanical loading paths in triaxial stress space.

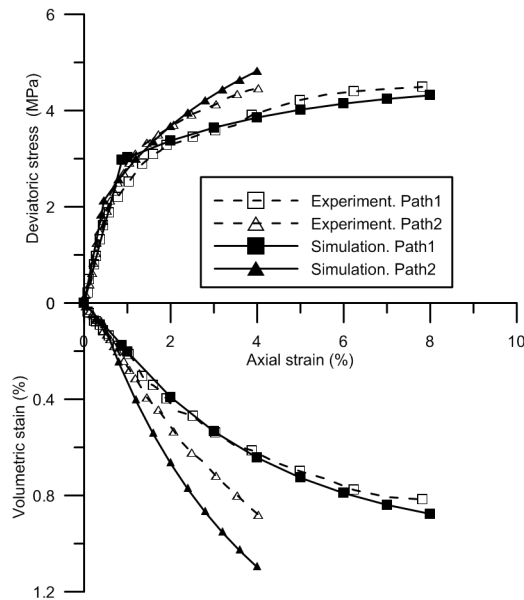


Figure 3.22: Drained triaxial compression tests on Boom Clay in Path 1 and 2 at 25°C.

solidation up to an effective stress of 7 MPa at room temperature (25°C) (A-E). A heating-cooling cycle 25°C-100°C-60°C was then applied before the specimen was sheared (C-G-F) at constant mean stress. Finally, a conventional triaxial compression was applied at 60°C (F-F').

The predictions of the triaxial shear tests at room temperature (paths 1 and 2) are shown in Figure 3.22. These predictions agree well with the experimental data except for the volumetric strain of Path 2, for which the simulation results in the plastic part are relatively inaccurate.

During Path 3, the sample is heated from 25°C to 100°C along C-G in the normal con-

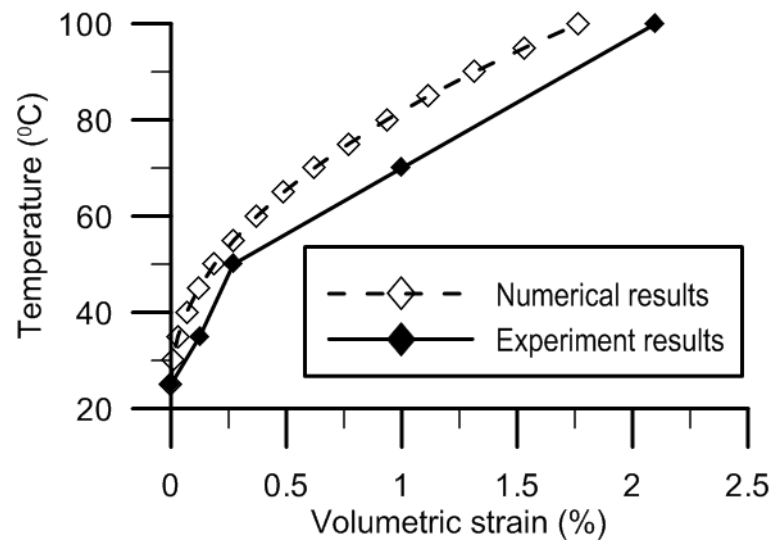


Figure 3.23: Numerical prediction of the volumetric strain induced by temperature changes.

solidation state. The numerical prediction of the volumetric change is shown in Figure 3.23. Due to temperature effects on the mechanical behavior, the yield surface has evolved during this heating stage. The model ability to predict drained shear behavior of Boom clay at high temperature is verified by simulating the shear test performed at the end of Path 3 (F-F'). Comparison between this blind prediction and experimental results is shown in Figure 3.24.

In the deviatoric stress-axial strain plane, model predictions agree quite well with the experimental results. However, the model predictions of the volumetric strain are not fully satisfactory. It is worth noting that good quality of volumetric strain measurements are quite difficult to obtain when testing Boom clay. Keeping this in mind, it may be remarked that the experimental results on volumetric deformation presented in Figure 3.24 show a trend which is questionable. Despite of this, an obvious difference exists between the model prediction and the experimental volumetric response of Boom clay. The relatively poor-quality prediction obtained for Path 2 at room temperature also supports this comment. This is due to the flow rule adopted by the Cam-clay model. An improvement could be obtained using a non-associated flow rule that would account for an increased dilatancy ratio.

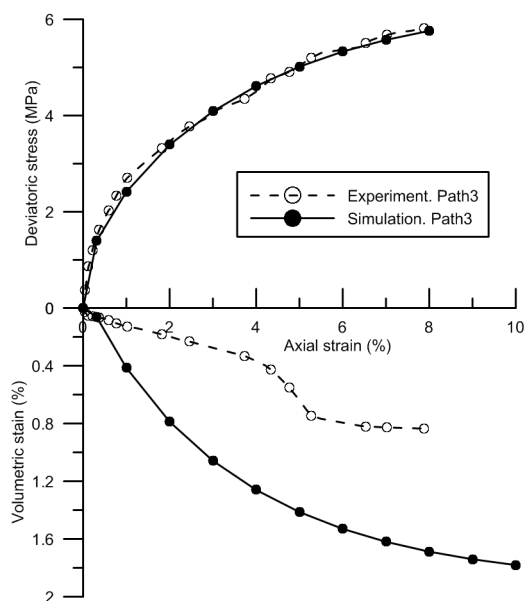


Figure 3.24: Drained triaxial compression tests on Boom Clay in Path 3 at 60°C.

3.3.5 Conclusion

The elasto-plastic constitutive equations of Cui *et al.*'s model for the thermo-mechanical behavior of clays have been recalled. The integration of this model at the stress point level using an explicit scheme with adaptive time stepping was investigated. With the temperature being considered as an additional stress component, a generalized strain including a temperature-driven component is introduced. The thermo-mechanical model has been reformulated using this new strain and its generalized stress counterpart which account for temperature.

A mixed control procedure is described to account for loading paths where total strain and temperature are imposed. An adaptive sub-stepping procedure accounting for non-isothermal loadings has been proposed. The proposed algorithm also considers the correction of the stress point drift from the yield surface. Specific technical points related to the presence of two plastic mechanisms that can be activated simultaneously have also been presented.

The efficiency of the developed algorithm has been investigated. The interest of using an adaptive time-stepping procedure in comparison to a constant size increments scheme

has been clearly shown. In particular, the computation time required to achieve a given accuracy is largely reduced if adaptive sub-stepping is considered, for both mechanical or thermal loadings.

The performance of the thermo-mechanical model in catching the main features of the behavior of saturated clays is finally studied. Numerical simulations are compared to experimental data on Boom clay for thermal loading tests and triaxial shear tests performed at various constant temperatures. The numerical results agree relatively well with the experimental results showing the good capabilities of the model as well as the relevance of the proposed algorithm.

Chapter 4

A Two-surface thermo-mechanical model

4.1 Introduction

Various thermo-mechanical models have been developed to describe the thermo-mechanical behavior of saturated soils, each having its own limitations from the theoretical point of view as seen in Chapter 3. In-depth examination showed that these models cannot adequately describe the shear behavior of natural Boom Clay. Indeed, as seen for ACC-2 in Chapter 2, such a Two-surface model is required to describe some key features of the mechanical behavior of natural Boom Clay such as a very limited elastic zone and a smooth transition from elastic to plastic regimes. The need of developing a thermo-mechanical model lying in the framework of Two-surface plastic mechanism of presented in Chapter 2 is therefore justified.

This chapter consists of two parts. In the first part, the isotropic thermo-mechanical constitutive model proposed by Cui et al. [22] is firstly revisited using the Two-surface concept. One of the new major developments is the extension of both TY and LY yield surfaces to a Two-surface plasticity concept. Then the Two-surface thermo-elasto-plastic model is implemented using an explicit integration scheme similar to that proposed in Chapter 3.

The proposed model is validated using the available experimental data. In the second part, the temperature effects on the shear behavior are firstly investigated by analysing the experimental results. The isotropic Two-surface thermo-mechanical model developed in the first part is extended to triaxial stress states. Simulations are also performed to validate the proposed model.

It should be pointed out that in this chapter the tests under drained conditions are used for the model validation.

4.2 An isotropic Two-surface thermo-mechanical model

4.2.1 Basic model features

The basic thermo-mechanical model follows the model proposed by Cui et al. [22] (referred to as Model C), which can capture the main features of the isotropic thermo-mechanical behavior of saturated clays. However, distinct plastic strain variables are introduced according to the active plastic mechanism and the followed loading paths (either mechanical or thermal loading path). These plastic strain variables are differentiated. And parameters for each loading path are required in Model C, as presented in Chapter 3. In this section, the plastic strain along a mechanical loading path and the one along a thermal loading path are linked based on Model C before introducing the Two-surface concept.

4.2.1.1 Thermo-mechanical elastic behavior

The total volumetric elastic strain increment $d\varepsilon_v^e$ associated with thermal loading and mechanical loading can be calculated using the thermo-mechanical model proposed by Model C, which permits to remain simple and relatively accurate in describing the thermo-

elastic behavior and to ensure that the elastic behavior is loading-path independent:

$$d\varepsilon_v^e = -\alpha_d dT + \frac{dp'}{K} \quad (4.1)$$

with bulk modulus K as the same as in MCC model:

$$K = \frac{v_0 p'}{\kappa} \quad (4.2)$$

where α_d is the drained thermal volumetric expansion coefficient which is assumed constant, κ is the elastic slope in $(v,')$ space which is temperature independent, v_0 is the initial specific volume.

4.2.1.2 Thermo-mechanical yield limit

Following Model C, an elastic zone delimited by two yield curves is adopted: the conventional thermo-mechanical yield curve controlling the evolution of the preconsolidation pressure with temperature denoted LY (loading yield limit), and the yield curve governing the thermal plastic behavior denoted TY (thermal yield limit). However, the definition and expression of TY are modified as shown in the following part.

The same expression for LY as that used in the model of Model C is adopted:

$$p'_{cT} = p'_{c0} \exp[-\alpha_0(T - T_0)] \quad (4.3)$$

where p'_{c0} and p'_{cT} are defined as the apparent preconsolidation pressures at an initial temperature T_0 and the actual temperature T respectively, α_0 governs the curvature of LY.

As shown in Figure 4.1(a), heating an overconsolidated clay leads to a thermal volumetric expansion followed by a contraction of the specimen. The higher the OCR values the higher the temperature of transition from expansion to contraction. It has been shown that the thermal expansion phase is characterised by a thermal elastic behavior while the thermal contraction corresponds to a thermo-plastic behavior. Thereby, the transition point

can be defined as a thermal yield point (or yield temperature). As shown in Figure 4.1(a), this yield point is defined as the intersection point (point Y1 and Y2) of the two linear parts of the $\varepsilon_v^T - T$ curve. The loci of these transition points define the TY curve. To conveniently incorporate TY into the Two-surface model, another function of TY which can provide a similar shape (see Figure 4.1(b)) as the one used in Model C is defined as follows:

$$T_{TY} = T_c - \frac{1}{\beta} \ln \left(\frac{p'}{p'_{ref}} \right) \quad (4.4)$$

where p'_{ref} is a reference pressure taken equal to the atmospheric pressure (0.1 MPa), T_{TY} and T_c are the yield temperature values corresponding to p' and p'_{ref} respectively, and T_c is taken as the hardening parameter controlling the hardening process, β is a parameter affecting the shape of TY curve.

4.2.1.3 Plastic mechanism

Thermo-plastic volumetric strain also occurs upon heating in the normally (or close to) consolidated state. This plastic mechanism is related to a decrease of the preconsolidation pressure (mechanical yield point defined in the common sense of soil mechanics) with temperature, known as thermal softening. Thermo-plastic volumetric strain is generated during a heating process at constant mean stress, compensating the thermal softening: the loading point lies on the loading yield curve (LY). In other words, thermo-plastic volumetric strain on LY curve is generated along heating paths because of the reduction of the preconsolidation pressure with temperature. The plastic strains along a mechanical loading path and a thermal loading path are linked from this theoretical point of view.

Commonly observed thermo-mechanical volumetric behavior shows that it is necessary to consider linking the plastic strain along mechanical loading path and the one along thermal loading path. For this purpose, consider a series of isotropic tests in which soil samples at a reference temperature (point 1 in Figure 4.2) are subjected to two different thermo-mechanical loading paths, denoted path A (1-3-1'-2) and path B (1-2) respectively.

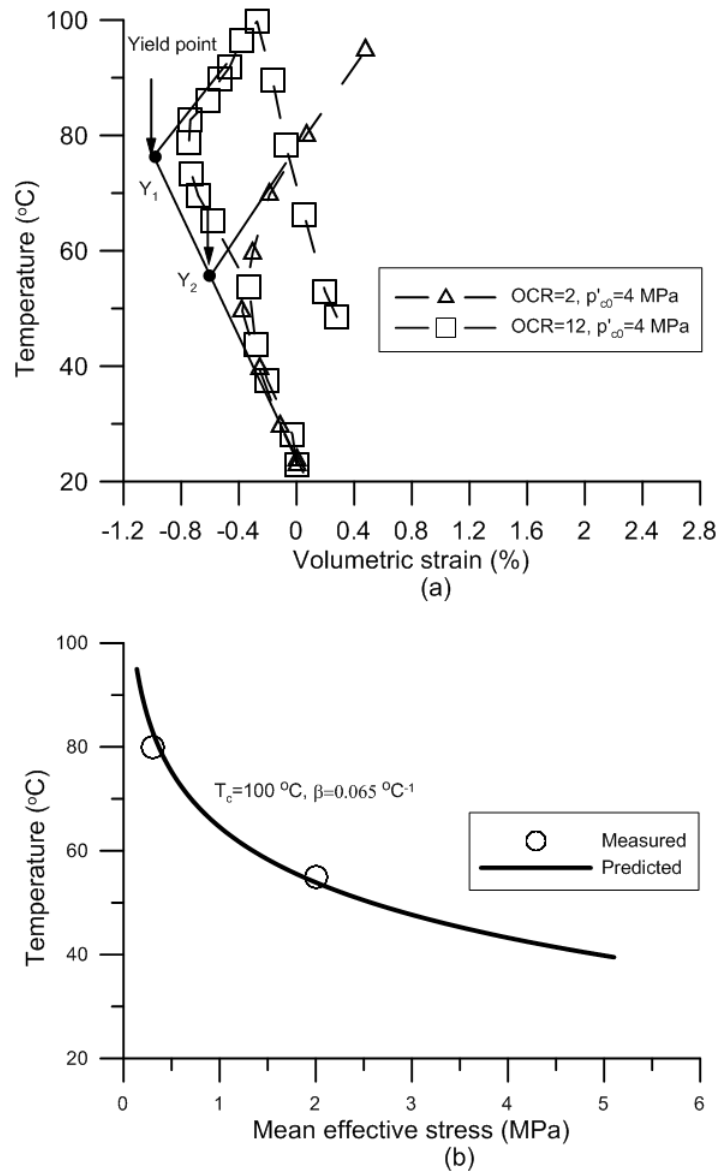


Figure 4.1: (a): Determination of the yield temperature for remolded Boom clay under different isotropic stresses according to Sultan et al. [80], (b): Comparison between the experimental yield points and the proposed thermal yield curve (TY).

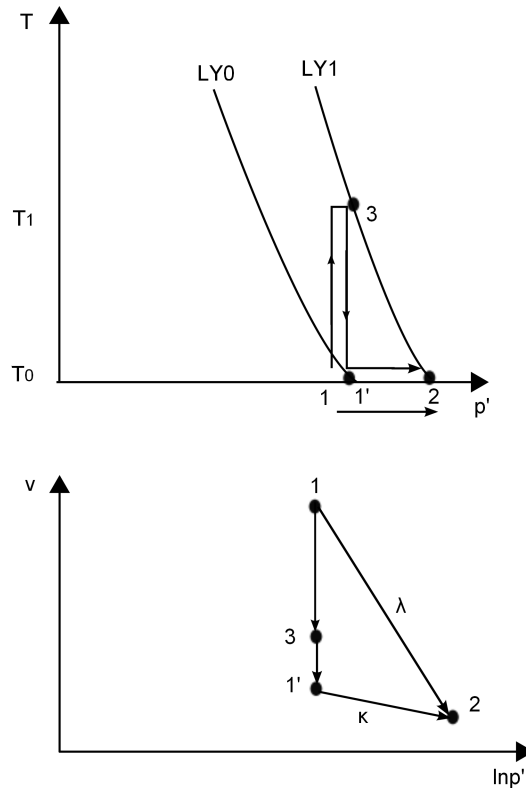


Figure 4.2: (a): Shape of LY in (p', T) plane and thermo-mechanical loading path, (b): Volumetric response of the thermo-mechanical loading for a normally consolidated clay in the (v, p') space.

Along path A, the soil is heated from 1 to 3 undergoing thermo-elasto-plastic path and purely thermal elastic strain occurs in the cooling process from 3 to 1'. Due to the thermal hardening effect, an elastic behavior is observed during the following mechanical loading from 1'-2. Along path B, normal compression behavior occurs with a slope λ in the (v, p') space being temperature independent. Plastic volume change occurring along path A must be equal to that along path B independently of the loading path, and can be expressed as:

$$\Delta v^p = v_1 - v_{1'} = (\lambda - \kappa) \ln \frac{p'_2}{p'_1} \quad (4.5)$$

Therefore, the plastic volumetric deformation ($d\varepsilon_{vLY}^p$) induced by different loading paths between LY_0 and LY_1 can be calculated from the change in size of the elastic domain. The

hardening law is thus deduced and reads:

$$dp'_{c0} = \frac{v_0}{(\lambda - \kappa)} p'_{c0} d\varepsilon_{vLY}^p \quad (4.6)$$

Experimental results show that the thermally induced plastic strain on TY is dependent on the given stress state (Overconsolidation Ratio –OCR– effect). From Equations 4.3 and 4.6, the increment of the thermally induced volumetric strain in normally consolidated states (that is on LY curve) can be calculated by:

$$dT = \frac{v_0}{(\lambda - \kappa)\alpha_0} d\varepsilon_{vLY}^p \quad (4.7)$$

And the increment of the thermally induced volumetric strain on TY ($d\varepsilon_{vTY}^p$) considering OCR effect can be determined by:

$$dT = \frac{v_0}{(\lambda - \kappa)\alpha_0} f(OCR) d\varepsilon_{vTY}^p \quad (4.8)$$

where $OCR = p'_{cT}/p'$ corresponds to the distance from the current stress state to the yield locus LY at a given temperature. $f(OCR)$ is a function describing the OCR effect. This function should satisfy the following conditions:

$$\begin{aligned} f(1) &= 1 \\ \lim_{OCR \rightarrow \infty} f &= +\infty \end{aligned} \quad (4.9)$$

This means that when no effective stress is applied, i.e. $OCR \rightarrow +\infty$, the thermal behavior is purely elastic, and when TY and LY intersect, the thermally induced volumetric strains associated to TY and LY are identical. The nature of function $f(OCR)$ is similar to a hardening modulus function in the Two-surface model of ACC-2. This will facilitate the insertion of the proposed model into the framework of the Two-surface plastic mechanism.

As a consequence, the hardening law of TY irrespective of the loading path is defined

as:

$$dT_c = \frac{v_0}{(\lambda - \kappa)\alpha_0} f(OCR) d\varepsilon_{vTY}^p \quad (4.10)$$

Following the experimental observations showing that LY curve hardens when TY is activated while activation of LY does not produce any hardening of TY, a unidirectional coupling between TY and LY is considered as in Model C. Therefore, the hardening law of Equation 4.6 for LY can be changed to:

$$dp'_{c0} = \frac{v_0}{(\lambda - \kappa)} p'_{c0} (d\varepsilon_{vTY}^p + d\varepsilon_{vLY}^p) \quad (4.11)$$

4.2.2 Extension to the Two-surface plasticity

To capture the smooth transition from the elastic regime to the plastic one that is observed for soils such as natural Boom Clay, the Two-surface plasticity is applied. Another reason for the adoption of this concept is that OCR effect associated with the TY plastic mechanism can conveniently be incorporated within this theoretical framework. Furthermore, as clearly shown in Chapter 2, only the Inner yield surface(s) has to be treated which will avoid some difficulties when implementing the model in computer codes.

Inner yield surfaces are introduced to describing the yielding behavior behavior with plastic strain inside the existing yield surfaces of the basic thermo-mechanical model called Yield surfaces. The hardening variables T_c and \bar{T}_c with respect to ITY (Inner yield surface of TY mechanism) and TY (Yield surface of TY mechanism), p'_{c0} and \bar{p}'_{c0} with respect to ILY (Inner yield surface of LY mechanism) and LY (Yield surface of LY mechanism) are introduced. Note that the notation of p'_{c0} and T_c are replaced by \bar{p}'_{c0} and \bar{T}_c , denoting the conventional yielding parameters, respectively. The variables T_c and p'_{c0} are analogous to \bar{T}_c and \bar{p}'_{c0} respectively, as illustrated in Figure 4.3.

Two scalars giving the ratios of the size of the Yield surface to that of the corresponding Inner yield surfaces are introduced for each mechanism. Their values are always smaller than or equal to 1 according to the Two-surface plasticity. For the LY plastic mechanism,

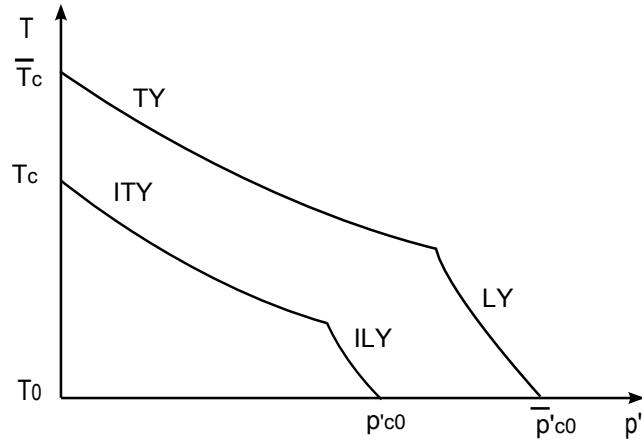


Figure 4.3: Inner yield surfaces and Yield surfaces.

this ratio is denoted r^{LY} and reads:

$$r^{LY} = \frac{p'_{c0}}{\bar{p}'_{c0}} \quad (4.12)$$

Similarly, for the TY mechanism, r^{TY} is defined by:

$$r^{TY} = \frac{T_c}{\bar{T}_c} \quad (4.13)$$

The expressions of Yield surfaces and the corresponding Inner yield surfaces are still given by Equations 4.3 and 4.4 but with redefined hardening variables reading as follows:

$$\mathbf{LY} : \quad p'_{cT} = \bar{p}'_{c0} \exp[-\alpha_0(T - T_0)] \quad (4.14)$$

$$\mathbf{ILY} : \quad p'_{cT} = r^{LY} \bar{p}'_{c0} \exp[-\alpha_0(T - T_0)] \quad (4.15)$$

$$\mathbf{TY} : \quad T_{TY} = \bar{T}_c - \frac{1}{\beta} \ln \left(\frac{p'}{p'_{ref}} \right) \quad (4.16)$$

$$\mathbf{ITY} : \quad T_{TY} = r^{TY} \bar{T}_c - \frac{1}{\beta} \ln \left(\frac{p'}{p'_{ref}} \right) \quad (4.17)$$

To describe the hardening modulus variation upon thermal loading, the hardening laws

associated with ILY and LY plastic mechanisms are defined similarly to ACC-2:

$$dr^{LY} = \frac{v_0}{\lambda - \kappa} s^{LY} (1 - r^{LY}) (d\varepsilon_{vTY}^p + d\varepsilon_{vLY}^p) \quad (4.18)$$

$$d\bar{p}'_{c0} = \frac{v_0}{\lambda - \kappa} \bar{p}'_{c0} (d\varepsilon_{vTY}^p + d\varepsilon_{vLY}^p) \quad (4.19)$$

where s^{LY} is a material constant, which controls the rate at which ILY approaches LY along thermo-mechanical loading paths. It actually intervenes in the evolution rate of r^{LY} variable.

The hardening laws for ITY and TY are defined as:

$$dr^{TY} = \frac{v_0}{(\lambda - \kappa)\alpha_0 T_c} f(OCR) (r^{TY} + s^{TY}) (1 - r^{TY}) d\varepsilon_{vTY}^p \quad (4.20)$$

$$d\bar{T}_c = \frac{v_0}{(\lambda - \kappa)\alpha_0} f(OCR) d\varepsilon_{vTY}^p \quad (4.21)$$

with the function $f(OCR)$ introduced previously now reading:

$$f(OCR) = [1 + s^{LY} (1/r^{LY} - 1)] \quad (4.22)$$

where s^{TY} is a material constant controlling the rate at which ITY approaches TY along thermo-mechanical loading paths. It actually intervenes in the evolution rate of r^{TY} variable. The above hardening laws of the basic model (namely Equation 4.10 and 4.11) can be recovered, if the Yield surfaces and the corresponding Inner yield surfaces coincide that is if $r^{TY}=1$ and $r^{LY}=1$. The Yield surfaces (TY and LY) part of the proposed model can thus be simply switched off making the extended model and the basic model equivalent.

4.2.3 Constitutive equations

The constitutive equation of the Two-surface model can be described in a way similar to conventional elastoplastic models. The plastic strain rate can be formulated using the consistency condition for the Inner yield surfaces (ITY or ILY or both). It is worth noting

that strain variables defined here are different from those used in Model C because a unique plastic strain is defined along different loading paths for each plastic mechanism. $d\varepsilon$ is the total strain increment which can be split into three parts: the elastic strain increment $d\varepsilon_{\sigma'}^e$, associated with effective stress changes, a stress independent thermal elastic increment $d\varepsilon_T^e$ due to temperature changes and plastic increment $d\varepsilon_Y^p$ associated with the corresponding activated plastic mechanism, due to effective stress and temperature changes:

$$d\varepsilon = d\varepsilon_{\sigma'}^e + d\varepsilon_T^e + d\varepsilon_Y^p \quad (4.23)$$

The elastic strain $d\varepsilon_T^e$ associated with changes of temperature is defined as:

$$d\varepsilon_T^e = -\frac{1}{3}\mathbf{m}\alpha_d dT \quad (4.24)$$

where \mathbf{m} is a unit vector $\mathbf{m}^t = (1, 1, 1)$, α_d is the drained volumetric thermal expansion coefficient. In the following part, the constitutive equations will be described in a general manner.

4.2.3.1 Yield function

The yield locus F^Y is defined in terms of effective stress, current temperature and a hardening parameter X^Y corresponding to the activated yield surface:

$$F^Y(\sigma', T, X^Y) = 0 \quad (4.25)$$

where the superscript Y stands for the considered Inner yield surface ILY or ITY .

4.2.3.2 Flow rule

The plastic strain increment is computed from the plastic potential:

$$d\varepsilon_Y^p = d\lambda^Y \frac{\partial G^Y}{\partial \sigma'} \quad (4.26)$$

where $d\lambda^Y$ is the plastic multiplier, positive scalar, and G^Y is the plastic potential corresponding to the activated plastic mechanism.

4.2.3.3 Hardening law

Similarly, the increment of the hardening parameter X^Y is computed from the increment of volumetric plastic strain ε_{vY}^p :

$$dX^Y = \frac{\partial X^Y}{\partial \varepsilon_{vY}^p} d\varepsilon_{vY}^p = \frac{\partial X^Y}{\partial \varepsilon_{vY}^p} d\lambda^Y \frac{\partial G^Y}{\partial p'} \quad (4.27)$$

4.2.3.4 Consistency condition

The consistency condition can be expressed as:

$$dF^Y = \frac{\partial F^Y}{\partial \boldsymbol{\sigma}'} d\boldsymbol{\sigma}' + \frac{\partial F^Y}{\partial T} dT + \frac{\partial F^Y}{\partial X^Y} dX^Y = 0 \quad (4.28)$$

4.2.3.5 Stress–temperature–strain relations

The stress increment can be expressed as:

$$d\boldsymbol{\sigma}' = \mathbf{D}_e d\boldsymbol{\varepsilon}_{\boldsymbol{\sigma}'}^e = \mathbf{D}_e (d\boldsymbol{\varepsilon} - d\boldsymbol{\varepsilon}_T^e - d\boldsymbol{\varepsilon}_Y^p) \quad (4.29)$$

where the elastic strain $d\boldsymbol{\varepsilon}_{\boldsymbol{\sigma}'}^e$ is calculated from Equations 4.23 and 4.24, given by the difference between the total strain $d\boldsymbol{\varepsilon}$ and the sum of the plastic strain $d\boldsymbol{\varepsilon}_Y^p$ plus the elastic strain associated with changes of temperature $d\boldsymbol{\varepsilon}_T^e$.

The following expression for the plastic multiplier is then obtained:

$$d\lambda^Y = \frac{(\mathbf{a}^Y)^t \mathbf{D}_e d\boldsymbol{\varepsilon} + (\mathbf{c}^Y - (\mathbf{a}^Y)^t \mathbf{D}_e \mathbf{b}) dT}{(\mathbf{a}^Y)^t \mathbf{D}_e \mathbf{g}^Y + h} \quad (4.30)$$

where: $\mathbf{a}^Y = \frac{\partial F^Y}{\partial \boldsymbol{\sigma}'}$, $\mathbf{b} = -\frac{1}{3} \mathbf{m} \alpha_d$, $\mathbf{c}^Y = \frac{\partial F^Y}{\partial T}$, $\mathbf{g}^Y = \frac{\partial G^Y}{\partial \boldsymbol{\sigma}'}$, $h = -\frac{\partial F^Y}{\partial X^Y} \frac{\partial X^Y}{\partial \varepsilon_{vY}^p} \frac{\partial G^Y}{\partial p'}$.

Combining Equations 4.29 and 4.30 gives:

$$d\boldsymbol{\sigma}' = \mathbf{D}_{ep}^\varepsilon d\boldsymbol{\varepsilon} + \mathbf{D}_{ep}^T dT \quad (4.31)$$

$$dX^Y = \mathbf{R}_{ep}^\varepsilon d\boldsymbol{\varepsilon} + \mathbf{R}_{ep}^T dT \quad (4.32)$$

where:

$$\mathbf{D}_{ep}^\varepsilon = \mathbf{D}_e - \frac{\mathbf{D}_e \mathbf{g}^Y (\mathbf{a}^Y)^t \mathbf{D}_e}{(\mathbf{a}^Y)^t \mathbf{D}_e \mathbf{g}^Y + h} \quad (4.33)$$

$$\mathbf{D}_{ep}^T = \frac{\mathbf{D}_e \mathbf{g}^Y \left((\mathbf{a}^Y)^t \mathbf{D}_e \mathbf{b} - \mathbf{c}^Y \right)}{(\mathbf{a}^Y)^t \mathbf{D}_e \mathbf{g}^Y + h} - \mathbf{D}_e \mathbf{b} \quad (4.34)$$

and

$$\mathbf{R}_{\varepsilon}^{ep} = \frac{B (\mathbf{a}^Y)^t \mathbf{D}_e}{(\mathbf{a}^Y)^t \mathbf{D}_e \mathbf{g}^Y + h} \quad (4.35)$$

$$\mathbf{R}_T^{ep} = \frac{B (\mathbf{c}^Y - (\mathbf{a}^Y)^t \mathbf{D}_e \mathbf{b})}{(\mathbf{a}^Y)^t \mathbf{D}_e \mathbf{g}^Y + h} \quad (4.36)$$

with $B = \frac{\partial X^Y}{\partial \varepsilon_{vY}^p} \frac{\partial G^Y}{\partial p'}$.

Treating the temperature increment as an extra strain increment $d\bar{\boldsymbol{\varepsilon}} = (d\boldsymbol{\varepsilon}, dT)^t$, $\mathbf{D}_{ep} = [\mathbf{D}_{ep}^\varepsilon, \mathbf{D}_{ep}^T]$, $\mathbf{R}_{ep} = [\mathbf{R}_{ep}^\varepsilon, \mathbf{R}_{ep}^T]$ can be obtained and the constitutive Equations 4.31 and 4.32 can be rewritten as:

$$d\boldsymbol{\sigma}' = \mathbf{D}_{ep}^Y d\bar{\boldsymbol{\varepsilon}} \quad (4.37)$$

$$dX^Y = \mathbf{R}_{ep}^Y d\bar{\boldsymbol{\varepsilon}} \quad (4.38)$$

At the intersection point of the two Inner yield surfaces (ITY and ILY), i.e. $F^{ITY} = 0$ and $F^{ILY} = 0$, both consistency conditions must be satisfied that is, from Equation 4.28:

$$\frac{\partial F^{ITY}}{\partial \boldsymbol{\sigma}'} d\boldsymbol{\sigma}' + \frac{\partial F^{ITY}}{\partial T} dT + \frac{\partial F^{ITY}}{\partial \bar{T}_c} d\bar{T}_c + \frac{\partial F^{ITY}}{\partial r^{TY}} dr^{TY} = 0 \quad (4.39)$$

$$\frac{\partial F^{ILY}}{\partial \boldsymbol{\sigma}'} d\boldsymbol{\sigma}' + \frac{\partial F^{ILY}}{\partial T} dT + \frac{\partial F^{ILY}}{\partial \bar{p}'_{c0}} \bar{p}'_{c0} + \frac{\partial F^{ILY}}{\partial r^{LY}} dr^{LY} = 0 \quad (4.40)$$

The total plastic strain increment is the sum of the plastic strains due to each mechanism (ITY and ILY):

$$\begin{aligned} d\boldsymbol{\varepsilon}^p &= d\boldsymbol{\varepsilon}_{ITY}^p + d\boldsymbol{\varepsilon}_{ILY}^p \\ &= d\lambda^{ITY} \mathbf{g}^{ITY} + d\lambda^{ILY} \mathbf{g}^{ILY} \end{aligned} \quad (4.41)$$

and the stress increment can be expressed as:

$$d\boldsymbol{\sigma}' = \mathbf{D}_e(d\boldsymbol{\varepsilon} - d\boldsymbol{\varepsilon}_T^e - \bar{\mathbf{g}}d\boldsymbol{\lambda}) \quad (4.42)$$

where $\bar{\mathbf{g}} = (\mathbf{g}^{ITY}, \mathbf{g}^{ILY})$, $d\boldsymbol{\lambda} = (d\lambda^{ITY}, d\lambda^{ILY})^t$.

The consistency condition given by Equation 4.39 and 4.40 can be re-written in a more general form:

$$\mathbf{A}_m \mathbf{D}_e d\bar{\boldsymbol{\varepsilon}} - \mathbf{H}_m d\boldsymbol{\lambda} = \mathbf{0} \quad (4.43)$$

where:

$$\mathbf{A}_m = \begin{bmatrix} (\mathbf{a}^{ITY})^t \mathbf{D}_e & \mathbf{c}^{ITY} - (\mathbf{a}^{ITY})^t \mathbf{D}_e \mathbf{b} \\ (\mathbf{a}^{ILY})^t \mathbf{D}_e & \mathbf{c}^{ILY} - (\mathbf{a}^{ILY})^t \mathbf{D}_e \mathbf{b} \end{bmatrix} \quad (4.44)$$

$$\mathbf{H}_m = \begin{bmatrix} \mathbf{H}_{m1} & \mathbf{H}_{m2} \\ \mathbf{H}_{m3} & \mathbf{H}_{m4} \end{bmatrix} \quad (4.45)$$

$$\mathbf{H}_{m1} = - \left(\frac{\partial F^{ITY}}{\partial T_c} \frac{\partial T_c}{\partial \varepsilon_{vTY}^p} + \frac{\partial F^{ITY}}{\partial r^{TY}} \frac{\partial r^{TY}}{\partial \varepsilon_{vTY}^p} \right) \frac{\partial G^{ITY}}{\partial p'} + (\mathbf{a}^{ITY})^t \mathbf{D}_e \mathbf{g}^{ITY} \quad (4.46)$$

$$\mathbf{H}_{m2} = (\mathbf{a}^{ITY})^t \mathbf{D}_e \mathbf{g}^{ILY} \quad (4.47)$$

$$\mathbf{H}_{m3} = - \left(\frac{\partial F^{ILY}}{\partial \bar{p}'_{c0}} \frac{\partial \bar{p}'_{c0}}{\partial \varepsilon_{vLY}^p} + \frac{\partial F^{ILY}}{\partial r^{LY}} \frac{\partial r^{LY}}{\partial \varepsilon_{vLY}^p} \right) \frac{\partial G^{ITY}}{\partial p'} + (\mathbf{a}^{ILY})^t \mathbf{D}_e \mathbf{g}^{ITY} \quad (4.48)$$

$$\mathbf{H}_{m4} = - \left(\frac{\partial F^{ILY}}{\partial \bar{p}'_{c0}} \frac{\partial \bar{p}'_{c0}}{\partial \varepsilon_{vLY}^p} + \frac{\partial F^{ILY}}{\partial r^{LY}} \frac{\partial r^{LY}}{\partial \varepsilon_{vLY}^p} \right) \frac{\partial G^{ILY}}{\partial p'} + (\mathbf{a}^{ILY})^t \mathbf{D}_e \mathbf{g}^{ILY} \quad (4.49)$$

The expression for the generalised plastic multiplier reads:

$$d\boldsymbol{\lambda} = -(\mathbf{H}_m)^{-1} (\mathbf{A}_m)^t \mathbf{D}_e d\bar{\boldsymbol{\varepsilon}} \quad (4.50)$$

As presented in Chapter 3, the activation state of each plastic mechanism can be determined from the values of plastic multiplier obtained using Equation 4.50.

4.2.4 Stress integration

With the Two-surface approach, the stress-temperature state is always on the Inner yield surfaces (ITY or ILY) during any thermo-mechanical loading path that induces plastic strains. The Inner loading surfaces evolve according to the stress-temperature state, and do never cross their respective Yield surfaces (TY or LY) thanks to the adopted hardening laws (see Equations 4.18-4.20). Therefore, it is not required to check whether the Inner surfaces (ITY or ILY) cross or not the Yield surfaces (TY or LY).

It should be noted that the essential feature of the elastic domain is that it is delimited by two smooth Inner yield surfaces (ITY and ILY) as seen in Figure 4.3, similarly to Model C, and can be defined as:

$$EM = \{(\sigma', X^Y) \mid F^Y(\sigma', X^Y) < 0, Y \in [ITY, ILY]\} \quad (4.51)$$

Treating stress paths that pass by or reach the intersection between the two Inner yield surfaces will require some adaptations accounting different situations. This can be done using the algorithms presented in Chapter 3 for the model of Model C. While using these algorithms, the size of Yield surfaces (TY and LY) is updated accordingly at each step together with the inner yield surfaces.

4.2.5 Determination of the parameters

The proposed isotropic thermo-mechanical model presented in the previous section has 11 material parameters ($\lambda, \kappa, \alpha_d, \alpha_0, \bar{p}'_{c0}, r_0^{LY}, s^{LY}, \beta, \bar{T}_{c0}, r_0^{TY}, s^{TY}$). The procedure for determining these parameters is described below.

The first two parameters of normal compressing and swelling slope in (ℓ, v) space, λ and κ , are the same as those of the MCC and can be obtained from a loading-unloading isotropic

compression test at any given temperature since they are temperature independent.

The drained thermal volumetric expansion coefficient of soil α_d is the same as that in Model C, which can be calibrated from the cooling stages of a drained heating-cooling test.

Parameter α_0 from Equation 4.3 describes the evolution of preconsolidation pressure with temperature and it can be determined from at least 2 compression tests on overconsolidated specimens at two constant temperatures.

\bar{p}'_{c0} has the same mechanical meaning as in Model C denoting conventional isotropic preconsolidation pressure at a reference temperature T_0 . r_0^{LY} specifies the size of ILY associated with the first occurrence of plastic strains. As defined in ACC-2, r_0^{LY} is the inverse of the initial OCR, as classically defined. Parameter s^{LY} influences the hardening rate of ILY. As stated previously, a higher value of s^{LY} leads to a higher hardening rate. These three parameters can be determined by an isotropic consolidation test. Additional details can be found in Chapter 2.

The initial TY yield curve is defined through the initial yield temperature \bar{T}_{c0} and shape parameter β by Equation 4.16. At least two heating tests at different overconsolidation ratios are required. $\varepsilon_v^T - T$ curves are then analysed to deduce the thermal yield point. The yield point of TY (point Y_1 and Y_2 in Figure 4.1(a)) is determined by the bilinear method. The values of \bar{T}_{c0} and β are then obtained from Equation 4.16 in order to best fit the yield values in $(p' - T)$ plane. In a similar manner to r^{LY} definition, r_0^{TY} specifies the size of ITY associated with the first occurrence of plastic strains. For the natural Boom clay, it is assumed that plastic strain is generated after heating from the reference temperature (T_0) in the in-situ effective stress state. With this stress-temperature state on the initial ITY, r_0^{TY} are then obtained from Equation 4.17. s^{TY} defines the hardening rate of ITY and can be calibrated from the $\varepsilon_v^T - T$ plot of isotropic heating test on an overconsolidated sample.

4.2.6 Validation of the proposed model

In the following, a numerical validation of the proposed model is performed using the thermomechanical experimental results on natural Boom Clay [7] and reconstituted Pontida

Table 4.1: Model parameters for the validation of the proposed model on natural Boom Clay and reconstituted Pontida Clay.

	reconstituted Pontida Clay (Baldi et al. 1988)	natural Boom Clay (Baldi et al. 1991)
Physical properties		
Initial void ratio, e_0	0.88	0.61
Liquid limit, w_L (%)	32.3	66.6
Plasticity index, I_P (%)	12.9	27-35
Model parameters		
λ	0.103	0.170
κ	0.013	0.02
α_d (1/°C)	0.00005	0.00005
α_0 (1/°C)	0.0035	0.0050
r_0^{LY}	1.0	0.33
\bar{p}'_{c0} (MPa)	0.1	6.0
s^{LY}	10*	10
β	0.072	0.021
r_0^{TY}	0.18	0.76
\bar{T}_{c0} (°C)	110	216.5
s^{TY}	12	0.1

* the parameter has no effect since $r_0^{LY}=1$.

Clay [6] reported in the literature. The physical properties and the adopted parameters are given in Table 4.1. The initial state for reconstituted Pontida Clay is defined by $p'=0.1$ MPa with $e_0=0.88$ and the soil is initially normally consolidated. While the initial state for natural Boom Clay is defined by $p'=2$ MPa with $e_0=0.61$ which is close to the in-situ state.

4.2.6.1 Tests on reconstituted Pontida Clay by Baldi et al. (1988)

Baldi et al. [6] performed three heating tests on reconstituted Pontida Clay. Three specimens were first loaded up to $p'=2.5$ MPa. Afterwards, two samples were unloaded to 1 MPa and 0.2 MPa, respectively. Thus, three specimens with three different overconsolidation ratios (1, 2.5, and 12.5) were obtained. From these consolidation pressures, a heating process was applied on each specimen. The results of the tests are presented in Figure 4.4. The parameters λ and κ are taken from the work of Hueckel et al. [43], calibrated from isotropic compression test at ambient temperature. With a preconsolidation pressure

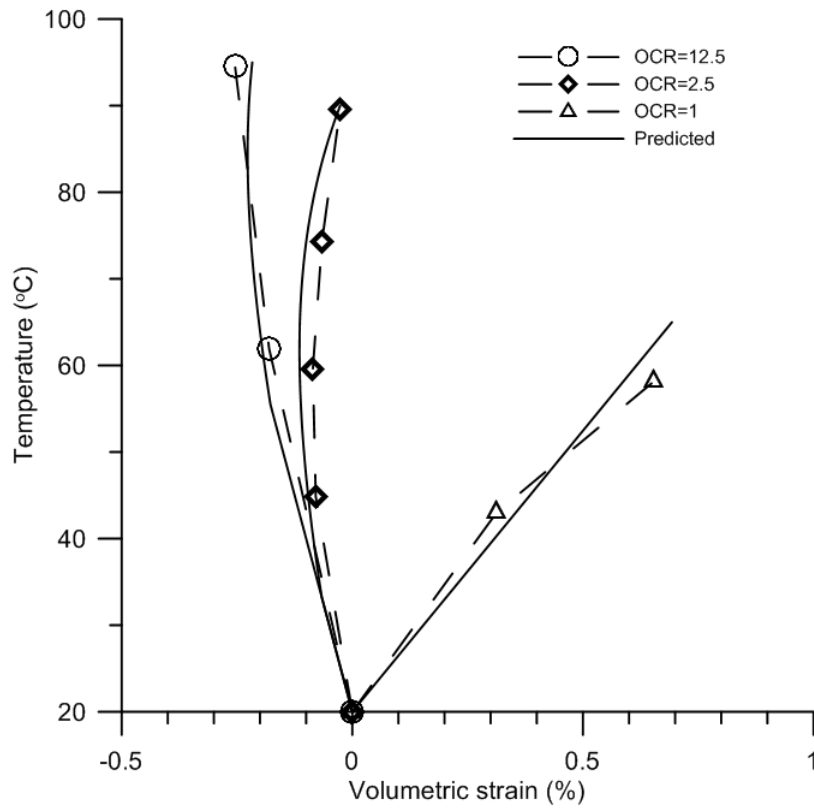


Figure 4.4: Comparison between predicted and measured results on reconstituted Pontida Clay [6].

decreased from 2.5 MPa at 20 °C to 1.90 MPa at 90 °C, parameter α_0 is obtained using Equation 4.3. The other parameters are determined based on the experimental results from the heating test on overconsolidated samples (OCR=2, 12.5). The comparison between experimentally observed and predicted thermally induced volume changes in different overconsolidated states are given in Figure 4.4.

It is useful to note that in the heating test at OCR=1, as seen in Figure 4.4, the thermally induced volume change is well predicted by considering the hardening of loading yield limit, showing the relevance of the coupling mechanism considered between thermal loading path and mechanic loading path. The corresponding numerical predictions in the overconsolidated state, which is controlled by the thermal yield plastic mechanism (ITY and TY), have a reasonable agreement with the experimental results. Thanks to the Two-surface plasticity, there is a smooth prediction in the overconsolidated state.

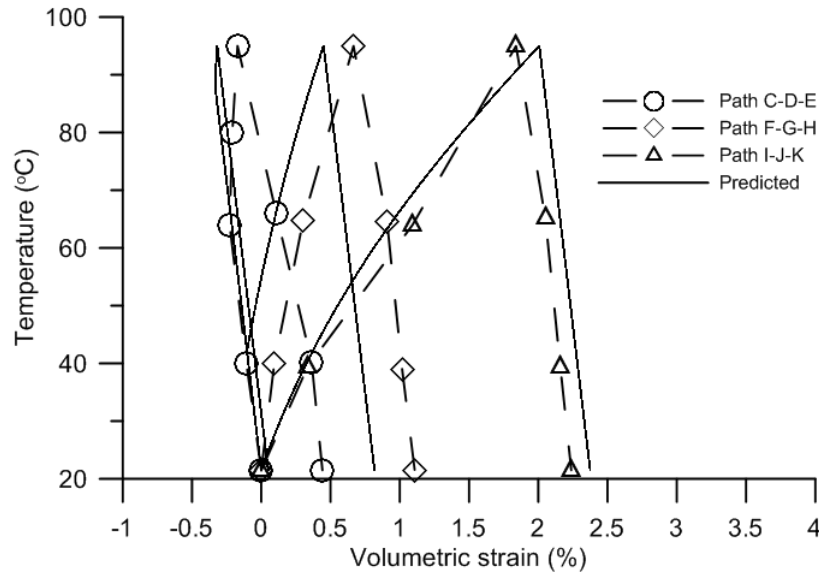


Figure 4.5: Comparison between the experimental results and numerical predictions for natural Boom Clay.

4.2.6.2 Tests on natural Boom Clay by Baldi et al. (1991)

The thermo-mechanical test on natural Boom Clay (TBoom9) reported by Baldi et al. [7] is considered. More details can be found in Chapter 3. Some of the isotropic parameters (λ , κ , r_0^{LY} , \bar{p}'_{c0} , s^{LY}) governing the mechanical response of the model have been already defined in the simulations of the isotropic compression test at ambient temperature in Chapter 2. The remaining parameters controlling the thermo-elastic and the thermo-plastic parts still have to be determined. α_0 can be obtained knowing that $\bar{p}'_{c0} = 6$ MPa at 21.5 °C and 4.2 MPa at 95 °C (see Figure 4.7). Parameters β , r_0^{TY} , \bar{T}_{c0} , s^{TY} are determined from the $\varepsilon_v - T$ plot along path C-D-E and F-G-H in the overconsolidation state as explained in Section 4.2.5. Comparison between the experimental results and numerical predictions is shown in Figure 4.5. On the whole, there is a reasonable agreement between the predicted values from the proposed model and the experimental test results.

To validate the performance of the proposed model along mechanical loading paths at an elevated temperature, tests TBoom10 and TBoom11 are considered. Experimental loading paths are given in the isotropic effective stress-temperature plane in Figure 4.6. Both paths

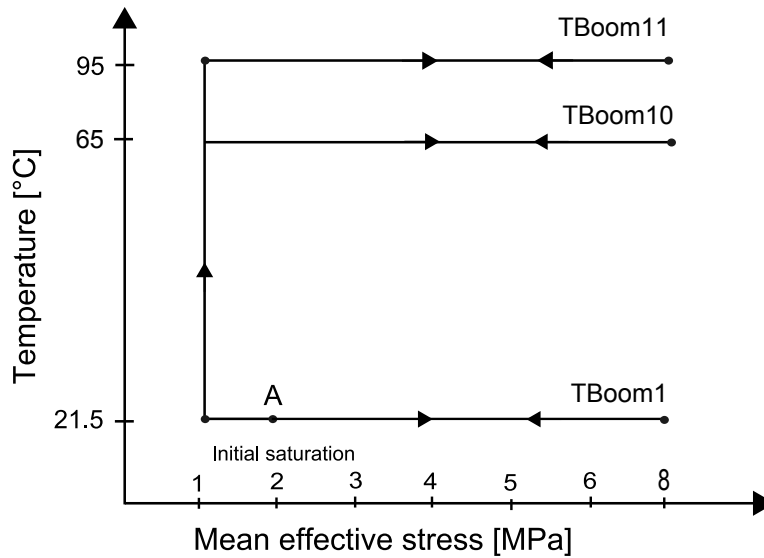


Figure 4.6: Test program for TBoom10 and TBoom11 tests.

include first a saturation process under a constant mean effective stress of 2 MPa which is close to the in situ effective stress of 2.3 MPa, an unloading stage from the initial stress of 2 MPa to 1 MPa, heating from 21.5°C to 65°C or 95°C respectively, followed by loading at 65°C or 95°C respectively, up to 8 MPa and then unloading to 1.0 MPa. The drained isotropic compression test TBoom1 at ambient temperature (21.5°C) is used to determine the isothermal isotropic parameters of the model. The loading path has been investigated in Chapter 2. All the model parameters are reported in Table 4.1. The numerical predictions of tests TBoom1, TBoom10 and TBoom11 at three different temperatures are shown in Figure 4.7. It shows predictions can follow the trend of the experimental behavior. Larger volumetric strain is observed in the isotropic compression test at a higher temperature since the elastic zone shrinks with preconsolidation pressure decrease due to temperature increase and thus larger volumetric strain is generated at a higher temperature. This difference can be well captured by the proposed model. Moreover, the smooth elastoplastic behavior in the mechanical compression test at an elevated temperature as at ambient temperature can be well predicted by the proposed Two-surface model.

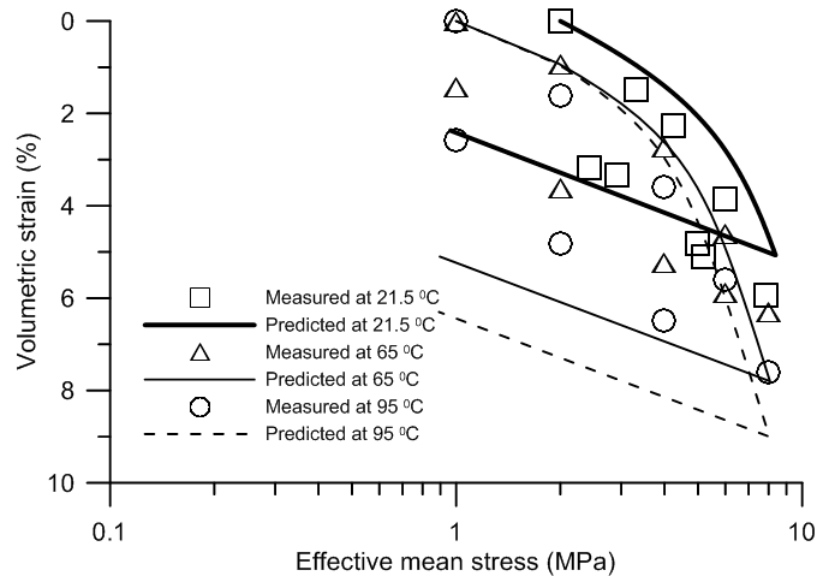


Figure 4.7: Numerical simulations of isotropic compression tests at different temperatures.

4.3 Extension of the model to triaxial stress states

4.3.1 Experimental behavior

In the context of research on deep nuclear waste disposal, the thermo-mechanical behavior in triaxial stress states of natural Boom Clay sampled at 223 m depth at Mol, Belgium, is now investigated. We firstly examine the temperature effects on yield, plastic and shear strength behavior based on the experimental observations. As described in Chapter 2, a number of experimental results shows that the saturation process plays an important role in the thermo-hydro-mechanical response of Boom Clay. Saturation of the sample under a small effective stress in the triaxial apparatus would result in swelling and leads to an unexpected behavior of Boom Clay such as unreasonably low values of yield stress

In this study, a series of non-isothermal triaxial shear tests conducted on Boom Clay specimens by Le [51] is carefully examined. The specimens were saturated under the in-situ stress state and no apparent swelling was observed. The specimens were trimmed from block samples that were extracted from the Mol site. Tests were performed in a triaxial cell equipped with a temperature control system. Two different thermo-mechanical loading

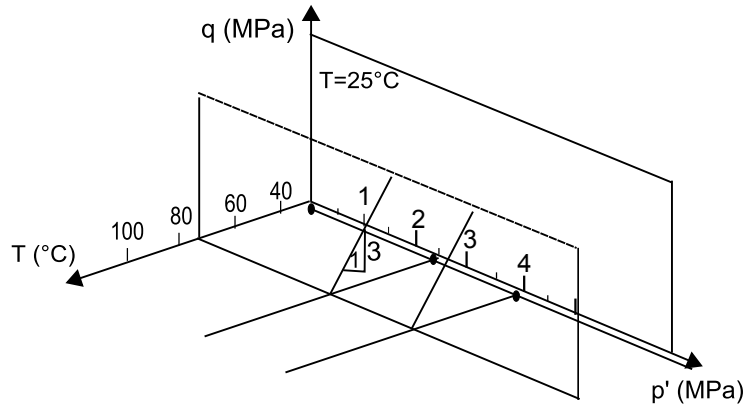


Figure 4.8: Thermo-mechanical loading paths in triaxial stress space.

paths were performed on two samples, as shown in Figure 4.8. The two samples (TCD-1, TCD-2) were saturated under a confining pressure of 3.5 MPa using a back pressure of 1 MPa to achieve the in-situ effective stress state. After saturation, one sample was isotropically consolidated to 3.8 MPa. Doing so, two specimens with two different effective mean stresses (2.5 MPa and 3.8 MPa respectively) and thus two distinct overconsolidation ratios ($OCR=2.4$ and 1.6 respectively) were obtained. From these consolidation pressures, each specimen was heated from 25°C to 76°C under drained conditions and constant mean effective stress. A standard drained triaxial shear test at constant confining pressure followed. Axial strain was measured by a displacement transducer and volumetric strain was measured using the back-pressure controller. Figure 4.9 shows the results of the drained triaxial shear tests in terms of variations of deviator stress (q) and volumetric strain (ε_v) against axial strain (ε_1). To clearly show the temperature effects on the shear behavior, the shear test results at an elevated temperature (76°C) are compared to those performed at ambient temperature (25°C). Two initial mean effective stresses are considered, as shown in Figure 4.9.

Features can be observed from TCD-1 and TCD-2: (a) all the tests exhibit purely contracting behavior; (b) after a very brief linear phase, $\varepsilon_1 - q$ curve becomes highly nonlinear until reaching failure as identified in the case of ambient temperature; (c) it can be shown that the volumetric strain increment is proportional to the initial mean effective stress p'_0 .

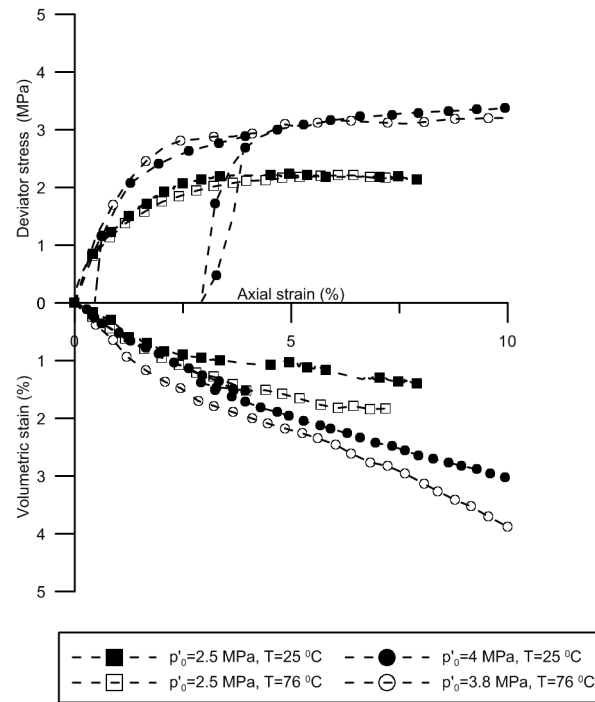


Figure 4.9: Comparison of drained triaxial shear at 25 °C and 76 °C from a same/similar initial mean effective stress.

From these results, two important aspects of temperature effects on the shear behavior are observed: (d) small differences are shown in $\varepsilon_1 - q$ response between the shear tests at 25°C and 76°C; (e) obvious differences are shown in $\varepsilon_1 - \varepsilon_v$ plane. Larger volumetric strain is generated at 76°C than at 25°C at a given axial strain level.

4.3.2 Temperature effects on shear strength

Heating may induce strength changes due to alteration of the physical properties such as adsorption forces in clay water [6]. However, existing experimental data does not give clear general trends of temperature effects on the slope M of the critical state line in (p', q) plane. This slope has been observed to increase, or remain constant or even decrease with temperature increase, depending on the soil type and the test conditions. For example, slope M for Pontida clay was observed to be temperature independent by Hueckel and Pellegrini [43] but to decrease with temperature increase by Cekerevac and Laloui [16]. In addition, Hueckel et al. [46] concluded that the dependence of shear strength on temperature is

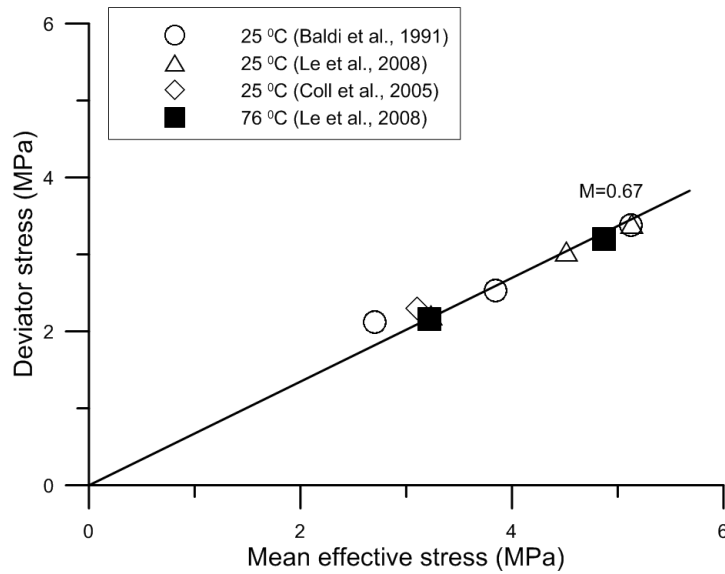


Figure 4.10: Critical state line.

material specific. It should also be mentioned that the differences of M values may be induced by the sample inhomogeneity [7, 27], specimen preparation process such as an inappropriate resaturation process which may alter the thermo-hydro-mechanical behavior [7, 18, 51, 80], the thermomechanical loading history, and the drainage conditions under which the heating is performed.

Here, the temperature effects on the slope M for natural Boom Clay are examined in depth based on the experimental results. To eliminate the effects related to the thermomechanical loading history, the variability in experimental techniques such as drainage conditions or more specifically the sample resaturation process, only drained triaxial experimental tests with an appropriate resaturation process as described in Section 4.3.1 are considered. The shear strength at critical state obtained from tests at 25°C and 76°C are plotted in Figure 4.10.

It seems that the shear strength of natural Boom Clay is not influenced by temperature. Since very few experiments on natural Boom Clay have been performed to evaluate the shear strength modifications at elevated temperatures, it is desirable to have more data to further investigate the influence of temperature on the shear strength at critical state.

4.3.3 Yield stress curve

For studying the stress-strain behavior of the clay, yielding is an important feature and the determination of the initial yield surface of such clay must be examined. As presented in Chapter 2, a number of approaches have been proposed to define the stress state upon yielding. The yield points can be determined by the sharp slope change in stress-strain plots, such as mean effective stress (p') against volumetric strain (ε_v), deviator stress (q) against shear strain (ε_s), etc. [23, 56, 82]. In this work, yield stresses are identified from both $p' - \varepsilon_v$ and $q - \varepsilon_s$ curves. The average of the two obtained values is taken as the yield stress. The yield point determination for drained triaxial experiments on natural Boom Clay at 76°C is shown in Figures 4.11 and 4.12. The yield stresses determined from $p' - \varepsilon_v$ curves are found to be similar to those from $q - \varepsilon_s$ curves.

Figure 4.13 shows the yield points obtained from the drained triaxial shear tests on natural Boom Clay at 25°C and 76°C. The predicted Yield surface (LY) from Equation 4.55 is also shown in Figure 4.13. In the following parts, all the parameters which have been calibrated from the mechanical behavior at ambient temperature and the thermoplastic part (see Chapter 2 and Section 4.2.6, respectively) are fixed as shown in Table 4.2. Figure 4.13 shows that the yield curve expression given by Equation 4.55 is suitable for fitting the experimental data at both 25°C and 76°C.

4.3.4 Model description in the triaxial state

In this section, the Two-surface thermo-mechanical model (termed TEAM model) in triaxial stress space ($p' - q - T$) is proposed by combining the isothermal Two-surface mechanical model (ACC-2) and the isotropic Two-surface thermo-mechanical model (Section 4.2). The temperature effects on the shear behavior of natural Boom Clay are taken into account. No additional parameter is introduced.

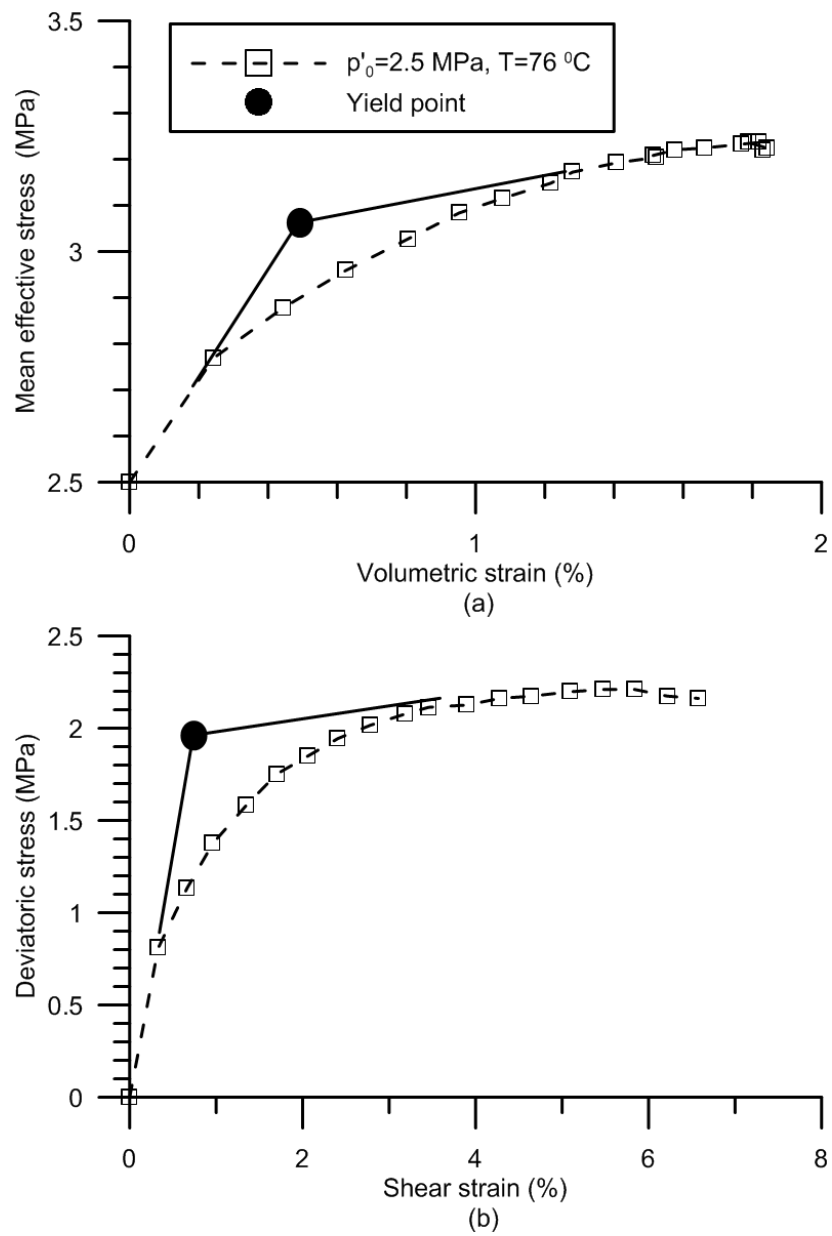


Figure 4.11: Yield stress determination for a drained triaxial shear test TCD-1 ($T=76$ °C, $p'_0=2.5$ MPa).

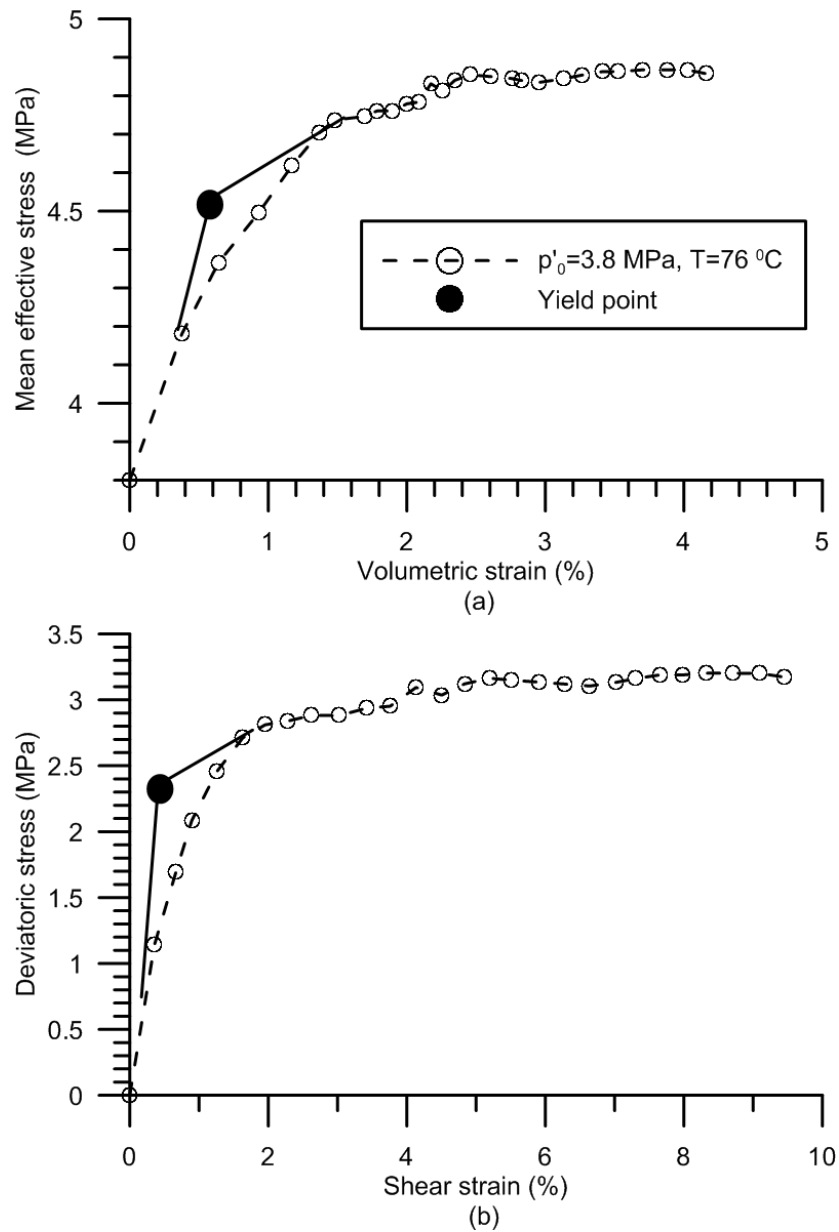


Figure 4.12: Yield stress determination for a drained triaxial shear test TCD-2 ($T=76^\circ\text{C}$, $p'_0=3.8\text{ MPa}$).

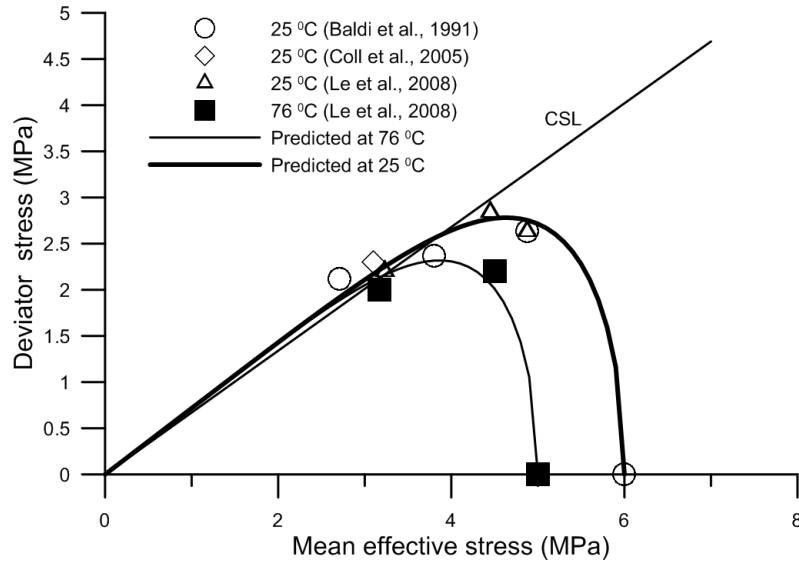


Figure 4.13: Yield surface of natural Boom clay at 25°C and 76°C .

4.3.4.1 Elastic behavior

The total elastic volumetric increment $d\varepsilon_v^e$ and elastic shear strain increment $d\varepsilon_s^e$ can be calculated using the equation proposed by Model C:

$$\begin{aligned} d\varepsilon_v^e &= -\alpha_d dT + \frac{dp'}{K} \\ d\varepsilon_s^e &= \frac{dq}{3G} \end{aligned} \quad (4.52)$$

with G being assumed temperature independent:

$$G = \frac{3(1-2\nu)}{2(1+\nu)} K \quad (4.53)$$

where ν is Poisson's ratio, assumed constant.

4.3.4.2 Yield surface

According to Section 4.2, the elastic domain is bounded by the Inner yield surfaces comprising ILY and ITY. Beyond this elastic domain, Yield surfaces exist and comprise LY and TY. The Yield surfaces are analogous to the corresponding Inner yield surfaces as seen

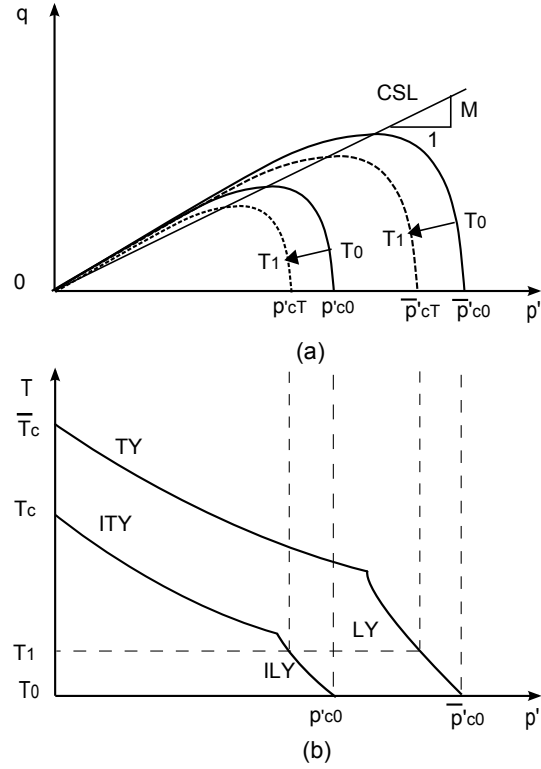


Figure 4.14: Yield locus in (a): $(p' - q)$ plane at two different temperatures (with $T_1 > T_0$) and (b): $(p' - T)$ plane.

in Figure 4.14. The expressions for the yield surfaces are defined as follows:

$$\begin{aligned}
 \mathbf{ITY} : \quad T_{TY} &= r^{TY} \bar{T}_c - \frac{1}{\beta} \ln \left(\frac{p'}{p'_{ref}} \right) \\
 \mathbf{TY} : \quad T_{TY} &= \bar{T}_c - \frac{1}{\beta} \ln \left(\frac{p'}{p'_{ref}} \right)
 \end{aligned} \tag{4.54}$$

$$\begin{aligned}
 \mathbf{ILY} : \quad q^2 + \frac{M_f^2}{1 - k_f} \left(\frac{p'}{r^{LY} \bar{p}'_{cT}} \right)^{2/k_f} (r^{LY} \bar{p}'_{cT})^2 - \frac{M_f^2 p'^2}{1 - k_f} &= 0 \\
 \mathbf{LY} : \quad q^2 + \frac{M_f^2}{1 - k_f} \left(\frac{p'}{\bar{p}'_{cT}} \right)^{2/k_f} \bar{p}'_{cT}^2 - \frac{M_f^2 p'^2}{1 - k_f} &= 0
 \end{aligned} \tag{4.55}$$

$$\text{with } \bar{p}'_{cT} = \bar{p}'_{c0} \exp[-\alpha_0(T - T_0)]$$

For the sake of brevity but without losing generality, it is assumed that k_f does not equal 1.

4.3.4.3 Hardening law

In line with the isotropic Two-surface thermo-mechanical model in Section 4.2, a volumetric hardening rule is adopted,

$$\begin{aligned} dr^{LY} &= \frac{v_0}{\lambda - \kappa} s^{LY} (1 - r^{LY}) (d\varepsilon_{vTY}^p + d\varepsilon_{vLY}^p) \\ d\bar{p}'_{c0} &= \frac{v_0}{\lambda - \kappa} \bar{p}'_{c0} (d\varepsilon_{vTY}^p + d\varepsilon_{vLY}^p) \end{aligned} \quad (4.56)$$

$$\begin{aligned} dr^{TY} &= \frac{v_0}{(\lambda - \kappa)\alpha_0 T_c} f(OCR) (r^{TY} + s^{TY}) (1 - r^{TY}) d\varepsilon_{vTY}^p \\ d\bar{T}_c &= \frac{v_0}{(\lambda - \kappa)\alpha_0} f(OCR) d\varepsilon_{vTY}^p \\ \text{with } f(OCR) &= [1 + s^{LY} (1/r^{LY} - 1)] \end{aligned} \quad (4.57)$$

4.3.4.4 Flow rule

For the plastic strain associated to ILY or LY, a non-associated flow rule in the constant temperature planes is given,

$$d = \frac{d\varepsilon_{vLY}^p}{d\varepsilon_{sLY}^p} = \frac{M_g^2 - \eta^2}{k_g \eta} \quad (4.58)$$

where $d\varepsilon_{vLY}^p$ and $d\varepsilon_{sLY}^p$ are increments of volumetric plastic strain and shear plastic strain, respectively, M_g is the slope of the critical state line, k_g is a soil parameter which defines the variation of the flow rule, η is the stress ratio q/p' . To consider the temperature effects on the shear strength and plastic strain increment ratio for specific materials, the flow rule can be easily extended by adopting temperature functions for $M_g(T)$ and $k_g(T)$. In this work, M_g and k_g are assumed to be temperature independent on the basis of the experimental observations on natural Boom Clay described previously.

For ITY or TY, the volumetric plastic strain and shear plastic strain increments will be $(d\varepsilon_{vTY}^p, 0)$, where $d\varepsilon_{vTY}^p$ is given by Equation 4.57.

Table 4.2: Model parameters for natural Boom Clay.

λ	κ	α_d (1/°C)	α_0 (1/°C)	r_0^{LY}	\bar{p}'_{c0} (MPa)	s^{LY}	β (1/°C)
0.170	0.02	0.00005	0.005	0.33	6	10	0.021
r_0^{TY}	\bar{T}_{c0}	s^{TY}	M_f	k_f	M_g	k_g	ν
0.76	216.5	0.1	0.60	0.30	0.67	0.7	0.3

4.3.4.5 Validation of the proposed model

A total of sixteen parameters are introduced in the model (λ , κ , α_d , α_0 , r_0^{LY} , \bar{p}'_{c0} , s^{LY} , β , r_0^{TY} , \bar{T}_{c0} , s^{TY} , M_g , M_f , k_f , k_g , ν). Good performance of the proposed model in predicting mechanical behavior at ambient temperature and isotropic thermo-mechanical behavior have been shown. In order to validate the model performance in the triaxial stress space under elevated temperatures, two tests (TCD-1 and TCD-2) presented in Figure 4.9 are simulated. All the parameters are listed in Table 4.2, all of which have been calibrated in the previous section and kept constant for the present simulations. In particular, the two tests, TCD-1 and TCD-2, do not pertain to the experimental data set used for the parameter determination. In this sense, the simulations presented here can be seen as blind predictions.

Numerical simulations of drained triaxial tests at 25°C and 76°C for different overconsolidated states have been performed and are compared with the experimental results in Figure 4.15 and 4.16. The results in the deviator stress-axial strain plane show a lower yield point in terms of deviator stress at 76°C than at 25°C for the overconsolidated stress paths, which is consistent with the experimental observations. This also results in larger volumetric strains at a higher temperature and allows the model predicts an important aspect of temperature effects on the shear behavior, that is, larger volumetric strain is generated at 76°C than at 25°C as shown in the Figure 4.15 and 4.16. It has been found that smooth and more realistic predictions are obtained, which is attributed to the use of a Two-surface plastic mechanism. In general, model predictions agree well with the experimental results, validating the proposed model in triaxial stress states at room and above.

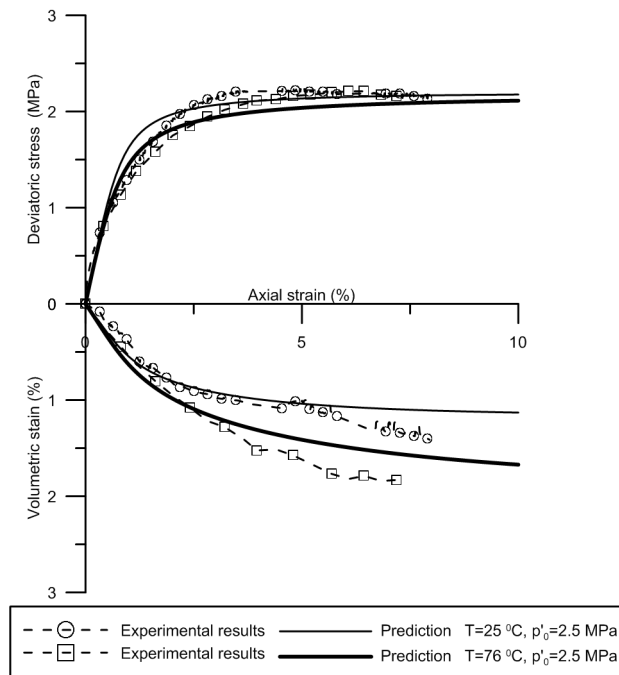


Figure 4.15: Numerical simulations of drained triaxial compression tests CD-4 ($T=25^{\circ}\text{C}$, $p'_0=2.5\text{ MPa}$) and TCD-1 ($T=76^{\circ}\text{C}$, $p'_0=2.5\text{ MPa}$).

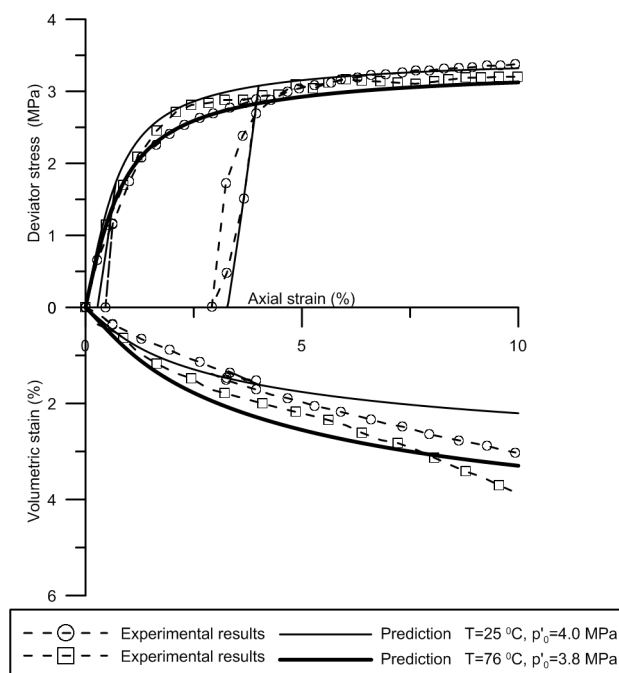


Figure 4.16: Numerical simulations of drained triaxial compression tests CD-3 ($T=25^{\circ}\text{C}$, $p'_0=4.0\text{ MPa}$) and TCD-2 ($T=76^{\circ}\text{C}$, $p'_0=3.8\text{ MPa}$).

4.4 Conclusion

The isotropic thermo-mechanical model was developed by linking the thermal plastic strain and the mechanical one and defining a unique plastic strain along different loading paths, and then extended to the Two-surface formulation for both TY and LY plastic mechanisms. This permits to predict smooth elasto-plastic behavior along both thermal loading path and mechanical loading path. This feature is one of the main characteristics presented by natural Boom Clay. Moreover, the stress integration algorithm was simply discussed based on algorithm developed for Model C considering that the Inner yield surfaces do not cross the Yield surfaces. Numerical validation was performed using experimental results on natural Boom Clay and reconstituted Pontida Clay in the isotropic state. The numerical results show that this model can capture the main thermo-mechanical features along different loading paths and give more realistic predictions.

This isotropic Two-surface thermo-mechanical model has been extended to triaxial stress states. Triaxial shear tests at an elevated temperature on natural Boom Clay specimens trimmed from blocks extracted at a depth of 223 in the URL of SCK-CEN in Mol (Belgium) performed by Le [51] were carefully examined to study its yielding and plastic behavior. These tests show that the limited elastic zone and the smooth elastoplastic transition that characterise Boom clay at room temperature are also presented at elevated temperatures. It should also be noted that the drained shear strength at the critical state of natural Boom Clay is temperature independent. The isotropic Two-surface thermo-mechanical model was extended to triaxial stress states by adopting a thermally dependent yield surface and a non-associated flow rule. Simulations of triaxial tests on natural Boom Clay have been carried out to validate and assess the performance of the proposed model. It has been found that the proposed model gives good predictions in the triaxial stress space, at room and elevated temperatures.

Chapter 5

Extension of TEAM model to undrained conditions

5.1 Introduction

Under undrained heating conditions, the excess pore water pressure in a saturated soil is thermally induced because of the higher thermal expansion of water than that of the soil skeleton. For instance, the thermal expansion coefficient of free water varies in a range around $[2.1 \times 10^{-4}; 6.6 \times 10^{-4}]$ ($1/^\circ\text{C}$) between temperature 20°C and 90°C [78], and that of the soil skeleton for natural Boom Clay is examined around 5×10^{-5} ($1/^\circ\text{C}$) (See section 5.7.1). This effect will lead to a decrease in mean effective stress, leading to a critical situation in engineering practice. It is therefore important to investigate the thermo-mechanical behaviour of clays under undrained heating.

According to the effective stress concept, the effective stress is defined as the stress part solely carried by soil skeleton [73, 84]. Different effective stress principles for saturated soils (or porous media) in the iso-thermal conditions have been proposed to describe the effective stress as a function of total stress and pore water pressure. These effective stress principles enable the constitutive equations formulated in the effective stress state to be converted to equations with combination of the total stress and pore water pressure. Thereby, the

pore water pressure or the undrained response can be determined if an additional condition is imposed for undrained loading process, such as a constant volume condition in the isothermal undrained condition. In non-isothermal condition, to extend the thermo-elasto-plastic constitutive equations for saturated soils formulated in terms of effective stress and temperature based on the drained heating tests in Chapter 4 to the situation with total stress, pore water pressure and temperature, an extension of the effective stress principle is required, in addition to an extra condition (ex. volumetric strain condition) along the undrained heating process for the pore water pressure calculation and undrained behaviour prediction.

The thermo-hydro-mechanical equations for the undrained response of saturated soils were presented by number of authors [15, 21, 33, 57]. Campanella and Mitchell [15] performed a precursory work and gave the expression for pore water pressure variation under undrained condition using a simple governing criterion stipulating that the total volume change of total soil mass due to both temperature and stress changes must be equal to the sum of the volume change of mineral solid and pore water. Coussy [21] analysed this process and proposed his equations in a thermo-poro-mechanical theoretical framework. In this study, their works are carefully investigated and compared to show their difference and compatibility in undrained heating analysis. A particular attention is paid to the non-isothermal effective stress principle for the case of thermo-mechanical loading. The volumetric strain condition in this process is imposed as an additional condition for the pore water pressure determination.

In the following, the main features of temperature effects on undrained saturated clays are first briefly analyzed. Then, the models developed by Campanella and Mitchell [15] and Coussy [21] for undrained heating are recalled and compared. Afterwards, the effective stress principle for thermo-mechanical loading is set up based on their works. Also, the volumetric strain expression in the elasto-plastic domain is developed with a new definition of plastic strain that accounts for the coupling between thermal loading path and mechanical loading path (see Chapter 4). Once the appropriate effective stress principle is set up and

the volumetric strain condition is determined, the thermo-elasto-plastic behaviour during undrained heating is analyzed with the model proposed (TEAM model) in Chapter 4. Finally, the validity of the model under undrained heating condition is examined based on some typical tests of natural Boom Clay and reconstituted Pontida Clay. Some phenomena observed during the undrained thermo-mechanical processes can be explained by the model.

5.2 Temperature effects under undrained conditions

Experimental evidence (e.g. [57]) clearly shows that excess pore water pressure is induced during undrained heating of saturated soils. Possible thermal failure may occur in undrained heating condition, in which effective stress decreases due to the increase of the thermally induced pore pressure, leading eventually to failure state. Such thermally induced failure was observed by Hueckel et al. [45] in a laboratory experiment on reconstituted Pontida Clay, in which failure occurred when temperature was increased to 90°C under undrained condition under constant stresses.

The mechanism of excess pore water pressure development upon heating can be simply analyzed. As shown in Figure 5.1, saturated soils are composed of mineral solid (solid grains) and pore water. The soil skeleton can be defined as the part formed by the mineral solid and the pore space emptied of pore water. Due to heating, the temperature of soil skeleton and pore water will increase so that they will experience volumetric expansion. Since pore water expands more than the solid skeleton, its pressure tends to increase. If the heating process is performed under drained conditions (provided that the characteristic time of pressure diffusion is much shorter than the characteristic time of heating), water will be able to drain out from the specimen and thus no excess pore water pressure will be generated. However, in undrained conditions, since water cannot be expelled, excess pore water pressure will be built up.

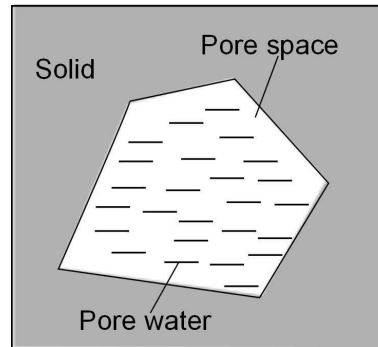


Figure 5.1: Saturated soil: soil skeleton and pore water.

5.3 Undrained heating analyses

To date, a number of authors [15, 21, 33, 57] presented thermo-mechanical equations of saturated soils (or porous media). In this section, typical works on undrained heating processes by Campanella and Mitchell [15] and Coussy [21] are recalled and compared. The work of Coussy [21] is rewritten using the sign convention of soil mechanics (compressive stress and strain as positive) to make the comparison easier. It should be noted that the mineral solid is considered as compressible in both cases.

5.3.1 Expressions of volume change and pore water pressure after Campanella and Mitchell (1968)

Under undrained condition, the volume change of the total soil mass due to both temperature and stress is equal to the sum of volume changes of mineral solid and pore water. The expression can be written as:

$$(dV_s)_{dT} + (dV_s)_{dp} + (dV_w)_{dT} + (dV_w)_{dp} = (dV)_{dT} + (dV)_{dp} \quad (5.1)$$

where dV_s , dV_w and dV are volume changes of mineral solid, pore water and soil mass, respectively, and the subscripts dT and dp denote 'due to' temperature change and mean stress change, respectively.

The volume change of mineral solid due to temperature and stress can be respectively expressed as:

$$(dV_s)_{dT} = V_s \alpha_s dT \quad (5.2)$$

and

$$(dV_s)_{dp} = -V_s C_s du - V_s C'_s dp' \quad (5.3)$$

where α_s is the volumetric thermal expansion coefficient of mineral solid (positive value), V_s is the volume of mineral solid, du is the pore water pressure change, C_s is the mineral solid volumetric compressibility under isotropic pressure, dp' is the mean effective stress or inter-granular stress, C'_s is the mineral solid volumetric compressibility when particles are subjected to concentrated loading, $C_s = C'_s$ is generally assumed.

The volume change of pore water due to temperature change and stress change can be respectively expressed as:

$$(dV_w)_{dT} = V_w \alpha_w dT \quad (5.4)$$

and

$$(dV_w)_{dp} = -V_w C_w du \quad (5.5)$$

where α_w is the volumetric thermal expansion coefficient of pore water, V_w is the volume of pore water, C_w is the volumetric compressibility of pore water.

Campanella and Mitchell [15] suggested that the soil mass would experience the same thermal volumetric strain as that of each mineral solid particle. In other words, the thermal expansion coefficient of the whole soil mass is assumed equal to that of the mineral solid. In addition, a further irreversible volume change of soil mass due to a temperature is taken into account. Thus, the volume change of soil mass due to temperature changes can be calculated by:

$$(dV)_{dT} = V \alpha_s dT - V \alpha_{sT} dT \quad (5.6)$$

where V is the volume of the total soil mass with $V = V_s + V_w$, α_{sT} is the coefficient of physico-chemical structural volume changes. The negative sign in the second term of

Equation 5.6 is necessary since compressive physico-chemical structural volume changes (negative) are produced during temperature increases.

The volume change of soil mass due to stress can be calculated by:

$$(dV)_{dp} = -VC_d dp' \quad (5.7)$$

where C_d is the volumetric compressibility of soil skeleton.

Combining Equations 5.1-5.7 and taking into account the Terzaghi's effective stress principle ($p' = p - u$) gives the expressions for incremental volumetric strain and pore water pressure, respectively:

$$d\varepsilon_v = -(n\alpha_w + (1-n)\alpha_s) dT + (nc_w + (1-n)c_s) du + (1-n)c_s dp' \quad (5.8)$$

$$du = \frac{(C_d - (1-n)C_s) dp + (n(\alpha_w - \alpha_s) + \alpha_{st}) dT}{(nC_w + C_d)} \quad (5.9)$$

where n is the soil porosity.

Under constant stress condition, Equation 5.9 is reduced to,

$$du = \frac{(n(\alpha_w - \alpha_s) + \alpha_{st}) dT}{(nC_w + C_d)} \quad (5.10)$$

5.3.2 Expressions of volume change and pore water pressure after Coussy (2004)

In this section, the undrained heating process is analyzed and all the formulations are derived on the basis of a thermo-poro-elastic theory. In the isotropic stress state and under non-isothermal condition, the total mean stress change (dp) and Lagrangian porosity change ($d\phi$) can be expressed by changes of volumetric strain ($d\varepsilon_v$), pore water pressure (du) and temperature (dT), as follows:

$$dp = \frac{1}{C_d} d\varepsilon_v + bdu + \frac{1}{C_d} \alpha_d dT \quad (5.11)$$

$$d\phi = -bd\varepsilon_v - \frac{1}{N}du + \alpha_\phi dT \quad (5.12)$$

where $\phi = \frac{V_\phi}{V_0}$ is the Lagrangian porosity defined as the ratio of the current porous volume to the initial soil volume. The volumetric compressibility of drained skeleton C_d , the Biot coefficient b and the volumetric thermal dilation coefficient of drained skeleton α_d appearing in Equation 5.11 are defined as:

$$\frac{1}{C_d} = \left(\frac{\partial p}{\partial \varepsilon_v} \right)_{u,T}, \quad b = \left(\frac{\partial p}{\partial u} \right)_{\varepsilon_v,T}, \quad \alpha_d = - \left(\frac{\partial \varepsilon_v}{\partial T} \right)_{p,u} \quad (5.13)$$

The Biot coefficient b , Biot modulus N and the volumetric thermal expansion coefficient of pores α_ϕ appearing in Equation 5.12 are defined as:

$$b = - \left(\frac{\partial \phi}{\partial \varepsilon_v} \right)_{u,T}, \quad \frac{1}{N} = - \left(\frac{\partial \phi}{\partial u} \right)_{\varepsilon_v,T}, \quad \alpha_\phi = \left(\frac{\partial \phi}{\partial T} \right)_{\varepsilon_v,u} \quad (5.14)$$

The Maxwell's symmetry condition gives:

$$b = \left(\frac{\partial p}{\partial u} \right)_{\varepsilon_v,T} = - \left(\frac{\partial \phi}{\partial \varepsilon_v} \right)_{u,T} \quad (5.15)$$

Equations 5.13-5.15 are partial differential equations and the subscripts indicate that the corresponding variables are kept constant, e.g. expression of $1/C_d$ corresponds to an isothermal drained compression test in which the pore water pressure and temperature are unchanged.

Considering the relations between the skeleton and mineral solid properties, the compatibility relations can be obtained:

$$b = 1 - \frac{C_s}{C_d}, \quad \frac{1}{N} = (\phi_0 - b) C_s \quad (5.16)$$

$$\alpha_d = \alpha_s, \quad \alpha_\phi = (\phi_0 - b) \alpha_s$$

where C_s and α_s are the compressibility coefficient and the thermal dilation coefficient of

mineral solid, respectively.

In a saturated porous medium, the current water mass (m_w) per unit volume can be expressed as:

$$m_w = \rho_w \phi \quad (5.17)$$

Differentiating Equation 5.17 gives:

$$\frac{dm_w}{\rho_w} = d\phi + \phi \frac{d\rho_w}{\rho_w} \quad (5.18)$$

The state equation of water writes as follows:

$$\frac{d\rho_w}{\rho_w} = C_w du - \alpha_w dT \quad (5.19)$$

where C_w is the volumetric compressibility of water.

Substituting Equations 5.11-5.12, 5.16 and 5.19 into 5.18 gives:

$$\frac{dm_w}{\rho_w} = -bd\varepsilon_v - ((\phi_0 - b) C_s - \phi C_w) du + ((\phi_0 - b) \alpha_s - \phi \alpha_w) dT \quad (5.20)$$

Substituting Equations 5.11-5.12 into 5.20 gives:

$$\frac{dm_w}{\rho_w} = -(C_d - C_s) dp - ((\phi_0 C_s - \phi C_w) - (C_d - C_s)) du + (\phi_0 \alpha_s - \phi \alpha_w) dT \quad (5.21)$$

In undrained conditions, the mass of the fluid phase is constant and $dm_w=0$ holds. Thus, the expressions for total volumetric strain and excess pore water pressure from Equations 5.11 and 5.21 can be obtained, as follows:

$$d\varepsilon_v = -(\phi \alpha_w + (1 - \phi_0) \alpha_s) dT + (\phi C_w + (1 - \phi_0) C_s) du + C_s (dp - du) \quad (5.22)$$

$$du = \frac{(C_d - C_s) dp + (\phi \alpha_w - \phi_0 \alpha_s) dT}{(C_d - C_s) + (\phi C_w - \phi_0 C_s)} \quad (5.23)$$

With infinitesimal transformation, Equations 5.22 and 5.23 can also be written using the

Eulerian porosity n ,

$$d\varepsilon_v = -(n\alpha_w + (1 - n)\alpha_s) dT + (nC_w + (1 - n)C_s) du + C_s(dp - du) \quad (5.24)$$

$$du = \frac{(C_d - C_s) dp + n(\alpha_w - \alpha_s) dT}{(C_d - C_s) + n(C_w - C_s)} \quad (5.25)$$

Under constant stress condition, Equation 5.25 is reduced to:

$$du = \frac{n(\alpha_w - \alpha_s) dT}{(C_d - C_s) + n(C_w - C_s)} \quad (5.26)$$

5.3.3 Comparison and discussion

Comparison of the final expressions for pore water pressure changes, i.e. Equations 5.9 and 5.25, suggests that the expression proposed by Campanella and Mitchell [15] is different from the one proposed by Coussy [21].

Firstly, Campanella and Mitchell [15] considered an irreversible part for the thermal strain ($\alpha_{st}dT$) whereas, Coussy [21] considered an elastic case. In particular, if $\alpha_{st} = 0$ holds in the thermo-elastic region and in addition the solid grain is assumed incompressible, i.e. $C_s = 0$, the two approaches unify.

Secondly, the volume change of mineral solid due to inter-granular stress is expressed as $C_s V_s dp'$ by Campanella and Mitchell [15] (see Equation 5.3). This implies that the mean inter-granular stress and the mean Terzaghi's effective stress are equivalent. This assumption may be questioned and requires further examination [64]. The mean effective stress p' is the stress part related to soil skeleton according to the Terzaghi's effective stress principle, and can be defined as:

$$p' = \frac{\sum N'}{A} \quad (5.27)$$

where $\sum N'$ is the sum of all the normal components of N' on the mineral solid, A is the

area of the soil mass. And the mean inter-granular stress p'_s can be defined as:

$$p'_s = \frac{\sum N'}{A_s} \quad (5.28)$$

where A_s is the area related to the mineral solid part. It should be noted that p' would have a smaller value than p'_s . If the ratio of A_s/A is taken equal to $(1 - n)$, p' and p'_s are linked through the relation:

$$p'_s = \frac{p'}{(1 - n)} \quad (5.29)$$

and the volume change of mineral solid due to the mean inter-granular stress is rewritten as $C_s v dp'$, which now has the same form as the one derived by Coussy [21].

Moreover, since a compressible mineral solid is considered by Campanella and Mitchell [15], Equation 5.7 for calculating the volume change of soil mass due to stress can be rewritten in a more precise fashion:

$$(dV)_{dp} = -VC_d dp' - VC_s du \quad (5.30)$$

Hence, using $\alpha_{st} = 0$ and Equations 5.29 and 5.30 in the approach of Campanella and Mitchell [15] provides the same expressions for the volumetric strain and pore water pressure as that of Coussy [21] in the thermo-elastic zone.

The equations proposed by Campanella and Mitchell [15] can also be examined from a mechanical point of view. For a non-isothermal loading process, the basic governing criterion under undrained condition (see Equation 5.1) works and holds. However, it should be noted that $(dV_s)_{dT} + (dV_w)_{dT} = (dV)_{dT}$ does not hold with the defined equations:

$$V_s \alpha_s dT + V_w \alpha_w dT \neq V \alpha_s dT \quad (5.31)$$

and thus:

$$(dV_s)_{dp} + (dV_w)_{dp} \neq (dV)_{dp} \quad (5.32)$$

This means that each term in Equation 5.31 and 5.32 that describe the temperature and stress effects, respectively, on the soil volume change are not defined in a decoupled fashion and thereby does not work independently. It appears then necessary to present the equations in a different form within the framework of Campanella and Mitchell [15], where each term is defined in a decoupled process to make the physical meaning clear. The non-isothermal loading process for the whole soil mass can be further divided to two processes: (i) a heating one with a temperature change dT and (ii) an isothermal loading one with a mean stress change dp . In a heating process (process i) under undrained condition, a temperature increase dT generates a pore water pressure (du_1), thus changing the mean effective stress ($dp'_1 = -du_1$). During this process, the volume changes of pore water, mineral solid and the whole mass due to temperature can be expressed as:

$$(dV_w)_{dT} = V_w \alpha_w dT - V_w C_w du_1 \quad (5.33)$$

$$(dV_s)_{dT} = V_s \alpha_s dT - V_s C_s du_1 - V C_s dp'_1 \quad (5.34)$$

$$(dV)_{dT} = V \alpha_s dT - V C_s du_1 - V C_d dp'_1 \quad (5.35)$$

In an isothermal loading process (process ii) under undrained condition, pore water pressure (du_2) is generated by the mean stress changes (dp). Accordingly, the mean effective stress changes ($dp'_2 = dp - du_2$). During this process, the volume change of pore water, mineral solid and the whole mass due to pressure can be expressed as:

$$(dV_w)_{dp} = -V_w C_w du_2 \quad (5.36)$$

$$(dV_s)_{dp} = -V_s C_s du_2 - V C_s dp'_2 \quad (5.37)$$

$$(dV)_{dp} = -V C_s du_2 - V C_d dp'_2 \quad (5.38)$$

Substituting Equations 5.33-5.38 into Equation 5.1 leads to the same expressions as Equations 5.24 and 5.25, showing the compatibility between the above two different ap-

proaches.

5.4 Thermo-elasto-plastic constitutive relations

The above work should be extended to the thermo-elasto-plastic regimes accounting for the plastic strain in undrained heating processes. As pointed out by Coussy [21], plastic evolutions are induced by the irreversible relative sliding of solid grains (or particles) forming the solid matrix of soils. Thus, the plastic change of the solid part is negligible, while the plastic strain of solid skeleton due to temperature and stress changes should be considered. The skeletal thermal strain is assumed to be entirely elastic ($\alpha_{st} = 0$). The mechanical stress-strain relation is elasto-plastic, considering the skeleton modulus changes due to both temperature and stress, i.e. coupling between mechanical loading path and temperature loading path. Equation 5.11 for the total strain is extended for this purpose:

$$d\boldsymbol{\varepsilon} = \mathbf{C} \left(d\boldsymbol{\sigma} - \mathbf{m}^t du \right) - \frac{1}{3} \mathbf{m}^t \alpha_d dT + \frac{1}{3} \mathbf{m}^t C_s du \quad (5.39)$$

where \mathbf{m} is a unit vector $\mathbf{m}^t = (1, 1, 1)$, \mathbf{C} is the elasto-plastic flexibility matrix of the drained solid skeleton.

The relation of stress-strain-temperature increments can be obtained from Equation 5.39:

$$d\boldsymbol{\sigma} - \left(\mathbf{m}^t - \frac{1}{3} \mathbf{D} \mathbf{m}^t C_s \right) du = \mathbf{D} d\boldsymbol{\varepsilon} + \frac{1}{3} \mathbf{D} \mathbf{m}^t \alpha_d dT \quad (5.40)$$

where $\mathbf{D} = \mathbf{C}^{-1}$ denotes the elasto-plastic stiffness matrix of the drained solid skeleton and has been defined in Chapter 4. This equation defines a Bishop-type generalized effective stress under non-isothermal condition.

In the isotropic stress state, the expression of the total mean stress change (dp) and Lagrangian porosity change ($d\phi$) are derived for the thermo-elasto-plasticity state:

$$dp = \frac{1}{C'_d} d\varepsilon_v + b du + \frac{1}{C'_d} \alpha_d dT \quad (5.41)$$

$$d\phi = -bd\varepsilon_v - \frac{1}{N}du + \alpha_\phi dT \quad (5.42)$$

where $b = 1 - \frac{C_s}{C'_d}$ with C'_d denoting the elasto-plastic compressibility of the drained solid skeleton.

Proceeding as in Section 5.3.2, the thermo-elasto-plastic expressions of volumetric strain and pore water pressure in the undrained heating process can be obtained:

$$d\varepsilon_v = -(n\alpha_w + (1-n)\alpha_s) dT + (nC_w + (1-n)C_s) du + C_s(dp - du) \quad (5.43)$$

$$du = \frac{(C'_d - C_s) dp + n(\alpha_w - \alpha_s) dT}{(C'_d - C_s) + n(C_w - C_s)} \quad (5.44)$$

As in Section 5.3, Equation 5.43 implies an undrained heating condition with a constant water mass content per unit volume ($dm_w=0$) and can be considered as an additional condition for the calculation of pore water pressure.

Following the method of Campanella and Mitchell [15], it gives the expression of the total thermo-elasto-plastic volumetric strain from Equations 5.6 and 5.30, as follows:

$$d\varepsilon_v = C_d dp' + C_s du - \alpha_s dT + \alpha_{st} dT \quad (5.45)$$

By comparing Equation 5.41 to Equation 5.45, it shows that the coefficient α_{st} can be identified as:

$$\alpha_{st} = \frac{(C'_d - C_d)(dp - du)}{dT} \quad (5.46)$$

where C_d is the elasto-plastic compressibility of the drained solid skeleton which is dependent on the stress state but independent of temperature.

Since the constitutive equations are developed from the formulations proposed by Coussy [21], the compressibility of mineral solid part is included. This is different from the conventional constitutive models for soils in undrained conditions. Thus, it is worthwhile to examine the effects of C_s on the results. For this purpose, a parametric study on C_s has been performed by numerical simulation of an undrained heating test of natural Boom Clay

Table 5.1: Numerical simulations of an undrained heating test with different values of C_s .

Simulation test	C_s MPa ⁻¹	C'_d * MPa ⁻¹	$b = 1 - C_s/C'_d$
A	2×10^{-3}	5.4×10^{-3}	0.63000
B	2×10^{-4}		0.96300
C	2×10^{-5}		0.99630
D	2×10^{-6}		0.99963
E	0		1

* value for the initial state with $p'=2.3$ MPa and $T=25^\circ\text{C}$.

(see Section 5.7.1). C_s varies from 2×10^{-3} to 0 MPa⁻¹. Note that the value $C_s=2 \times 10^{-6}$ MPa⁻¹ is the actual value according to Mctigue [55]. The other parameters are fixed (see Table 5.1) and the thermal expansion coefficient of adsorbed water is used. Details of the test and the other parameters determination can be seen in Section 5.7.1.

Figure 5.2 presents the results of this parametric study. Taking simulation E ($C_s=0$) as the reference calculation, it is found that with Biot coefficient b ranging from 0.96300 to 1, varying C_s from 0 to 2×10^{-4} (MPa⁻¹) has a negligible effect on the simulation results (Simulation B, C and D). However, with $b = 0.63$, a significant effect is observed when C_s reaches 2×10^{-3} (MPa⁻¹) (Simulation A). It is worth noting that the compressibility of solid grain (C_s) and the drained soil skeleton (C'_d) in saturated porous rock and concrete are of the same order of magnitude, i.e., the value of b may be as low as 0.5, and the C_s effect could not be neglected. On the contrary, C_s is much smaller than C'_d for most soils, i.e., $b \approx 1$, and the compressibility of solid grain can be neglected in this case ($C_s=0$) [15, 73]. In other words, the incremental expression of stress-strain-temperature can be applied with $C_s=0$:

$$d\boldsymbol{\sigma} = \mathbf{D}d\boldsymbol{\varepsilon} + \mathbf{m}^t du + \frac{1}{3}\mathbf{D}\mathbf{m}^t \alpha_d dT \quad (5.47)$$

with the volumetric strain in the undrained heating process:

$$d\varepsilon_v = -(n\alpha_w + (1-n)\alpha_s) dT + nC_w du \quad (5.48)$$

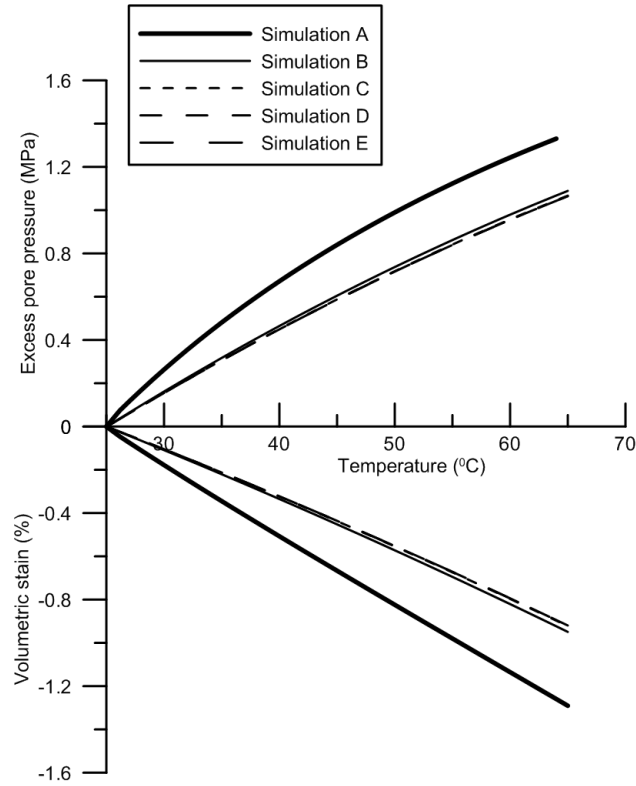


Figure 5.2: Numerical simulation results with different C_s values.

Combining the thermo-mechanical model (Chapter 4), the expressions for effective stress principle (Equation 5.47) and the volumetric strain condition (Equation 5.48), the undrained thermo-mechanical behaviour can be described.

5.5 Thermo-mechanical model for undrained heating process

In this section, the thermo-elasto-plastic undrained behavior is analyzed based on the proposed thermo-mechanical model. During the undrained heating processes, purely elastic or elasto-plastic behaviour will occur, as shown in Figure 5.3. As described by the model, the yield limit shrinks when temperature increases. Meanwhile, the thermally induced pore water pressure reduces the mean effective stress under constant total stress condition. As a result, at point A with a mean effective stress p'_{c0} (see Figure 5.3), three cases exist,

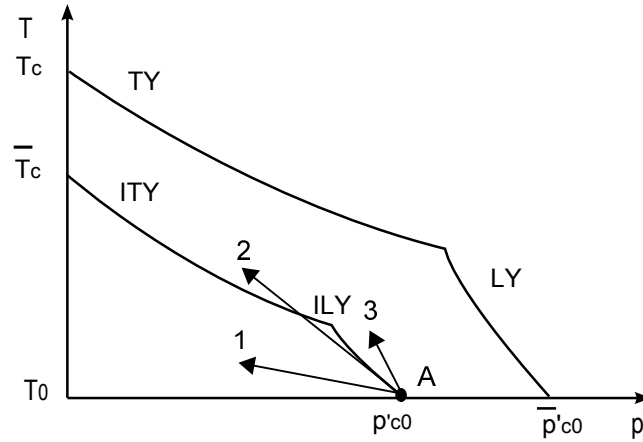


Figure 5.3: Different possibilities during undrained heating process.

depending on the mean effective stress-temperature path ($p' - T$):

1. If the decrease rate of the mean effective stress due to thermally induced pore water pressure increase is faster than the thermal softening rate of ITY surface, a purely elastic unloading process occurs;
2. If the decrease rate of the mean effective stress with temperature is slower than the thermal softening rate of ITY surface but higher than that of ILY surface, the thermo-mechanical loading path will eventually reach the ITY surface, the soil thus undergoing an initial elastic unloading process followed by an elasto-plastic behaviour on the ITY surface;
3. If the decrease rate of the mean effective stress with temperature is lower than the thermal softening rate of ILY surface, the ILY plastic mechanism is activated and elasto-plastic behaviour occurs on ILY. When the effective stress-temperature path reaches the intersection point of ITY and ILY, the actual number of active plastic mechanisms must be determined from the values of the respective plastic multiplier. Three different possible plastic regimes are involved: only ITY mechanism is active; only ILY mechanism is active; both ITY and ILY mechanisms are active.

The aforementioned cases depend on soil type and can easily be determined by considering the initial state $F_0^Y(T, \sigma'_0, X^Y)$ and the elastic trial state $F_1^Y(T, \sigma'_1, X^Y)$. These

different situations can be treated similarly as the solutions described in Chapter 3. No additional algorithm is required.

5.6 Determination of the additional parameters

For the undrained behaviour prediction, the calculation requires determining the thermal expansion coefficients of pore water and mineral solid (α_w and α_s respectively) as well as the compressibility coefficient of pore water (C_w).

Since the thermal expansion coefficient of solid (α_s) is the same as that of drained soil skeleton (α_d) (see Equation 5.16), α_s takes the value of α_d . α_s can be also determined using the data from a physical handbook for the substances similar to the clay minerals, as recommended by Campanella and Mitchell [15].

As described in the international-standard IAPWS-IF97 steam tables, the thermal expansion coefficient and compressibility of free bulk water, α_w and C_w , vary with temperature and pressure [20, 87]. Figure 5.4 presents the values of α_w and C_w at different temperatures and pressures [78]. It shows that α_w varies significantly with temperature but less with pressure, while C_w varies in a small range ($[4.6 \times 10^{-4}; 4.8 \times 10^{-4}]$ (MPa⁻¹) for the values of temperatures (20°C; 90°C) and pressures considered in this study.

The thermal expansion coefficient of free water α_w can be approximated by the following function involving the current pore pressure and temperature [6]:

$$\alpha_w(T, u) = x_0 + (x_1 + y_1 T) \ln(mu) + (x_2 + y_2 T) (\ln(mu))^2 \quad (5.49)$$

where parameters x_0 , x_1 , x_2 , y_1 , y_2 and m are determined by fitting the data in Figure 5.4(a): $x_0 = 4.2 \times 10^{-4} \text{ }^\circ\text{C}^{-1}$, $x_1 = 5.7 \times 10^{-5} \text{ }^\circ\text{C}^{-1}$, $x_2 = 2.4 \times 10^{-6} \text{ }^\circ\text{C}^{-1}$, $y_1 = -1.3 \times 10^{-6} \text{ }^\circ\text{C}^{-2}$, $y_2 = -5.6 \times 10^{-6} \text{ }^\circ\text{C}^{-2}$, $m = 0.0001 \text{ MPa}^{-1}$.

However, Baldi et al. [6] observed from drained heating tests that the prediction for the thermal expansion coefficient of free water is not applicable for the pore water in low-

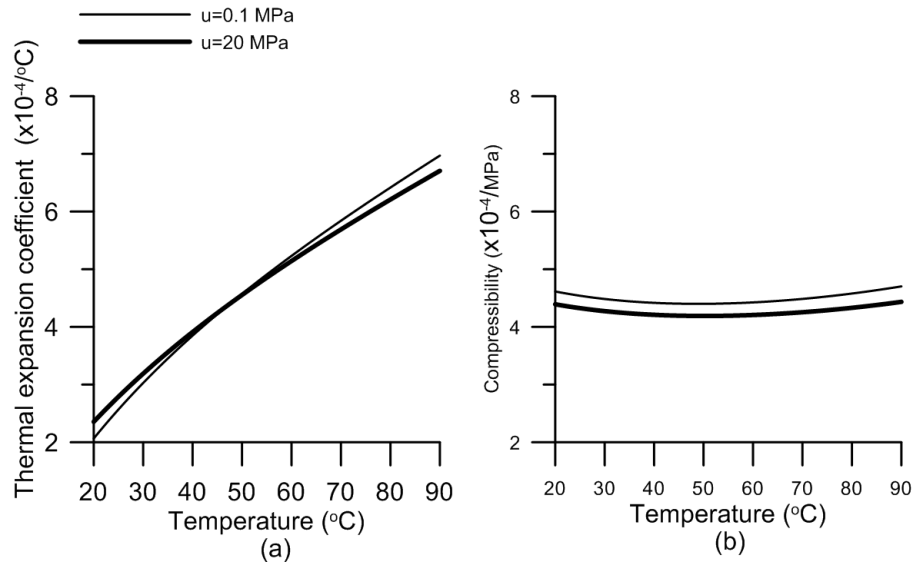


Figure 5.4: Variation of properties of free water with temperature and pressure: (a) thermal expansion coefficient; (b) compressibility.

porosity clay such as the natural Boom Clay. This abnormal phenomenon is also supported by the findings from other experimental observations that the thermal expansion of water in clay pores is different from that of bulk free water [30, 53]. Considering adsorbed water in low-porosity plastic clays, Baldi et al. [6] proposed an alternative expression to Equation 5.49 for the thermal expansion of adsorbed water:

$$\alpha'_w = \frac{\Delta V_a S_s \rho_d}{n} \quad (5.50)$$

where ΔV_a is the volume of expanded adsorbed water per unit surface area of mineral solid and per Kelvin, S_s is the specific surface of soil, and ρ_d is the dry unit mass of soil. To determine the actual thermal expansion coefficient of pore water, Equation 5.49 and Equation 5.50 will be used and compared on the basis of experimental data from undrained heating tests. Furthermore, the compressibility of pore water is assumed to be equal to the one of free bulk water.

5.7 Experimental validation

The capability of the proposed model in describing the undrained behaviour of saturated clays has been validated based on some undrained heating tests on natural Boom Clay and reconstituted Pontida Clay.

5.7.1 Undrained heating test on natural Boom Clay by Monfared et al. (2011)

A undrained heating test on natural Boom Clay was performed using a temperature-controlled triaxial equipment [57]. The sample was saturated under the in-situ mean effective stress of 2.25 MPa and a back pressure of 1 MPa. Then the sample was submitted to a heating process from 25°C to 65°C under undrained condition at a constant total stress of 3.25 MPa. The heating rate was 1 °C/hour. The pore water pressure change was monitored by a pressure transducer at the bottom of the sample and the volume change of the sample was monitored by local LVDT transducers. The experimental results are shown in Figure 5.6.

For the parameters determination, α_s (same as α_d) was calibrated based on the cooling stage of the drained heating test and a value of -5×10^{-5} (1/°C) was found. A constant value for the compressibility of free water, $C_w = 4.7 \times 10^{-4}$ MPa⁻¹, is chosen since it does not vary significantly, as mentioned before. For comparison purposes, both α_w for free water and that accounting for adsorbed water calculated using Equation 5.49 and Equation 5.50 respectively, are used in the simulations. These two cases are referred to as Simulation 1 and Simulation 2, respectively. For Equation 5.50, the required physical parameters were not measured in this test and thus are taken from other studies. The following typical values for the initial state of natural Boom Clay of the site (at the level of the underground laboratory of Mol) after full saturation are adopted [6, 7, 28, 32, 38]: $\Delta V_a = (505.2 + 3.79T) \times 10^{-15}$ m³/°C, with $S_s = 177$ m²/g, $\rho_d = 1.7$ Mg/m³, $n = 37.8\%$ and $w = 27.5\%$. Other soil parameters related to the drained soil skeleton are fixed (see Table 4.1, Chapter

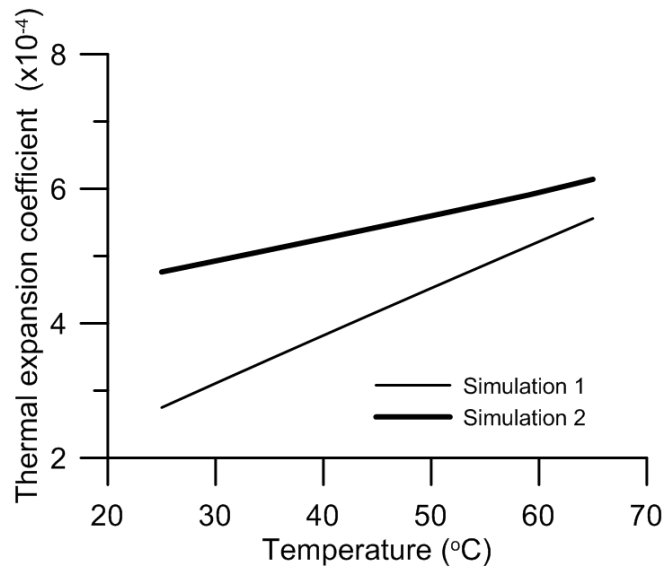


Figure 5.5: Thermal expansion coefficients of free bulk water and adsorbed pore water (Simulation 1 and 2, respectively).

4).

Figure 5.5 presents the thermal expansion coefficients in Simulation 1 and Simulation 2. It is found that the thermal expansion coefficient of adsorbed water is larger than that of free bulk water, at 25°C. On the other hand, the increase rate of the thermal expansion of adsorbed pore water with temperature is slower than that of free bulk water. The same phenomenon has been experimentally observed by Derjaguin et al. [30] who studied the thermal expansion of water confined in nano-pores of silica gel (5 nm in diameter).

Figure 5.6 presents the excess pore water pressure and volumetric strain calculated with both the thermal expansion coefficient of free water and adsorbed water. Comparison of the obtained results (Simulation 1 and Simulation 2) with the experimental data shows that the prediction results with the thermal expansion coefficient of adsorbed water agree better with the experimental results.

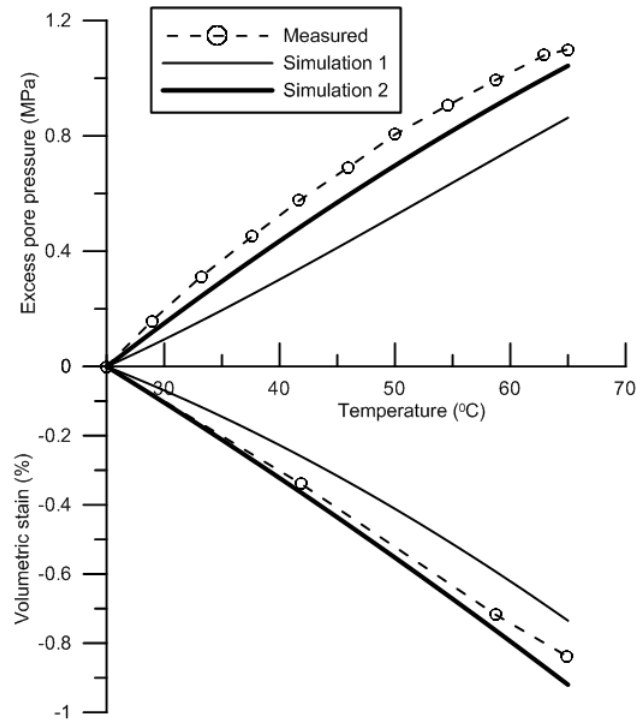


Figure 5.6: Undrained heating test on natural Boom clay from 25°C to 65°C.

5.7.2 Undrained heating test on the reconstituted Pontida Clay by Hueckel et al. (1991).

Hueckel et al. [45] reported the results from undrained heating-cooling tests on reconstituted Pontida Clay. From an initial mean effective stress of 2.5 MPa, the sample was submitted to a heating-cooling cycle from 22°C to 65°C and back to 22°C, then a heating to 95°C under a constant total isotropic stress. The experimental results are shown in Figure 5.8. The thermal expansion coefficient of solids α_s (or α_d) is -5×10^{-5} (1/°C). α_w of both free water and adsorbed water are considered in the simulation. These two situations are referred to as Simulation 3 and Simulation 4, respectively. For adsorbed water, before heating, the following parameters are adopted according to Baldi et al. [6]: $\Delta V_a = (1787.01 + 8.02T) \times 10^{-15}$ m/°C, with $S_s = 37$ m²/g, $\rho_d = 1.5$ Mg/m³, $n = 35\%$, $w = 18.0\%$ and $C_w = 4.7 \times 10^{-4}$ MPa⁻¹. Other soil parameters related to the drained soil skeleton are fixed (see Table 4.1, Chapter 4).

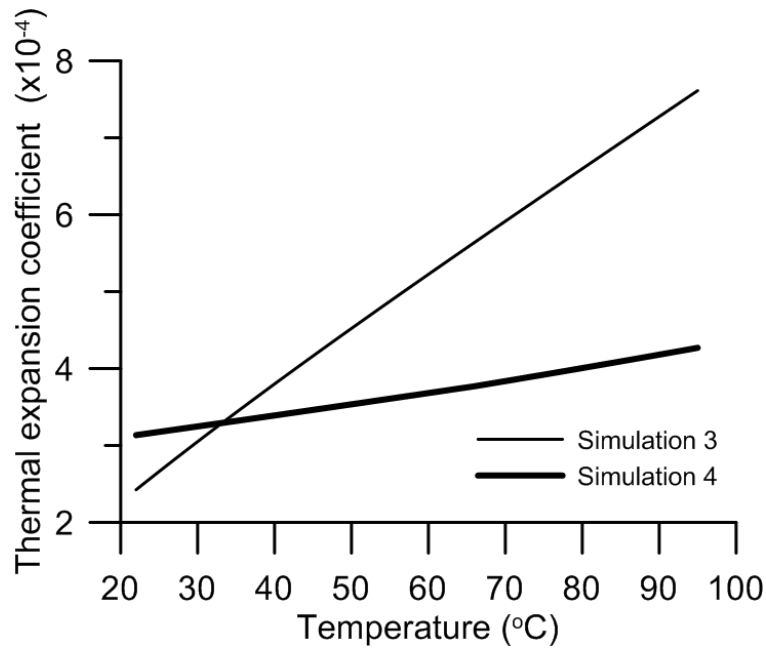


Figure 5.7: Thermal expansion coefficients of free bulk water and adsorbed pore water (Simulation 3 and 4, respectively).

As for natural Boom Clay, at room temperature (around 25°C), the thermal expansion coefficient of adsorbed water is larger and have a smaller increase rate with temperature than that of free bulk water, as shown in Figure 5.7.

The simulation results of excess pore water pressure (Simulation 3 and Simulation 4) are compared with the experimental data in Figure 5.8. It is seen that the simulation results with thermal expansion coefficient of adsorbed water agrees better with the experimental data. The prediction of the pore water pressure with the thermal expansion coefficient of free water differs significantly from the experimental data, especially when temperature is above 65°C.

In the heating-cooling phase from 22°C to 65°C and back to 22°C, irreversible pore water pressure change is observed, and this behaviour is well captured by the proposed model. During the heating stage, the effective stress-temperature path ($T - p'$) reaches ITY plastic mechanism, as in case (2) shown in Figure 5.3. With the plastic hardening of ITY, excess pore water pressure is increased while the loading state remains on the ITY surface. Then during the cooling stage, the response is purely elastic and the pore water

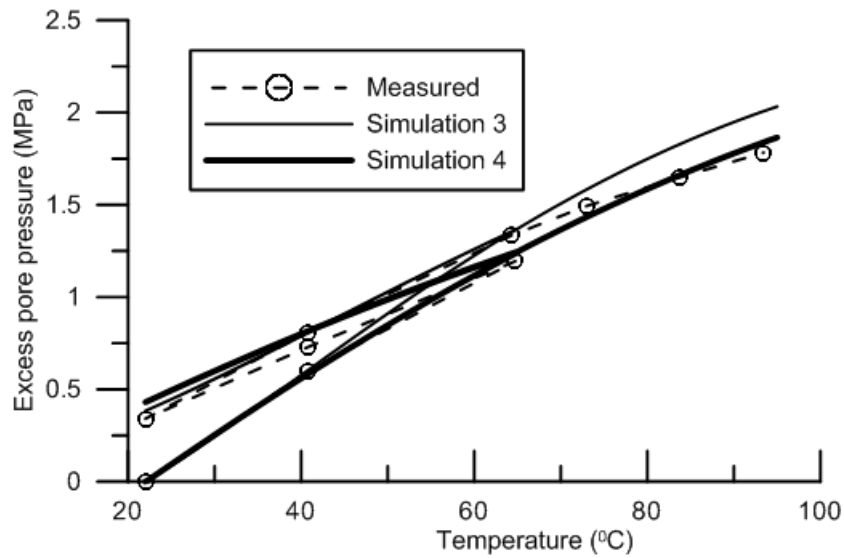


Figure 5.8: Undrained heating-cooling test on reconstituted Pontida Clay.

pressure is thus decreased. Thereby, an irreversible excess pore water pressure is predicted after the heating-cooling cycle because of the plastic regime attained during the heating stage. The model prediction fits experimental data very well. During the re-heating, the soil response is firstly elastic and then elasto-plastic after the $T - p'$ loading path reaches ITY surface again. The irreversible response of the excess pore water pressure upon this heating-cooling process justifies the introduction of a thermal yield mechanism, such as the ITY plastic mechanism in a complete thermo-mechanical model.

5.7.3 Discussion of the simulation results

The numerical simulation results show that the thermal expansion coefficient of pore water in natural Boom Clay and reconstituted Pontida Clay is abnormal, different from the one of free bulk water. Indeed, the thermal expansion coefficient calculated by assuming only adsorbed water in pores gives better simulation results in undrained heating test. However, it should be emphasized that such a calculation based on the assumption of only adsorbed water in pores is only supported by macro-experimental observations. The assumption of only absorbed pore water in clays is required further validation from a more

consistent microstructural mechanism. For the moment, the provided expression of thermal expansion coefficient of adsorbed water seems to be an appropriate and practical choice.

It has been observed that the pore water pressure induced in the undrained heating process depends greatly on the actual thermal expansion coefficient of pore water. It is therefore important to determine this physical parameter for the prediction purposes. Further systematic study on the thermal expansion coefficient of pore water and the corresponding mechanisms are therefore needed for better describing the thermo-mechanical undrained heating process.

5.8 Conclusion

The thermo-elastic equations for undrained heating processes proposed by Campanella and Mitchell [15] and Coussy [21] has been presented. The work of Campanella and Mitchell [15] has been improved and the same equations as those derived by Coussy [21] have been obtained, showing the compatibility of these two approaches.

Based on the work of Coussy [21], the thermo-mechanical model proposed in Chapter 4 (TEAM model) has been extended to account for undrained conditions. This extended formulation introduces two additional parameters: thermal expansion coefficient of pore water α_w , pore water compressibility C_w . The mineral solid compressibility C_s can be neglected since it shows negligible effect on the soil behaviour prediction (C_s being much smaller than C'_d for soils).

The proposed model gives good predictions for the responses of natural Boom clay and reconstituted Pontida Clay under undrained heating conditions, and can well capture the irreversible response of pore water pressure in a heating-cooling process. Besides, accounting the thermal expansion coefficient of adsorbed water provides better simulations, for both natural Boom clay and reconstituted Pontida Clay.

Conclusion

In order to develop a thermo-mechanical constitutive model with an efficient stress integration algorithm for saturated stiff clays, the mechanical behavior of natural Boom Clay in isothermal conditions was first characterized and an adapted Cam Clay model was developed by introducing a Two-surface plastic mechanism allowing satisfactory prediction of the main features of the mechanical behavior of Boom Clay. Afterwards, the thermal effects were considered by assessing the performance of some advanced thermo-mechanical models and by developing an explicit stress integration algorithm for the thermo-mechanical models with a specifically designed adaptive time-stepping scheme. Finally, a new thermo-mechanical model was proposed in the framework of the Two-surface plastic mechanism. The proposed model was validated for the cases of both drained and undrained heating based on the available experimental results. In each stage of development, there was confrontation between experimental data and model predictions. Note that the experimental data are mainly from the laboratory tests on natural Boom Clay.

On the whole, the natural Boom Clay behavior under isothermal conditions is characterized by a limited elastic zone, a highly nonlinear stress-strain response after a brief linear stress-strain behavior and a smooth transition from elastic to plastic response. The Modified Cam Clay model (MCC) was first applied to simulate the natural Boom Clay behavior. It has been found that the MCC gives poor-quality predictions. This may be because the yield surface defined in the MCC cannot well capture the yield behavior of stiff clays as the Boom Clay along different loading paths. In addition, the MCC is based on the classic plasticity with a sharp elastic–plastic transition and thus cannot describe the

smooth elasto-plastic transition behavior.

To overcome the deficiency of MCC in predicting the natural Boom Clay behaviour, an adapted Cam Clay model was developed. This development was conducted in two stages. In the first-level model (ACC-1), we introduced new yield and plastic potential functions. Classic nonlinear elastic rules were also admitted inside the yield surface. It has been found that ACC-1 is better in yield shear stresses prediction than MCC. However, the volumetric predictions of ACC-1 are not consistently better than those of MCC. It has also been found that the adopted nonlinear elastic rules are too simple to adequately describe the smooth behavior of natural Boom Clay inside the ACC-1 surface.

Further analysis of the experimental observations allowed developing a simple Two-surface model (ACC-2) which is derived from the ACC-1. To account for the plastic behavior inside the ACC-1 yield surface (called Yield surface), a new plastic mechanism was proposed with introduction of an additional yield surface called the Inner yield surface. A respective hardening law associated with the Inner yield surface was introduced, enabling the plastic modulus to vary flexibly when the stress approaches the Yield surface and the Inner surface approaches but not goes across the Yield surface. An important feature of this model is that the constitutive equation can be simply formulated based on the consistency condition for the Inner yield surface. Since only the Inner yield surface has to be dealt with, ACC-2 can be efficiently implemented using an explicit stress integration scheme with automatic sub-stepping and error control as for ACC-1. It has been observed that ACC-2 gives better predictions than ACC-1. In particular, the smooth stress-strain behavior can be captured, and in addition, the volumetric strain is well predicted.

As far as the non-isothermal conditions are concerned, an assessment of the existing advanced models, proposed by Cui et al. (2000), Abuel-Naga et al. (2007) and Laloui and François (2008, 2009), was carried out. The capability of the models to capture the observed behavior of clays was assessed on the basis of the experimental evidence. It has been observed that all the three models provide reasonable predictions of the thermo-mechanical behavior of saturated clays. However, each constitutive model has its own

limitations or unclear points from the theoretical point of view.

The stress integration algorithm of the thermo-mechanical model proposed by Cui et al. (2000) at the stress point level using an explicit scheme with adaptive time stepping was developed. A mixed control procedure was described to account for loading paths where both total strain and temperature are imposed. An adaptive sub-stepping procedure accounting for non-isothermal loadings has been proposed. The proposed algorithm also considers the correction of the stress point drift from the yield surface. Specific technical points related to the presence of two plastic mechanisms that can be activated simultaneously have also been discussed. The efficiency of the developed algorithm has been investigated. The interest of using an adaptive time-stepping procedure in comparison to a constant size increments scheme has been evidenced. In particular, the computation time required to achieve a given accuracy is largely reduced if adaptive sub-stepping is considered, for both mechanical and thermal loadings.

A Two-surface thermo-mechanical model (TEAM model) was developed in the framework of the Two-surface plastic mechanism. In the case of isotropic loading, the proposed model extended the model of Cui et al. (2000) to Two-surface formulation after linking the thermal plastic strain and the mechanical one and defining a unique plastic strain along different loading paths. In the case of triaxial loading, the experimental results show that, as at room temperature, the elastic zone is also limited and there is also a smooth elasto-plastic transition for natural Boom clay at high temperatures. It should be noted that the drained shear strength at the critical state of natural Boom Clay is not temperature dependent. The TEAM model adopts a thermally dependent yield surface and a non-associated flow rule. The stress integration algorithm can be effectively implemented based on the algorithm developed for the model of Cui et al. (2000), considering that the Inner yield surface does not cross the Yield surface. The simulation of the drained test shows that this model can capture the main thermo-mechanical features along different loading paths.

The TEAM model was then extended to undrained conditions. The thermo-elastic equations for undrained heating process proposed by Campanella and Mitchell (1968) and

Coussy (2004) were analyzed. The work of Campanella and Mitchell (1968) has been improved and the same equations as those derived by Coussy (2004) have been obtained, showing the compatibility of these two approaches. The extension to undrained conditions required two additional parameters: the thermal expansion coefficient of pore water α_w , and the pore water compressibility C_w . The proposed model can give good predictions for the natural Boom clay and the reconstituted Pontida Clay under undrained heating conditions, and can well capture the irreversible response of pore water pressure in heating-cooling process. Moreover, it was observed that accounting the thermal expansion coefficient of adsorbed water provides better simulations, for both natural Boom clay and reconstituted Pontida Clay.

Bibliography

- [1] H. Abuel-Naga, D. Bergado, A. Bouazza, and G. Ramana. Volume change behaviour of saturated clays under drained heating conditions: Experimental results and constitutive modeling. *Canadian Geotechnical Journal*, 44(8):94–956, 2007.
- [2] H. Abuel-Naga, D. Bergado, A. Bouazza, and M. Pender. Thermomechanical model for saturated clays. *Geotechnique*, 59(3):273–278, 2009.
- [3] H. M. Abuel-Naga, D. T. Bergado, and A. Bouazza. Thermally induced volume change and excess pore water pressure of soft bangkok clay. *Engineering Geology*, 89(1-2):144–154, 2007.
- [4] A. Al Tabbaa and D. M. Wood. An experimentally based bubble model for clay. In *Proceedings of the 3rd International Symposium on Numerical Models in Geomechanics (NUMOG III)*, pages 90–99. Elsevier, 1989.
- [5] G. Baldi, M. Borsetto, T. Hueckel, R. Commission of the European Communities. Directorate-General for Science, and Development. *Calibration of mathematical models for simulation of thermal, seepage and mechanical behaviour of Boom clay*. Commission of the European Communities, Directorate-General Science, Research and Development, 1987.
- [6] G. Baldi, T. Hueckel, and R. Pellegrini. Thermal volume changes of the mineral-water system in low-porosity clay soils. *Canadian geotechnical journal*, 25(4):807–825, 1988.
- [7] G. Baldi, T. Hueckel, A. Peano, and R. Pellegrini. Developments in modelling of thermo-hydro-geomechanical behaviour of boom clay and clay-based buffer materials. *Commission of the European Communities, Nuclear Science and Technology*, page EUR 13365/1 and EUR 13365/2, 1991.
- [8] J. Bardet. Bounding surface plasticity model for sands. *Journal of engineering mechanics*, 112(11):1198–1217, 1986.
- [9] A. Basermann and P. Weidner. A parallel algorithm for determining all eigenvalues of large real symmetric tridiagonal matrices. *Parallel Computing*, 18(10):1129–1141, 1992.
- [10] F. Bernier, G. Volckaert, E. Alonso, and M. Villar. Suction-controlled experiments on boom clay. *Engineering Geology*, 47(4):325–338, 1997.
- [11] F. Bernier, X. L. Li, and W. Bastiaens. Twenty-five years’ geotechnical observation and testing in the tertiary boom clay formation. *Géotechnique*, 57(2):229–237, 2007.
- [12] F. Bernier, X. L. Li, W. Bastiaens, L. Ortiz, M. Van Geet, L. Wouters, B. Frieg, P. Blümling, J. Desrues, G. Viaggiani, et al. Fractures and self-healing within the excavation disturbed zone in clays (selfrac). *Final report to EC (Project FIKW-CT2001-00182)*. EUR, 22585, 2007.

- [13] R. I. Borja. Cam-clay plasticity, part ii. implicit integration of constitutive equation based on a nonlinear elastic stress predictor. *Computer Methods in Applied Mechanics and Engineering*, 88(2):225 – 240, 1991.
- [14] R. I. Borja and S. R. Lee. Cam-clay plasticity. part i. implicit integration of elastoplastic constitutive relations. *Computer Methods in Applied Mechanics and Engineering*, 78(1):49 – 72, 1990.
- [15] R. Campanella and J. Mitchell. Influence of temperature variations on soil behavior. *Journal of the Soil Mechanics and Foundations Division, ASCE*, 94:709–734, 1968.
- [16] C. Cekerevac and L. Laloui. Experimental study of thermal effects on the mechanical behaviour of a clay. *International Journal for Numerical and Analytical Methods in Geomechanics*, 28(3):209 – 228, 2004.
- [17] R. Charlier. Thermal impact on the damaged zone around a radioactive waste disposal in clay host rocks-deliverable d13 – simulation of lab and in situ tests, 2011.
- [18] C. Coll. *Endommagement des roches argileuses et perméabilité induite au voisinage d'ouvrages souterrains*. PhD thesis, Université Joseph-Fourier-Grenoble I, 2005.
- [19] I. Collins and P. Kelly. A thermomechanical analysis of a family of soil models. *Geotechnique*, 52(7):507–518, 2002.
- [20] J. R. Cooper et al. Revised release on the iapws industrial formulation 1997 for the thermodynamic properties of water and steam. *The International Association for the Properties of Water and Steam*, pages 1–48, 2007.
- [21] O. Coussy. *Poromechanics*. John Wiley & Sons Inc, 2004.
- [22] Y. Cui, N. Sultan, and P. Delage. A thermomechanical model for saturated clays. *Canadian Geotechnical Journal*, 37(3):607 – 620, 2000.
- [23] Y. J. Cui and P. Delage. Yielding and plastic behaviour of an unsaturated compacted silt. *Géotechnique*, 46(2):291–311, 1996.
- [24] Y. Dafalias. Bounding surface plasticity. i: Mathematical foundation and hypoplasticity. *Journal of Engineering Mechanics*, 112(9):966–987, 1986.
- [25] Y. Dafalias and L. Herrmann. A bounding surface soil plasticity model. In *International Symposium on Soils under Cyclic and Transient Loading, Swansea, UK*, volume 1, pages 335–345, 1980.
- [26] Y. Dafalias and E. Popov. A model of nonlinearly hardening materials for complex loading. *Acta Mechanica*, 21(3):173–192, 1975.
- [27] C. Del Olmo, V. Fioravante, F. Gera, T. Hueckel, J. Mayor, and R. Pellegrini. Thermomechanical properties of deep argillaceous formations. *Engineering geology*, 41(1): 87–102, 1996.

- [28] P. Delage, T. T. Le, A. M. Tang, Y. J. Cui, and X. L. Li. Suction effects in deep boom clay block samples. *Géotechnique*, 57(1):239–244, 2007.
- [29] C. Delahaye and E. Alonso. Soil heterogeneity and preferential paths for gas migration. *Engineering geology*, 64(2):251–271, 2002.
- [30] B. Derjaguin, V. Karasev, and E. Khromova. Thermal expansion of water in fine pores. *Journal of colloid and interface science*, 109(2):586–587, 1986.
- [31] B. François. Thermo-plasticity of fine-grained soils at various saturation states: Application to nuclear waste disposal. *Ph.D. thesis*, 2008.
- [32] A. Gens, J. Vaunat, B. Garitte, and Y. Wileveau. In situ behaviour of a stiff layered clay subject to thermal loading: observations and interpretation. *Géotechnique*, 57(2):207–228, 2007.
- [33] S. Ghabezloo, J. Sulem, and J. Saint-Marc. The effect of undrained heating on a fluid-saturated hardened cement paste. *Cement and Concrete Research*, 39(1):54–64, 2009.
- [34] J. Graham, N. Tanaka, T. Crilly, and M. Alfaro. Modified cam-clay modelling of temperature effects in clays. *Canadian Geotechnical Journal*, 38(3):608 – 621, 2001.
- [35] B. Hardin. The nature of stress-strain behavior for soils. In *Volume I of Earthquake Engineering and Soil Dynamics—Proceedings of the ASCE Geotechnical Engineering Division Specialty Conference, June 19-21, 1978, Pasadena, California. Sponsored by Geotechnical Engineering Division of ASCE*, number Proceeding, 1978.
- [36] P. Y. Hong, J. M. Pereira, Y. J. Cui, and A. M. Tang. Explicit integration of a thermo-mechanical model for clays. *Computers and Geotechnics*, 46(0):13 – 25, 2012.
- [37] P. Y. Hong, J. M. Pereira, A. M. Tang, and Y. J. Cui. On some advanced thermo-mechanical models for saturated clays. *International Journal for Numerical and Analytical Methods in Geomechanics*, page (in print), 2013. doi: 10.1002/nag.2170.
- [38] S. Horseman, M. Winter, and D. Entwistle. Geotechnical characterization of boom clay in relation to the disposal of radioactive waste. 1987.
- [39] S. Horseman, M. Winter, and D. Entwisle. Triaxial experiments on boom clay. *Engineering Geology Special Publication*, pages 35–35, 1993.
- [40] G. Houlsby and A. Puzrin. *Principles of hyperplasticity: an approach to plasticity theory based on thermodynamic principles*. Springer, 2006.
- [41] G. Houlsby and C. Wroth. The variation of shear modulus of a clay with pressure and overconsolidation ratio. *Soils and Foundation*, 31(3):138–143, 1991.
- [42] G. Houlsby, A. Amorosi, and E. Rojas. Elastic moduli of soils dependent on pressure: a hyperelastic formulation. *Géotechnique*, 55(5):383–392, 2005.

- [43] T. Hueckel and G. Baldi. Thermoplasticity of saturated clays. experimental constitutive study. *Journal of geotechnical engineering*, 116(12):1778 – 1796, 1990.
- [44] T. Hueckel and M. Borsetto. Thermoplasticity of saturated soils and shales. constitutive equations. *Journal of geotechnical engineering*, 116(12):1765 – 1777, 1990.
- [45] T. Hueckel and R. Pellegrini. Thermoplastic modeling of undrained failure of saturated clay due to heating. *Soils and Foundations*, 31(3):1–16, 1991.
- [46] T. Hueckel, B. Francois, and L. Laloui. Explaining thermal failure in saturated clays. *Geotechnique*, 59(3):197 – 212, 2009.
- [47] J. Hujeux. *Calcul numérique de problèmes de consolidation élastoplastique*. PhD thesis, Ecole centrale de Paris, 1979.
- [48] R. D. Krieg. A practical two surface plasticity theory. *Journal of Applied Mechanics*, 42(3):641–646, 1975.
- [49] L. Laloui and C. Cekerevac. Thermo-plasticity of clays: An isotropic yield mechanism. *Computers and Geotechnics*, 30(8):649 – 660, 2003.
- [50] L. Laloui and François. Acme-g-t: Soil thermoplasticity model. *Journal of Engineering Mechanics*, 135:932–944, 2009.
- [51] T. Lê. Comportement thermo-hydro-mécanique de l’argile de boom. *Ph.D. thesis*, 2008.
- [52] X. L. Li, F. Bernier, T. Vietor, and P. Lebon. Thermal impact on the damaged zone around a radioactive waste disposal in clay host rocks-technical annex 1. *Final report to EC (Contract Number: FI6W-CT-2007-036449)*. EUR, 2011.
- [53] P. Low. Nature and properties of water in montmorillonite-water systems. *Soil Science Society of America Journal*, 43(4):651–658, 1979.
- [54] G. McDowell and K. Hau. A generalised modified cam clay model for clay and sand incorporating kinematic hardening and bounding surface plasticity. *Granular Matter*, 6(1):11–16, 2004.
- [55] D. McTigue. Thermoelastic response of fluid-saturated porous rock. *Journal of Geophysical Research*, 91(B9):9533–9542, 1986.
- [56] R. Mitchell. On the yielding and mechanical strength of leda clays. *Canadian Geotechnical Journal*, 7(3):297–312, 1970.
- [57] M. Monfared, J. Sulem, P. Delage, and M. Mohajerani. On the thm behaviour of a sheared boom clay sample: Application to the behaviour and sealing properties of the edz. *Engineering Geology*, 2011.
- [58] Z. Mroz, V. Norris, and O. Zienkiewicz. The application of an anisotropic hardening model in the analysis of elasto-plastic deformation of soils. *Geotechnique*, 29(1), 1979.

- [59] D. Muir Wood. Kinematic hardening model for structured soil. *Numerical Models in Geomechanics*, pages 83–88, 1995.
- [60] NIRAS/ONDRAF. Safety assessment and feasibility interim report (safir) 2. Technical report, Technical overview of the SAFIR 2 report, NIRAS/ONDRAF, 2001.
- [61] D. Potts and L. Zdravković. *Finite element analysis in geotechnical engineering: theory*. Telford, 1999.
- [62] D. Potts and L. Zdravkovic. Some pitfalls when using modified cam clay. *Imperial College, London, UK*, 2000.
- [63] S. Rampello, G. Viggiani, and A. Amorosi. Small-strain stiffness of reconstituted clay compressed along constant triaxial effective stress ratio paths. *Pre-Failure Deformation Behaviour of Geomaterials*, page 89, 1998.
- [64] G. Ranjan and A. Rao. *Basic and applied soil mechanics*. New Age International, 2007.
- [65] J.-C. Robinet, A. Rahbaoui, F. Plas, and P. Lebon. Constitutive thermomechanical model for saturated clays. *Engineering Geology*, 41(1-4):145 – 169, 1996.
- [66] Romero. Characterization and thermo-hydro-mechanical behaviour of unsaturated boom clay : an experimental study. *PhD. Thesis*, UPC, 1999.
- [67] K. Roscoe and J. Burland. On the generalised stress-strain behaviour of "wet" clay. In *Heyman J, Leckie FA, editors. Engineering plasticity*, pages 535–609, Cambridge University Press, 1968.
- [68] M. Rouainia and D. Wood. A kinematic hardening constitutive model for natural clays with loss of structure. *Geotechnique*, 50(2):153–164, 2000.
- [69] A. Schofield and P. Wroth. Critical state soil mechanics. 1968.
- [70] H. Seneviratne, J. Carter, D. Airey, and J. Booker. Review of models for predicting the thermomechanical behaviour of soft clays. *International Journal for Numerical and Analytical Methods in Geomechanics*, 17(10):715 – 733, 1993.
- [71] D. Sheng, S. Sloan, A. Gens, and D. Smith. Finite element formulation and algorithms for unsaturated soils. part i: Theory. *International Journal for Numerical and Analytical Methods in Geomechanics*, 27(9):745–765, AUG 10 2003.
- [72] D. Sheng, D. W. Smith, S. W. Sloan, and A. Gens. Finite element formulation and algorithms for unsaturated soils. part ii: Verification and application. *International Journal for Numerical and Analytical Methods in Geomechanics*, 27(9):767 – 790, 2003.
- [73] A. Skempton. Effective stress in soils, concrete and rocks. In *Pore Pressure and Suction in Soils*, Butterworths, London, pages 4–16, 1961.

- [74] S. Sloan. Substepping schemes for the numerical integration of elastoplastic stress-strain relations. *International Journal for Numerical Methods in Engineering*, 24(5): 893 – 911, 1987.
- [75] S. Sloan, A. Abbo, and D. Sheng. Refined explicit integration of elastoplastic models with automatic error control. *Engineering Computations*, 18(1-2):121–154, 2001.
- [76] P. Smith, R. Jardine, and D. Hight. The yielding of bothkennar clay. *Géotechnique*, 42(2):257–274, 1992.
- [77] W. T. Solowski and D. Gallipoli. Explicit stress integration with error control for the barcelona basic model. part i: Algorithms formulations. *Computers and Geotechnics*, 37(1-2):59 – 67, 2010.
- [78] B. Spang. Excel add-in for properties of water and steam in si-units, 2002. Available from <http://www.cheresources.com/iapwsif97.shtml>, 2002.
- [79] S. Stallebrass and R. Taylor. The development and evaluation of a constitutive model for the prediction of ground movements in overconsolidated clay. *Geotechnique*, 47: 235–253, 1997.
- [80] N. Sultan. Etude du comportement thermo-mécanique de l'argile de boom: expériences et modélisation. *Ph.D. thesis*, 1997.
- [81] N. Sultan, P. Delage, and Y. Cui. Temperature effects on the volume change behaviour of boom clay. *Engineering Geology*, 64(2-3):135 – 145, 2002.
- [82] F. Tavenas, S. Leroueil, P. La Rochelle, and M. Roy. Creep behaviour of an undisturbed lightly overconsolidated clay. *Canadian Geotechnical Journal*, 15(3):402–423, 1978.
- [83] F. Tavenas, J. Des Rosiers, S. Leroueil, P. La Rochelle, and M. Roy. The use of strain energy as a yield and creep criterion for lightly overconsolidated clays. *Geotechnique*, 29(3):285–303, 1979.
- [84] K. Terzaghi. The shearing resistance of saturated soils and the angle between the planes of shear. In *Proceedings of the 1st International Conference on Soil Mechanics and Foundation Engineering*, volume 1, pages 54–56, 1936.
- [85] L. Van Cauteren. Instrumentation programme near the face of an advancing tunnel in boom clay. *The Geotechnics of Hard Soils*, 2:953, 1998.
- [86] J. Vaunat, J. C. Cante, A. Ledesma, and A. Gens. A stress point algorithm for an elastoplastic model in unsaturated soils. *International Journal of Plasticity*, 16(2):121 – 141, 2000.
- [87] W. Wagner, J. Cooper, A. Dittmann, J. Kijima, H. Kretschmar, A. Kruse, R. Mareš, K. Oguchi, H. Sato, I. Stöcker, et al. The iapws industrial formulation 1997 for the thermodynamic properties of water and steam. *Journal of Engineering for Gas Turbines and Power*, 122:150–182, 2000.

-
- [88] S. Wheeler. A rotational hardening elasto-plastic model for clays. In *Proceedings of the International Conference on Soil Mechanics and Foundation Engineering*, volume 1, pages 431–434. AA BALKEMA, 1997.
- [89] S. Wheeler, A. Naatanen, M. Karstunen, and M. Lojander. An anisotropic elastoplastic model for soft clays. *Canadian Geotechnical Journal*, 40(2):403–418, 2003. ISSN 1208-6010.
- [90] D. Wood. *Soil behaviour and critical state soil mechanics*. Cambridge Univ Pr, 1990.
- [91] D. Wood. Experimental inspiration for kinematic hardening soil models. *Journal of engineering mechanics*, 130:656, 2004.
- [92] H. S. Yu, C. Khong, and J. Wang. A unified plasticity model for cyclic behaviour of clay and sand. *Mechanics Research Communications*, 34(2):97–114, 2007.
- [93] M. Zytynski, M. Randolph, R. Nova, and C. Wroth. On modelling the unloading-reloading behaviour of soils. *International Journal for Numerical and Analytical Methods in Geomechanics*, 2(1):87–93, 1978.